THERMOPHORESIS OF AEROSOL PARTICLES
IN TWO—DIMENSIONAL LAMINAR FLOW

A Thesis Submitted
In Partial Fulfilment of the Requirements
for the Degree of

DOCTOR OF PHILOSOPHY

by

S. JAYARAJ

to the

DEPARTMENT OF MECHANICAL ENGINEERING

INDIAN INSTITUTE OF TECHNOLOGY, KANPUR

APRIL, 1988

CERTIFICATE

This is to certify that this thesis titled,
"Thermophoresis of Aerosol Particles in Two-Dimensional
Laminar Flow", by S. Jayaraj is a record of work carried
out under my supervision and has not been submitted
elsewhere for a degree.
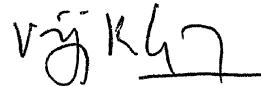
(Dr. Vijay K. Garg)
Professor
Department of Mechanical Engineering
Indian Institute of Technology
Kanpur.

April 1988.

To

the memory of my

Loving Grand Mother Santhammal

ACKNOWLEDGEMENTS

CONTENTS

LIST OF TABLES

LIST OF FIGURES

Figure   Page

LIST OF SYMBOLS

Lower case symbols given in parentheses are the
dimensional counterparts of the dimensionless equivalents
written on the same line.

a_1, a_2, b_1, b_2	constants used in Eqn. (2.33)
A_1, B_1, C_1	constants used in Eqn. (1.4)
C,(c)	aerosol particle concentration
C_f	local skin friction coefficient
C_m	coefficient of gas kinetic isothermal slip
C_p	specific heat at constant pressure
C_t	temperature jump coefficient
D	Brownian diffusion coefficient
Ec	Eckert number $(= u_\infty^2 / C_p t_\infty)$
E_T	cumulative particle deposition efficiency
Gr_x	local Grashof number
h	local heat transfer coefficient
h_1, h_2	jet thicknesses (Fig. 2.2)
H	ratio of jet nozzle height from the plate to L
k_g	thermal conductivity of gas
k_p	thermal conductivity of particle
k_t	thermal slip coefficient
K	thermophoretic coefficient

L	characteristic length (either the slot jet thickness in Figs. 2.2 and 2.3 or the radius of the cylinder in Fig. 2.7
$\mathcal{L}$	fluid thickness measured from the surface, used for grid adaptation (Eqn. 3.19)
M	Mach number
m	wedge constant
n	total number of steps in the Y-direction
Nu	local Nusselt number
Nu_m	mean Nusselt number
P,(p)	pressure
Pr	Prandtl number
Re	Reynolds number $(= u_\infty L/\nu)$
R_p	particle radius
T,(t)	temperature
U,(u)	velocity component in the X-direction
U_s,(u_s)	potential flow velocity on the body surface
V,(v)	velocity component in the Y-direction
V_T,(v_t)	thermophoretic velocity in the Y-direction
w	weight function for grid adaptation
$\vec{w}_t$	thermophoretic velocity vector
X,(x)	streamwise coordinate along the body surface
Y,(y)	transverse coordinate normal to the body surface

Y_c	dimensionless critical layer thickness
$Z,(z)$	complex variable $Z = X+iY$, $(z = x+iy)$ for potential flow calculation (Eqns. (2.33) and (2.37)
α,β,γ	angles between jets (Fig. 2.2)
δ_c	concentration boundary layer thickness
δ_u	hydrodynamic boundary layer thickness
δ_θ	thermal boundary layer thickness
δ_1	displacement thickness
δ_2	momentum thickness
η	similarity variable for the wedge
θ	normalised temperature $[=(t-t_\infty)/(t_w-t_\infty)]$
θ_1	normalised wall temperature $[=t_w/(t_\infty-t_w)]$ in Eqn. (1.5)
λ	mean free path
μ	dynamic viscosity of the fluid
ν	kinematic viscosity of the fluid
$\epsilon,(\xi)$	complex velocity in potential flow calculation
ρ	density of the fluid
σ	ratio of smaller to larger mesh size
Φ	angle measured from stagnation point for flow past a cylinder
Ψ	stream function

Subscripts

j	location in X-direction
k	location in Y-direction
w	wall
∞	free stream
sep.	separation

Superscript

*	value from previous iteration

SYNOPSIS

The phenomenon of thermophoresis plays a vital role
in the mass transfer mechanism of several devices involving
small micron sized particles and large temperature gra-
dients in the flow field. This dissertation analyses the
two-dimensional, laminar, thermophoretic flow over an
inclined plate and over a circular cylinder, and presents
results for the hydrodynamic, thermal and particle concen-
tration boundary layers over a wide range of parameters
for cold,heated and adiabatic wall conditions. Special
emphasis is placed on the external aerosol deposition
process.

The governing boundary layer equations are solved
using an implicit finite-difference scheme. A marching
solution procedure is employed whereby the velocity, tem-
perature and particle concentration distributions at any
downstream location are determined knowing only the flow
field upstream of that location. Solution is thus obtained
in a series of steps covering the complete flow field

starting from the stagnation point. While a non-uniform grid is used in the marching direction, the grid in the transverse direction is self-adapted to the gradient of a selected function (velocity or temperature or particle concentration) in the flow field. A variable mesh technique is employed to preserve the second order accuracy of the velocity and temperature profiles in the transverse direction.

For flow resulting from the impingement of a slot jet over an inclined plate, the unsymmetrical pressure distribution on either side of the stagnation point is computed by considering the direct impingement of two unequal inviscid jets. The hydrodynamic and thermal boundary layer results obtained using the present procedure at zero incidence are in perfect agreement with the standard similarity solution (Blasius flow). Results for local skin friction coefficient and Nusselt number in the case of 90° angle of inclination of the plate are also in complete agreement with earlier results. For angles other than 0 and 90°, this is the first study.

The behaviour of the particle concentration boundary layer for the cold plate condition is found to be similar to that of the velocity and thermal boundary layers for different angles of inclination, β, of the plate. Near the

stagnation point the hydrodynamic, thermal and concentra-
tion boundary layer thicknesses decrease as β is reduced.
Away from the stagnation point the situation is reversed
except for $\beta = 90^\circ$. Also, for $\beta = 90^\circ$, all boundary layer
thicknesses are almost constant over half the jet thickness
on either side of the stagnation point. The presence of
the stagnation point (at non-zero angles of inclination)
changes the transverse velocity distribution considerably.
While it is always positive for $\beta = 0$, it is negative over
most of the plate length when $\beta \neq 0$. The local skin fri-
ction coefficient displays a large value close to the
stagnation point for small values of angle β. For $\beta = 15^\circ$
the local Nusselt number near the stagnation point is
about ten times that far away from the stagnation point.
However, this ratio is only about two for $\beta = 90^\circ$.

For cold plate conditions the particle concentration
at the wall, C_w, is found to depend mainly on the wall tempe-
rature, T_w and the thermophoretic coefficient, K. It remain:
almost independent of the angle of inclination of the plate,
and the location along the plate as long as K and
T_w are constant. The wall concentration increases
as the wall temperature increases or as the thermophoretic
coefficient decreases; the increase being marginal at
higher K values. However, with zero angle of inclination

of the plate, the wall concentration drops towards zero for thermophoretic coefficients very close to zero. For any other angle of inclination the dimensionless wall concentration reaches unity at $K = 0$. For heated plate conditions the presence of a critical layer adjacent to the wall is demonstrated. It is established that irrespective of the angle of inclination the particle concentration in the critical layer near the heated plate approaches $\pm \infty$ when Pr.K $\gtrless$ 1. The critical layer thickness increases as

(i)   the thermophoretic coefficient increases; the increase being linear at larger K values

(ii) the hot wall temperature increases

(iii) the distance from the stagnation point increases; the increase being appreciable for smaller angles of inclination, and

(iv) the angle of inclination increases.

The cold wall temperature profiles exhibit a peak within the thermal boundary layer at higher Eckert number, Ec, values. Accordingly, the particle concentration at the inclined plate surface decreases as Ec increases. Moreover, for smaller inclination angles the dimensionless concentration profiles also exhibit a peak value (> 1) for

Ec $\gtrsim$ 3. For adiabatic plate conditions the concentra-
tion profiles are similar to those for the hot plate
except that C_w = O and the particle concentration gradient
at the plate is zero.

For flow past a circular cylinder both theoretical
and experimental pressure distributions are considered
for the boundary layer analysis. The hydrodynamic points
of separation obtained in both cases, (105.5^o and 81° res-
pectively), are in perfect agreement with the values
reported in literature. A comparison of the boundary
layer results for theoretical and experimental pressure
distributions at a location $\Phi \lesssim$ 60° from the stagnation
point shows slightly larger (velocity, thermal and parti-
cle concentration) boundary layer thicknesses in the latter
case. However, near Φ = 81°, this difference is consi-
derable. For flow past a cold cylinder also, the wall
concentration is constant with respect to the nature of
the pressure distribution over the cylinder (experimental
or theoretical), and location along the cylinder surface,
as long as the wall temperature and K are constant. A
similar observation for flow over an inclined plate
implies an almost uniform particle

concentration at any two-dimensional surface in laminar flow as long as T_w (< 1) and K are constant. At large Ec the peak in temperature profile is quite appreciable and occurs very close to the cylinder surface. Accordingly, the particle concentration within the boundary layer increases as high as 20% above that of the free stream value (at Ec = 10). With adiabatic wall condition (C_w = 0) this increase is still higher (> 40% at Ec = 10). The cold cylinder wall concentration reduces as Ec > 0 and reaches zero at Ec approaching a value of 10. The critical concentration layer thickness for a heated cylinder increases as we move away from the stagnation point. Eventhough the overall effect of the pressure gradient, dP/dX, on the cold wall particle concentration is found to be negligible for Ec = 0, it is significant over either a hot wall or a cold wall with viscous dissipation. Hence in practical situations (where generally Ec ≠ 0) it is essential to consider the pressure gradient effect.

From a comparison among the different cases studied, smaller angles of inclination when the wall is long, and larger angles of inclination when it is short are preferred to obtain best results on the hot side of heat exchanger equipment where the

aim is to minimize particle deposition on the walls. The reverse is appropriate for the cold side. Also one should be careful about the parameter Pr.K for hot wall applications as theoretically $C_w = +\infty$ when Pr.K > 1. These considerations are critical for high temperature gas turbine applications as the thermophoretic phenomena could off-set remarkably the advantages of transpiration cooling of the blade surface. The external small particle deposition process provides one of the main mechanisms by which the optical fiber preforms are constructed using the Outside Vapour Deposition (OVD) process.

PUBLICATIONS BASED ON THE PRESENT WORK

Based on the present investigation the following publications/presentations have resulted so far :

1.   'Thermophoresis of Aerosol Particles in Laminar Flow Over Inclined Plates', Int. J. Heat Mass Transfer, Vol. 31, No.4, 1988, pp. 875-890.

2.   'Boundary Layer Analysis for Two-Dimensional Slot Jet Impingement on Inclined Plates', J. Heat Transfer, accepted for publication (2/88).

3.   'Thermophoretic Deposition over a Cylinder', AIAA J. Thermophys. and Heat Transfer, submitted.

4.   'Analysis of Laminar Flow and Heat Transfer for Two-Dimensional Jet Impingement Over Inclined Plates', Proc. Int. Conf. Computational Mech., Tokyo, May 1986, pp. VIII201-VIII206.

5.   'Application of Self-Adaptive Grid Method in Thermo-Phoretic Flow with Non-Zero Pressure Gradient', Proc. 15th, Nat. Conf. Fluid Mech. and Fluid Power, Srinagar, July 1987, pp. 595-600.

6.   'Thermophoretic Deposition Due to Jet Impingement on an Inclined Plate', in 'Numerical Methods in Heat Transfer', (eds.) A. F. Emery and R. W. Douglass, HTD-Vol. 88, ASME, New York, 1987, pp. 59-66.

7. 'Thermophoretic Transport of Small Particles in Cross Flow Over a Circular Cylinder,' AIAA Paper No. 88-0656, <u>AIAA 26th Aerospace Sci. Meet,</u> Reno, Nevada, Jan. 1988.

8. 'Computational Analysis of Fluid Flow and Heat Transfer Characteristics of Obliquely Impinging Jets,' <u>Proc. Int. Conf. Computational Engg. Sci.,</u> Atlanta, April 1988.

CHAPTER   1

INTRODUCTION

Thermophoresis is the phenomenon by which submicron
sized particles suspended in a gas acquire a velocity in
the direction of decreasing temperature. This phenomenon
causes the aerosol particles to be driven away from a hot
surface and towards a cold one. This is similar to the
phenomenon of photophoresis caused by an intense beam of
light making the particles to move either in the direction
of radiation flux or against it. The thermophoretic force
experienced by the small particles is caused by differen-
tial molecular bombardment giving rise to a radiometric
force (Green and Lane, 1964). The latter, like other
interactions between particles and a gas, depends essen-
tially upon the ratio of the particle radius to the mean
free path of the gas molecules. The resulting thermopho-
retic force is proportional to the temperature gradient
and depends upon the thermal conductivity of aerosol
particles and carrier gas. Thermophoresis is of consi-
derable importance for particles as large as 10 μm in

radius and temperature gradients of the order of
5 K/mm.

The phenomenon of thermophoresis is of considerable
practical importance as detailed by Green and Lane (1964)
and by Fuchs (1966). Vapour and/or particle mass trans-
port and/or deposition is central to a variety of engineer-
ing fields, including materials technology (electronic
device fabrication, chemical coating of metals, etc.), gas
clean-up (e.g., filteration), and the corrosion and/or
fouling of heat exchangers and gas turbine equipment. In
the latter case the sharply increasing cost of high-grade
fuels has stimulated a renewed interest in the combustion
of coal derived or lower grade residual petroleum derived
fuels, each associated with inorganic impurities which form
ash or salt deposits. At the same time, the need for
higher turbine inlet temperature, required for lower fuel
consumption, demands novel, more efficient turbine blade
cooling schemes, such as film cooling or full coverage
transpiration cooling. Under these combined circumstances
thermal diffusion (i.e., thermophoresis for small parti-
cles) plays an important role in determining mass deposi-
tion rates, as demonstrated (principally in the absence
of viscous dissipation and/or transpiration or film cooling)

by Goren (1977) and in the more general case by Gokoglu
and Rosner (1986). It has been demonstrated that thermo-
phoresis is the dominant mass transfer mechanism in the
Modified Chemical Vapour Deposition (MCVD) and Outside
Vapour Deposition (OVD) processes (used in the fabrication
of optical fiber preforms) by comparing experimental mea-
surements and quantitative theoretical predictions
(Simpkins et al., 1979; Walker et al., 1980; Alam and
Mehrotra, 1987). Moreover this subject is currently
of importance in view of its relevance to postulated
accidents by radioactive particle deposition in nuclear
reactors. The fact that scrubbing is more effective when
dusty air is preheated has been ascribed to thermophoresis.
Another effect of thermophoresis, namely, the repulsion of
particles from a hot wall and the formation of a dust-free
layer around hot objects, has also been observed.

1.1 Literature Survey

Movement of particles in a thermal gradient has been
studied by a number of workers specially in connection with
the dust-free space surrounding hot bodies. The fundamental
physical process responsible for the phenomenon of thermo-
phoresis was first investigated by Maxwell (cf. Kennard,
1938), in an attempt to explain the radiometric effect.

The extensive literature on thermophoresis contains a
number of conflicting results, both theoretical and
experimental. The following gives a brief review of the
existing important experimental and theoretical studies
on this problem.

1.1.1 Thermophoretic Coefficient

The phenomenon of thermophoresis is caused by the
so-called radiometric forces, which because of the gaseous
medium act upon non-uniformly heated particles present in
the medium. The radiometric force is developed due to
the fact that gaseous molecules are repulsed from the
hotter side of a particle with a greater velocity than
from the cooler side. That is why particles transmit im-
pulses directed toward a lower temperature. The velocity
acquired by the small particles relative to the gas velo-
city is known as the thermophoretic velocity. The initial
studies of thermophoretic transport involved the simple
one-dimensional flows for the measurement of this velocity.
The thermophoretic velocity, $\vec{w}_t$, is found to be proportional
to the product of the temperature gradient in the flow
field and ν/t, where ν is the kinematic viscosity of the
gas and t is its absolute temperature. The proportionality
constant in the expression for $\vec{w}_t$ is termed as the

thermophoretic coefficient, K. The value of this
coefficient depends on the molecular flow regime. A
measure of this regime is provided by the Knudsen number
which is the ratio of the molecular mean free path, λ ,
to the diameter of the particle, $2R_p$. For $R_p \ll \lambda$ (free
molecular flow), Waldmann (1959) observed that the thermo-
phoretic velocity is independent of the particle radius
and the thermophoretic coefficient has a constant value
close to 0.75 for elastic collisions of molecules with
the aerosol particles and 0.54 for collisions resulting in
condensation and reevaporation. Epstein was the first to
calculate the thermophoretic velocity in the limit of
large size particles ($R_p \gg \lambda$; slip flow) by solving the
equations of viscous hydrodynamics (cf. Derjaguin et al.,
1976). With an arbitrary value of thermal slip coeffi-
cient, $k_t = 0.75$, the Epstein formula for thermophoretic
coefficient is

$$K = k_t \frac{k_g}{k_g + k_p/2} \qquad (1.1)$$

where k_g and k_p are, respectively, the thermal conductivity
of the gas and of the particles. Brock (1962) made the
formula more precise by using an approximate solution of

the Navier-Stokes equations for the velocity field near a particle while taking into account the particle radius of the order of the mean free path, (i.e., $R_p \simeq \lambda$). His formula for K is

$$K = k_t \frac{1 + C_t \ \lambda/R_p \cdot k_p/k_g}{(1+k_p/2k_g + C_t \ \lambda/R_p \cdot k_p/k_g)(1+2C_m \cdot \lambda/R_p)} \qquad (1.2)$$

where C_t is the temperature jump coefficient and C_m is the coefficient of the gas kinetic isothermal slip. Here again k_t is assumed to be 0.75. The values of C_t range from 1.875 to 2.48 and values of C_m range from 1.00 to 1.27. A review of these values and deductions may be seen in the paper by Street (1960). Brock's result, with $k_t = 0.75$, is found not to be in good agreement with the experimental data for particles of high thermal conductivity, although the discrepancy is much less than that obtained using the Epstein result.

Following a different approach Derjaguin et al. (1965 and 1966) reported the following relation for K :

$$K = k_t \frac{1+C_t \ \lambda/R_p \cdot k_p/k_g}{1+k_p/2k_g+C_t \ \lambda/R_p \cdot k_p/k_g} \qquad . \qquad (1.3)$$

In the first approximation k_t was assumed to be equal to

1.5. Careful experimental measurements with oil mist and NaCl aerosol by Derjaguin et al. (1976) indicate that K has a maximum value of 0.93 at $\lambda/R_p = 1.8$. Equation (1.3) for K is found to hold good over a large range of λ/R_p values and also for a variety of aerosols. Using the experimental value of thermophoretic velocity as the basis, following values of k_t were derived by Derjaguin et al. (1976) :

$$k_t = 1.13 \text{ from Eqn. (1.1)},$$
$$k_t = 1.09 \text{ from Eqn. (1.2)},$$
$$\text{and } k_t = 1.07 \text{ from Eqn. (1.3)}.$$

Springer (1970) made an attempt to construct an interpolation formula which matches the theory in the entire Knudsen number range from near-continuum conditions to free molecular (collisionless) limit. However, his formula was rather complicated eventhough it agreed reasonably well with experimental results. Moreover for the slip flow limit, the empirical equation used by Springer employed the Maxwell value for k_t, which requires for the best fit an unrealistic value for C_t. A critical review of the data and the theoretical expressions for thermophoretic coefficients was given by Talbot et al. (1980). An empirical expression for K approximately valid for all Knudsen

numbers has also been given by Talbot et al.,

$$K = 2k_t \frac{(k_g/k_p + C_t \, \lambda/R_p)[1 + \lambda/R_p(A_1 + B_1 \, e^{-C_1 R_p/\lambda})]}{(1 + 3C_m \, \lambda/R_p)(1 + 2k_g/k_p + 2C_t \, \lambda/R_p)} \qquad (1.4)$$

in which the constants have the values $A_1 = 1.20$, $B_1 = 0.41$, $C_1 = 0.88$, $k_t = 1.17$, $C_m = 1.14$ and $C_t = 2.18$. After a series of comparisons with the available data on thermo-phoresis, Talbot et al. reported that the empirical rela-tion (1.4) appears reasonably satisfactory for the entire range, $0 \leq \lambda/R_p \leq \infty$. Nevertheless, in all the theoretical thermophoretic flow analysis reviewed in Section 1.1.2, (except that of Gokoglu and Rosner), it was justified that K can be treated as a specified constant of order 1 and independent of the temperature in the flow field.

Thermophoresis in laminar flows has been studied experimentally by Goldsmith and May (1966), Waldmann and Schmitt (1966), Fulford et al. (1971), Derjaguin et al. (1976), Talbot et al. (1980), and others. Most of the recent experimental determinations of the thermophoretic force or velocity have been carried out by one of the two methods. One method employs a modified Millikan cell wherein a charged particle is held at rest or its velocity

measured under the combined action of gravity, thermal and electrostatic forces (Waldman and Schmitt, 1966). The other method involves the observation of particles moving along a narrow channel, either horizontal or vertical, under the action of a parallel or transverse temperature gradient (Derjaguin et al. 1976). A Laser-Doppler Velocimeter (LDV) study (by Talbot et al. 1980) of the velocity profiles in the laminar boundary layer adjacent to a heated flat plate at zero incidence revealed that the seed particles used for LDV measurements were driven away from the plate surface by thermophoretic forces, causing a particle-free region within the boundary layer of approximately one half the boundary layer thickness. For a review of the experimental data on thermophoresis Fuchs (1966) should be consulted.

1.1.2 Thermophoretic Flow Investigations

Thermophoretic deposition of small particles in laminar tube flow and in natural convection flow over a vertical plate have been analysed by Walker et al. (1979) and Epstein et al. (1985), respectively. These two studies are similar to that of Goren (1977) which will be elaborated later in this section. However, the scope of both these studies is limited to cold surface conditions only.

Assuming a fully developed laminar incompressible flow in the circular tube Walker et al. (1979) found that a fraction of the particles present initially in the stream get deposited on the cold tube wall. The effects of Brownian diffusion were rigorously included by the use of matched asymptotic expansions. However, their similarity solution is valid only within a short axial distance of the start of constant wall temperature, t_w. Using numerical methods, the solution was extended downstream and the cumulative deposition efficiency at any wall temperature and Pr.K value was found to rapidly approach an asymptotic limit. Here, Pr is the Prandtl number. The value of this limit, E_T, is related to Pr.K, the normalised wall temperature, θ_1 [$= t_w/(t_\infty - t_w)$], and the wall concentration, C_w, as

$$E_T = (Pr.K.C_w)/ \theta_1 .\qquad (1.5)$$

Both laminar and turbulent natural convection boundary layer flow on a cold vertical plate have been considered for thermophoretic analysis by Epstein et al. (1985). The governing equations reduce to second order ordinary differential equations which are solved numerically for specified Pr, K and wall temperature. Results similar to

Goren (1977) were obtained for wall concentration in both laminar and turbulent natural convection flows. Also it was noted that while the particle concentration distribution for laminar flow differs notably in shape from that for the turbulent flow both profiles converge to practically the same particle concentration at the wall. Also the change in Grashof number, Gr_x, has no significant effect on the wall concentration, C_w. Epstein et al. derived a relation between particle concentration, C_w and its gradient at the surface, $C'(0)$, as

$$C_w = - \frac{t_w/t_\infty}{1-t_w/t_\infty} \cdot \frac{C'(0)}{\theta'(0)} \qquad (1.6)$$

where $\theta'(0)$ is the derivative of the normalised temperature, $\theta[=(t-t_\infty)/(t_w-t_\infty)]$, at the wall. Accordingly, it was argued that the change in concentration gradient on the surface accompanied by a corresponding change in the wall temperature gradient keeps the particle concentration at the wall almost constant. The simple function

$$C_w = \frac{1-(K.Pr)^{1.25t_w/t_\infty}}{1-(K.Pr)^{1.25}} \, , \qquad (1.7)$$

was found to relate the computed values of C_w within a

relative error of < 3% for the values of Pr, Gr_x, K and t_w/t_∞ investigated by Epstein et al. Moreover, by replacing the numerical exponent 1.25 by 1.1 in the numerator and denominator of equation (1.7), the calculated results of Goren (1977) for deposition in forced incompressible laminar flow over a cold flat plate can be accurately reproduced.

Including a volumetric heating term in the energy equation the thermophoretic flow through a circular tube has been studied by Morse and co-workers. These studies have direct application in the laser modification of thermophoretic deposition in MCVD process used in the manufacture of optical fiber preforms. The first work (Morse and Cipolla Jr., 1984) deals with a tubular flow of particle laden gas axially heated by the absorption of laser energy, neglecting emission and scattering. By a series of simplifications they reduced the governing equations for temperature and particle concentration into those for a one-dimensional problem and solved them for two limiting forms of distribution of laser energy throughout the tube cross section. Accordingly, it was found that with laser radiation of modest power (10 W), almost all the aerosol is evacuated from the central region of the tube causing quite

a large aerosol concentration in the vicinity of the tube wall. A consequence is that in sufficiently long tubes the total deposition efficiency can be made to approach unity. However, since highly focussed radiation interacts with very few particles (causing local heating) which through thermophoresis are then repelled from the heating zone, the consequent increase in concentration elsewhere is negligible.

Morse et al. (1985) extended their earlier work with the addition of another heat source in the wall with an arbitrary temperature distribution apart from the axial laser radiation in the circular tube. Solution in this case is carried out for a set of property values by a finite-difference marching technique. It is found that the particle deposition rate increases with the laser intensity. The presence of wall heat source further increases the deposition efficiency as the heated wall forces the particles towards the centre of the tube (region of maximum laser intensity). The buoyancy effect of axial laser heating (constant intensity) on the thermophoretic flow in a vertical tube is the concern of Wang et al. (1985). The particle trajectories are calculated from a one-dimensional formulation of the combined natural convection problem with constant wall temperature boundary condition.

A universal velocity profile has been found that minimizes the length over which 99% of the particles are deposited on the wall. However, these results are only qualitative since the assumption of no variation of velocity and temperature in the axial direction is not true.

A detailed theoretical analysis of laminar thermophoretic flow over a flat plate at zero incidence was provided by Goren (1977). A similarity formulation of the boundary layer equations was carried out by him in the absence of Brownian diffusion whose effect is only to form a very thin sublayer even on the boundary layer scale. For a cold wall the particle concentration decreases monotonically from the free stream value as the wall is approached and a finite concentration at the wall is attained depending upon the wall temperature. With the increase of thermophoretic coefficient, K, the wall concentration is found to decrease for the flat plate at zero incidence. For a heated wall the presence of a critical layer within the concentration boundary layer over a flat plate is proved by Goren. He also elaborated the importance of the factor Pr.K in determining the concentration profile over a hot wall. For zero free stream Mach number M_∞ (no viscous dissipation),

the concentration profile becomes identical to the tempera-
ture profile when Pr.K = 1. Moreover, the particle concen-
tration at the critical layer near the heated flat plate
suddenly approaches $\pm \infty$ when Pr.K $\gtrless$ 1. The thickness of
the critical concentration layer is found to be a function
of the wall temperature and it increases parabolically
with K. The effect of M_∞ greater than zero (non-zero
viscous dissipation) has also been studied by Goren for
the flow past a flat plate at zero incidence.

The first thermophoretic analysis for an external flow
in the presence of a non-zero pressure gradient has been
provided by Homsy et al. (1981). They apply the Blasius
series solution to the transverse flow past a circular
cylinder. Results are presented for the particle flux
coefficients as functions of K and wall temperature for
Pr = 0.71. Knowing the characterizing constants of any
outer potential flow, one can calculate the corresponding
deposition profile from these particle flux coefficients.
The local flux profile shown for flow past a circular
cylinder is parabolic with a maximum value $\simeq$ 0.24 at the
stagnation point and zero near the cylinder angle, $\phi = 90^o$.
For still larger ϕ physically impossible negative values
result. The total deposition rate was found to decrease

monotonically with increasing wall temperature. However, it should be noted that, in the light of the arguments of Epstein et al. (1985) a change in the surface concentration flux does not essentially imply a change in the absolute wall concentration value as temperature gradient at the wall also will be different accordingly (cf. Eqn. (1.6)). Alam and Mehrotra (1987) studied the problem of thermophoretic flow past a circular cylinder specially applied to OVD process by using a finite-difference technique. The results of this numerical approach compared well with the analytical solution of Homsy et al. (1981).

The common assumptions (to derive the particle concentration equation)in all the foregoing thermophoretic flow investigations are :

(i)   the physical properties of the particle-gas mixture
      are those of the gas phase,

(ii) gas physical property variations are negligible,

(iii) particles of only a single size are present in the
      gas and the particle concentration is sufficiently
      dilute,

(iv) the particles are small enough so that in the absence
      of thermophoresis the particles move with the local
      gas velocity,

(v) thermophoretic velocity component normal to the plate is the only one to be considered, and

(vi) the effect of Brownian diffusion is restricted only to an extremely thin layer next to the surface, and can therefore be neglected.

Quite recently, Gokoglu and Rosner (1984a,b; 1985a,b; 1986) have brought out a series of theoretical studies regarding thermophoretically augmented particle transport in free and/or forced convection with variable properties, transpiration cooling and/or viscous dissipation. However, all their studies are in connection with cold wall boundary conditions and without any radiation effects. Forced convection laminar boundary layers with variable fluid thermo-physical properties and particle transport properties are treated by them (1986) and mass transfer rate predictions are made based on rigorous numerical calculations for solid surfaces. While a decrease in mass transfer rate is predicted for large sized particles, the flux value increases with wall temperature (see also Walker et al., 1979). Gokoglu and Rosner (1986) present results only for a flat plate and two-dimensional stagnation point flow for laminar boundary layers. The mass transfer ratio associated with thermophoresis shows a little increase for two-dimensional stagnation point flow, although the increase is appreciable

(thousand fold) when compared with non-thermophoretic flows (especially, for larger sized particles). In another work by the same authors (1984a) a rational and general, yet simple, correlation suitable for engineering predictions and optimizations is developed. It is argued that the effect of thermophoresis is to introduce a suc- tion - like convective term due to $\vec{w_t}$ and a reaction - like sink term with an effective rate constant into the mass transfer boundary layer equations. The reported laminar and turbulent boundary layer correlation in the presence of thermophoresis, viscous dissipation and transpiration cooling was found in good agreement (within an average error of about 7%) with the numerical calculations. Results were also presented by Gokoglu and Rosner (1985a) for the effect of viscous dissipation on the thermophoretic aerosol particle transport across laminar boundary layers. It was inferred that as the ratio of cold wall temperature to free stream temperature departs from unity, increasing the importance of thermophoresis, the dissipation induced modi- fication of temperature profiles diminishes, decreasing the relative importance of viscous dissipation. It is estimated that viscous dissipation should increase particle deposition rates by about 25% at $t_w/t_\infty = 0.8$ but only about 5% at $t_w/t_\infty = 0.6$ irrespective of particle diameter in the

range 0.3×10^{-2} µm $\leq R_p \leq 0.15$ µm. The reduction in particle deposition at increased M_∞ was attributed to the thermophoretic sink operating outside the Brownian diffusion sublayer. In the case of transpiration cooled surfaces, while real blowing dramatically reduces the rate at which particles can diffuse (by Brownian diffusion) to the wall, the thermophoretic suction associated with the reduced wall temperature offsets some of the fouling rate advantages expected due to blowing alone (Gokoglu and Rosner, 1984b). It was observed that for a fixed blowing rate and wall temperature ratio, the larger particles are easily blown away due to their smaller Brownian diffusion coefficients. Moreover, larger particles experience a stronger counter current in the thinner mass transfer Brownian diffusion sublayer, which is completely embedded in the momentum and energy transfer boundary layers. It was noted that the effect of increasing blowing rate on shifting the particle mass concentration profile (away from the wall and reducing the concentration gradient at the wall) was appreciable eventhough the corresponding profiles of velocity and temperature are not much affected for these blowing rates. Also, for the larger particles very small blowing rates are sufficient to reduce deposition rates considerably,

but the effect of thermophoresis in offsetting that reduction is also correspondingly greater. As the blowing rate increased, the deposition rate is seen to decrease dramatically, but, in principle, no finite blowing rate would reduce the deposition rate to zero. A generalised 'law-of-the wall' representation for the constant property turbulent boundary layer structure was obtained with a fully developed Couette-flow type approximation and a mixing length law modified by blowing or suction (Rosner and Fernandez de la Mora, 1982; Gokoglu and Rosner 1985b). Since they use law of the wall profile for turbulent boundary layer only energy and particle concentration equations need to be solved. Turbulent boundary layer calculations show that thermophoresis increases the deposition rate almost in proportion to the temperature ratio, the enhancement being dependent on the particle size (for large particles the increase is linear with respect to t_∞/t_w). It was also shown that transpiration cooling especially reduces the deposition rate of larger particles; however, due to the thermophoresis the reduction is also offset more for larger particles and higher blowing rates (cooler surfaces).

1.2 Present Investigation

From the foregoing literature survey it is evident
that thermophoretic analysis for non-zero pressure gradient
external flows are very limited. The methodology of Homsy
et al. (1981) has its own limitations because of the use
of Blasius series for solution. Moreover, they have given
importance to the surface concentration flux which (as per
Eqn. (1.6)) is not so relevant a quantity as the practically
important value of wall particle concentration. The latter
is true for the study of Gokoglu and Rosner (1986) as well.
Moreover, Gokoglu and Rosner neglect the streamwise varia-
tion of all dependent variables, even in the convective
terms. This simplifies the analysis but is unrealistic.
In addition, with the exception of Goren (1977) all the
studies are confined only to the cold wall condition. Non-
zero pressure gradient in the boundary layer over a body
occurs commonly in practical thermophoretic applications
either due to the shape of the body or due to its orienta-
tion with respect to the main flow.

Accordingly, for the present analysis a laminar thermo-
phoretic flow is considered when an arbitrary pressure dis-
tribution is imposed on the boundary layer over a two-
dimensional body. The governing differential equations are
solved by a relatively simple finite-difference marching

technique. The fluid properties are assumed constant.
However, the computer code can easily handle variable pro-
perties. Self-adaptive grid generation in the transverse
direction and prespecified variable mesh size in the march-
ing direction are used.

The particle concentration boundary layer adjacent to
the solid surface is studied for a wide range of parameters.
Both cold and heated walls are analysed with different
ratios of the wall to free stream temperature in each case.
Moreover, adiabatic wall is also studied. The critical
layer in the vicinity of a heated wall that has received
little attention so far in theoretical thermophoretic flow
studies is analysed in great detail. Assuming the working
fluid to be air, the Prandtl number is kept constant at
0.7 for most of the present study. Viscous dissipation
in the boundary layer is considered with Eckert number
variation from 0 to 10. The thermophoretic coefficient K
is treated as a specified constant of O(1).

Two specific examples are considered for the two-
dimensional flow with non-zero pressure gradient in the
boundary layer. First the flow due to the impingement of
a slot jet over an arbitrarily inclined plate is analysed.
The pressure distribution over the inclined plate is

computed by considering the direct impingement of two un-
equal, inviscid jets. Secondly, the flow past a circular
cylinder is analysed for both theoretical and experimental
pressure distributions in the boundary layer over the
cylinder.

CHAPTER 2

FORMULATION OF THE PROBLEM

2.1 Governing Equations

Consider a gas containing suspended aerosol particles exposed to a solid surface as shown in Fig. 2.1. The particle concentration is assumed to be dilute enough for the velocity and temperature profiles to pertain to those for a particle-free gas. For particles of unit density, (i.e., particle density comparable to that of the gas) and 1 μm radius, this assumption limits the analysis to aerosol concentrations less than about 10^7 particles per cubic centimeter of the gas at normal temperature and pressure (Goren, 1977). This is indeed the case for most thermophoretic applications. The velocity and temperature distributions are therefore governed by the usual boundary layer equations.

For a steady, laminar, two-dimensional, incompressible flow with constant properties, these equations are (Schlichting, 1979) :

continuity : $\frac{\partial u}{\partial x} + \frac{\partial v}{\partial y} = 0$, $\qquad\qquad$ (2.1)

momentum : $\rho(u \frac{\partial u}{\partial x} + v \frac{\partial u}{\partial y}) = - \frac{dp}{dx} + \mu \frac{\partial^2 u}{\partial y^2}$, $\qquad$ (2.2)

energy : $\rho C_p(u \frac{\partial t}{\partial x} + v \frac{\partial t}{\partial y}) = k_g \frac{\partial^2 t}{\partial y^2} + \mu (\frac{\partial u}{\partial y})^2$, $\qquad$ (2.3)

where (u, v) are the velocity components in (x,y) dire-
ctions (see Fig. 2.1), ρ , p and t are, respectively, the
density, pressure and temperature of the gas, and μ, C_p
and k_g are respectively, the dynamic viscosity, specific
heat at constant pressure, and thermal conductivity of
the gas.

The boundary conditions are :

$u(x,0) = 0$,

$v(x,0) = 0$,

$u(x,\infty) = u_s(x)$,

$u(0,y) = u_s(0)$,

$t(x,0) = t_w(x)$ for a specified wall temperature ,

or $\frac{\partial t}{\partial y} (x,0) = 0$ for an adiabatic wall ,

$t(x,\infty) = t_\infty$,

$t(0,y) = t_\infty$, $\qquad\qquad$ (2.4)

where $u_s(x)$ is the potential flow velocity at the body
surface, t_∞ is the free stream temperature, and t_w is
the surface temperature.

It should be pointed out that the boundary layer equations are really not valid at x = 0   In the close vicinity of the stagnation point, the full Navier-Stokes and energy equations including the diffusion terms in the x-direction must be used.

Later in Sec. 4.1.3 we will look at the actual limiting values of X for which the boundary layer analysis for a laminar slot jet is valid. Numerically the effect of singularity at the stagnation point is confined to a region very close to the stagnation point by taking a very small step size initially in the X-direction (Hornbeck, 1973). More details are given in Sec. 3.3.

As discussed in Chapter 1, the particles are driven away from a hot surface or deposited on a cold one by thermophoresis. The velocity acquired by the small particles relative to the gas velocity is known as the thermophoretic velocity. Theoretically the thermophoretic velocity vector, $\vec{w}_t$, is related to the temperature gradient in the flow field by the equation

$$\vec{w}_t = -K \frac{\nu}{t} \, \nabla t \, , \qquad\qquad (2.5)$$

where $\nu = \frac{\mu}{\rho}$ is the kinematic viscosity, and K is the thermophoretic coefficient which depends mainly on the Knudsen number. A number of formulations are available in the literature for the determination of K depending upon the regime of flow past the particle (cf. Chapter 1). The

semi-empirical formula proposed by Talbot et al. (1980) can be used for a wide range of Knudsen numbers. The numerical value of the coefficient K lies between 0.25 to 1.25 in most of the cases. For the present work, however, K is treated as a specified constant independent of temperature. Due to the boundary layer behaviour, the temperature gradient in the direction normal to the surface, $\partial t/\partial y$, is much larger than $\partial t/\partial x$. Also, the gas velocity component u is large compared to v. Since the thermophoretic velocity components are given by Eqn. (2.5) it is clear that the thermophoretic velocity component normal to the surface, v_t, is the only one of importance. It is given by

$$v_t = -K \frac{\nu}{t} \frac{\partial t}{\partial y} .$$

(2.6)

Additional assumptions usually made for thermophoretic analysis (Goren, 1977; Walker et al., 1979; Talbot et al., 1980; Epstein et al., 1985) are :

(i)   Thermal radiation effect is neglected. In fact, in the presence of absorbing aerosol, radiation, if present, can significantly affect the temperature distribution. This is therefore a weak assumption.

(ii) The particles are assumed to be sufficiently small so that the relaxation time scale for particle motion is several orders of magnitude smaller than that for the gas flow. This means that in the absence of

thermophoresis the particles move with the local gas velocity.

With the foregoing considerations and with the usual boundary layer approximations the following conservation law is valid for the aerosol particle concentration, c, per unit volume of the gas

$$\frac{\partial(cu)}{\partial x} + \frac{\partial[c(v+v_t)]}{\partial y} = D \frac{\partial^2 c}{\partial y^2} , \qquad (2.7)$$

where D is the Brownian diffusion coefficient for the particles. This equation is rewritten with the help of continuity equation (2.1) as

$$u \frac{\partial c}{\partial x} + v \frac{\partial c}{\partial y} + \frac{\partial(cv_t)}{\partial y} = D \frac{\partial^2 c}{\partial y^2} . \qquad (2.8)$$

The boundary conditions for this second order differential equation are

$$c(0,y) = c_\infty,$$

$$c(x,\infty) = c_\infty,$$

and $\qquad c(x,0) = 0, \qquad (2.9)$

if the wall is totally absorbing. Here c_∞ is the particle concentration in the free stream.

For micron sized particles in air at normal tempera-
ture and pressure the Schmidt number (ratio of ν to D) is
of the order of 10^5. This means that the Brownian diffu-
sion sublayer is so thin, even on the boundary layer scale,
that it does not alter the thermophoretic particle deposi-
tion rate (Goren, 1977; Walker et al., 1979). Hence the
only effect of Brownian diffusion is to create an extre-
mely thin particle concentration sublayer adjacent to the
wall when the wall is colder than the surrounding gas and
near a critical layer away from the wall when it is heated.
Accordingly, the second order diffusion term could be dro-
pped from   Eqn.   (2.8), which is rewritten as

$$u \frac{\partial c}{\partial x} + v \frac{\partial c}{\partial y} + \frac{\partial(cv_t)}{\partial y} = 0 \ . \tag{2.10}$$

It should be noted that by neglecting the Brownian
diffusion term, Eqn. (2.10) has become first order in y
and hence only the boundary condition at infinity in (2.9)
can be satisfied by it. For the cold wall condition, a
non-zero particle concentration at $y = 0$ is expected in the
absence of diffusion. This is determined by solving Eqn.
(2.10) using only the boundary condition at infinity in
(2.9). Essentially, this concentration is the one at the

outer edge of the very thin Brownian sublayer adjacent to the solid surface.

For a heated wall, the presence of a critical layer near the wall in the absence of Brownian diffusion can be ascertained from a similarity analysis (Goren, 1977). While Goren's analysis is for a flat plate at zero incidence, we carry it out for thermophoretic flow over a wedge.

The similarity variable, η, for flow past a wedge is taken to be

$$\eta = y \sqrt{\frac{m+1}{2} \frac{u_s}{\nu x}} \, , \qquad (2.11)$$

where m is the wedge constant related the wedge angle $\pi\beta$, by

$$m = \frac{\beta}{2-\beta} \, . \qquad (2.12)$$

In the neighbourhood of the stagnation point, the potential flow velocity $u_s(x)$ over the wedge is related to the length coordinate, x, measured from the stagnation point by

$$u_s(x) \propto x^m \, . \qquad (2.13)$$

For the similarity solution, continuity equation is taken care of by defining a stream function $\Psi(x,y)$ as

$$\Psi(x,y) = \sqrt{\frac{2}{m+1}} \ \sqrt{\nu x u_s} \ f(\eta) . \tag{2.14}$$

This leads to velocity components u and v as

$$u = u_s f'(\eta) , \tag{2.15}$$

$$v = -\sqrt{\frac{m+1}{2} \ \frac{\nu u_s}{x}} \ [f + \frac{m-1}{m+1} \ \eta \ f'] , \tag{2.16}$$

and the momentum equation reduces to the famous Falkner-Skan equation

$$f''' + f f'' + \frac{2m}{m+1} (1-f'^2) = 0 , \tag{2.17}$$

with the boundary conditions

$$f(0) = f'(0) = 0, \quad f'(\infty) = 1 . \tag{2.18}$$

Here primes denote differentiation with respect to η.

For the thermal boundary layer over an isothermal wall, it is known (Schlichting, 1979) that the similarity solution is possible only for flow over a flat plate if viscous dissipation is included. However, if viscous dissipation is neglected, similarity solution exists for

flow over a wedge even when the wall temperature varies as

$$[t_w(x) - t_\infty] \propto x^n \; . \qquad (2.19)$$

For an isothermal wall, of course, n = 0. In this case the energy equation reduces to

$$\frac{t''}{t'} = -Pr \; f(\eta) \; , \qquad (2.20)$$

where $t' = dt/d\eta$. Thus the temperature is a function of the similarity variable η. With this, the thermophoretic velocity is given by

$$v_t = -\sqrt{\frac{m+1}{2} \frac{\nu u_s}{x}} \; K \; \frac{t'}{t} \; , \qquad (2.21)$$

from which it follows that

$$\frac{\partial v_t}{\partial y} = \frac{m+1}{2} \frac{u_s}{x} \left(K \frac{t'^2}{t^2} - K \frac{t''}{t} \right) \qquad (2.22)$$

The simplification of the particle concentration equation (Eqn. (2.10)) using the foregoing relations yields

$$\left(K \frac{t'}{t} + f \right) c' - \left[\frac{t'}{t} \left(K \frac{t'}{t} + K \cdot Pr \; f \right) \right] c = 0 \; , \qquad (2.23)$$

where $c' = dc/d\eta$. This first order differential equation in c can be integrated with free stream boundary condition for the particle concentration $c(\infty) = c_\infty$ to yield

$$\frac{c}{c_\infty} = \exp\left[-\int_\eta^\infty \frac{\frac{t'}{t}(K\frac{t'}{t} + K\,Pr\,f)}{(K\frac{t'}{t} + f)}\,d\eta\right].\qquad (2.24)$$

The equation for particle concentration of Goren (1977) without the viscous dissipation term is exactly the same as Eqn. (2.24) above. Accordingly, the arguments of Goren about the behaviour of the concentration boundary layer over a flat plate are applicable to the flow over a wedge as well. Thus, a critical layer, exists near a heated wedge as well. There is no reason to believe that such would not be the case for flow over any heated surface.

There is a value η, say η_c, at which the denominator of the integrand in (2.24) goes to zero and at which a singularity in the dust concentration profile in the absence of Brownian diffusion can be expected. The dust concentration near the singularity depends upon whether Pr.K is less than or greater than unity, for the numerator in (2.24) also changes sign at some value of η. For Pr.K < 1 the numerator changes sign at a value of η larger

than η_c, and the dust concentration very rapidly approaches zero at the critical layer. For $Pr.K > 1$ the numerator changes sign at a value of η smaller than η_c, and the dust concentration rapidly becomes infinite. Thus depending upon $Pr.K \gtrless 1$, $c \rightarrow \pm \infty$ as $y \rightarrow 0$ for a hot wall.

2.2 Strategy for Solution

Analytical solutions to Eqns (2.1) to (2.3) are rare due to the presence of nonlinear terms. As is well known, an analytical (similarity) solution for Eqns. (2.1) and (2.2) with appropriate boundary conditions in Eqn. (2.4) is possible but for a very restricted class of non-zero pressure gradient, dp/dx. The familiar examples include the stagnation point flow, the converging channel flow, and the wedge flows, and are well documented in almost every text on Fluid Mechanics. Even these solutions, however, are valid only in a narrow region close to the stagnation point due to the limitations of the function representing the pressure gradient term. To obtain the similarity solution for the energy equation (2.3) as well, additional constraints are required on the variation of t_w. Thus an analytical solution for a general dp/dx is not possible.

The system of partial differential equations (2.1) and (2.2) is of parabolic type which can be solved easily by finite-difference techniques while marching downstream in the x-direction. Moreover, the nonlinear inertia terms in the momentum equation present no particular problem to the finite-difference method. Since the energy equation is decoupled from the continuity and momentum equations, it can be solved once u and v are known. Finally the particle concentration equation (2.10) can be solved.

2.3 Dimensionless Representation

Before obtaining a numerical solution the governing equations are placed in dimensionless form by using the following dimensionless variables :

$$X = x/L \quad ,$$

$$Y = (y/L)\,Re^{1/2},$$

$$U = u/u_\infty \quad ,$$

$$V = (v/u_\infty)\,Re^{1/2},$$

$$T = t/t_\infty \quad ,$$

$$P = (p-p_\infty)/(\rho u_\infty^2),$$

$$V_T = v_t(L/\nu)\,Re^{-1/2},$$

and $\quad C = c/c_\infty$.

$$(2.25)$$

Here L is a characteristic length, and Re is the Reynolds number defined as $Re = u_\infty L/\nu$. For the inclined plate considered here, L is the width of the impinging jet (Fig. 2.2), but for the circular cylinder, L is the radius of the cylinder. In addition the following dimensionless numbers are introduced to further simplify the energy equation :

Prandtl number : $Pr = \mu\, C_p/k_g$,

Eckert number : $Ec = u_\infty^2/C_p t_\infty$. (2.26)

All these quantities are now substituted in the governing equations (2.1) to (2.3), (2.6) and (2.10). The resulting non-dimensional equations are

continuity : $\dfrac{\partial U}{\partial X} + \dfrac{\partial V}{\partial Y} = 0$, (2.27)

momentum : $U\dfrac{\partial U}{\partial X} + V\dfrac{\partial U}{\partial Y} = \dfrac{\partial^2 U}{\partial Y^2} - \dfrac{dP}{dX}$, (2.28)

energy : $U\dfrac{\partial T}{\partial X} + V\dfrac{\partial T}{\partial Y} = \dfrac{1}{Pr}\dfrac{\partial^2 T}{\partial Y^2} + Ec\left(\dfrac{\partial U}{\partial Y}\right)^2$, (2.29)

thermophoretic
velocity : $V_T = -\dfrac{K}{T}\dfrac{\partial T}{\partial Y}$, (2.30)

particle
concentration : $U\dfrac{\partial C}{\partial X} + V\dfrac{\partial C}{\partial Y} + \dfrac{\partial(C\,V_T)}{\partial Y} = 0$. (2.31)

The general boundary conditions (2.4) and (2.9) rewritten for the dimensionless problem become :

$$U(X,0) \quad = 0 \quad ,$$

$$V(X,0) \quad = 0 \quad ,$$

$$U(X,\infty) \quad = U_s(X) \, ,$$

$$U(0,Y) \quad = U_s(0) \, ,$$

$$T(X,0) \quad = T_w \text{ (isothermal wall)},$$

$$\text{or } \frac{\partial T(X,0)}{\partial Y} \quad = 0 \text{ (adiabatic wall)},$$

$$T(X,\infty) \quad = 1 \, ,$$

$$T(0,Y) \quad = 1 \, ,$$

$$C(X,\infty) \quad = 1 \, ,$$

$$\text{and } C(0,Y) \quad = 1 \, , \tag{2.32}$$

where $\quad U_s \quad = u_s/u_\infty$.

2.4 Pressure Distribution

The estimation of the correct pressure gradient in the boundary layer is essential before solving the momentum equation. The pressure gradient is usually computed by considering inviscid flow over the body surface. Two examples are considered for analysis here. The first one

deals with the oblique impingement of a slot jet on a plane wall. The pressure distribution in this case is unsymmetrical about the stagnation point. The second example is the flow past a circular cylinder which has a symmetrical pressure distribution with respect to the stagnation point.

2.4.1 Flow Over an Inclined Plate

In order to estimate the pressure gradient in this case, a direct impact of two unequal jets is considered as shown in Fig. 2.2. It is assumed that the flow is inviscid and the outgoing jets (B and D) are of equal width L. In this general case, the equation relating the complex variable z with the complex velocity ξ is (Milne-Thomson, 1960) :

$$z = \frac{u_\infty}{\pi} \left[\frac{h_1}{a_1} \ln(1 - \frac{\xi}{a_1}) + \frac{h_2}{a_2} \ln(1 - \frac{\xi}{a_2}) \right.$$

$$\left. - \frac{L}{b_1} \ln(1 - \frac{\xi}{b_1}) - \frac{L}{b_2} \ln(1 - \frac{\xi}{b_2}) \right] , \qquad (2.33)$$

where, $a_1 = -u_\infty = -a_2$,

$$b_1 = u_\infty e^{-i\beta} ,$$

and $\qquad b_2 = u_\infty e^{i\beta} .$ \qquad (2.34)

Also the following relations are applicable between the widths of the jets.

$$h_1 = L (1 - \cos \beta) , \tag{2.35}$$

$$h_2 = L (1 + \cos \beta) . \tag{2.36}$$

Substituting Eqns. (2.34) to (2.36) into Eqn. (2.33) and simplifying results in the following relation :

$$\pi Z + \ln(1 + \epsilon) - \ln (1 - \epsilon) - \cos \beta \ln (1 - \epsilon^2)$$

$$+ e^{i\beta} \ln(1 - \epsilon e^{i\beta}) + e^{-i\beta} \ln (1 - \epsilon e^{-i\beta}) = 0, \tag{2.37}$$

where $Z = z/L$ and $\epsilon = \xi/u_\infty$.

Without loss of generality, the configuration shown in Fig. 2.2 can be regarded as the jet from D impinging on the plane wall along the line AC, which is at an angle β to the oncoming slot jet (Fig. 2.3). Hence the dimensionless complex velocity, ϵ , obtained by solving Eqn. (2.37) can be used directly in order to compute the pressure distribution over the plane wall AC. In fact, since we are interested only in the potential flow velocity $U_s(X)$ at the plate, we set $Z = -X$ and $\epsilon = U_s$ in Eqn. (2.37) to obtain:

$$\pi X = -\ln \left(\frac{1-U_s}{1+U_s}\right) + \cos \beta \, \ln \left(\frac{1+U_s^2 - 2U_s \cos \beta}{1 - U_s^2}\right)$$

$$+ \, 2 \sin \beta \, \tan^{-1} \left(\frac{U_s \sin \beta}{1-U_s \cos \beta}\right) \, . \tag{2.38}$$

Thus for a given value of angle β, $U_s(X)$ is a solution of Eqn. (2.38). This equation is identical to Eqn. (3) of Miyazaki and Silberman (1972) in the limit $H \rightarrow \infty$. The pressure distribution and the pressure gradient in the boundary layer over the plane wall are given by

$$2P = 1 - U_s^2 \, , \tag{2.39}$$

and

$$\frac{dP}{dX} = -U_s \frac{dU_s}{dX} \, . \tag{2.40}$$

This pressure gradient is used in the momentum equation (2.28).

The pressure distribution in the boundary layer at various angles of inclination of the plate is given in Fig. 2.4. The curves are shown at 15° intervals from 0 to 90°. As observed experimentally by Gardon and Akfirat (1966) in Fig. 7 of their paper, the pressure distribution on the plate for normal impingement ($\beta = 90^\circ$)

is symmetrical about the stagnation point (X=0). It is clear from Fig. 2.4 that except for the 90° angle the distribution is unsymmetrical about the stagnation point. Also the symmetrical distribution for $\beta' = 90^\circ$ cuts across the unsymmetrical distribution for smaller angles at some positive values of X. The presence of the stagnation point for angles other than zero considerably modifies the distribution especially near the stagnation point. In the positive X-direction, pressure reaches a nearly zero value at $X \simeq 3.0$ for all angles, but in the negative X-direction, zero pressure is obtained at different X-locations depending upon the value of β. The pressure profiles in the negative X-direction come very close to the P-axis for smaller angles ($\beta < 30^\circ$) as seen from Fig. 2.4. Thus for $\beta = 15^\circ$, $P \simeq 0$ for $X \lesssim -0.3$. Moreover, for all values of β, $P \simeq 0$ for $X \gtrsim 3.0$. The reason for this lies in the smaller thickness (h_1) of the outgoing stream on the (X < 0) side of the plate at smaller values of β (see Eqn. (2.35) and Fig. 2.3). In the limiting case of $\beta \to 0$, $h_1 \to 0$ and we get the flow over a flat plate at zero incidence. The pressure gradient with respect to X is shown in Fig. 2.5. Note the sharply changing values of dP/dX near the stagnation point

for small angles of impingement of the slot jet.
Figure 2.6 illustrates the potential flow velocity at
the plate as a function of distance along the plate with
β as a parameter. The effect of pressure distribution
on the plate is very clearly reflected in these curves.

2.4.2 Flow Past a Circular Cylinder

This configuration is shown in Fig. 2.7. The invis-
cid flow analysis (superimposing a uniform stream with a
doublet) yields the following expression for non-dimen-
sional velocity over the cylinder

$$U_s = 2 \sin X .\qquad(2.41)$$

Here X corresponds to the location on the cylinder sur-
face from the stagnation point ($\Phi = x/L = X$). The
pressure gradient follows from Eqn. (2.41) as

$$\frac{dP}{dX} = -U_s \frac{dU_s}{dX} ,$$

or $\qquad \dfrac{dP}{dX} = -4 \sin X \cos X .\qquad(2.42)$

Numerical solution of the boundary layer equations
(2.27) and (2.28) for incompressible flow past a circular

The theoretical and experimental pressure distributions in the boundary layer at different locations on the circular cylinder are shown in Fig. 2.8. From this figure it is clear that the pressure gradient, dP/dX, changes sign at 90° and 70°, respectively, for the theoretical and experimental distributions. Hence a point of inflection is expected in the laminar velocity profiles at angles larger than these.
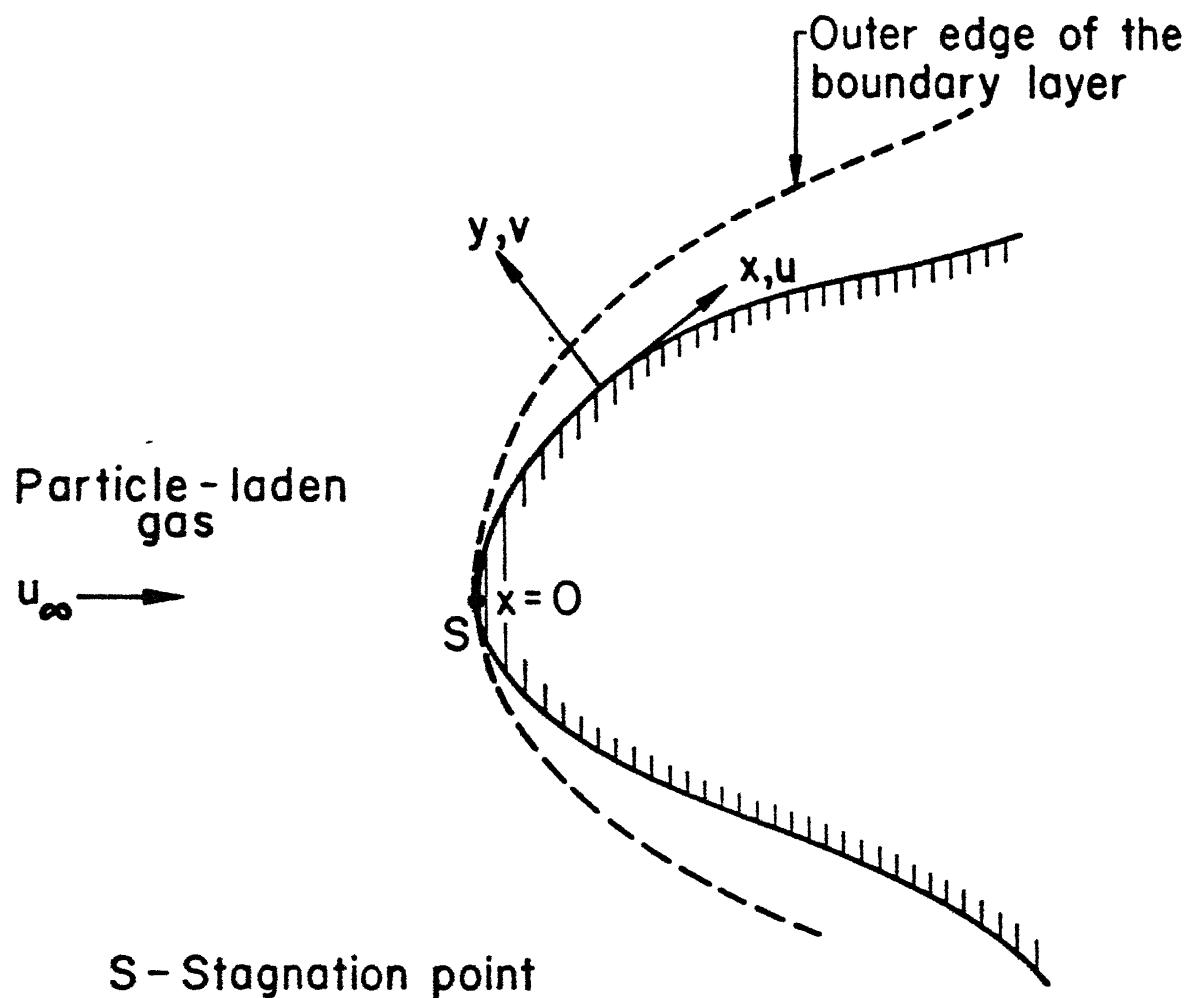
Fig.2.I Typical two-dimensional boundary layer configuration

$$\alpha = \pi$$
$$\gamma = 2\pi - \beta$$
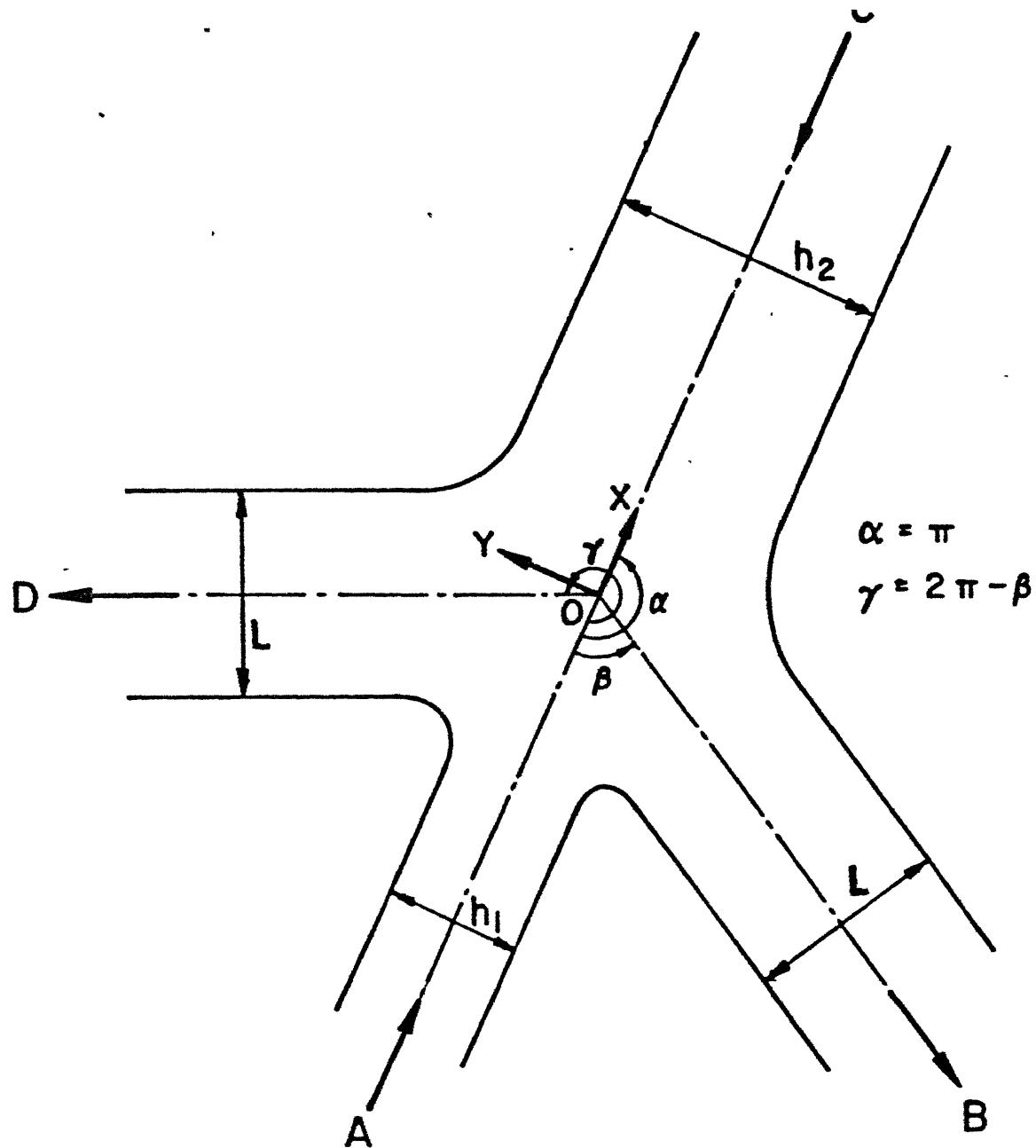
Fig. 2.2 Direct impact of two unequal jets
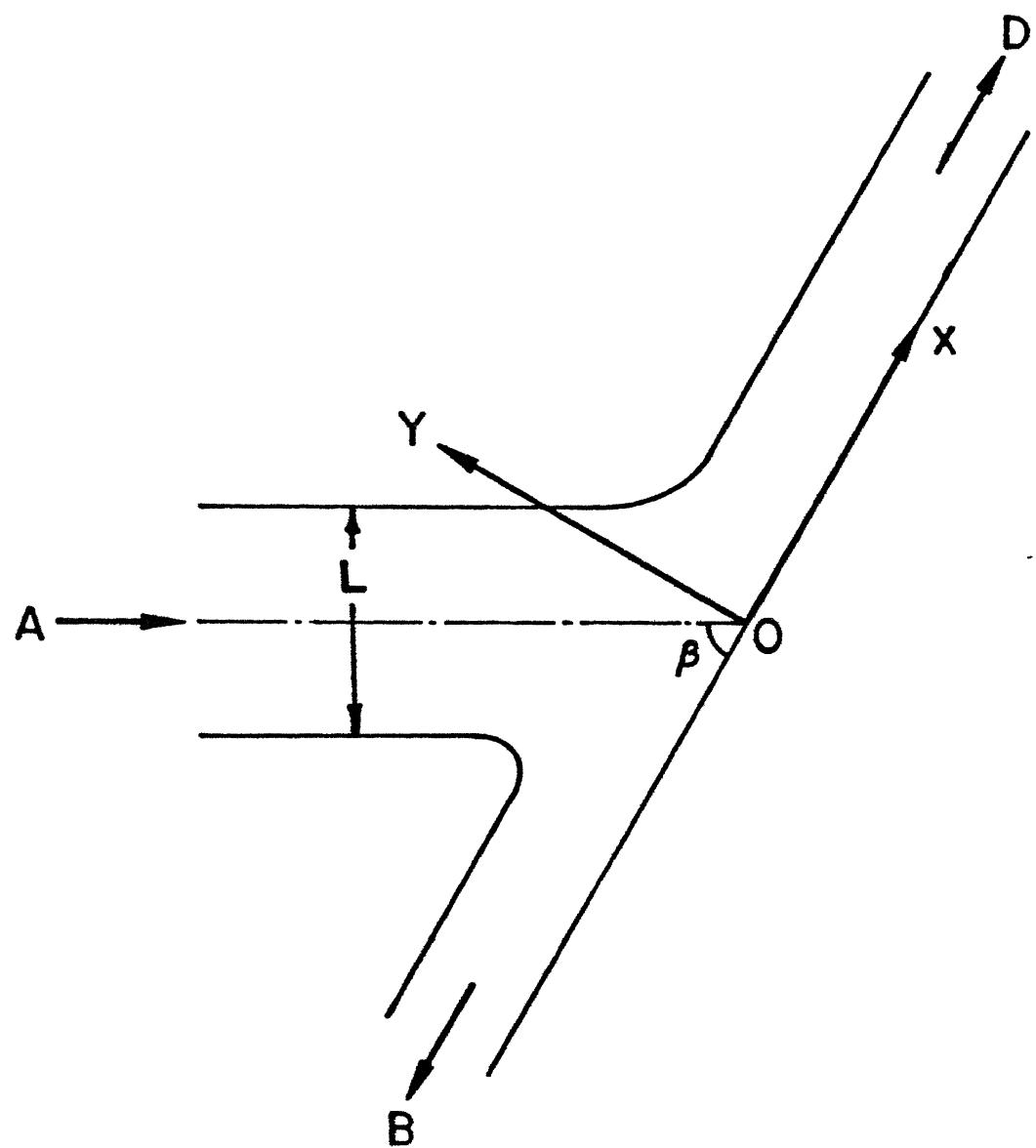
Fig.2.3 Flow over an inclined plate
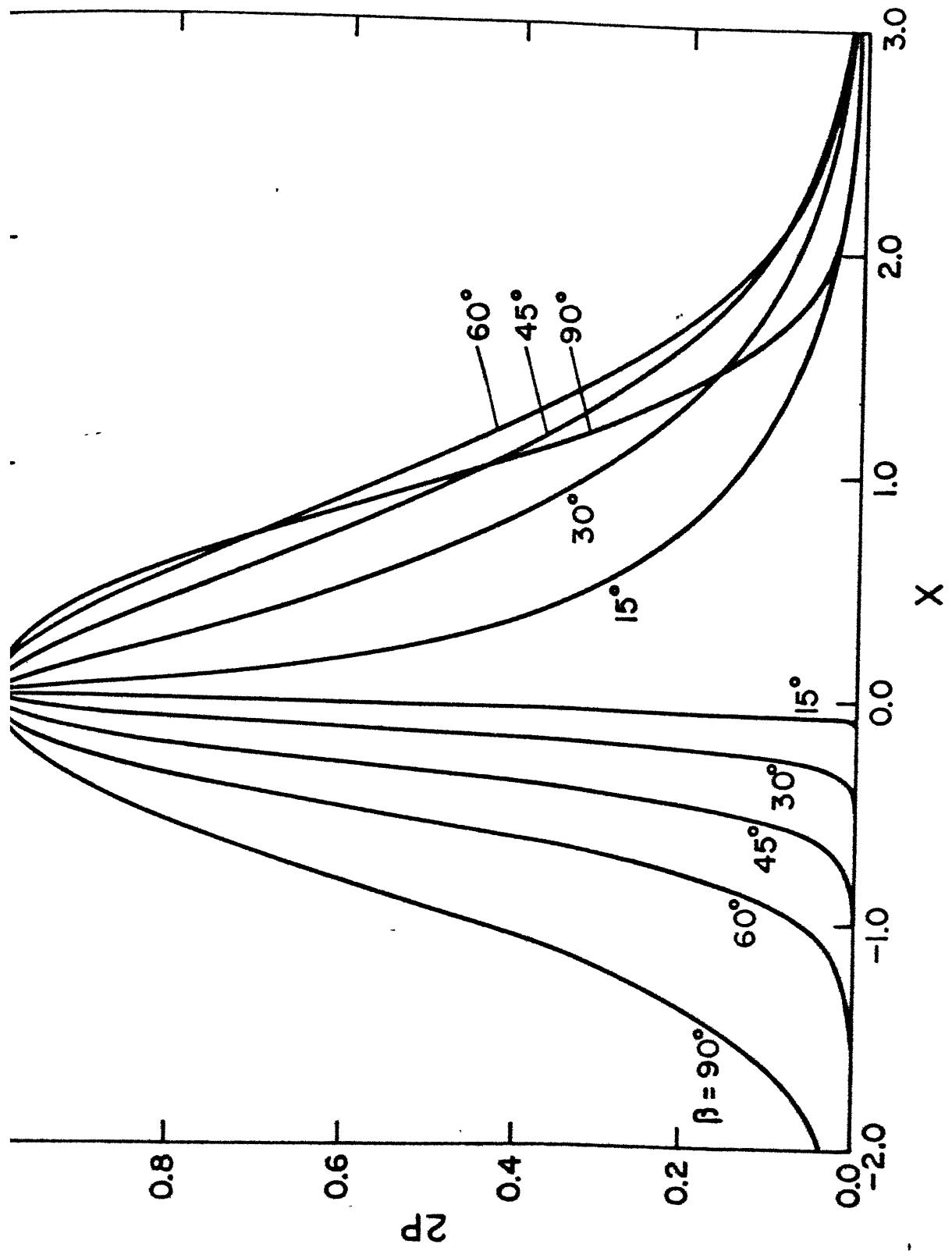
Fig. 2.4 Pressure distribution in the boundary layer for flow over an inclined plate
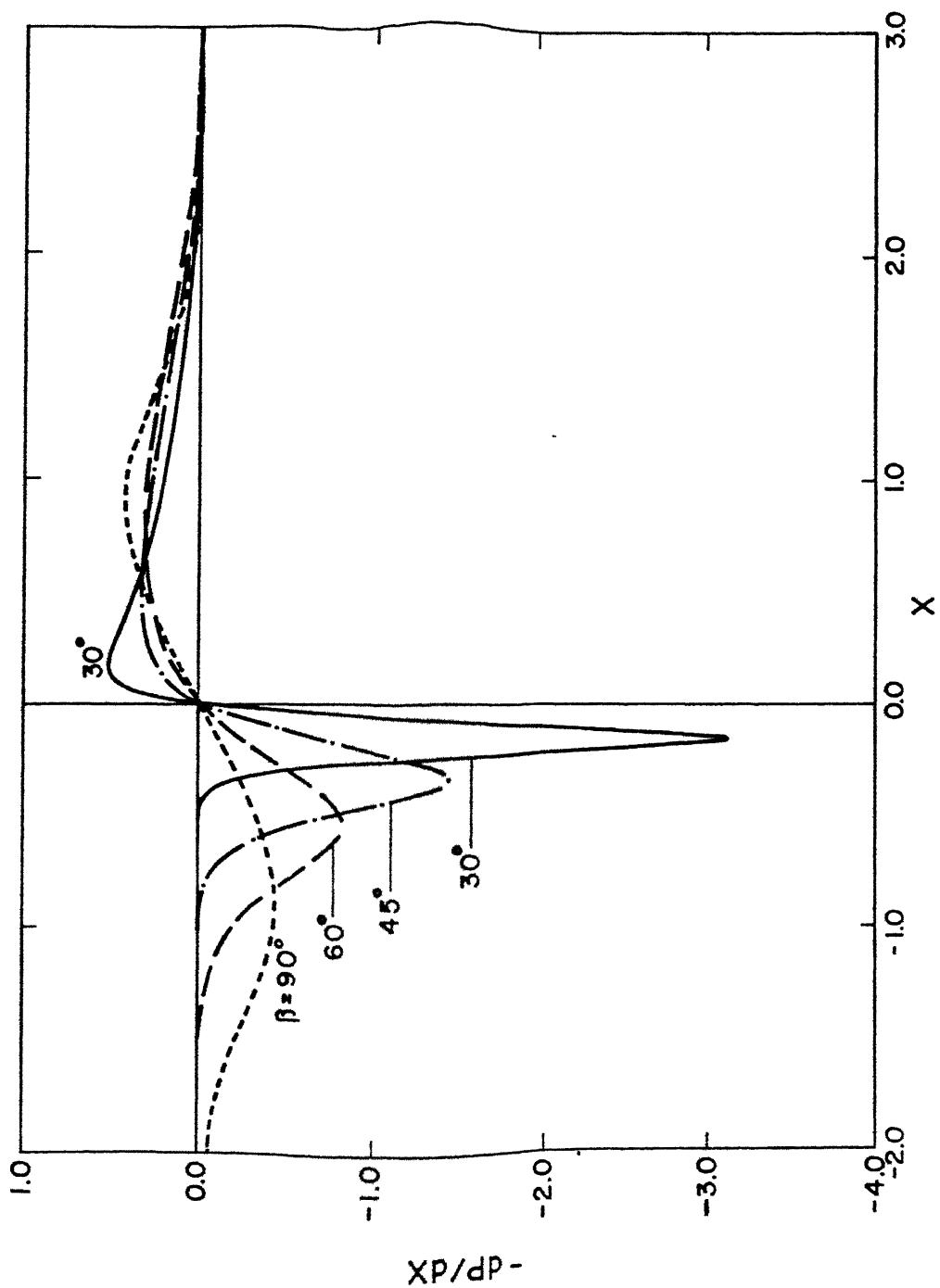
Fig. 2.5 Pressure gradient in the boundary layer on the plate
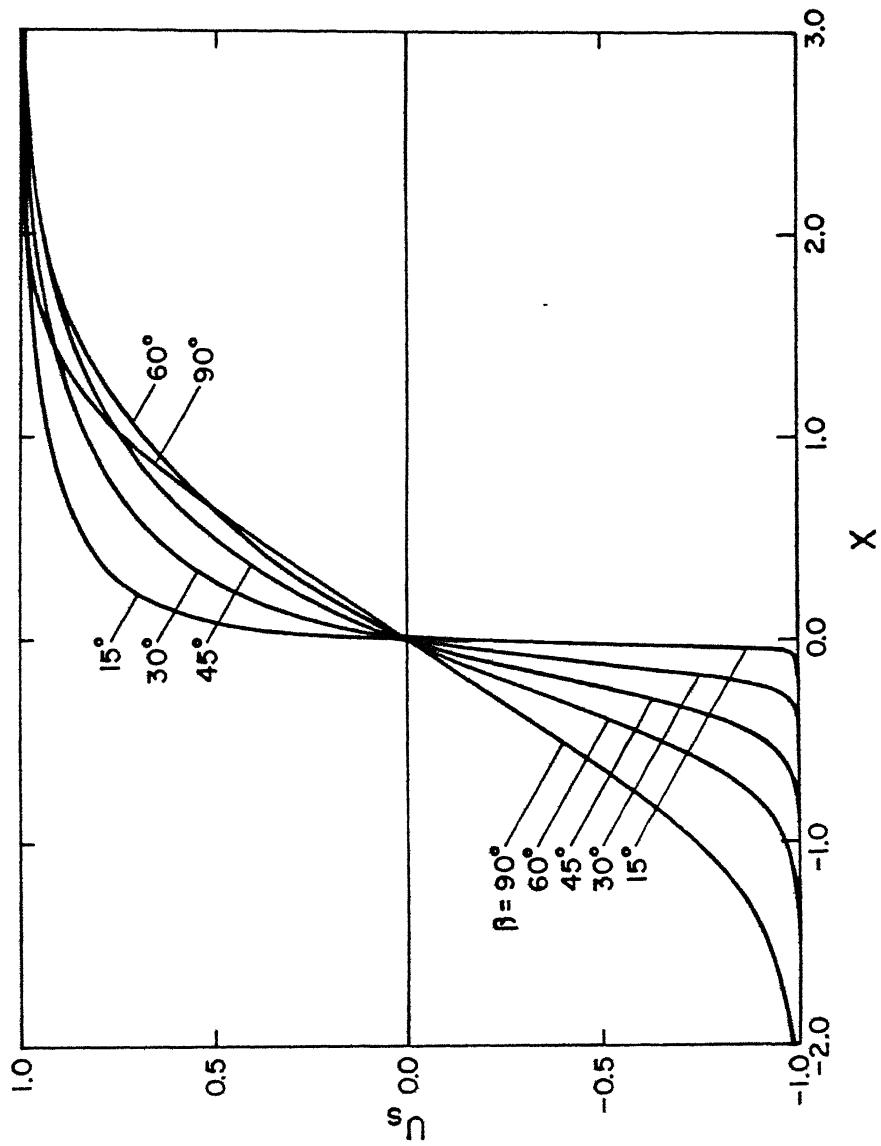
Fig. 2.6 Potential flow velocity at the plate
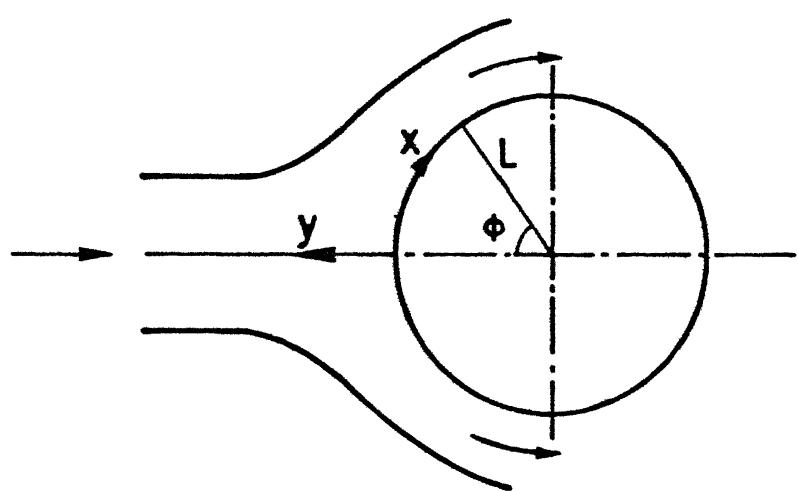
Fig.2.7 Flow past a circular cylinder
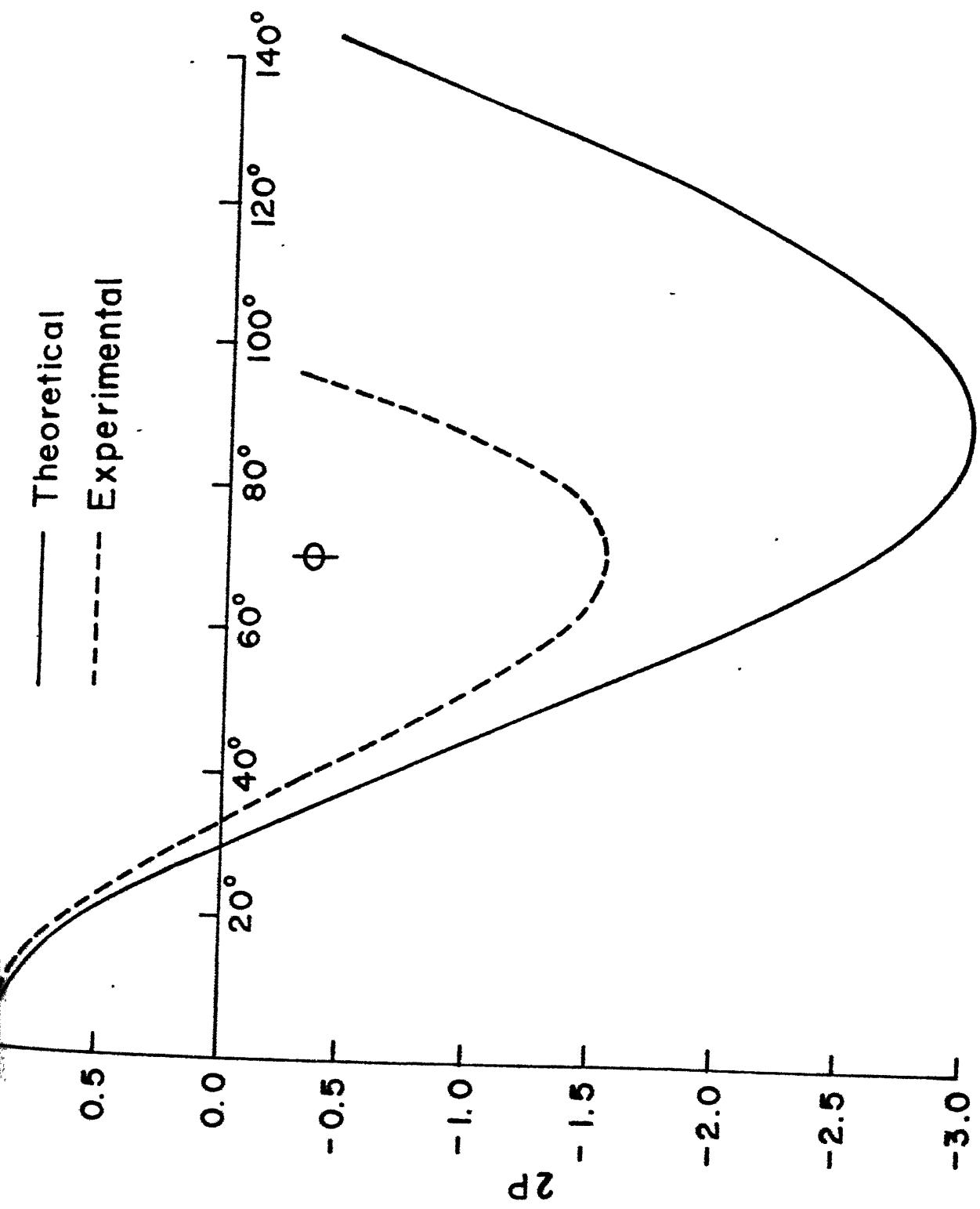
Fig. 2.8   Pressure distributions in the boundary layer for flow past a circular cylinder

CHAPTER   3

FINITE-DIFFERENCE SOLUTION

3.1   Discretization of the Governing Equations

In order to represent the dimensionless differential equations (2.27) to (2.31) in finite-difference form, a rectangular mesh is superimposed on the flow field. Indices (j, k) are used to indicate position in the (X, Y) directions respectively. The finite-difference coordinates are chosen to correspond to the spatial coordinates (shown in Figs. 2.3 and 2.7) so that j = 0 corresponds to X = 0 and k = 0 corresponds to Y = 0. Accordingly, (0, 0) represents the stagnation point both in terms of indices and spatial coordinates. A small change in the X-coordinate (ΔX) increases j by 1 and similarly an increment by ΔY in the Y-coordinate increases k by 1. The wall is represented by k = 0 and edge of the boundary layer by k = n+1.

The discretization of the governing equations is made in such a way that the solution can be carried out by a marching procedure in the X-direction. The momentum, energy

and concentration equations are solved implicitly at every X-location, whereas the continuity equation is solved in a stepwise manner. Following Hornbeck (1973) forward differencing in the marching X-direction and central differencing in the Y-direction are employed in Eqns. (2.28) and (2.29), whereas only forward differencing is employed in Eqns. (2.27) and (2.30). The finite-difference form of these equations is written as :

Continuity Equation :

$$\frac{U_{j+1,k+1} - U_{j,k+1}}{\Delta X} + \frac{V_{j+1,k+1} - V_{j+1,k}}{\Delta Y} = 0 \quad , \qquad (3.1)$$

Momentum Equation :

$$U_{j+1,k} \frac{U_{j+1,k} - U_{j,k}}{\Delta X} + V_{j+1,k} \frac{U_{j+1,k+1} - U_{j+1,k-1}}{2(\Delta Y)}$$

$$= \frac{U_{j+1,k+1} - 2U_{j+1,k} + U_{j+1,k-1}}{(\Delta Y)^2} - \frac{dP}{dX} \quad , \qquad (3.2)$$

Energy Equation :

$$U_{j+1,k} \frac{T_{j+1,k} - T_{j,k}}{\Delta X} + V_{j+1,k} \frac{T_{j+1,k+1} - T_{j+1,k-1}}{2(\Delta Y)}$$

$$= \frac{1}{Pr} \frac{T_{j+1,k+1} - 2T_{j+1,k} + T_{j+1,k-1}}{(\Delta Y)^2}$$

$$+ Ec \left[\frac{U_{j+1,k+1} - U_{j+1,k-1}}{2(\Delta Y)} \right]^2 \quad , \qquad (3.3)$$

Thermophoretic Velocity :

$$V_{T_{j+1,k}} = - \frac{K}{\Delta Y} \left[\frac{T_{j+1,k+1} - T_{j+1,k}}{T_{j+1,k}} \right] \quad . \qquad (3.4)$$

These discretizations are second order accurate in ΔY for U and T.

While obtaining the solution by the Thomas algorithm (Appendix A), the sufficient conditions to be satisfied by the tridiagonal coefficient matrix elements are (Roache, 1982) :

(i)   the diagonal elements should be positive,

(ii) the off-diagonal elements should be negative or zero,

(iii) the magnitude of the diagonal element should be greater than or equal to the total magnitude of the two off-diagonal elements in each row.

In order to satisfy these conditions, the particle concentration equation (2.31) is discretized in four different ways depending upon the signs of V and V_T, and the wall temperature condition as follows :

Cold Wall (V < 0) :
$$U_{j+1,k} \frac{C_{j+1,k} - C_{j,k}}{\Delta X} + V_{j+1,k} \frac{C_{j+1,k+1} - C_{j+1,k}}{\Delta Y}$$
$$+ \frac{C_{j+1,k+1} V_{T_{j+1,k+1}} - C_{j+1,k} V_{T_{j+1,k}}}{\Delta Y} = 0 , \qquad (3.5)$$

Cold Wall (V > 0) :

$$U_{j+1,k} \frac{C_{j+1,k} - C_{j,k}}{\Delta X} + V_{j+1,k} \frac{C_{j+1,k} - C_{j+1,k-1}}{\Delta Y}$$

$$+ \frac{C_{j+1,k+1} {}^V T_{j+1,k+1} - C_{j+1,k} {}^V T_{j+1,k}}{\Delta Y} = 0 \quad , \qquad (3.6)$$

Hot Wall (V < 0) :

$$U_{j+1,k} \frac{C_{j+1,k} - C_{j,k}}{\Delta X} + V_{j+1,k} \frac{C_{j+1,k+1} - C_{j+1,k}}{\Delta Y}$$

$$+ \frac{C_{j+1,k} {}^V T_{j+1,k} - C_{j+1,k-1} {}^V T_{j+1,k-1}}{\Delta Y} = 0 \quad , \qquad (3.7)$$

Hot Wall (V > 0) :

$$U_{j+1,k} \frac{C_{j+1,k} - C_{j,k}}{\Delta X} + V_{j+1,k} \frac{C_{j+1,k} - C_{j+1,k-1}}{\Delta Y}$$

$$+ \frac{C_{j+1,k} {}^V T_{j+1,k} - C_{j+1,k-1} {}^V T_{j+1,k-1}}{\Delta Y} = 0 \quad . \qquad (3.8)$$

These discretizations are first order accurate in ΔX and ΔY for C. It should be mentioned here that V does not change sign at all Y-locations at a particular X. Values of V close to the plate become positive first. Hence it is difficult to strictly satisfy the three conditions mentioned above. However, satisfactory results are

obtained for all the cases studied here when the sign of V at 25 ΔY below $Y = \infty$ is used as the criteria for changing the scheme for concentration calculation (Eqns. (3.5) to (3.8)).

The finite-difference forms of the boundary conditions (2.32) are obvious except for the adiabatic wall condition. A difference form for the gradient which is consistent in truncation error with the discretised energy equation (3.3) is

$$\frac{\partial T(X,0)}{\partial Y} = \frac{-3T_{j+1,0} + 4T_{j+1,1} - T_{j+1,2}}{2(\Delta Y)}, \tag{3.9}$$

where $T_{j+1,0}$ is the unknown surface temperature.

3.2 Method of Solution

Equations (3.1) to (3.3) and (3.5) to (3.8) are rewritten in forms which are more readily adaptable for solution.

Continuity Equation :

$$V_{j+1,k+1} = V_{j+1,k} + [U_{j,k+1} - U_{j+1,k+1}] \frac{\Delta Y}{\Delta X} \tag{3.10}$$

Momentum Equation :

$$[- \frac{V^*_{j+1,k}}{2(\Delta Y)} - \frac{1}{(\Delta Y)^2}]\, U_{j+1,k-1} + [\frac{U^*_{j+1,k}}{\Delta X} + \frac{2}{(\Delta Y)^2}]\, U_{j+1,k}$$

$$+ [\frac{V^*_{j+1,k}}{2(\Delta Y)} - \frac{1}{(\Delta Y)^2}]\, U_{j+1,k+1} = \frac{U^*_{j+1,k}}{\Delta X}\, U_{j,k} - \frac{dP}{dX} \qquad (3.11)$$

Energy Equation :

$$[- \frac{V_{j+1,k}}{2(\Delta Y)} - \frac{1}{Pr(\Delta Y)^2}]\, T_{j+1,k-1} + [\frac{U_{j+1,k}}{\Delta X} + \frac{2}{Pr(\Delta Y)^2}]\, T_{j+1,k}$$

$$+ [\frac{V_{j+1,k}}{2(\Delta Y)} - \frac{1}{Pr(\Delta Y)^2}]\, T_{j+1,k+1} = \frac{U_{j+1,k}}{\Delta X}\, T_{j,k}$$

$$+ Ec[\frac{U_{j+1,k+1} - U_{j+1,k-1}}{2(\Delta Y)}]^2$$

$$(3.12)$$

Concentration Equation :

Hot Wall (V > O) :

$$[- \frac{V_{j+1,k}}{\Delta Y} - \frac{V_{T_{j+1,k-1}}}{\Delta Y}]\, C_{j+1,k-1}$$

$$+ [\frac{U_{j+1,k}}{\Delta X} + \frac{V_{j+1,k}}{\Delta Y} + \frac{V_{T_{j+1,k}}}{\Delta Y}]\, C_{j+1,k} = \frac{U_{j+1,k}}{\Delta X}\, C_{j,k}$$

$$(3.13)$$

Hot Wall (V < 0) :

$$- \frac{V_{T_{j+1,k-1}}}{\Delta Y} C_{j+1,k-1} + [\frac{U_{j+1,k}}{\Delta X} - \frac{V_{j+1,k}}{\Delta Y} + \frac{V_{T_{j+1,k}}}{\Delta Y}] C_{j+1,k}$$

$$+ \frac{V_{j+1,k}}{\Delta Y} C_{j+1,k+1} = \frac{U_{j+1,k}}{\Delta X} C_{j,k} \qquad (3.14)$$

Cold Wall (V > 0) :

$$- \frac{V_{j+1,k}}{\Delta Y} C_{j+1,k-1} + [\frac{U_{j+1,k}}{\Delta X} + \frac{V_{j+1,k}}{\Delta Y} - \frac{V_{T_{j+1,k}}}{\Delta Y}] C_{j+1,k}$$

$$+ \frac{V_{T_{j+1,k+1}}}{\Delta Y} C_{j+1,k+1} = \frac{U_{j+1,k}}{\Delta X} C_{j,k} \qquad (3.15)$$

Cold Wall (V < 0) :

$$[- \frac{V_{j+1,k}}{\Delta Y} + \frac{U_{j+1,k}}{\Delta X} - \frac{V_{T_{j+1,k}}}{\Delta Y}] C_{j+1,k}$$

$$+ [\frac{V_{j+1,k}}{\Delta Y} + \frac{V_{T_{j+1,k+1}}}{\Delta Y}] C_{j+1,k+1} = \frac{U_{j+1,k}}{\Delta X} C_{j,k} \quad \cdot \quad (3.16)$$

As mentioned earlier, the solution for the variables U, V, T and C is carried out in a marching procedure start- ing from the stagnation point (X=0). The discretized momen- tum equation (3.11) written for k = 1 (1) n leads to a set

of n nonlinear equations for n unknown values of U at the X-location $(j+1)$. This set is reduced to a linear set by replacing the coefficients $U_{j+1,k}$ and $V_{j+1,k}$ in (3.2) by their known values at the previous iteration (indicated by the superscript * in Eqn. (3.11)). The linearised tridiagonal set is solved iteratively using the discretized continuity equation (3.10) to update V at the location $(j+1)$.

Once values U and V have been determined at $(j+1)$, the discretized energy equation (3.12) written for $k = 1$ (1) n leads to a tridiagonal set of n linear equations that can be easily solved for n unknown values of T at the location $(j+1)$. If the adiabatic wall boundary condition is used the additional unknown wall temperature requires an additional equation for solution which is obtained from Eqn. (3.9). In this case, the last element in the first row of the coefficient matrix requires to be eliminated to preserve the tridiagonal character of the system of equations. This is done using the Gaussian elimination.

The temperature values computed at the $(j+1)$ location are substituted in Eqn. (3.4) to determine the thermophoretic velocity at this location.

Solution can then be obtained for the discretized
concentration equations (3.13) to (3.16) by substituting
the calculated U, V and V_T values at the (j+1) location.
For a hot wall, Eqn. (3.13) or (3.14) is selected to repre-
sent the conservation of the particles in the flow field
depending, respectively, upon whether V is positive or
negative. Equation (3.13) written for k = 1 (1) n leads
to a bidiagonal set of n linear equations whereas Eqn. (3.14)
leads to a tridiagonal set of the same number of equations.
The n unknown values of C at the location (j+1) are obtained
by solving this set of n equations.

There is a critical layer present near a hot wall. As
discussed in Sec. 2.1, the particle concentration gradient at
the edge of this critical layer is very large. Thus, C $\longrightarrow \pm \infty$
as Y $\longrightarrow$ O depending upon the value of PrK being $\gtrless$ 1. For
gases, of course, PrK > 1 is of academic interest only since
Pr $\simeq$ 0.7 and K < 1. Since the thickness of this critical
layer is unknown apriori, the large concentration gradient at

the edge of this layer can be satisfied by imposing $C = \pm \infty$ at the wall depending upon the value of PrK. For PrK < 1, the physical solution corresponds to C = 0 within the (particle-free) layer, and the particle concentration rising sharply at the edge of this layer. Unfortunately, an asymptotic solution of Eqn. (2.31) lends no help since this equation reduces to $\partial C/\partial Y \longrightarrow 0$ as $Y \longrightarrow \infty$; a well known fact. At any other value of Y, simplification of Eqn. (2.31) is not possible. We checked our solution in several ways so as to ensure that we had a unique solution. For a flat plate at zero incidence, it matched perfectly with Goren's results (Goren, 1977). More details are available in Sec. 4.3.3.

For the cold wall condition, the particle concentration is finite at the wall as observed earlier (see Sec. 2.1). In the case of negative V, Eqn. (3.16) is selected as the discretized concentration equation. This equation written for k = 0 (1) n leads to a bidiagonal set of (n+1) linear equations for the (n+1) unknown

values of C at the X-location (j+1). In the case of
positive V, Eqn. (3.15) is selected to represent the
particle conservation. However, this equation can not be
written at k = 0, where again Eqn. (3.16) has to be writ-
ten and multiplied by a negative sign throughout in
order to satisfy the conditions given in Sec. 3.1. This
equation and Eqn. (3.15) written for k = 1 (1) n together
give a tridiagonal set of n+1 linear equations for the
n+1 unknown values of C at the (j+1) location.

Thus the U, V, T, V_T and C values are obtained in
sequence at every (j+1) location during the marching pro-
cedure along the X-direction.

3.3 Computational Details

The computer programme takes care of the fact that
the boundary layer thickness has to be increased as we
move away from the stagnation point. Thus the value of n
is chosen so as to ensure that there are atleast 3 to 4
points for $k \leq n$ for which $U \simeq U_s$ for velocity boundary
layer. Similar adjustments are done separately for tem-
perature and concentration boundary layers in which case
the comparison is done with T and C respectively at the
edge of the boundary layer.

For computational efficiency, but without sacrificing accuracy, the step size ΔX is changed systematically as we march along the X-direction. Initially while starting from the stagnation point ΔX is very small (of the order of 10^{-5}). The ΔX value is approximately doubled at an interval of about 10 marching steps. However, beyond $|X| = 0.1$, marching is done for a large number of steps with the same ΔX (as ΔX has become sufficiently large). Thus in the span of X from 0 (stagnation point) to 3 (far away from the stagnation point), eleven different step sizes (ΔX) were used for computation. The set of ΔX and the number of steps marched with each ΔX are given in Table 3.1. For a small enough value of the initial ΔX, such as 10^{-5} used here, it is found that the singularity at the stagnation point is confined to about $5(\Delta X)$ on either side of the stagnation point.

While ΔX can be assigned any value without difficulty, it is easier to keep ΔY uniform due to central differencing employed for several terms in the Y-direction. However, due to large gradients of velocity, temperature and concentration (hot wall) around the critical layer, ΔY must be kept quite small near these regions. Then if ΔY is uniform across the boundary layer thickness, the number of simultaneous equations increases excessively. Solution

Table 3.1 Marching Pattern along X-direction

erial o.	$|\Delta X|$	Number of steps marched	Final $|X|$ value
1	0.00001	20	0.0002
2	0.00002	10	0.0004
3	0.00005	12	0.0010
4	0.00010	10	0.0020
5	0.00020	10	0.0040
6	0.00050	12	0.0100
7	0.00100	10	0.0200
8	0.00200	10	0.0400
9	0.00500	12	0.1000
0	0.01000	90	1.0000
1	0.02000	100	3.0000

of such large number of equations not only requires excessive computer time but also involves large round-off error. A practical solution is to use a fine mesh size (ΔY) in regions of large gradients and a relatively coarse grid away from it. This requires modification of the discretized equations (as explained in Appendix B) at locations where the mesh size changes. The sudden change in the concentration gradient especially near the critical layer (in the case of hot wall) makes the assignment of different ΔY in different regions unpredictable. This situation is averted by the use of an efficient self-adaptive grid scheme along the Y-direction (Section 3.4). Also this makes the programme more efficient apart from yielding more accurate results at the expense of a marginal increase in the computational time.

3.4   Adaptive Grid Generation

The self-adaptive grid scheme employed is essentially the same as that suggested by Nakahashi and Deiwert (1984, 1986, 1987). Based on the variational principle, a spring analogy is used in this method to redistribute the grid points in an optimal sense in order to reduce the overall solution error. Only one user specified parameter (for one-dimensional adaptation) denoting the ratio of maximum to minimum grid spacing desired is used to define all the important constants, thereby minimizing empiricism and making the method self-adaptive.

In the one-dimensional adaptation procedure, grid points in one direction, say, the Y-direction are re-arranged so as to equidistribute some positive weight function w(Y) over the field, i.e.,

$$\int_{Y_k}^{Y_{k+1}} w(Y) \, dY = \text{constant} \, . \qquad (3.17)$$

In discrete form this equation is represented as

$$\Delta Y_k \, w_k = \text{constant} \, , \qquad (3.18)$$

where $\Delta Y_k = Y_{k+1} - Y_k$, and w_k is fixed over the interval ΔY_k. For the equidistribution scheme with n number of grid intervals over a length £ in the physical space, grid spacing is given by

$$\Delta Y_k = \pounds / [w_k \sum_{i=1}^{n} \frac{1}{w_i}] \, . \qquad (3.19)$$

As suggested by Nakahashi and Deiwert (1987), the expression for weight function, w is chosen to be

$$w_k = 1 + A \, \overline{f}_k^B \, , \qquad (3.20)$$

where $\overline{f}_k = (f_k - f_{min})/(f_{max} - f_{min})$.

Equation (3.20) has been normalised so that the first constant is unity. When the constant A is zero, grid points are equally spaced. f_k is any non-negative function (at the grid point k) based on the solution of the problem. It is usually taken to be the gradient of the flow solution at the grid point k. A and B are positive constants, and f_{min} and f_{max} are the minimum and maximum values of the function f.

The constant A controls the ratio of maximum to minimum grid spacing desired. This ratio Max $|\Delta Y_k|$/Min $|\Delta Y_k|$, is equal to the ratio of the weight functions, Max$|w_k|$/Min$|w_k|$, as evident from Eqn. (3.19). Therefore,

$$A = \frac{\Delta Y_{max}}{\Delta Y_{min}} - 1 \ .$$ (3.21)

Thus (A+1) is initially specified as the desirable ratio of maximum to minimum grid spacing. The constant B is chosen such that the minimum grid spacing Min$|\Delta Y_k|$ is equal to the specified ΔY_{min}, and this can be achieved by finding solution to the equation

$$F(B) = Min|\Delta Y_k| - \Delta Y_{min} = 0 \ .$$ (3.22)

The Newton-Raphson method can be used to solve this equation iteratively using the following equation

$$B^{N+1} = B^N + \Delta B^N , \qquad (3.23)$$

where

$$\Delta B^N = \frac{F(B^N)}{\dfrac{\partial F(B^N)}{\partial B}} = \frac{Min|\Delta Y_k| - \Delta Y_{min}}{\dfrac{\partial Min|\Delta Y_k|}{\partial B}} \qquad (3.24)$$

The derivative in the denominator of Eqn. (3.24) can be evaluated using Eqns. (3.19) and (3.20) as

$$\frac{\partial Min|\Delta Y_k|}{\partial B} = -A \sum_{i=1}^{n} [\Delta Y_k(\delta_{ki} \frac{1}{w_k}$$

$$- \frac{w_k}{w_i^2} \frac{\Delta Y_k}{\pounds}) \bar{f}_i^B \ln \bar{f}_i] , \qquad (3.25)$$

where δ_{ki} is the Kronecker delta, and w_k and ΔY_k correspond to $Min|\Delta Y_k|$. The iteration for B starts with an initial guess (B^O) and the Eqns. (3.19) through (3.25) are solved to find a new value of B, namely B^1. The solution function, the gradient of which is used in Eqn. (3.20) as f, is interpolated on the new grid resulting from Eqn. (3.19). Lagrangian interpolation is used for this purpose. With the new value of B, the whole process is repeated till a reasonable low value of $|\Delta B|$

The Newton-Raphson method can be used to solve this equation iteratively using the following equation

$$B^{N+1} = B^N + \Delta B^N \; , \tag{3.23}$$

where

$$\Delta B^N = \frac{F(B^N)}{\frac{\partial F(B^N)}{\partial B}} = \frac{Min|\Delta Y_k| - \Delta Y_{min}}{\frac{\partial Min|\Delta Y_k|}{\partial B}} \tag{3.24}$$

The derivative in the denominator of Eqn. (3.24) can be evaluated using Eqns. (3.19) and (3.20) as

$$\frac{\partial Min|\Delta Y_k|}{\partial B} = -A \sum_{i=1}^{n} [\Delta Y_k (\delta_{ki} \frac{1}{w_k}$$

$$- \frac{w_k}{w_i^2} \frac{\Delta Y_k}{\ell}) \frac{B}{\bar{f}_i} \ln \bar{f}_i] \; , \tag{3.25}$$

where δ_{ki} is the Kronecker delta, and w_k and ΔY_k correspond to $Min|\Delta Y_k|$. The iteration for B starts with an initial guess (B^O) and the Eqns. (3.19) through (3.25) are solved to find a new value of B, namely B^1. The solution function, the gradient of which is used in Eqn. (3.20) as f, is interpolated on the new grid resulting from Eqn. (3.19). Lagrangian interpolation is used for this purpose. With the new value of B, the whole process is repeated till a reasonable low value of $|\Delta B|$ in Eqn. (3.23) is achieved.

A FORTRAN code is written for the self-adaptation of grid in the Y-direction following the above steps. This

subroutine is called at pre-specified X-locations in the marching direction so as to readapt the grid points along the Y-direction. Any one of the boundary layer solutions (U, T or C) can be selected to provide values of f as the Y-gradient of U, T or C for adaptation of the grid. However, for the hot wall case the particle concentration C, which has a rapid variation near the critical layer thickness, is more appropriate. Section 4.3.3 provides a token comparison of concentration profiles with and without grid adaptation.

The minimum value of ΔY is set at 0.005 and the maximum at 0.05. The self-adaptive grid generation technique distributes values of ΔY within this range. As many as 500 steps in the Y-direction are required for some values of angle β at the farthest downstream location $X = 3$. This discretization is used following considerable experimentation keeping the error incurred and reasonable computer time in view. The test case for error analysis is the Blasius solution for the flat plate at zero incidence. Our values of U and V for $\beta = 0$ are found to match exactly with the Blasius solution for all $X \geq 10^{-4}$. Similar results are obtained for Θ for which the exact solution corresponding to $\beta = 0$ is given by Schlichting (1979). During the testing phase, values of local skin friction coefficient and Nusselt number for normal impingement of the slot jet on the plate $(\beta = 90^{\circ})$ are also found to match exactly with those given by Miyazaki and Silberman (1972) for their $H \geq 3$. (See also Secs. 4.1.5 and 4.2.2).

CHAPTER 4

RESULTS FOR AN INCLINED PLATE

The computer code developed for the inclined plate
solution was tested thoroughly for the hydrodynamic and
thermal boundary layer calculations on a flat plate at
zero incidence ($\beta = 0$) and for flow past a wedge. In
these cases, of course, a similarity solution is possible
under certain conditions (Schlichting, 1979). Results
for the velocity and temperature profiles computed nume-
rically agreed perfectly with the standard similarity
solution in both cases. Following this validation of
the computer code for the solution of momentum and energy
equations, results were computed for the particle concen-
tration distribution due to thermophoresis on a plate at
zero incidence, and found to be in complete agreement
with those of Goren (1977). These tests were done for
various values of T_w, Ec and K.

Results were then computed for thermophoresis over
a plate inclined at various angles ($\beta = 15^{\circ}$, 30°, 45°,
60° and 90°). While the Prandtl number was kept constant
at 0.7 for most of the results, the effect of other

parameters such as the Eckert number, thermophoretic coefficient, and plate temperature was investigated. Also studied was the thermophoresis over an adiabatic plate. Most of the results are reported at five X-locations, two in the vicinity of the stagnation point ($X = \pm 0.01$), and the other three away from the stagnation point at $X = \pm 1.0$ and 3.0.

4.1 Hydrodynamic Boundary Layer

The only parameter that affects the velocity profiles is the pressure gradient in the momentum equation (2.28). This in turn depends upon the angle of inclination, β, of the plate.

4.1.1 Longitudinal Velocity Profiles

The normalised streamwise velocity (U/U_s) profiles in the boundary layer at various angles of inclination of the plate (β) are shown in Figs. 4.1 to 4.3. It may be noted from these figures that near the stagnation point, ($X = 0.01$), the hydrodynamic boundary layer thickness increases with β while the opposite is true away from the stagnation point ($|X| \geq 1.0$). There is perfect agreement between the present results and the standard similarity

solution at zero incidence (Blasius flow) denoted by 'o'
in Fig. 4.1. The velocity profiles in the negative X-
direction are also shown in Figs. 4.2 and 4.3. These
figures show that at a small angle of inclination, like
$\beta = 15^{\circ}$, the velocity profiles are different even when
one moves only a small distance on either side of the
stagnation point. The differences increase and are appre-
ciable for larger values of β also as one moves away from
the stagnation point, as expected.

4.1.2 Transverse Velocity Profiles

A consequence of the drastic change in the pressure
distribution, for incidence angles other than zero, is
more clearly reflected in the transverse velocity (V)
distribution reported in Figs. 4.4 to 4.6. Except for the
zero incidence angle, the transverse velocity component is
negative over the entire characteristic length ($|X| \leq 0.5$).
However, at larger $|X|$ values the transverse velocity tends
to become positive, and as expected, for smaller angles of
inclination first. The reason for V being negative is the
presence of a stagnation point at non-zero angles of inci-
dence of the plate. Near the stagnation point, the negative

transverse velocity increases with the angle of incidence
(Fig. 4.5), but away from the stagnation point at X = 1.0,
it decreases as the angle of incidence increases (Fig. 4.6).
The symbols '.0' in Fig. 4.4 again represent the Blasius
similarity solution thereby showing perfect agreement of the
present results for β = 0. The profiles in the negative X-
direction are also shown in Figs. 4.5 and 4.6. A behaviour
similar to that for the longitudinal velocity is also exhi-
bited by the transverse velocity in the negative X-region
of the plate.

4.1.3 Hydrodynamic Boundary Layer Thicknesses

The various hydrodynamic boundary layer thicknesses
are shown in Figs. 4.7 to 4.9. The 'stars' on these figures
correspond to the exact values for a flat plate at zero
incidence. Clearly, the presently computed results for β = 0
are in very good agreement with the exact results. The
integrals involved in the computation of displacement and
momentum thicknesses are evaluated using the trapezoidal
rule. The hydrodynamic boundary layer thickness in Fig. 4.7
corresponds to the usual U/U_s = 0.99. Note that the boun-
dary layer thickness is non-zero at X = 0 for β ≠ 0 as ex-
pected. Also, for β = 90°, all boundary layer thicknesses
are almost constant for $|X| \leq 0.5$. For other values of β,
minimum value of δ is reached in X < 0 region, as expected.

The location of this minima shifts away from the stagnation point as β increases, except for $\beta = 90^\circ$. For large values of $|X|$ the curves for different β are almost parallel except for $\beta = 90^\circ$. Thus while $\delta|x|^{-1/2}$ is a constant for $\beta = 0$ for all $x>0$ it is a constant for non-zero β ($\neq 90^\circ$) for large $|X|$ only. Also, while δ gets larger near the stagnation point as β increases, it decreases with β away from the stagnation point except for $\beta = 90^\circ$. Here δ refers to any of the three thicknesses under consideration.

Note that close to the stagnation point, $Re^{1/2} \delta/L$ is of order unity. For the boundary layer analysis to be valid, it is required that δ/x be small. Thus it appears that for $X \rightarrow 0$, the present results would be valid for $Re \rightarrow \infty$. At such a high Re, the assumption that the slot jet be laminar would no longer hold. According to Hanks and Ruo (1966), the upper limit of Re for ensuring a laminar slot jet would be about 2800. Thus the present results based on the boundary layer analysis of a laminar slot jet are expected to hold good experimentally in the region $|X| \geq 0.1$.

4.1.4 Flow Characteristics

Figures 4.10 through 4.13 show the streamlines over a cold plate at different angles of inclination. The values of dimensionless stream function Ψ noted on the various curves in these figures were computed from

$$\Psi = \int_0^Y U \, dY \; . \tag{4.1}$$

Note that the streamline pattern is unsymmetrical about the Y-axis for non-zero values of $\beta < 90^{\circ}$ but becomes symmetrical for $\beta = 90^{\circ}$. Note also that in these as well as in Figs. 4.14 to 4.16, we use the boundary layer coordinate Y instead of the physical coordinate y. Thus it may be difficult to visualize that the streamline pattern in Figs. 4.10 through 4.12 corresponds to the angle β as noted.

Figures 4.14 and 4.15 show the gas and particle velocity vectors, respectively, in the vicinity of a cold plate inclined at $\beta = 15^{\circ}$. Clearly, while the gas velocity vectors follow the streamlines of Fig. 4.10 (note the ratio of ordinate scales on Figs. 4.10 and 4.14), the aerosol particles fall to the cold plate in the normal direction due to the thermophoretic velocity component V_T. Recall that while U and V are zero at the plate, V_T is negative at the cold plate. On these figures the length of the velocity vectors is proportional to the magnitude of the velocity at the mid-point of the vector. The ratio of the proportionality constant for the length of the vectors in Fig. 4.14 to that of the vectors in Fig. 4.15 is 25. Similar results are obtained at other inclinations of the plate. From the streamline plots (Figs. 4.10 through 4.13) the nature of isovelocity curves can be easily guessed. A sample set of isovelocity curves, U/U_s, is shown in Fig. 4.16 for $\beta = 15^{\circ}$. The sharp turn in the curve is clearly visible

near the stagnation point, specially in the $X < 0$ region.
The hydrodynamic boundary layer thickness curve for $\beta = 15^{\circ}$
in Fig. 4.7 is the same as the curve corresponding to
$U/U_s = 0.99$ in Fig. 4.16. The isovelocity curves obtained
for other inclinations of the plate are similar to those
shown in Fig. 4.16.

4.1.5 Skin Friction

The local skin friction coefficient is calculated
using the relation

$$\frac{1}{2} C_f \ Re^{1/2} = (\partial U/\partial Y)_{Y=0} . \tag{4.2}$$

This parameter on both sides of the stagnation point and
at different angles of impingement is shown in Fig. 4.17.
At $X = 0$, the friction factor is zero for $\beta \neq 0$. This
obviously follows from the fact that for non-zero angles
of impingement there is no velocity gradient in the trans-
verse direction at the stagnation point. The effect of
potential flow velocity distribution at the plate for
different angles, β, shown in Fig. 2.6 is very clearly
reflected on the local skin friction coefficient. Far
downstream from the stagnation point ($X \geq 3$) the potential
flow velocity at the plate U_s approaches the free stream
velocity U_∞ so that the skin friction coefficient for any
non-zero angle of impingement tends to vary as that for

the flow over a flat plate at zero incidence. The latter, as computed presently, is also shown in Fig. 4.17, and matches perfectly with the exact values (Schlichting, 1979). For non-zero angles of impingement the skin friction co-efficient, starting from a zero value at the stagnation point, increases and reaches a maximum value close to the stagnation point owing to the small boundary layer thick-ness and large value of U_s in this region. The maxima shifts towards the stagnation point with decrease in the angle of impingement since the potential flow velocity U_s approaches the free stream velocity more rapidly for small values of β (see Fig. 2.6). Particularly striking is the shape of the curve in $X < 0$ region for small values of β owing to the rapid increase in U_s for such cases. The curve for $\beta = 90^\circ$ in Fig. 4.17 agrees perfectly with that corresponding to $H \rightarrow \infty$ in Fig. 3 of Miyazaki and Silberman (1972).

4.2   Thermal Boundary Layer

Apart from the angle of inclination of the plate, the thermal boundary condition on the plate, and the Prandtl and Eckert numbers also affect the temperature distribu-tion in the thermal boundary layer.   Considering air as the carrier fluid, the Prandtl number is assumed to be 0.7 for most of the results presented.   However, the

effect of different Pr and Ec is also studied. Two thermal conditions on the plate, isothermal and adiabatic plate, are considered.

4.2.1 Temperature Distribution

4.2.1.1 Isothermal Plate Without Viscous Dissipation

Figures 4.18 to 4.20 show the normalised dimensionless temperature $[\theta = (T-1)/(T_w-1)]$distribution for selected angles of inclination of the isothermal plate at different X-locations from the stagnation point for Pr = 0.7, Ec = 0. The behaviour of the temperature profiles vis-a-vis the angle of impingement β and distance X is very similar to that of the velocity profiles in Figs. 4.1 to 4.3. The symbols 'o' in Fig. 4.18 again correspond to the exact solution for a flat plate at zero incidence (Schlichting, 1979), thus validating the present results. Computations were also carried out for Prandtl numbers of 0.07, 0.2, 2.0 and 7.0 and also by taking into consideration the viscous dissipation term with Ec = 1. Results for these cases were found to be quite similar to those shown in Figs. 4.18 to 4.20 and confirmed the fact that larger Prandtl numbers make the thermal boundary layer thinner. The thermal boundary layer thickness, δ_θ, corresponding

to the usual value $\theta = 0.01$, is shown in Fig. 4.21 for an isothermal plate with Pr = 0.7 and Ec = 0. Similar results hold for other Pr and Ec values. These curves for δ_θ are similar to those for the hydrodynamic boundary layer thicknesses in Figs. 4.7 through 4.9. For a plate inclined at $\beta = 15^\circ$, the isotherms within the thermal boundary layer are shown in Fig. 4.22. These isotherms are quite similar to the isovelocity curves shown for $\beta = 15^\circ$ in Fig. 4.16. The thermal boundary layer thickness curve for $\beta = 15^\circ$ in Fig. 4.21 is the same as the curve corresponding to $\Theta = 0.01$ in Fig. 4.22. Similar isotherms are obtained for other angles of inclination of the plate.

4.2.1.2 Isothermal Plate with Viscous Dissipation

The temperature profiles for a large value of Ec (= 10) are shown in Figs. 4.23 and 4.24 respectively, for $T_w = 0.6$ and 0.8. Note that for non-zero Ec, θ depends upon T_w. The effect of viscous dissipation is illustrated in these figures for four selected angles of inclination of the plate between 0 to 90° at X = 0.01, 1.0 and 3.0. It is clear from these figures that the effect of viscous dissipation is profound as one moves away from the stagnation point. A temperature maximum within the

boundary layer is evident at such a large value of Ec.
Note that for $T_w < 1$, the minima in θ corresponds to the
maxima in T. For the flat plate flow ($\beta = 0$), the dissi-
pation of mechanical energy is too rapid for the wall to
absorb all the heat generated and the temperature exhibits
a maxima even at X = 0.01. However, for larger angles of
inclination of the plate, one needs to move sufficiently
far from the stagnation point before the temperature pro-
file exhibits a maxima. Also, the peak value obtained at
larger β is smaller at any X value compared to that at
$\beta = 0$. The effect of larger wall temperature ($T_w < 1$) is,
obviously, to produce a still larger peak temperature
value within the thermal boundary layer (see Fig. 4.24).
However, the nature of variation of the temperature pro-
file remains similar to that for a lower T_w.

4.2.1.3 Adiabatic Plate with Viscous Dissipation

Viscous dissipation with adiabatic wall condition
slightly increases the thermal boundary layer thickness
at any X-location. Figures 4.25 and 4.26 show the norma-
lised temperature profiles for various angles at Ec = 1
and 10, respectively. Note that the profiles are similar
to those without viscous dissipation (Fig. 4.18) except

that $\partial\theta/\partial Y = 0$ at the plate. Different Ec value also, have only marginal effect on the θ profiles. However, it should be mentioned here that, proportional to the amount of viscous dissipation the plate surface will be getting heated up. Hence when $Ec \neq 0$, the plate will be quite hot ($T_w > 1$) even at a small distance away from the stagnation point.

4.2.2 Nusselt Number

The Nusselt number is calculated using the relation

$$Nu = hL/k_f = Re^{1/2} (1-T_w)^{-1} (\partial T/\partial Y)_{Y=0}, \qquad (4.3)$$

where h is the local heat transfer coefficient. Figures 4.27 to 4.30 display the local Nusselt number (based on the slot jet thickness L) or the normalised temperature gradient in the transverse direction at the plate surface obtained for $Pr = 0.7, 1.0, 5.0$ and 10.0, and isothermal wall condition with $Ec = 0$. Here again the curves for $\beta = 90^o$ agree exactly with that for $H \rightarrow \infty$ in Figs. 4 to 7 of Miyazaki and Silberman (1972). For $\beta = 90^o$, the Nusselt number variation is symmetrical about the stagnation point, and Nu at $X = 0$ is about twice that at $X = 3.0$. There is a substantial change in the $Nu/Re^{1/2}$

profiles for other values of angle β. The maxima in these profiles lies in the X < 0 region, and shifts towards the stagnation point as β decreases. At $\beta = 15^o$ for Pr = 0.7, the maximum value of local Nusselt number is as much 10 times that at X = 3 (Fig. 4.27). At higher Prandtl numbers this ratio is even higher (Figs. 4.28 to 4.30). However, this maxima lies in the region $|X| < 0.1$, and is therefore not very meaningful for the laminar slot jet as per the discussion in Sec. 4.1.3. Heat transfer is enhanced considerably by an increase in the Prandtl number because a large Prandtl number implies a large thermal capacity of the fluid, enabling the fluid to carry more heat for the same temperature difference $(t_w - t_\infty)$. The increase in the Nusselt number at small values of β is also more pronounced for large Prandtl numbers. It should be noted that the large change in Nusselt number values with respect to β occurs only in the range −1 < X < 1. Outside this range the Nusselt number is very close to that for the flow over a flat plate at zero incidence. The latter is also shown in Figs. 4.27 to 4.30 based on present computations and matches perfectly with the exact values (Schlichting, 1979).

The mean Nusselt number over the length X of the plate can be computed using the relation

$$Nu_m \ Re^{-1/2} = -\ \frac{1}{X} \int_0^X (\partial\theta/\partial Y)_{Y=0} \ dX \ . \qquad (4.4)$$

The variation of mean Nusselt number computed over a length of the plate equal to the slot jet thickness on either side of the stagnation point is shown in Fig. 4.31 for selected values of angle β and Eckert number. As expected, the mean Nusselt number increases with the Prandtl number. The presence of viscous dissipation with Ec = 1 further increases the mean Nusselt number as shown in Fig. 4.31. Also note that on a log-log plot $Nu_m \ Re^{-1/2}$ varies linearly with Pr. Thus we have

$$Nu_m \ Re^{-1/2} \ \propto \ Pr^m \ , \qquad (4.5)$$

where the exponent m depends upon β and Ec, and for the results shown in Fig. 4.31 varies from 1/3 to 1/2.

4.3 Concentration Boundary Layer

In addition to the angle of inclination of the plate,

and Prandtl and Eckert numbers, the parameters that affect the particle concentration are the thermophoretic coefficient and thermal boundary condition on the wall ($T_w > 1$ or $T_w < 1$ or $(\partial T/\partial Y)_{Y=0} = 0$). While the Prandtl number is kept constant at 0.7 throughout most of the present analysis (assuming air as the carrier fluid), effect of all other parameters is studied. Results for the flat plate at zero incidence are included here for the sake of completeness and comparison. They match exactly with those obtained by Goren (1977) using the similarity analysis.

4.3.1 Particle Concentration Profiles for a Cold Wall

From Eqn. (2.30) it follows that for cold wall conditions ($T_w < 1$) the thermophoretic velocity is directed towards the wall. In this case a non-zero concentration at the wall is expected from the solution of Eqn. (2.31). In Fig. 4.32 a number of aerosol particle concentration profiles are given for various angles of inclination of the plate; all for $Pr = 0.7$, $T_w = 0.25$, $Ec = 0$ and $K = 0.75$. These profiles are drawn at $X = \pm 0.01$, ± 1.0 and 3.0, and are very similar to the U-velocity profiles in Figs. 4.1 to 4.3 except that unlike U, $C \neq 0$ at the cold plate. The concentration profiles at $90°$ angle

of inclination of the plate are almost stationary with respect to X over $|X| \leq 1$.

It is interesting to note that the wall concentration (at $Y = O$) is almost independent of the angle of inclination of the plate and of the distance from the stagnation point. The reason for this could be attributed to the coupled variation of the temperature and concentration gradient at the wall for any β (see Eqn. (1.6)). For the conditions pertaining to Fig. 4.32 the value of wall concentration varies from 0.31 to 0.32. Actual variation of C_w is discussed later.

The nature of particle concentration profiles is not altered by changing the wall temperature as long as $T_w < 1$. Figures 4.33 to 4.35 report the results for different T_w values for two representative angles of inclination of the plate ($\beta = 45^o$ and 90°). Figure 4.33 shows the profiles close to the stagnation point ($X = \pm 0.01$) while Figs. 4.34 and 4.35 represent the same away from the stagnation point ($X = \pm 1.0$ and 3.0, respectively). The particle concentration at the wall increases with T_w as the concentration distribution becomes flatter. At high T_w values (but $T_w < 1$) there is hardly any difference in the concentration profiles for

different angles especially at larger X values (see Figs. 4.34 and 4.35).

The effect of Prandtl number on the heat transfer characteristics was presented in Section 4.2.2. In Fig. 4.32 the particle concentration profiles were illustrated for a cold plate at $Pr = 0.7$ and with $Ec = 0$, $K = 0.75$ and $T_w = 0.25$. Keeping other conditions the same computations were carried out for higher values of the Prandtl number. The results are presented in Figs. 4.36 to 4.38 for $Pr = 1$, 5 and 10, respectively. Each of these figurues shows the concentration profiles for five selected angles ($\beta = 0$,15°,30°,60° and 90°) at three X-locations ($X = 0.01$, 1 and 3). The important inference of these results is that the wall concentration decreases for larger Prandtl number fluids. This is caused by the larger heat transfer due to the higher temperature gradient at the wall (see Figs. 4.27 to 4.30). Also, the wall concentration gradient is smaller at higher Pr values as seen from Figs. 4.36 to 4.38.

The concentration boundary layer thickness correspon-ding to $C = 0.99$ is shown in Fig. 4.39, for an isothermal plate with $Pr = 0.7$, $Ec = 0$, $K = 0.75$ and $T_w = 0.25$. Simi-lar results hold for other Pr, Ec, K and T_w (< 1) values.

Clearly the curves for δ_c in Fig. 4.39 are similar

to those for the hydrodynamic and thermal boundary

layer thicknesses in Figs. 4.7 and 4.21 respectively.

Very close to the stagnation point (X $\simeq$ 0.01) the

concentration boundary layer thickness decreases as

the angle of incidence decreases. However, the

situation at X $\simeq$ 1.0 is just the opposite as

shown in Fig. 4.39. The maximum concentration bou-

ndary layer growth occurs for the flow past a

flat plate at zero incidence. For the cold iso-

thermal plate inclined at $\beta = 15^o$, isoconcentration

curves are shown in Fig. 4.40 for Pr = 0.7, Ec = 0,

K = 0.75 and T_w = 0.25. These curves are quite simi-

lar to the isovelocity curves and isotherms shown

in Figs. 4.16 and 4.22 respectively. The concentrat-

ion boundary layer thickness curve for $\beta = 15^o$ in

Fig. 4.39 is the same as the line corresponding

to C = 0.99 in Fig. 4.40. Similar isoconcentration

curves are obtained for other angles of inclination

of the cold plate.

4.3.2 Particle Concentration at a Cold Wall

In Fig. 4.41 the particle concentration at the wall, C_w, is plotted against the thermophoretic coefficient for Ec = 0 and Pr = 0.7. This shows clearly the effect on C_w due to the presence of the stagnation point for $\beta \neq 0$. Any non-zero angle of inclination of the plate is represented by a single curve for a particular T_w irrespective of the X-location. Such curves are shown for T_w = 0.25, 0.5 and 0.9 in Fig. 4.41. Clearly, the value of C_w at the cold plate increases as T_w increases and K decreases, except when β = 0 and K → 0. The curves for $\beta \neq 0$ approach unity as K approaches zero. However, for β = 0 the behaviour of C_w is quite different for small values of K. In this case C_w → 0 as K → 0. When K = 0, there is no thermophoresis and the aerosol particles move with the same velocity as the gas particles (V_T = 0). For β = 0, V is positive and hence the particles move away from the plate making C_w → 0. The situation is reversed for $\beta \neq 0$, as V is negative in which case C_w → 1 as K → 0. The wall concentration also varies with X in the absence of the stagnation point (β = 0) as shown in Fig. 4.42 at X = 0.01 and X = 1.0. The particle concentration values at the

cold wall corresponding to Fig. 4.41 and Fig. 4.42 are given in Table 4.1.

The variation of wall concentration with respect to distance X at different angles of impingement is shown in Fig. 4.43 for Pr = 0.7, Ec = 0, K = 0.7 and T_w = 0.25. This confirms the finding of Gokoglu and Rosner (1986) that the mass transfer due to thermophoresis is enhanced for non-zero pressure gradients in the boundary layer. The major variation of C_w is noted in β = 0 profile. For all other angles the C_w value remains between 0.31 and 0.32 throughout the flow field as mentioned in the earlier section. However, a sudden decrease in the wall concentration (from 0.32 to 0.31) is noted very close to the stagnation point in the negative X-region for lower angles of inclination of the plate. The reason for this is better understood by the wall concentration gradient curves plotted for identical conditions in Fig. 4.44. The concentration gradient at the wall exhibits a sharp peak for smaller angles of impingement very close to the stagnation point in (X < 0) region. The local dimensionless concentration flux at the wall $-(CV_T)_w$, as defined by Homsy et al. (1981), is shown in Fig. 4.45. It may be noted that the nature of curves in Figs. 4.44 and 4.45 is quite similar to that of

Table 4.1 Particle concentration at a cold wall for Pr = 0.7, Ec = 0

| K | β = 0 | | | | | | β ≠ 0 (X=0.01; the values change in the 3rd significant place for other values of X) | | |
| | T_w = 0.25 | | T_w = 0.5 | | T_w = 0.9 | | $T_w=0.25$ | $T_w=0.5$ | $T_w=0.9$ |
	X=0.01	X=1.0	X=0.01	X=1.0	X=0.01	X=1.0			
0.01	0.2925	0.5417	0.4741	0.6054	0.7200	0.7279	0.7780	0.9292	0.9956
0.05	0.3475	0.5804	0.5096	0.7518	0.7226	0.7603	0.6317	0.8651	0.9911
0.10	0.3700	0.5500	0.5349	0.7675	0.7257	0.7936	0.5800	0.8100	0.9800
0.20	0.3681	0.4590	0.5585	0.7339	0.7314	0.8402	0.4753	0.7543	0.9754
0.50	0.3300	0.3593	0.5600	0.6397	0.7453	0.8970	0.3657	0.6472	0.9719
1.20	0.2586	0.2668	0.5000	0.5236	0.7637	0.8992	0.2657	0.5220	0.9091
2.00	0.2120	0.2169	0.4386	0.4496	0.7695	0.8826	0.2128	0.4432	0.8702

the Nusselt number in Figs. 4.27 to 4.30.

Efforts were also made to find the suitability of Eqns. (1.6) and (1.7) for determining the particle concentration at an inclined plate. Table 4.2 gives a token comparison of C_w values obtained by solving the particle concentration equation (2.31), and by using Eqns. (1.6) and (1.7). The values seems to match quite well.

4.3.3 Particle Concentration Profiles for a Hot Wall

As mentioned earlier a hot wall ($T_w > 1$) repels the aerosol particles away from it. It is also evident from Eqn. (2.30) that $T_w > 1$ yields a positive thermophoretic velocity. Thus a critical layer is formed adjacent to a hot wall. However, the particle concentration at the edge of the critical layer depends upon the product Pr.K being less than or greater than unity. The similarity analysis in Sec. 2.1 for thermophoresis over a wedge shows that the particle concentration approaches $\pm\infty$ as the hot plate is approached according as Pr.K $\gtrless$ 1.

Numerically the presence of the critical layer near a hot surface creates a problem for the solution of the particle concentration equation (2.31). Theoretically the solution of particle conservation equation should

Table 4.2 Comparison of C_w values obtained from Eqns. (2.31), (1.6) and (1.7) for Pr = 0.7, Ec = 0, K = 0.75

T_w	X	β = 0		β = 15°		β = 45°		β = 90°		
		Eqn. (2.31)	Eqn. (1.6)	Eqn. (2.31)	Eqn. (1.6)	Eqn. (2.31)	Eqn. (1.6)	Eqn. (2.31)	Eqn. (1.6)	Eqn. (1.7)
0.6	0.01	0.6037	0.5926	0.6882	0.6886	0.6909	0.6909	0.6914	0.6914	
	0.10	0.6352	0.6336	0.6878	0.6879	0.6909	0.6910	0.6914	0.6914	
	1.00	0.6684	0.6680	0.6864	0.6864	0.6902	0.6902	0.6911	0.6913	0.6928
	2.00	0.6752	0.6754	0.6854	0.6856	0.6893	0.6894	0.6893	0.6892	
	3.00	0.6782	0.6785	0.6848	0.6851	0.6883	0.6883	0.6877	0.6877	
0.8	0.01	0.6994	0.6102	0.8605	0.8620	0.8175	0.8338	0.8636	0.8643	
	0.10	0.7779	0.7631	0.8603	0.8604	0.8620	0.8615	0.8627	0.8626	
	1.00	0.8230	0.8193	0.8599	0.8600	0.8621	0.8623	0.8626	0.8627	0.8588
	2.00	0.8340	0.8318	0.8596	0.8594	0.8618	0.8620	0.8619	0.8625	
	3.00	0.8396	0.8381	0.8592	0.8599	0.8614	0.8612	0.8612	0.8613	

yield $C = \pm \infty$ at the wall ($Y = 0$) depending upon the value of Pr.K. However, $\pm \infty$ cannot be used in computations. A number of numerical experiments were carried out in this regard. Based on comparison of critical layer thickness with results of Goren (1977) for a flat plate at zero incidence, it was found that using $C(X,0) = \pm 10$ for Pr.K $\gtrless 1$ in the computations adequately represented the theoretical value ($\pm \infty$). Due to very high values of concentration gradient, $|\partial C/\partial Y|$, at the edge of the critical layer, use of a grid adapted in the Y-direction on the basis of $\partial C/\partial Y$ is essential for accurate results. Figures 4.46 and 4.47 give a token comparison of results obtained for Pr.K < 1 with and without the use of adapted grid. Similar results were found for Pr.K > 1. Grids adapted on the basis of $\partial U/\partial Y$ and $\partial T/\partial Y$ were also tried but $\partial C/\partial Y$-adapted grids yielded the best comparison with Goren's results for a flat plate at zero incidence. All the results were therefore found using $\partial C/\partial Y$-adapted grid in the Y-direction.

Figure 4.48 displays the concentration profiles at various locations on a hot plate for different angles of inclination of the plate with $T_w = 2.0$, Pr = 0.7, Ec = 0 and K = 0.75 so that Pr.K < 1. Particularly striking is

the sudden drop to zero of the particle concentration at
the critical layer, which is in accord with the observed
sharpness of the boundary of the particle free layer on
hot objects. It is evident from Fig. 4.48, that the cri-
tical layer thickness depends upon both the X-location and
the angle of inclination of the plate. Similar to the
behaviour of concentration profiles over a cold plate, the
change in the concentration profile with respect to X is
minimum for $\beta = 90^{\circ}$ and maximum for $\beta = 0$. At higher
wall temperatures the concentration drop is more gradual
as also observed by Goren (1977) for $\beta = 0$. For hot wall
conditions $(T_w > 1)$, the particles are repelled from the
wall when Pr.K < 1, whereas the concentration at $Y \rightarrow \infty$ is
maintained at C = 1 by the external flow. Hence a peak
in the concentration profile (C > 1) is obtained outside
the critical layer and C suddenly drops to zero at the
edge of the critical layer. The peak concentration value
attained adjacent to the critical layer is larger for non-
zero pressure gradient flow $(\beta \neq 0)$ than for the flow
without the pressure gradient $(\beta = 0)$. However, far away
from the stagnation point (X = 1.0 and 3.0) only a margi-
nal difference can be noted in the maximum concentration
value between the two cases. For $T_w = 2.0$ the maximum
concentration value obtained is about 1.18 near the

stagnation point. Other hot plate temperatures for Pr.K < 1 show similar profiles except that the maximum concentration, attained near the edge of the critical layer, increases with the wall temperature at all angles of inclination of the plate.

Figure 4.49 illustrates the particle concentration profiles on a heated wall for the case of Pr.K > 1 with Pr = 0.7, Ec = 0, T_w = 2.0 and K = 1.5. As expected from the earlier discussion, the particle concentration becomes infinite as the wall is approached. But for this change, the behaviour of the concentration profiles for different angles of inclination is similar to that discussed for Pr.K < 1. It may be noted, however, that Pr ≃ 0.7 for a gas. Thus for Pr.K to be greater than unity, K would have to be greater than about 1.4. This is outside the range of

values for K (cf. Chapter 2). Therefore the case
of Pr.K > 1 is one of academic interest only, as long
as the carrier fluid is a gas.

4.3.4 Critical Layer Thickness near a Hot Wall

Figures 4.50 and 4.51 give the thickness of the cri-
tical layer, Y_c, near a hot wall as a function of the
thermophoretic coefficient for three different angles of
inclination of the plate ($\beta = 0$, 15° and 90°) at the
locations X = 1.0 and 3.0 respectively. Curves are shown
for various values of $T_w > 1$ and for Pr = 0.7 and Ec = 0.
As expected, the critical layer thickness increases with
the wall temperature and K. Away from the stagnation
point (at X = 1.0 and 3.0) Y_c is minimum for $\beta = 90^o$ and
maximum for $\beta = 0$. The variation in critical layer thick-
ness with K and X-location (upto X = 1.0) is shown in
Figs. 4.52 to 4.54 for three different angles, 0, 15° and
90°, respectively. The curves are shown at X = 0.01, 0.1
and 1.0 for three different wall temperatures (T_w = 2.0,
1.25 and 1.1) and with Ec = 0 and Pr = 0.7. For a given
K, the effect of increasing X as well as T_w on the cri-
tical layer thickness diminishes as β increases. Tables 4.3

Table 4.3 Critical layer thickness near a hot wall
($\beta = 0$, $Pr = 0.7$, $Ec = 0$)

K	$T_w = 2.0$		$T_w = 1.25$		$T_w = 1.1$	
	$X = 0.01$	$X = 1.0$	$X = 0.01$	$X = 1.0$	$X = 0.01$	$X = 1.0$
0.05	0.0930	0.4321	0.0910	0.3545	0.0200	0.0990
0.20	0.1271	0.7610	0.0957	0.4922	0.0927	0.3968
0.50	0.1523	1.1243	0.1254	0.7404	0.0966	0.5125
1.20	0.1967	1.6904	0.1470	1.0566	0.1088	0.7067
2.00	0.2213	2.0710	0.1671	1.3204	0.1228	0.8951

Table 4.4 Critical layer thickness near a hot wall
($\beta = 15°$, $Pr = 0.7$, $Ec = 0$)

K	$T_w = 2.0$		$T_w = 1.25$		$T_w = 1.1$	
	$X = 0.01$	$X = 1.0$	$X = 0.01$	$X = 1.0$	$X = 0.01$	$X = 1.0$
0.05	0.0692	0.2506	0.0491	0.1596	0.0316	0.1122
0.20	0.1364	0.5074	0.0857	0.3130	0.0602	0.2144
0.50	0.2190	0.8219	0.1332	0.4951	0.0926	0.3341
1.20	0.3481	1.3089	0.2063	0.7718	0.1430	0.5118
2.00	0.4561	1.7064	0.2668	1.0005	0.1825	0.6601

Table 4.5 Critical layer thickness near a hot wall
(β = 90°, Pr = 0.7, Ec = 0)

K	$T_W = 2.0$		$T_W = 1.25$		$T_W = 1.1$	
	X = 0.01	X = 1.0	X = 0.01	X = 1.0	X = 0.01	X = 1.0
0.05	0.1844	0.2016	0.1167	0.1278	0.0809	0.0875
0.20	0.3732	0.4075	0.2300	0.2513	0.1561	0.1702
0.50	0.6080	0.6625	0.3642	0.3975	0.2448	0.2673
1.20	0.9862	1.0708	0.5707	0.6221	0.3791	0.4136
2.00	1.3058	1.4145	0.7448	0.8109	0.4915	0.5354

to 4.5 give the critical layer thickness, respectively,
for $\beta = 0$, 15° and 90° for five selected values of K with
$T_w = 2.0$, 1.25 and 1.1 at X = 0.01 and 1.0.

In Figs. 4.55 and 4.56 the variation of critical
layer thickness with respect to wall temperature is shown
for K = 0.5 and 2.0, respectively. For the same two K
values Figs. 4.57 and 4.58 give the variation of Y_c with
respect to the angle of inclination of the plate. In
these figures curves are shown for Y_c at X = 0.01 and 1.0.
From Figs. 4.55 and 4.56 it may be noted that the critical
layer thickness changes only a little with X over $X \leq 1$
for $\beta = 90^{\circ}$ but for $\beta = 0$, it changes a lot. Figs. 4.57
and 4.58 show that while Y_c increases almost linearly
with β at X = 0.01, it decreases first sharply (for
$\beta \lesssim 20^{\circ}$) and then gradually as β increases at X = 1.0.

4.3.5 Viscous Dissipation Effect

The effect of viscous dissipation becomes important
at high speeds, i.e., for Ec of the order of unity. Re-
sults were therefore computed for both cold and adiabatic
wall boundary conditions for Ec ranging from 1 to 10.
$T_w > 1$ boundary condition leads to results very similar to
those for the adiabatic wall and therefore results for
heated wall when Ec $\neq 0$ are not presented.

4.3.5.1 Cold Wall

Figures 4.59 to 4.62 illustrate the effect of viscous dissipation at four selected angles of inclination of the plate between 0 to 90°. These figures show the particle concentration profiles for $Pr = 0.7$, $T_w = 0.6$ and $K = 0.75$ at $X = 0.01$, 1.0 and 3.0. Near the stagnation point ($X = 0.01$) the profiles are almost independent of the Eckert number except for $\beta = 0$. Particularly striking is the drop in C_w as Ec is raised from 0 to 10. As illustrated in Figs. 4. 23 and 4.24 the isothermal plate temperature profiles exhibit a maxima within the boundary layer at large values of Ec. Correspondingly, the temperature gradient ($\partial T/\partial Y$) is negative in a major portion within the thermal boundary layer. Hence with non-zero viscous dissipation the thermophoretic velocity (directly proportional to $\partial T/\partial Y$) becomes positive in the region where the temperature gradient is negative. Due to this the particles are blown away from the surface although V_T is more or less the same at the wall for any value of Ec. Consequently, a significant reduction in particle concentration is noted near the plate along with a corresponding increase in values greater than unity a little away from the plate. The peak concentration value

obtained decreases marginally and shifts closer to the plate as β increases (see Figs. 4.59 to 4.62). For $\beta = 0$, the wall concentration remains almost constant over the entire plate surface for any value of Ec. However, when the stagnation point is present ($\beta \neq 0$), the wall concentration decreases as X increases. Similar results were also obtained with larger cold wall temperature ($T_w = 0.8$). They are presented in Figs. 4.63 through 4.66. The curves for nondimensional concentration profiles in Figs. 4.59 through 4.66 are in perfect agreement with the results of Goren (1977) and Gokoglu and Rosner (1985) shown in their Figs. 6 and 5, respectively. It may also be noted that the wall concentration depends upon T_w only at lower values of Ec. Irrespective of the angle of inclination, the wall concentration (away from the stagnation point) is higher at larger T_w values when Ec $\lesssim$ 3.0.

4.3.5.2 Adiabatic Wall

For the flow over an adiabatic inclined plate, Figs. 4.67 to 4.70 show the particle concentration profiles for a series of Eckert numbers (Ec = 0, 1, 3, 5 and 10) and angles of inclination ($\beta = 0$, 15° 45° and 90°). Here again the profiles are shown at X = 0.01, 1.0 and 3.0 for Pr = 0.7

and K = 0.75. These profiles exhibit a behaviour similar to that for the hot wall condition explained in Sec. 4.3.3, except near the wall ($Y \simeq 0$) where $V_T = 0$ for the present case since $(\partial T/\partial Y)_{Y=0} = 0$ leading to $C_w = 0$. It can be observed that the effect of Ec as well as X-location on the concentration profile diminishes as β increases. This follows from the negligible variation of temperature profiles over an adiabatic plate at non-zero angles of inclination for $Ec \neq 0$ (Sec. 4.2.1.3 and Figs. 4.25 and 4.26).
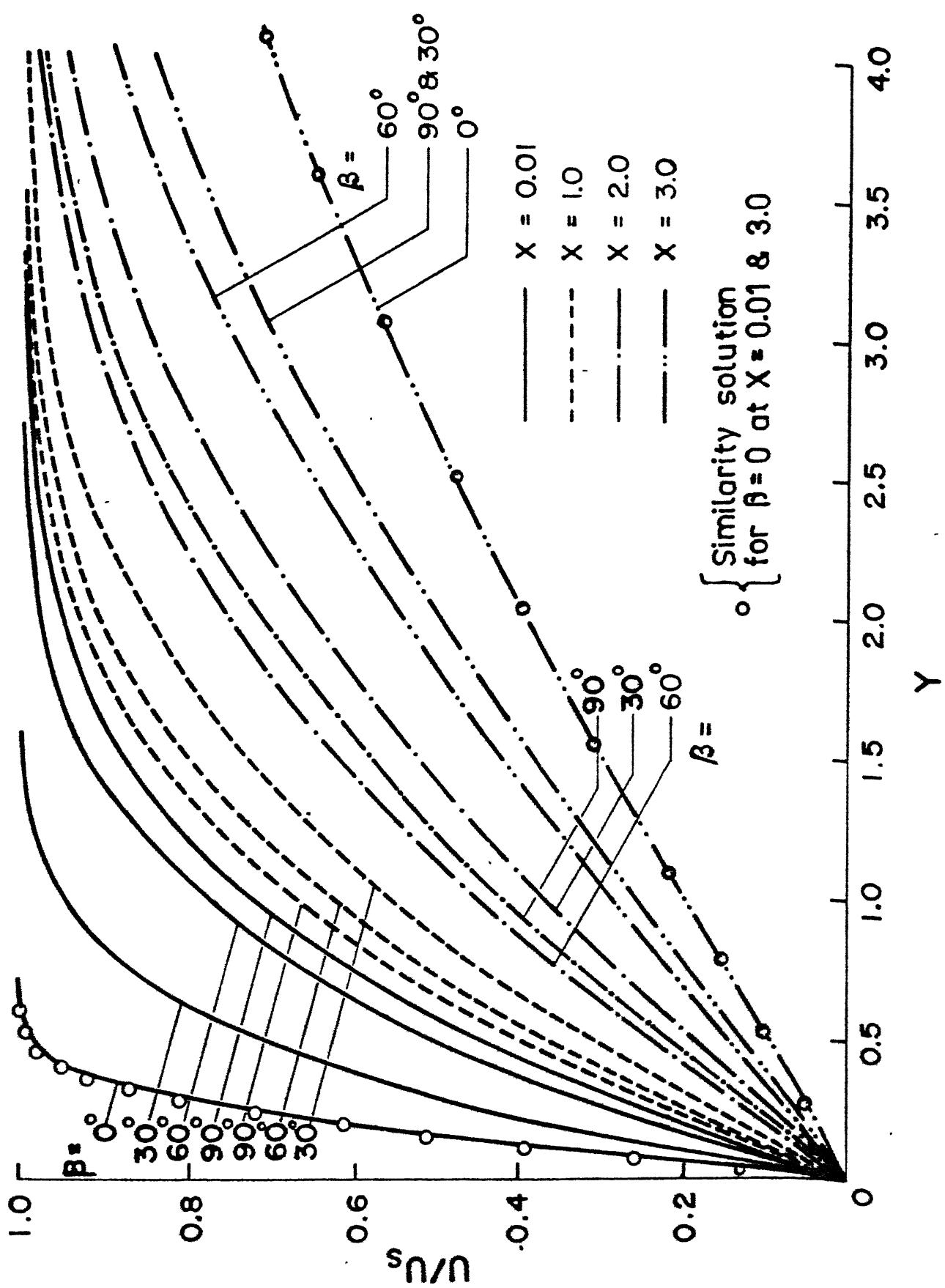
Fig. 4.1 Longitudinal velocity profiles for flow over an inclined plate
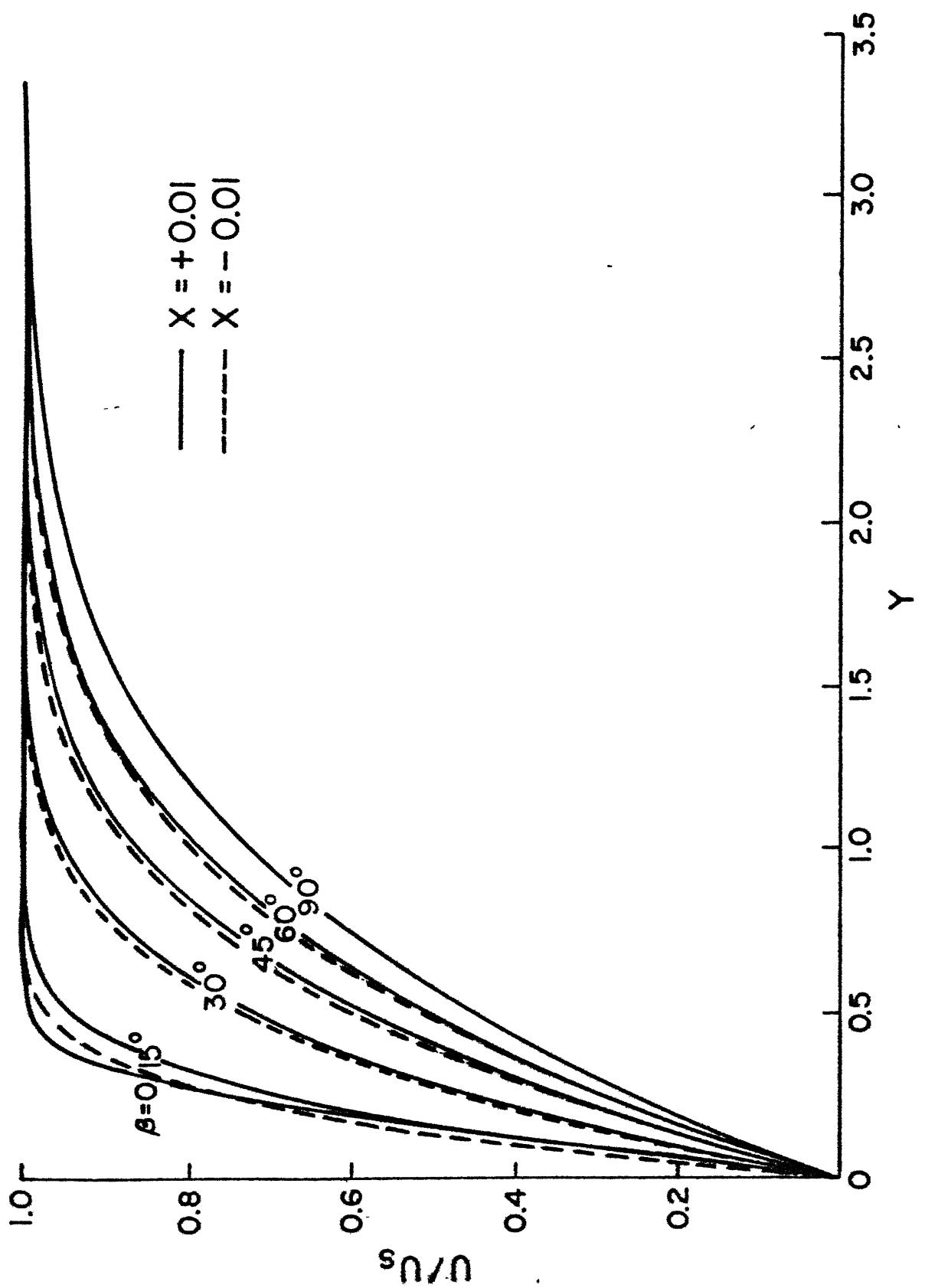
Fig.4.2 Longitudinal velocity distribution for flow over an inclined plate
(X = ± 0.01)
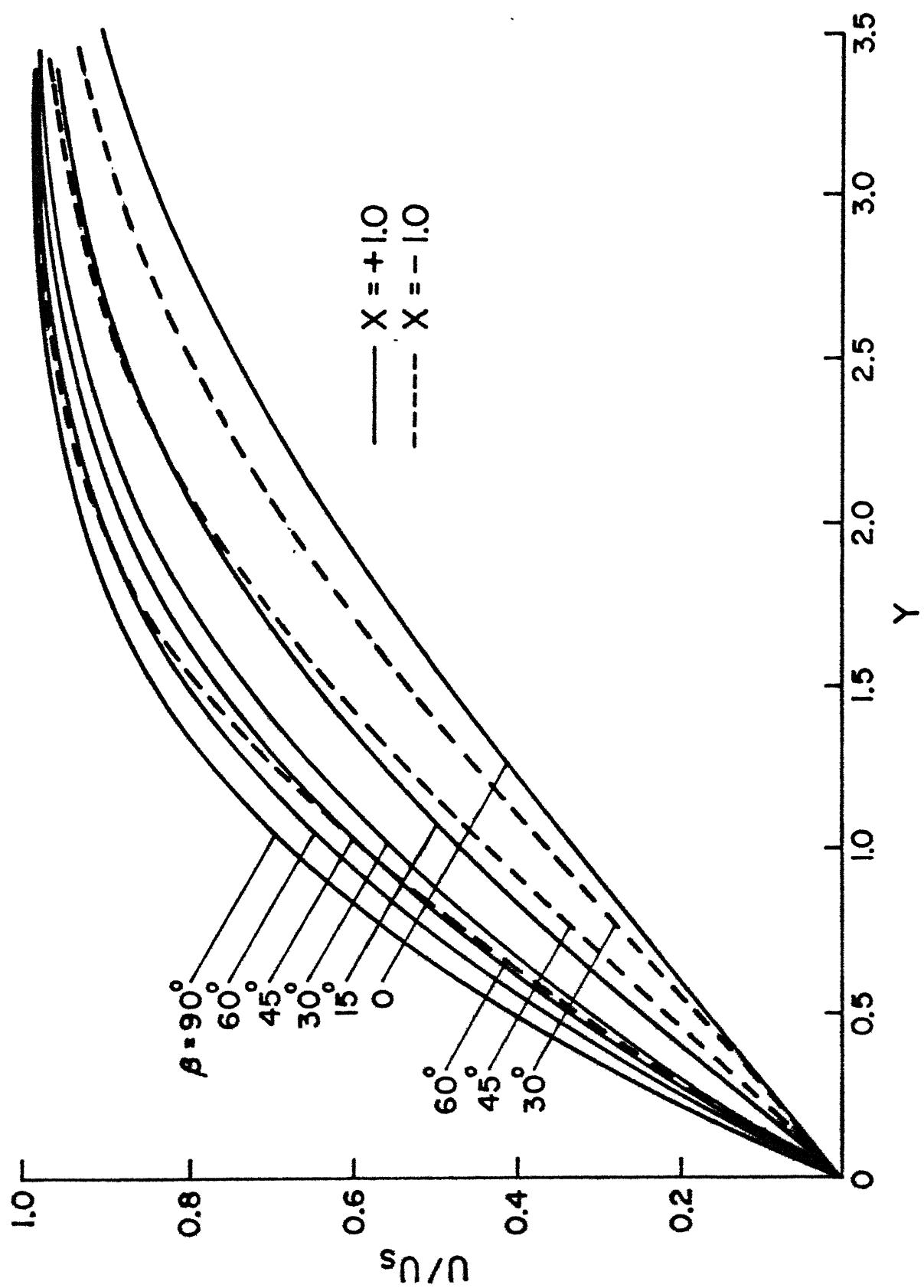
Fig. 4.3   Longitudinal velocity distribution for flow over an inclined
plate $(X = \pm 1.0)$
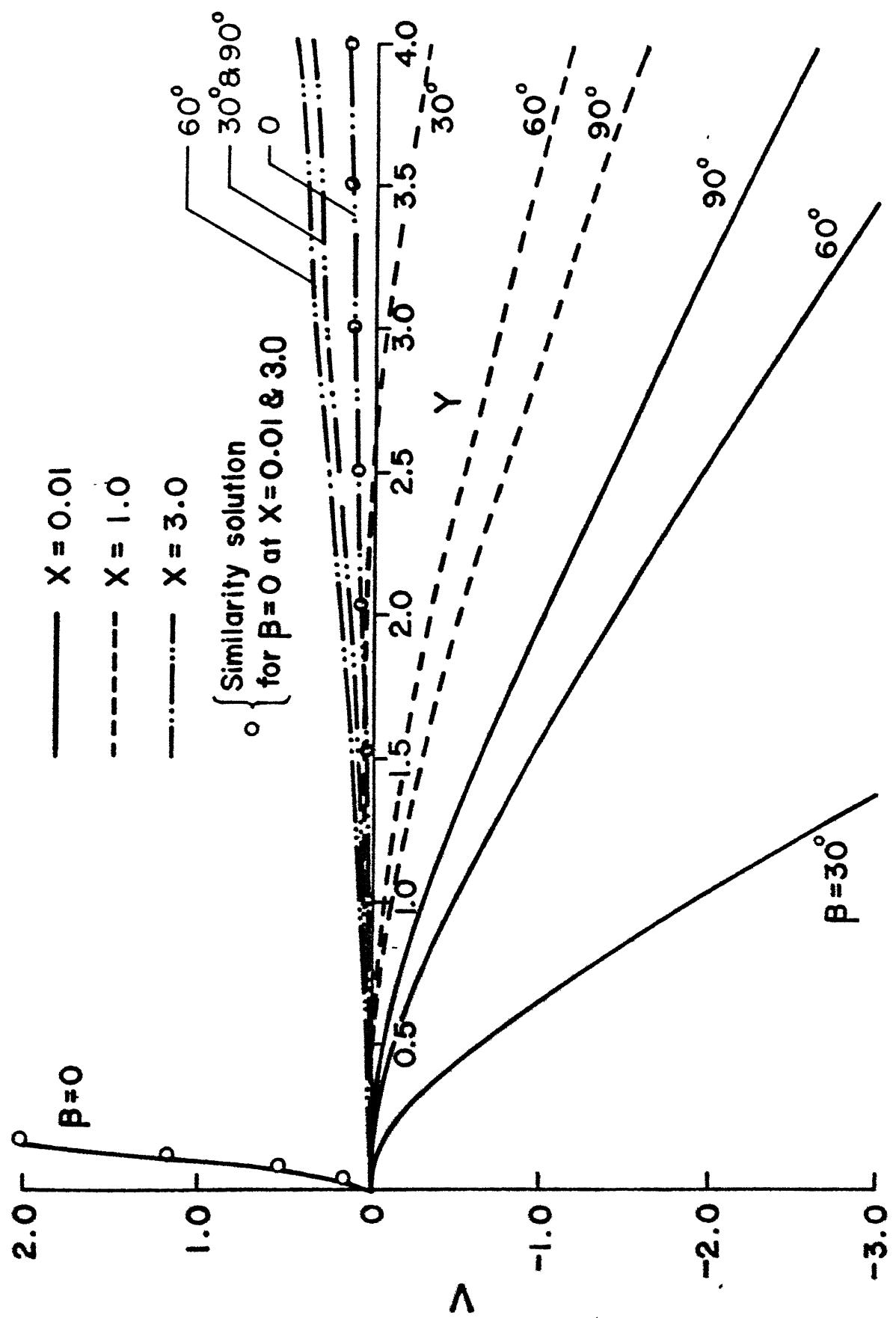
Fig. 4.4. Transeverse velocity profiles for flow over an inclined plate
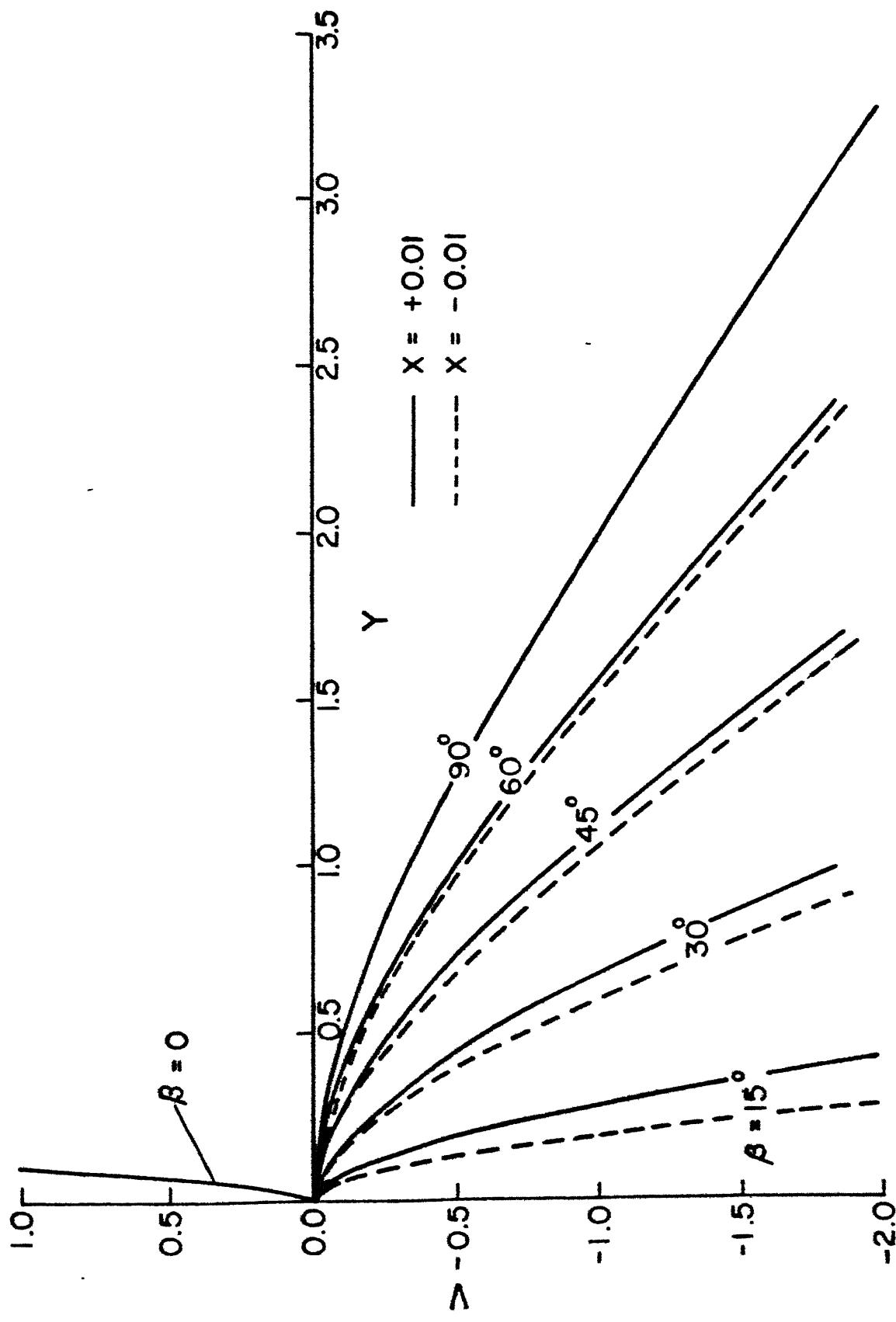
Fig. 4.5 Transverse velocity distribution for flow over an inclined plate (X = ±0.01)
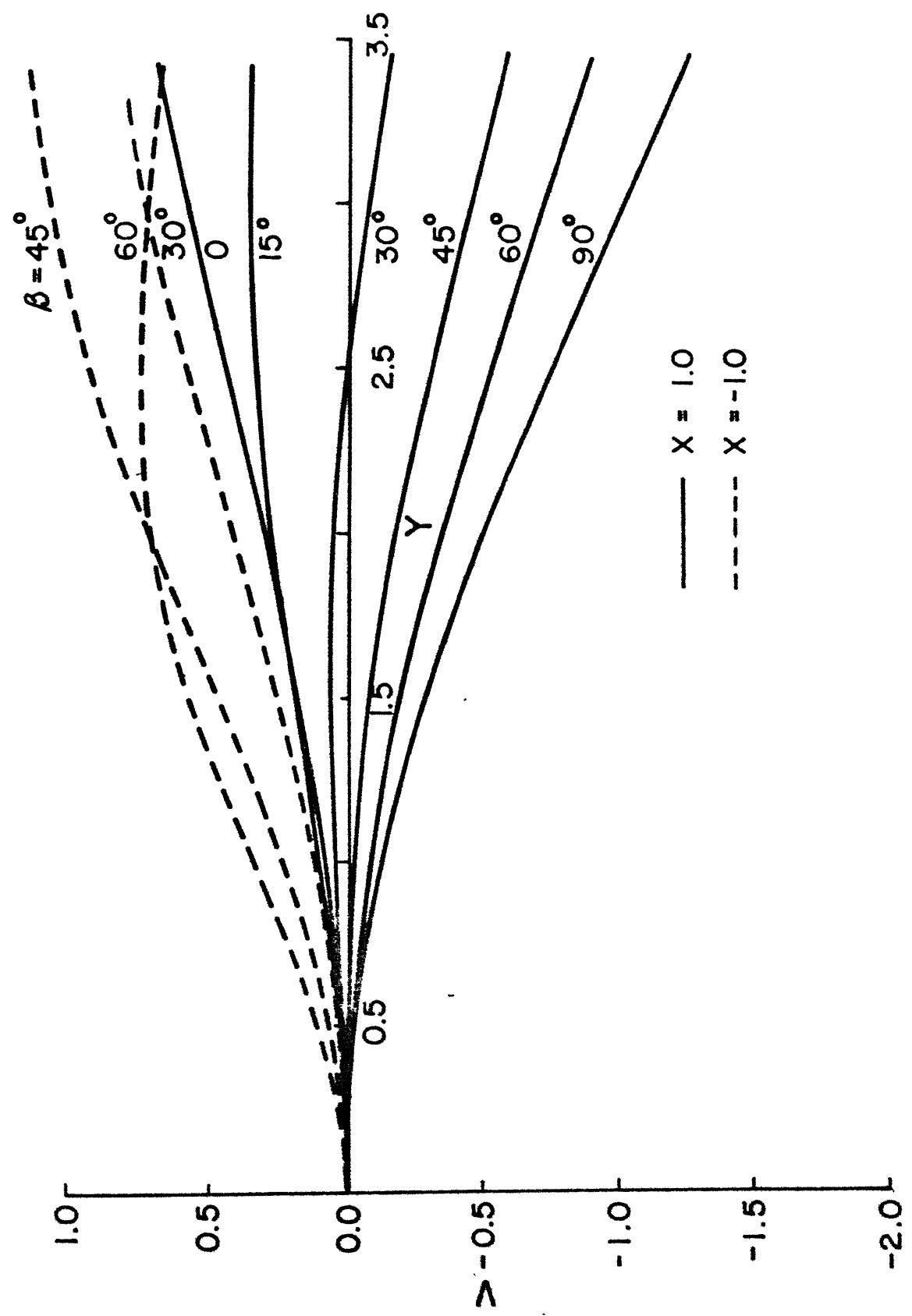
Fig. 4.6 Transverse velocity distribution for flow over an inclined plate (X = ±10)
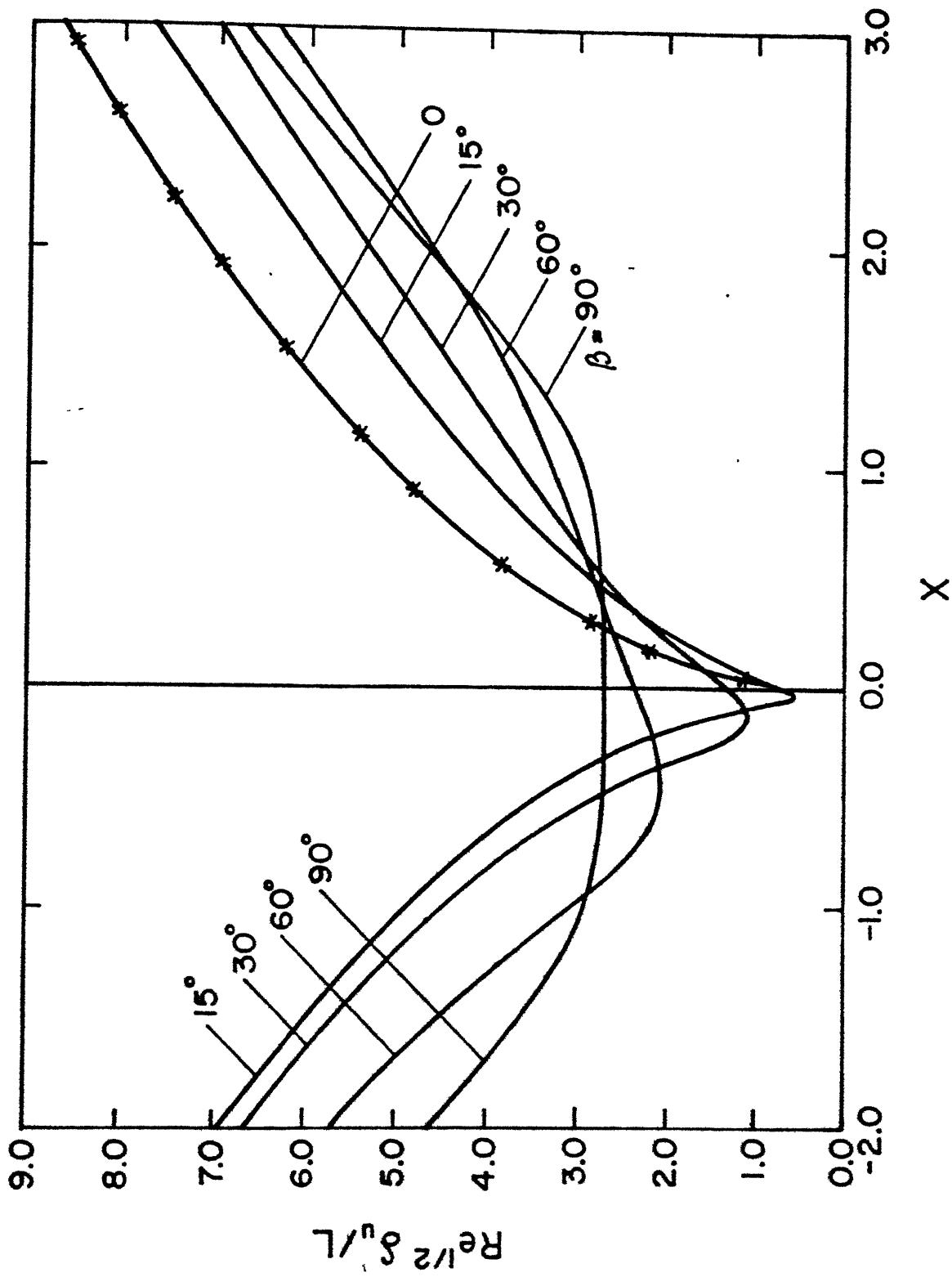
Fig.4.7 Hydrodynamic boundary layer thickness Vs X for various values of β
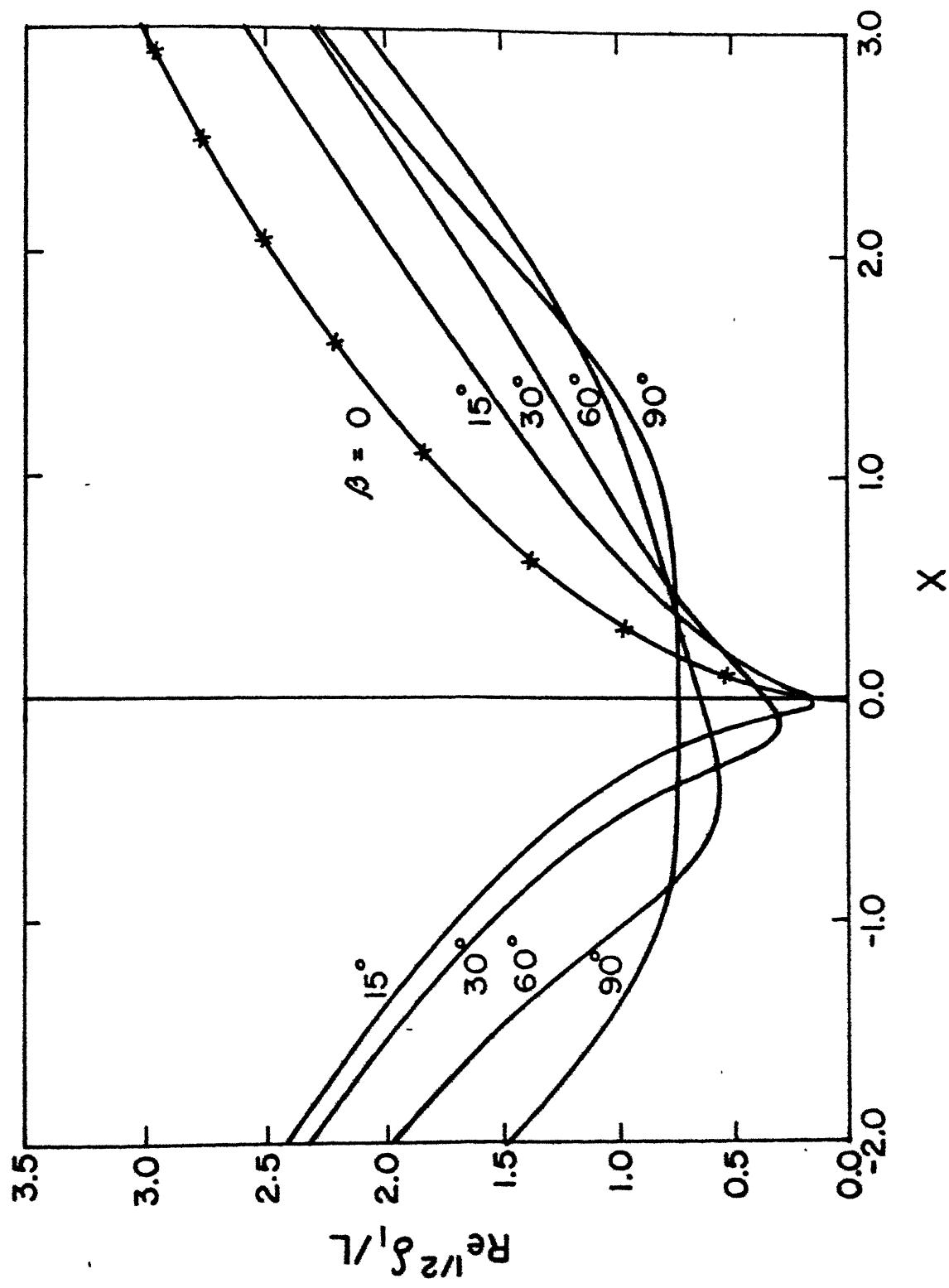
Fig.4.8 Displacement thickness Vs X for various values of β
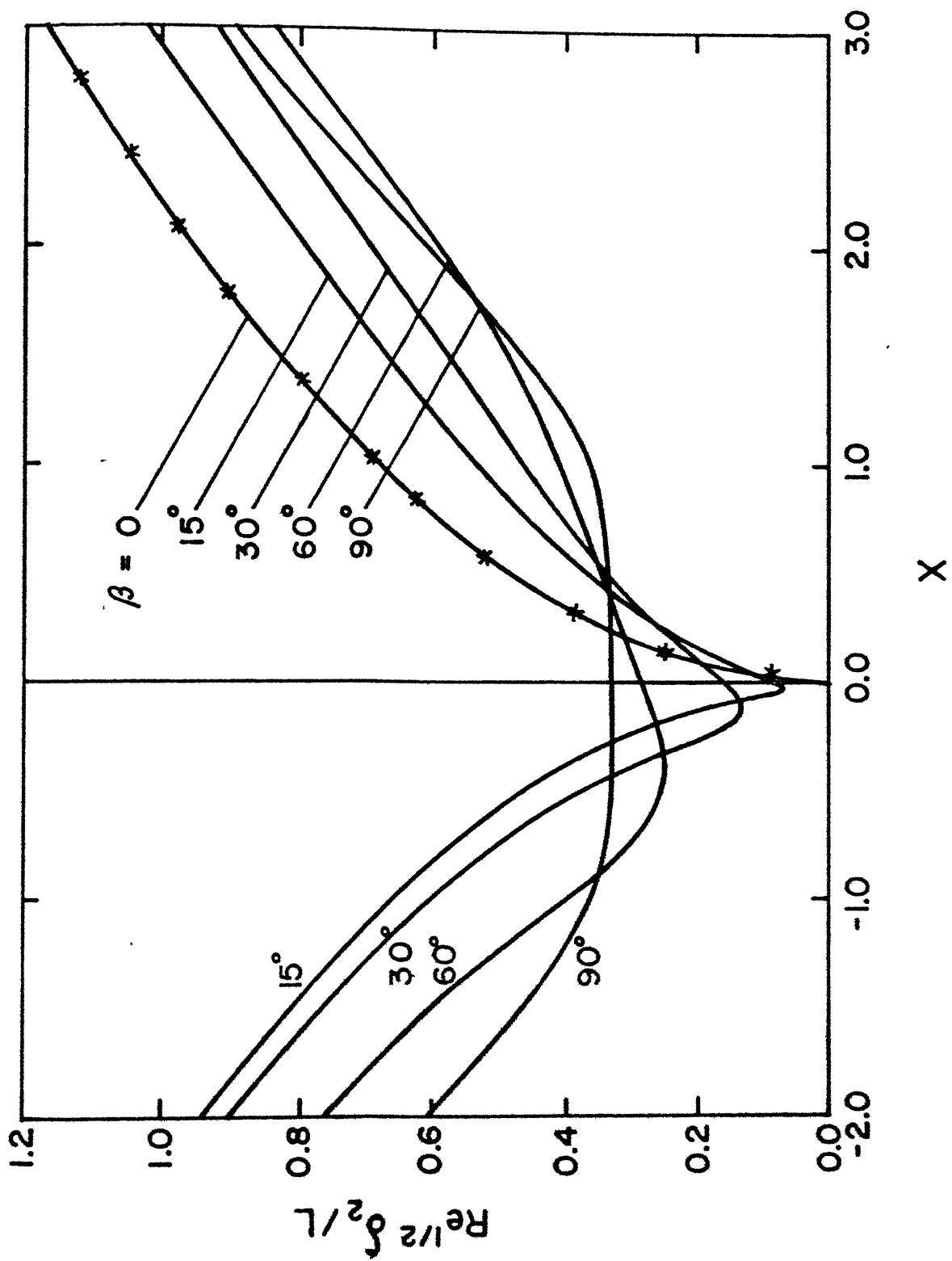
Fig.4.9 Momentum thickness Vs X for various values of β
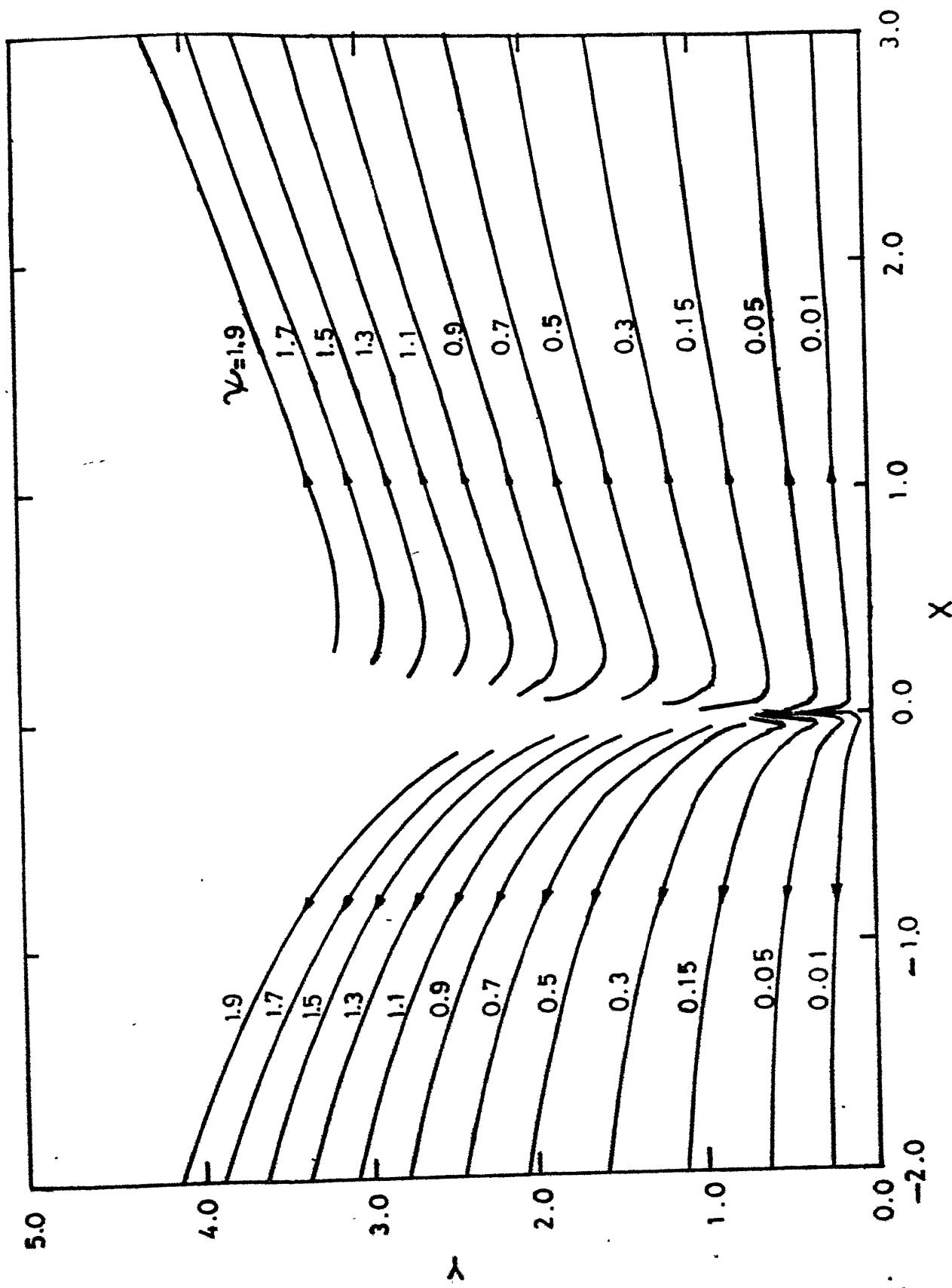
Fig 4.10 Flow field stream lines for $\beta = 15°$
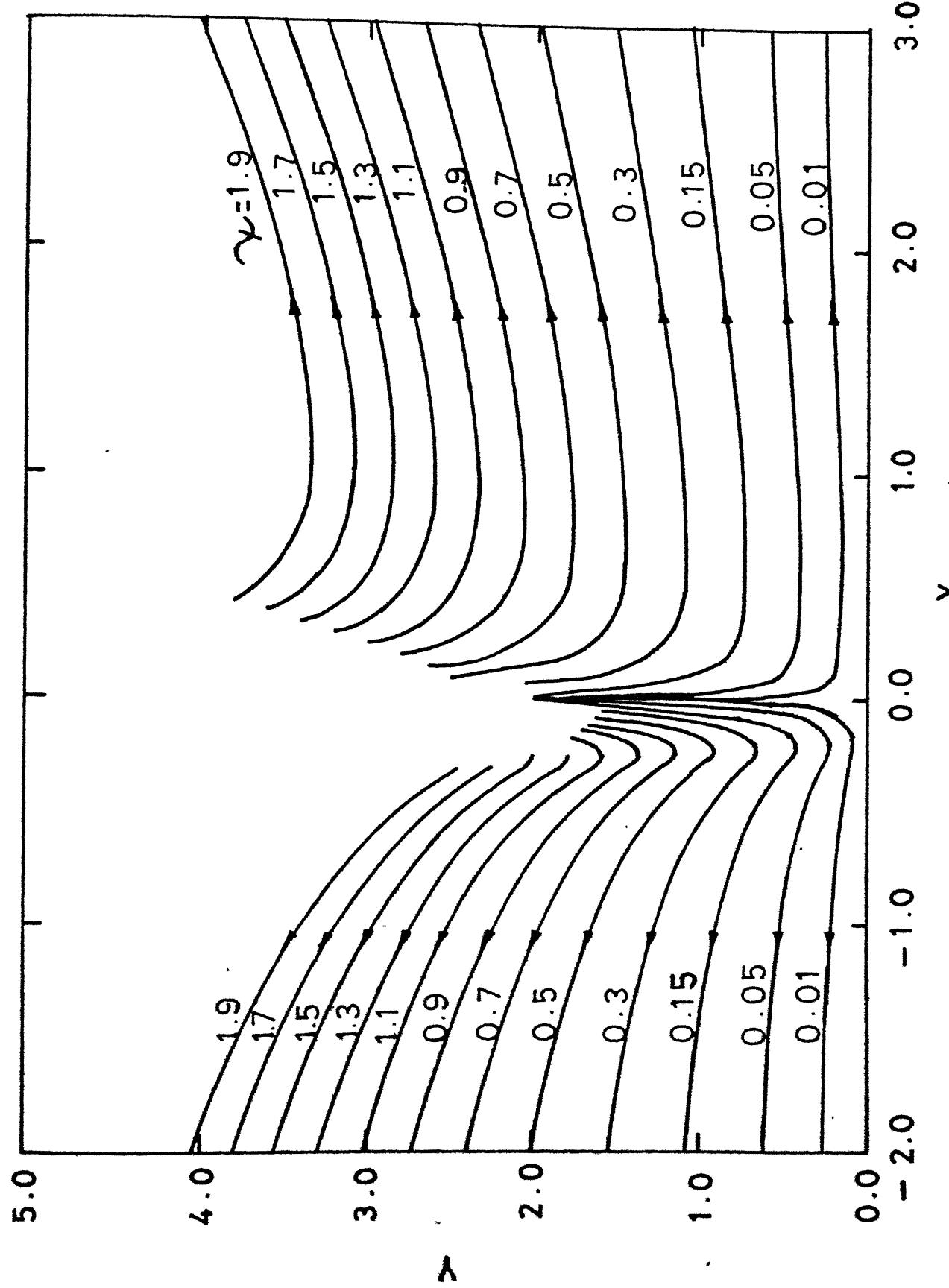
Fig. 4.11 Flow field stream lines for $\beta = 30^\circ$
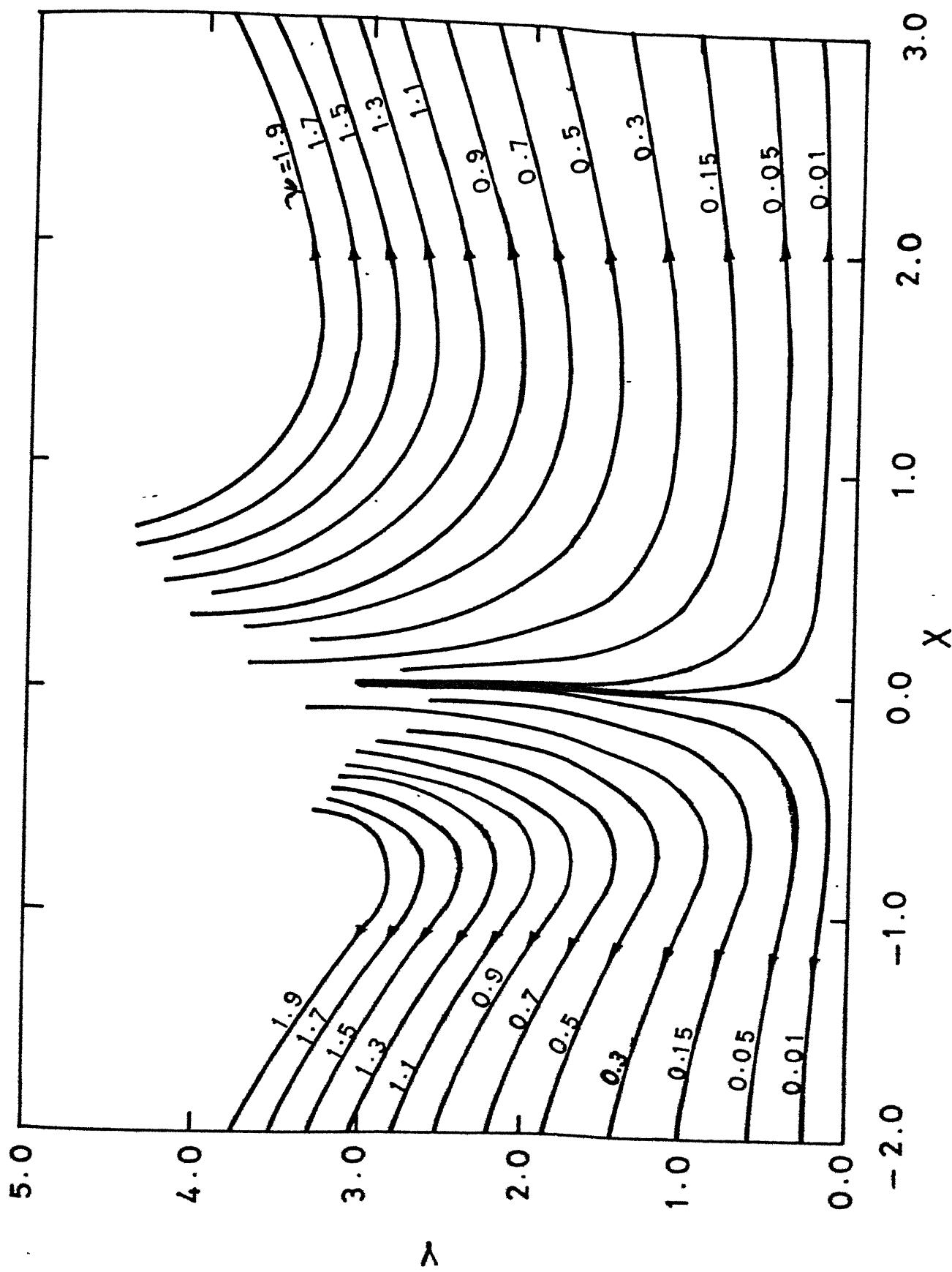
Fig. 4.12 Flow field stream lines for $\beta = 60°$
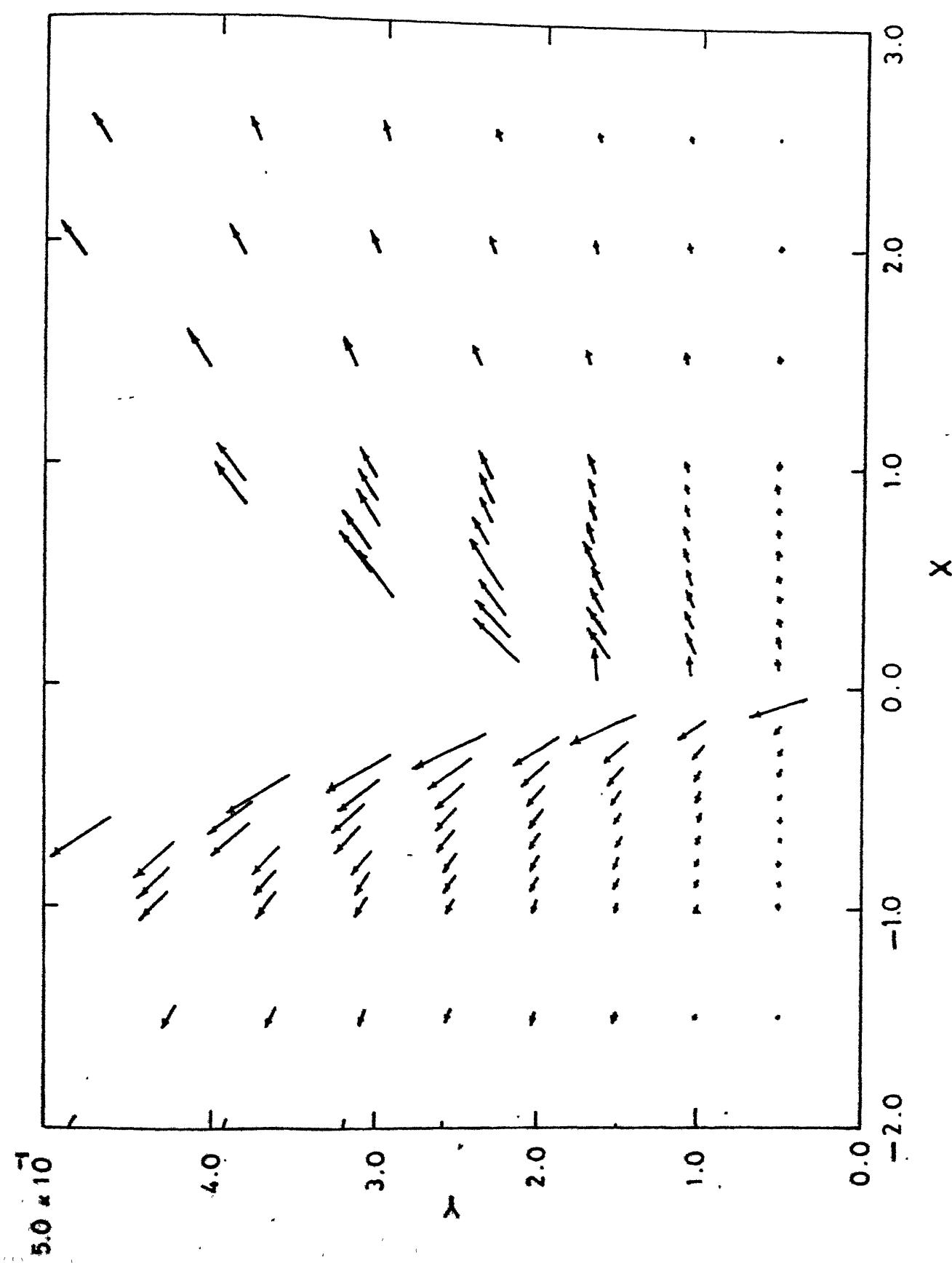
Fig. 4.14 Gas velocity vectors in the vicinity of a cold inclined plate for $\beta = 15°$
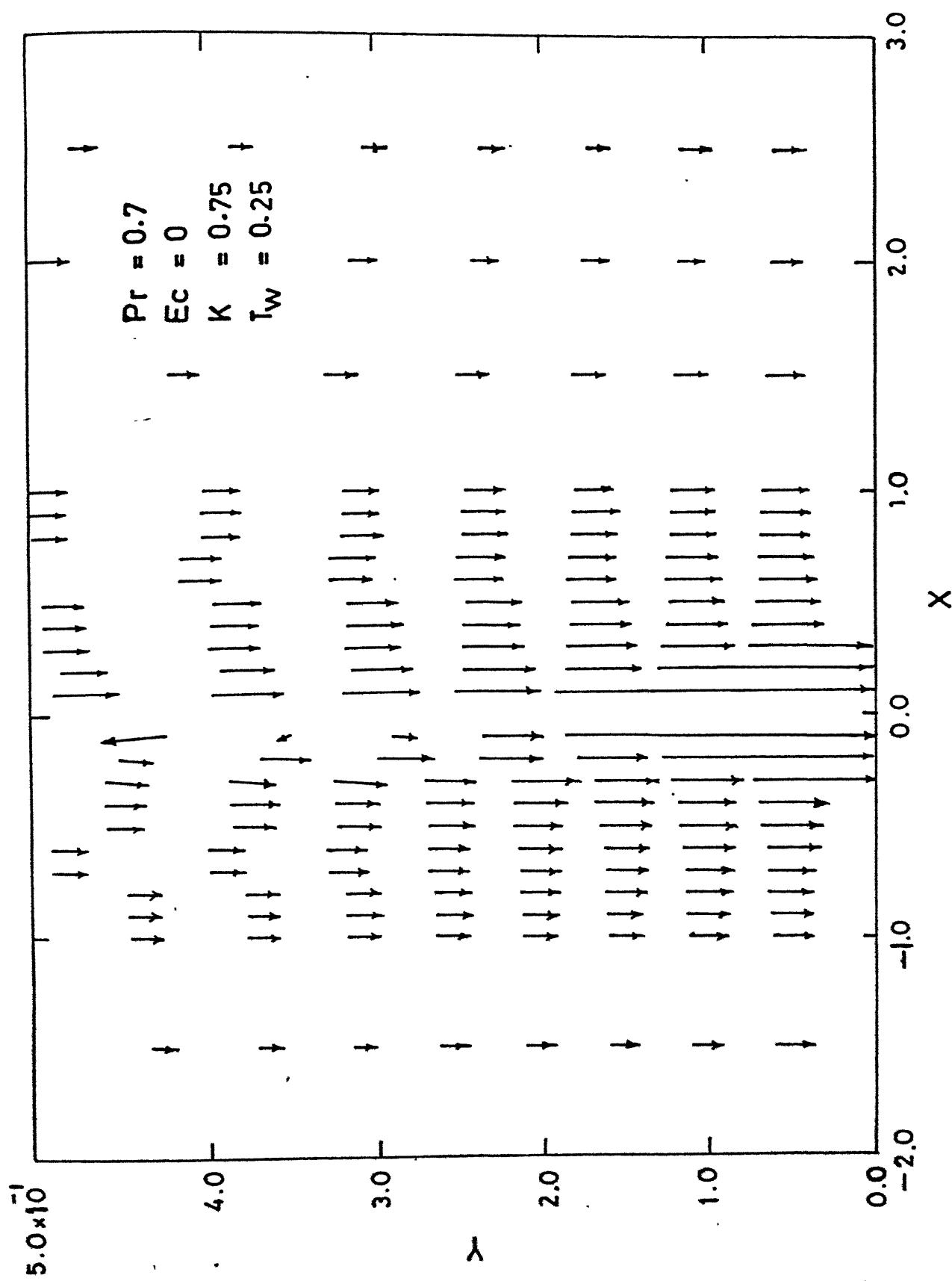
Fig. 4.15 Particle velocity vectors in the vicinity of a cold inclined plate for β=15°
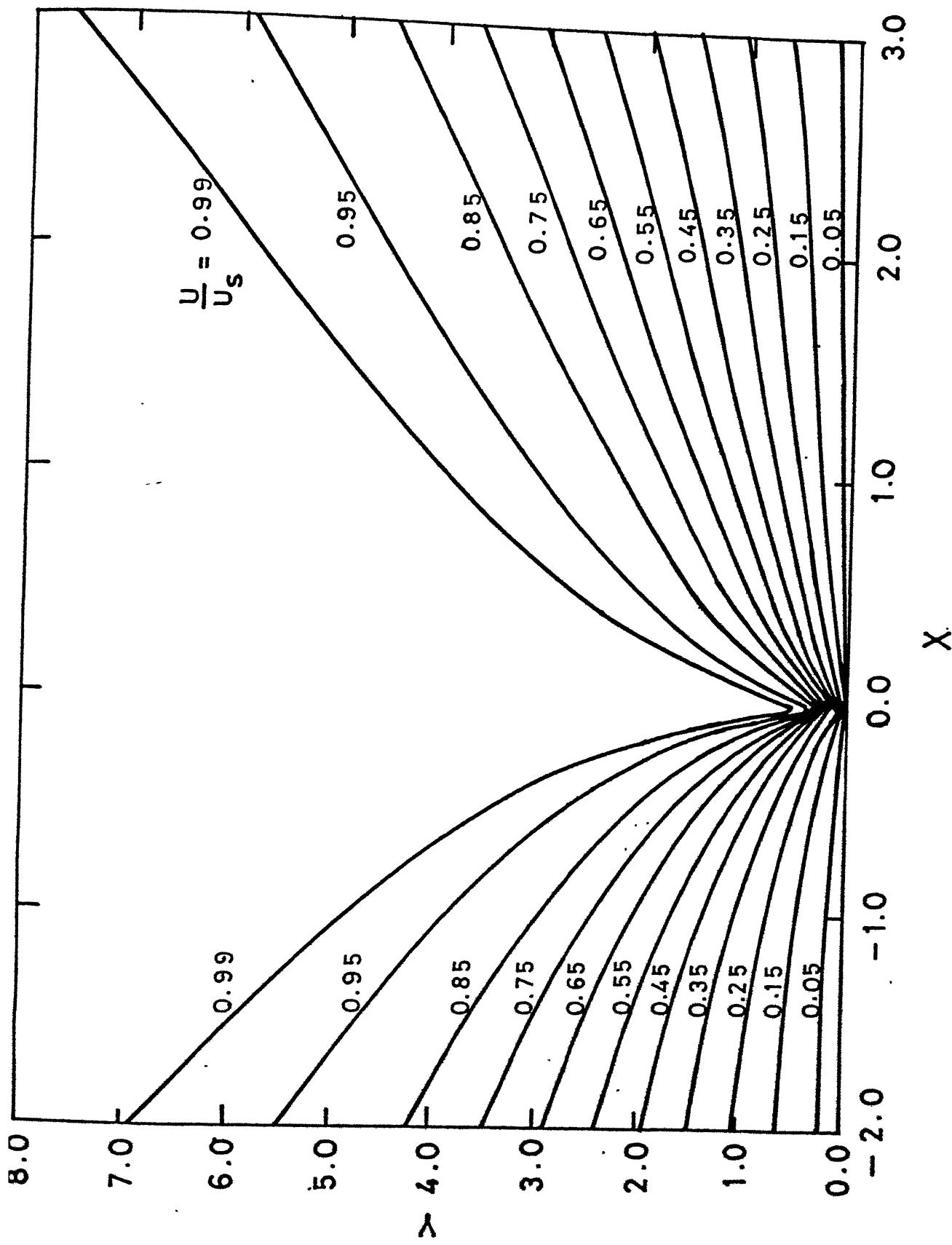
Fig.4.16 Isovelocity curves for $\beta = 15°$
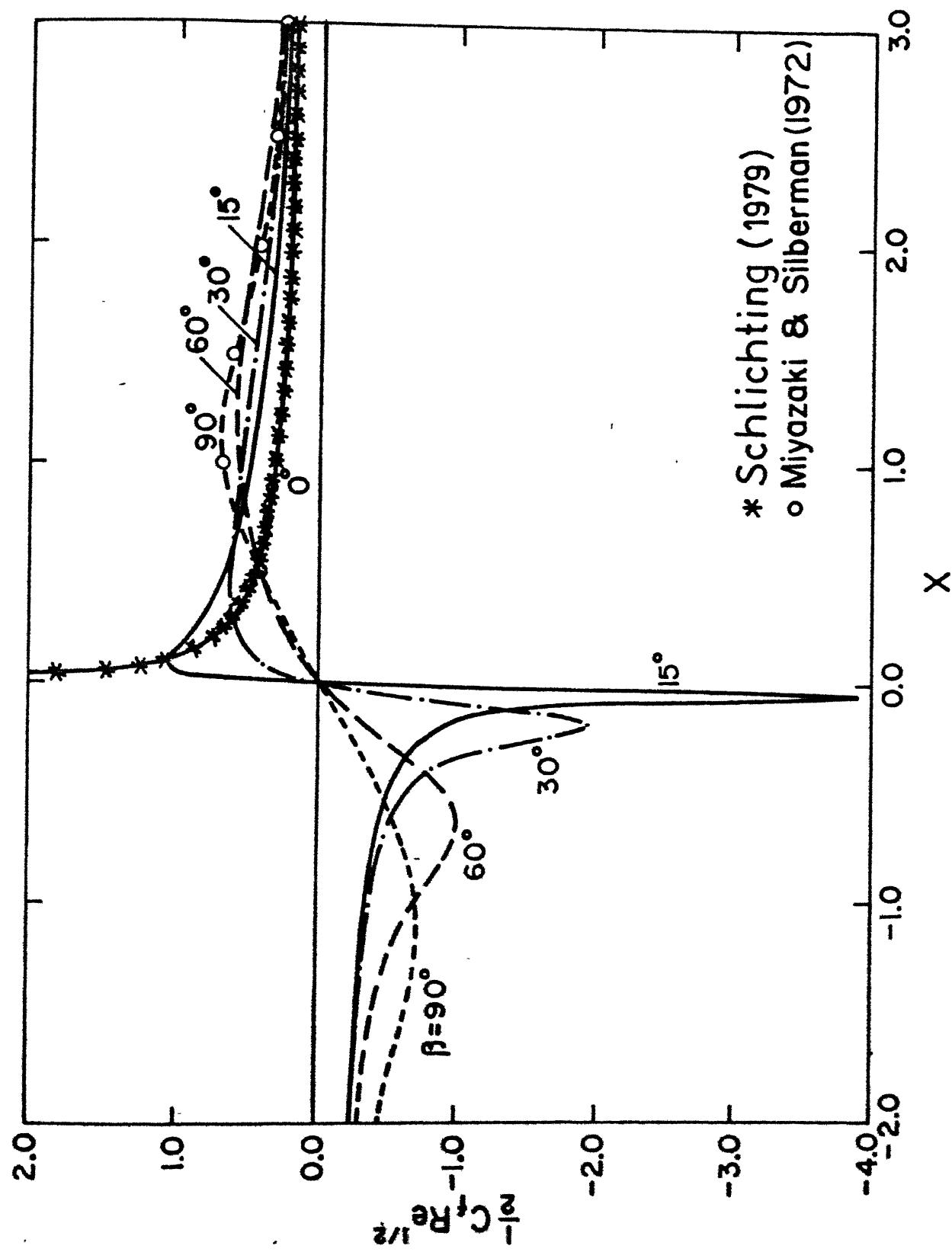
Fig. 4.17 Local skin friction coefficient over an inclined plate
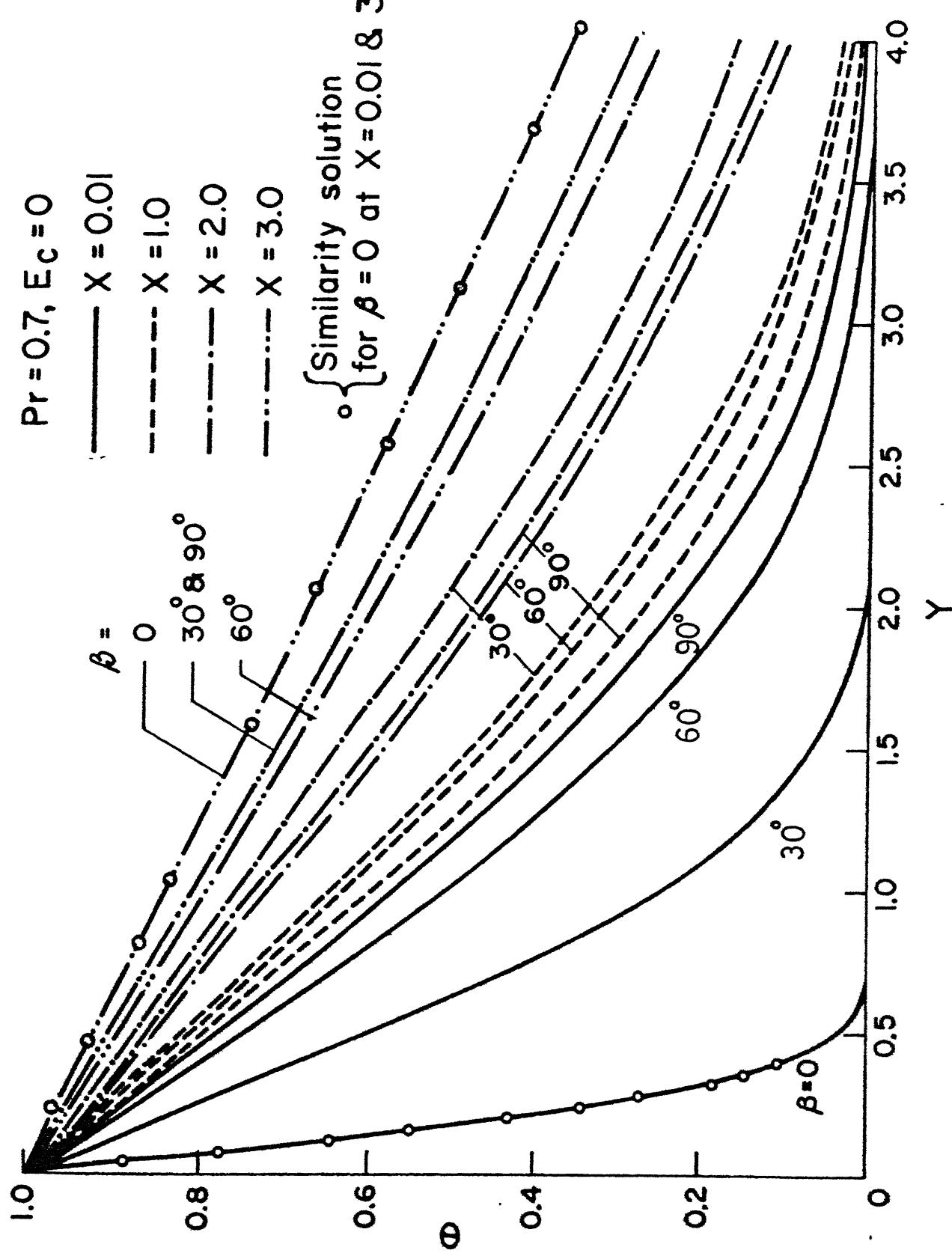
Fig.4.18 Normalised temperature profiles over an isothermal plate
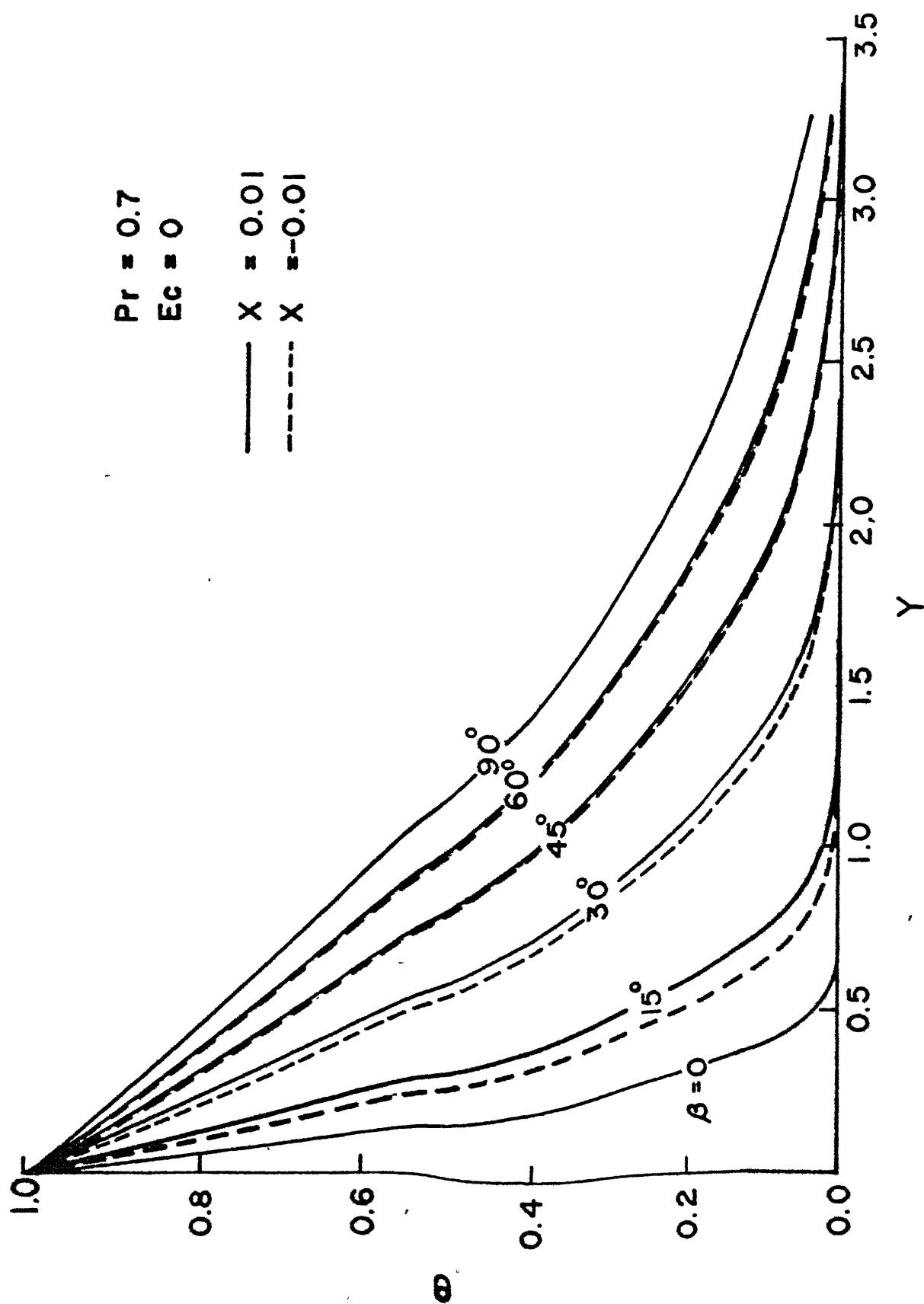
Fig. 4.19 Normalised temperature distribution for flow over an isothermal plate ($X = \pm 0.01$)
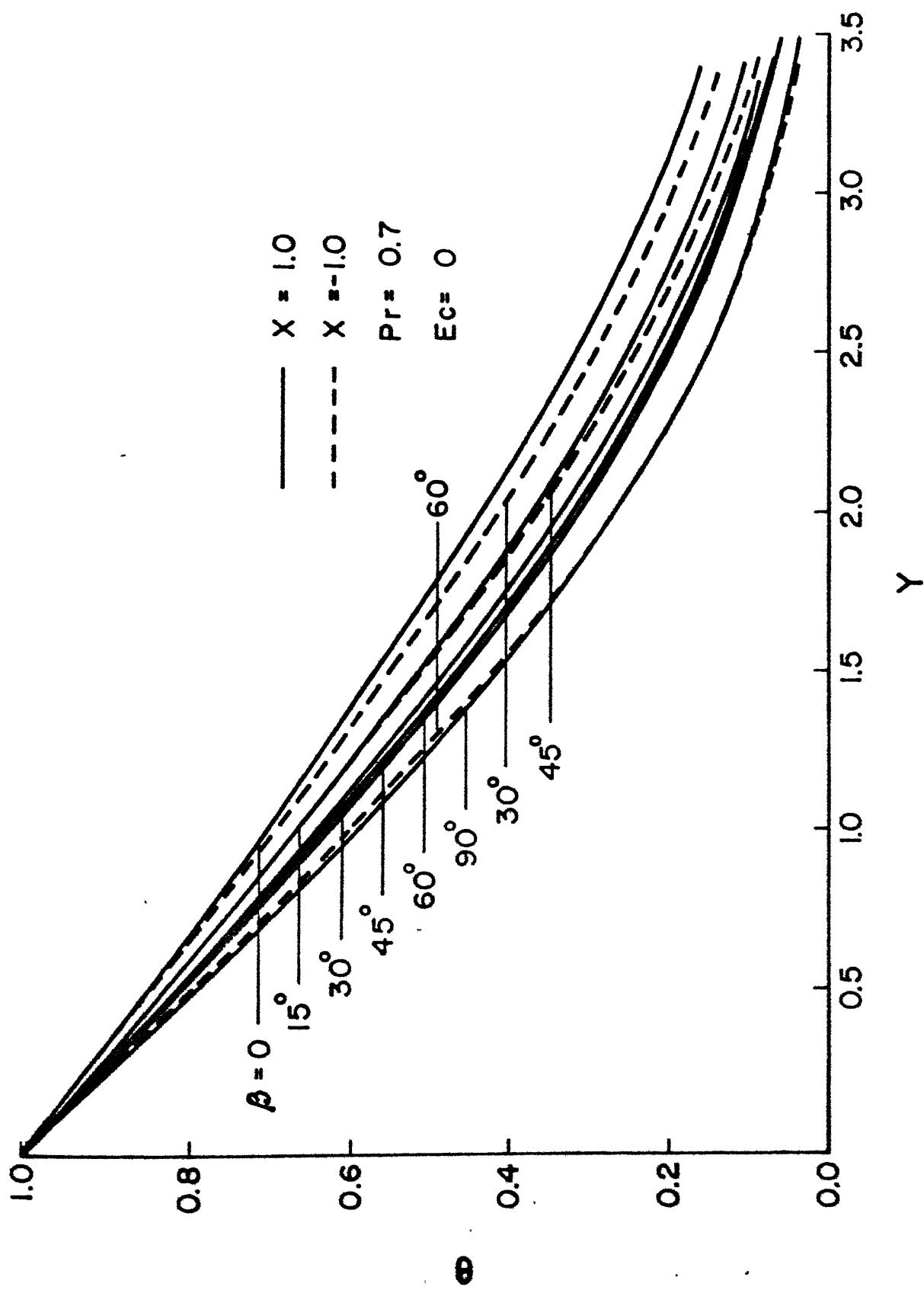
Fig.4.20 Normalised temperature distribution for flow over an isothermal plate (X = ± 1.0)
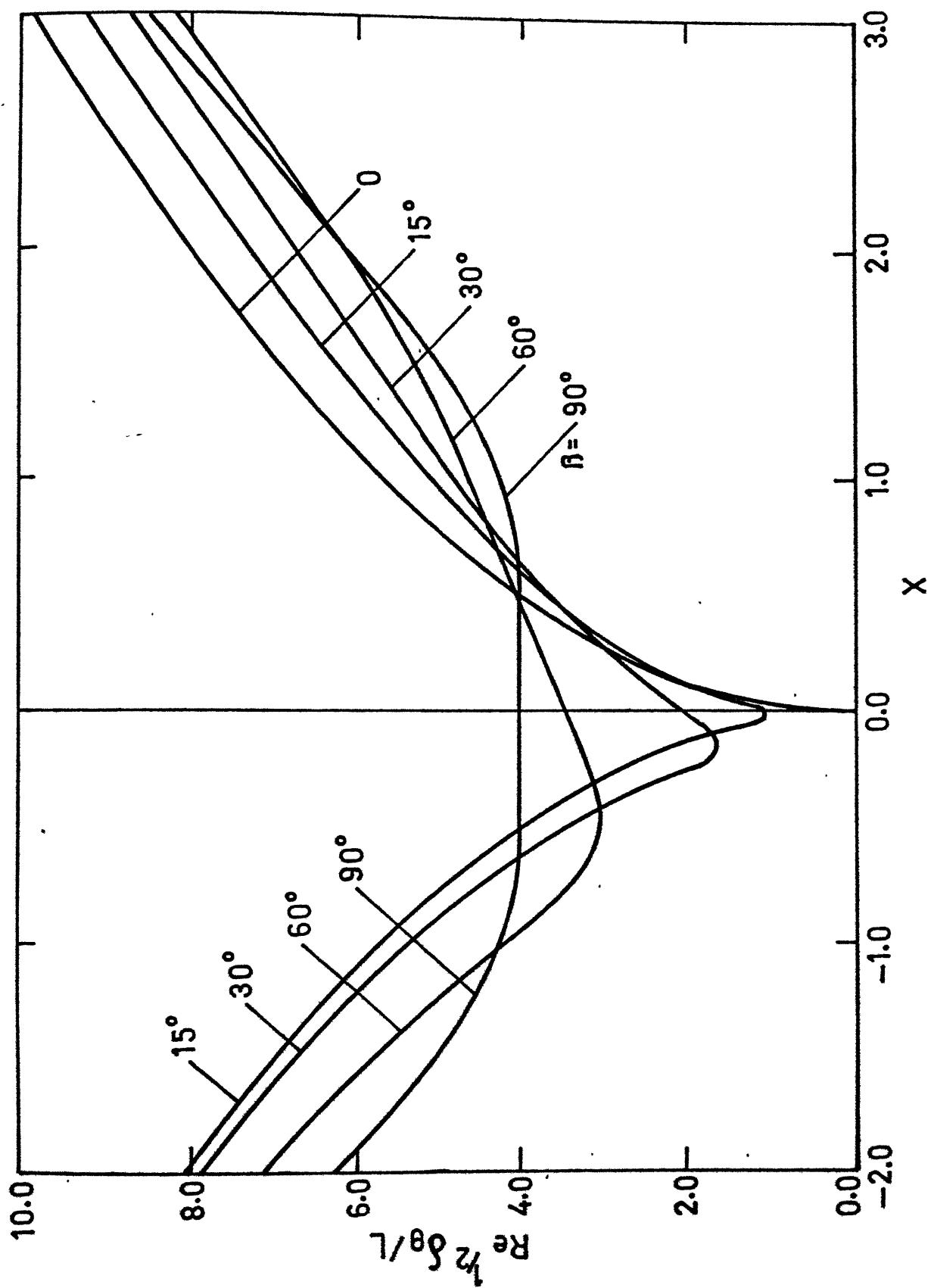
Fig.4.21 Thermal boundary layer thickness over an isothermal plate (Pr=0.7, Ec=0)
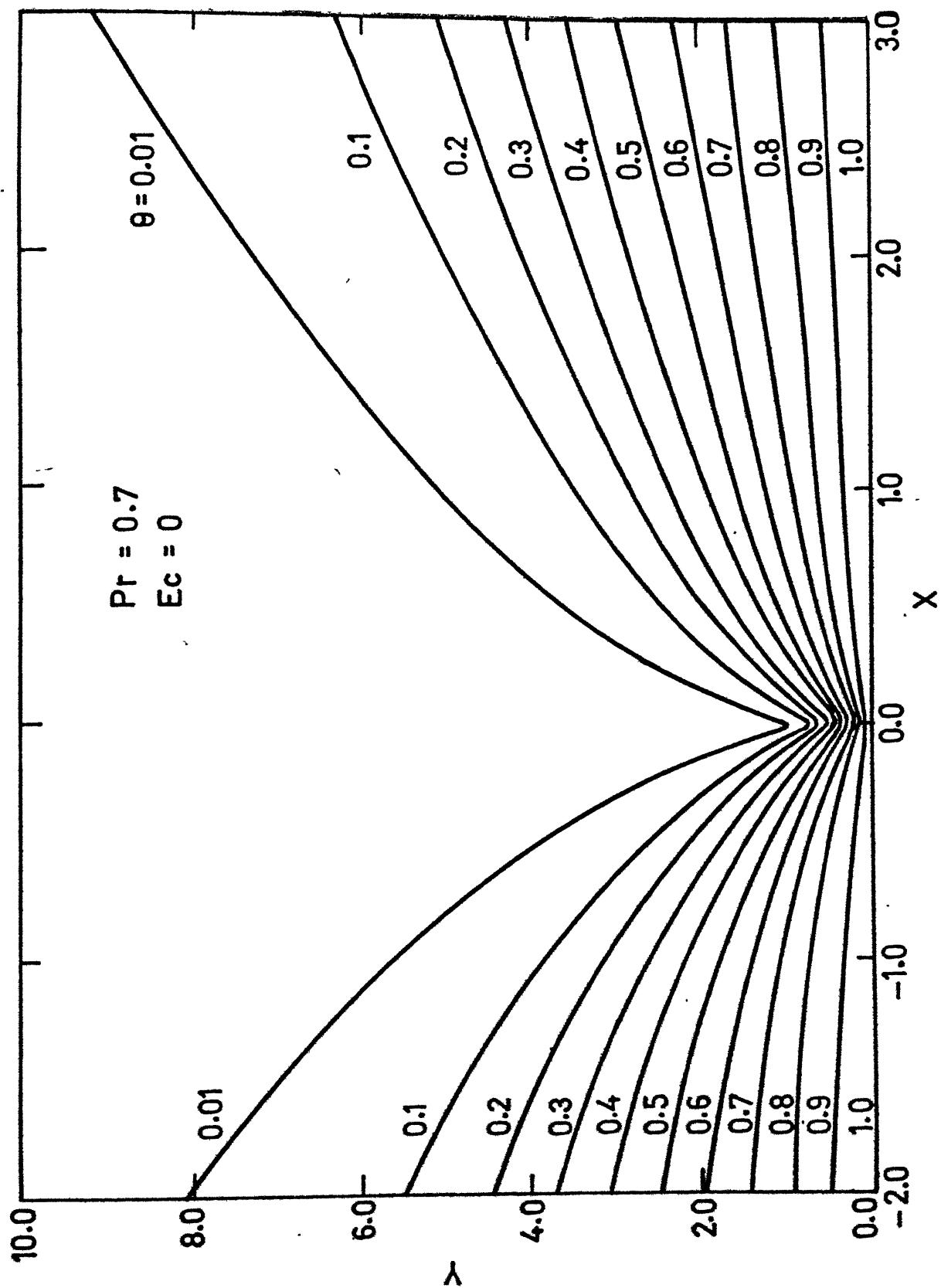
Fig.4.22 Isotherms for β = 15°
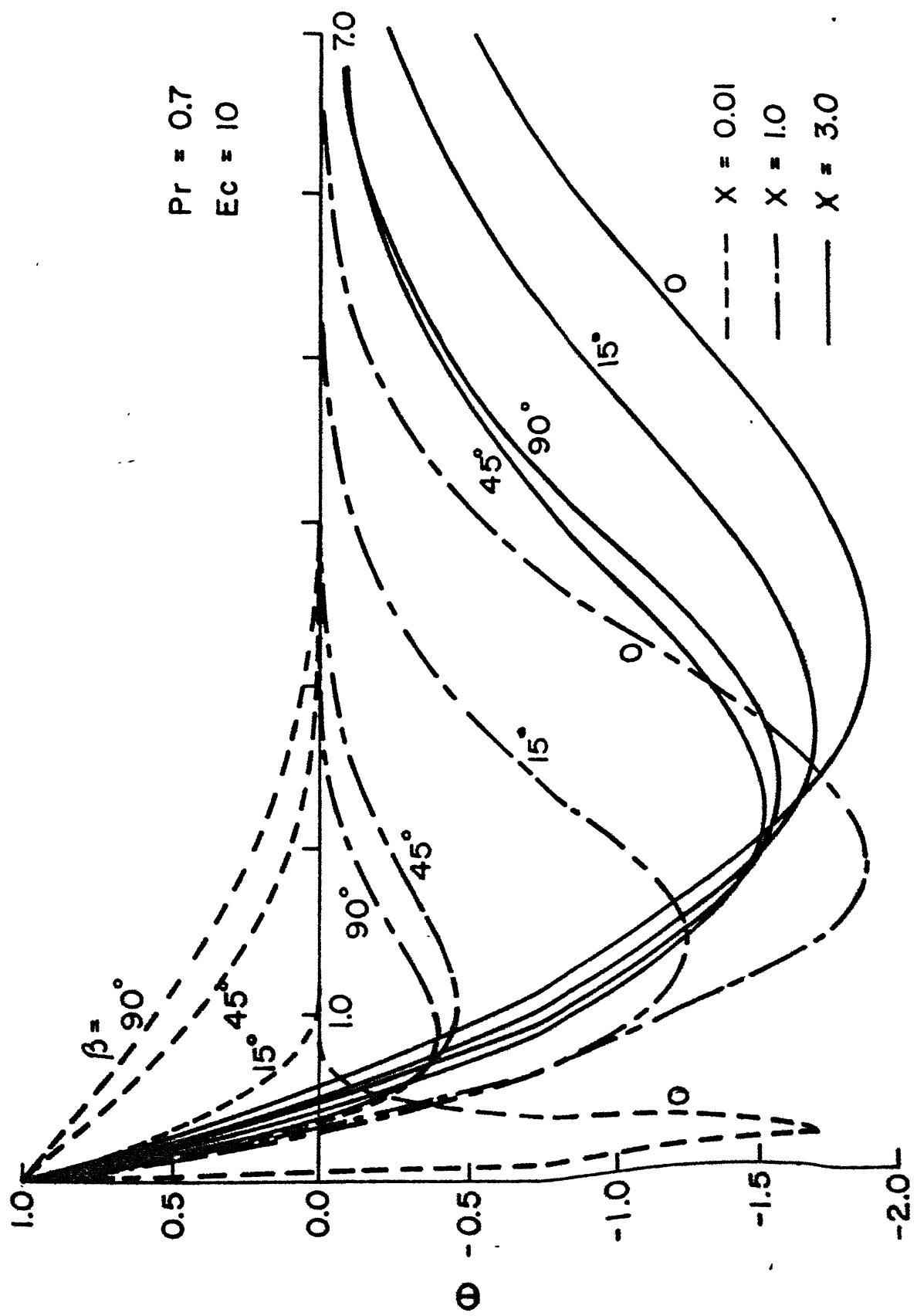
Fig.4.23 Normalised temperature profiles with viscous dissipation $(T_w = 0.6)$
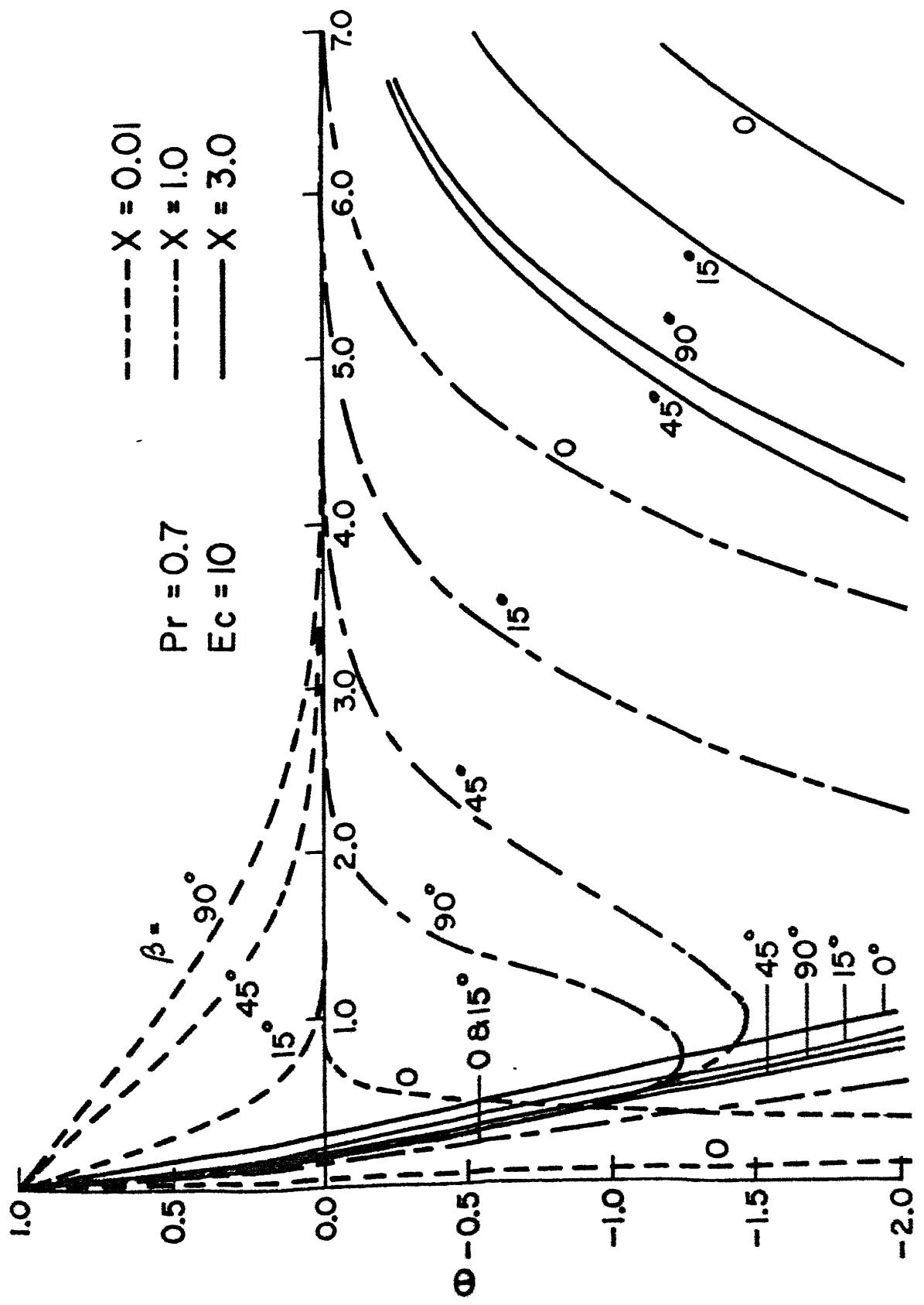
Fig. 4.24 Normalised temperature profiles with viscous dissipation ($T_W = 0.8$)
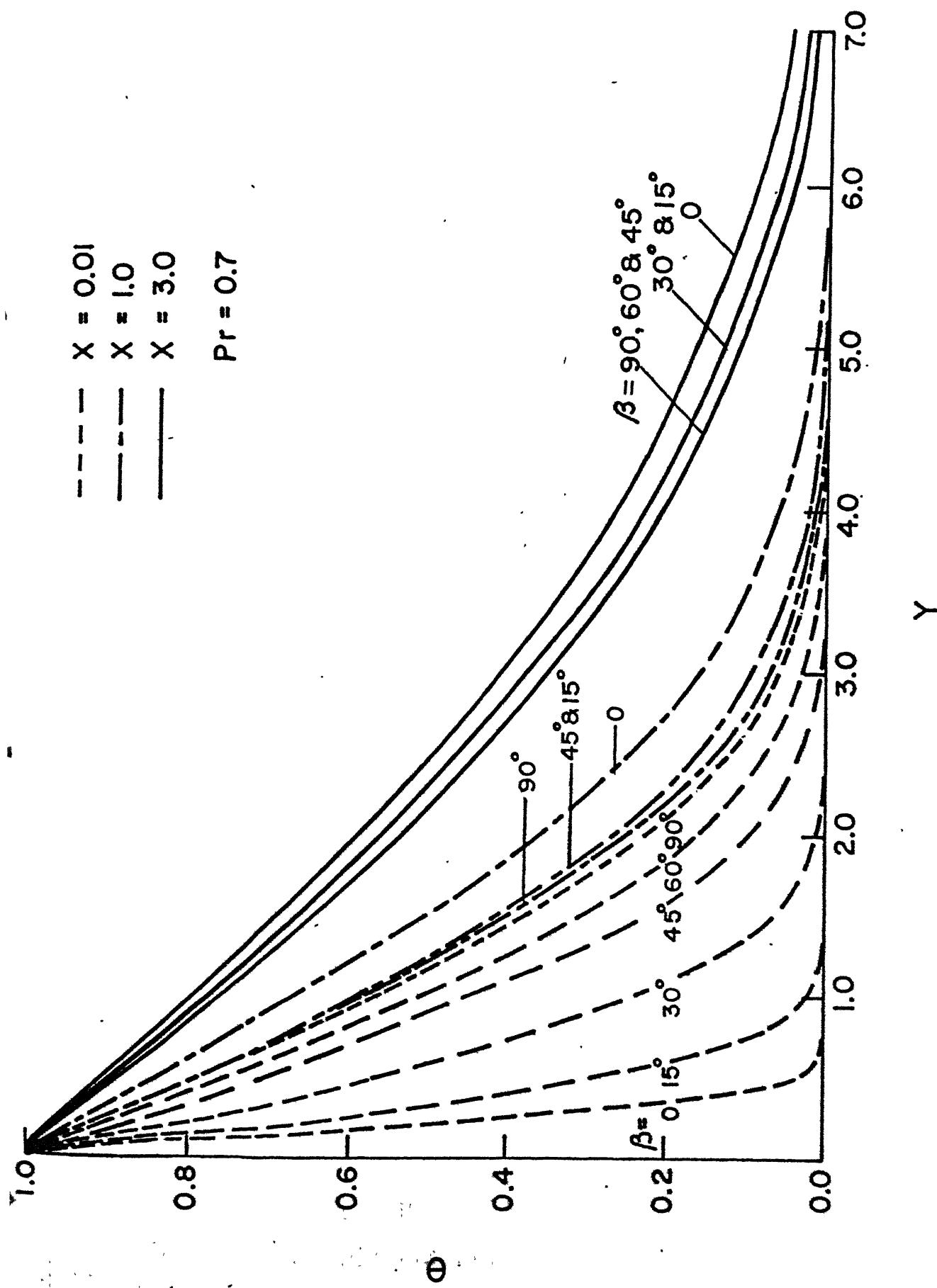
Fig. 4.25 Temperature profiles over an adiabatic plate (Ec = 1)
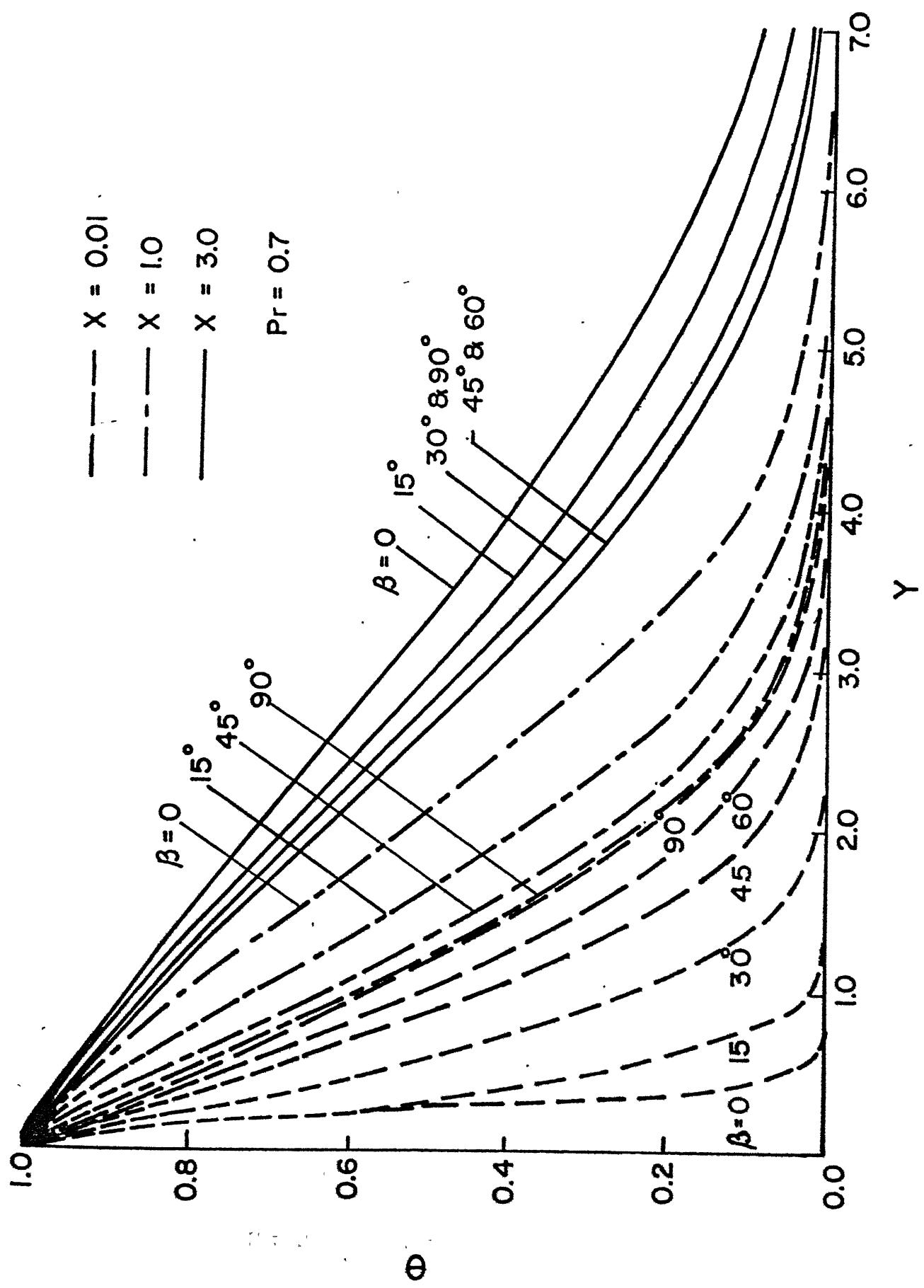
Fig. 4.26 Temperature profiles over an adiabatic plate (Ec=10)
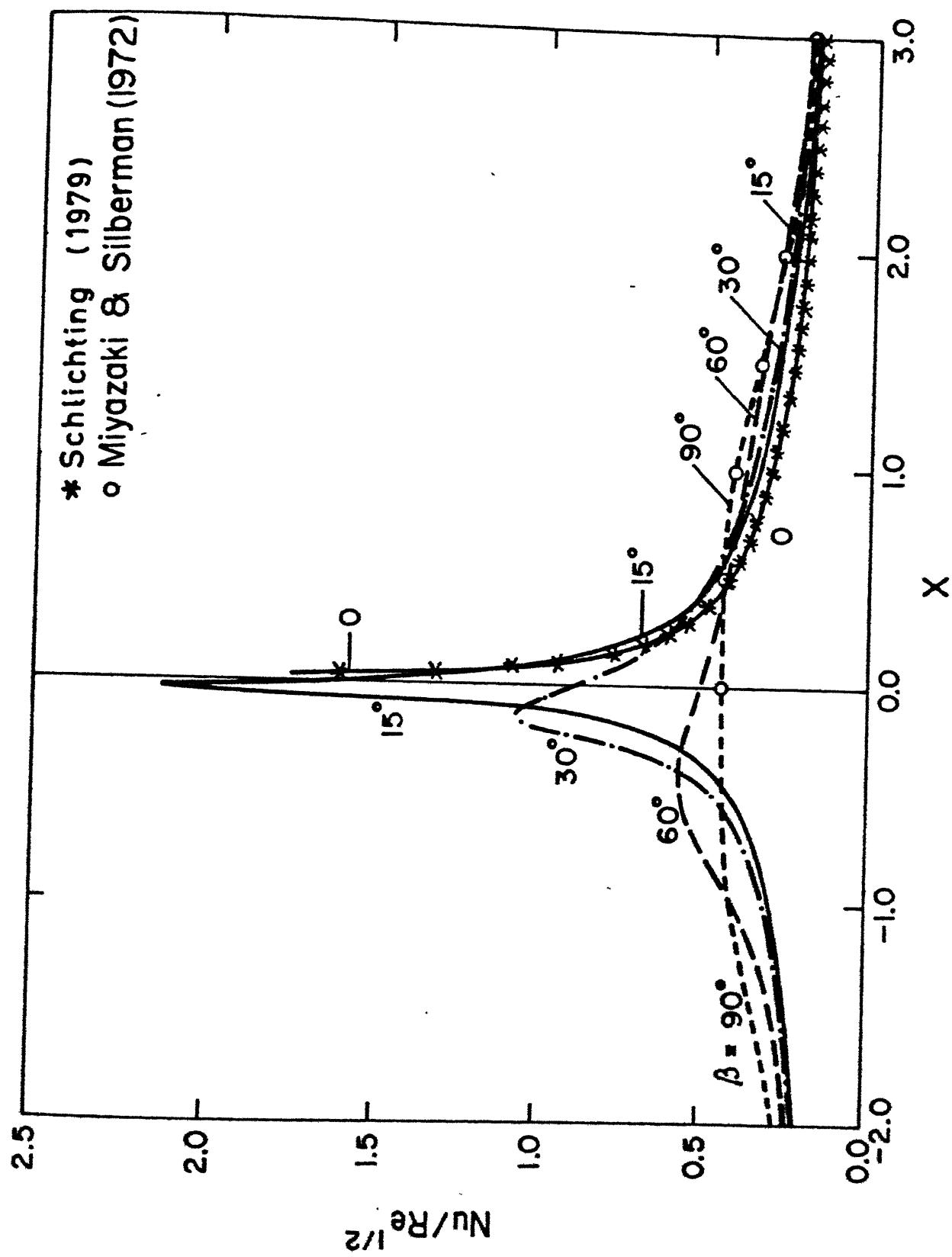
Fig. 4.27 Local Nusselt number over an isothermal plate
(Pr = 0.7, Ec = 0)
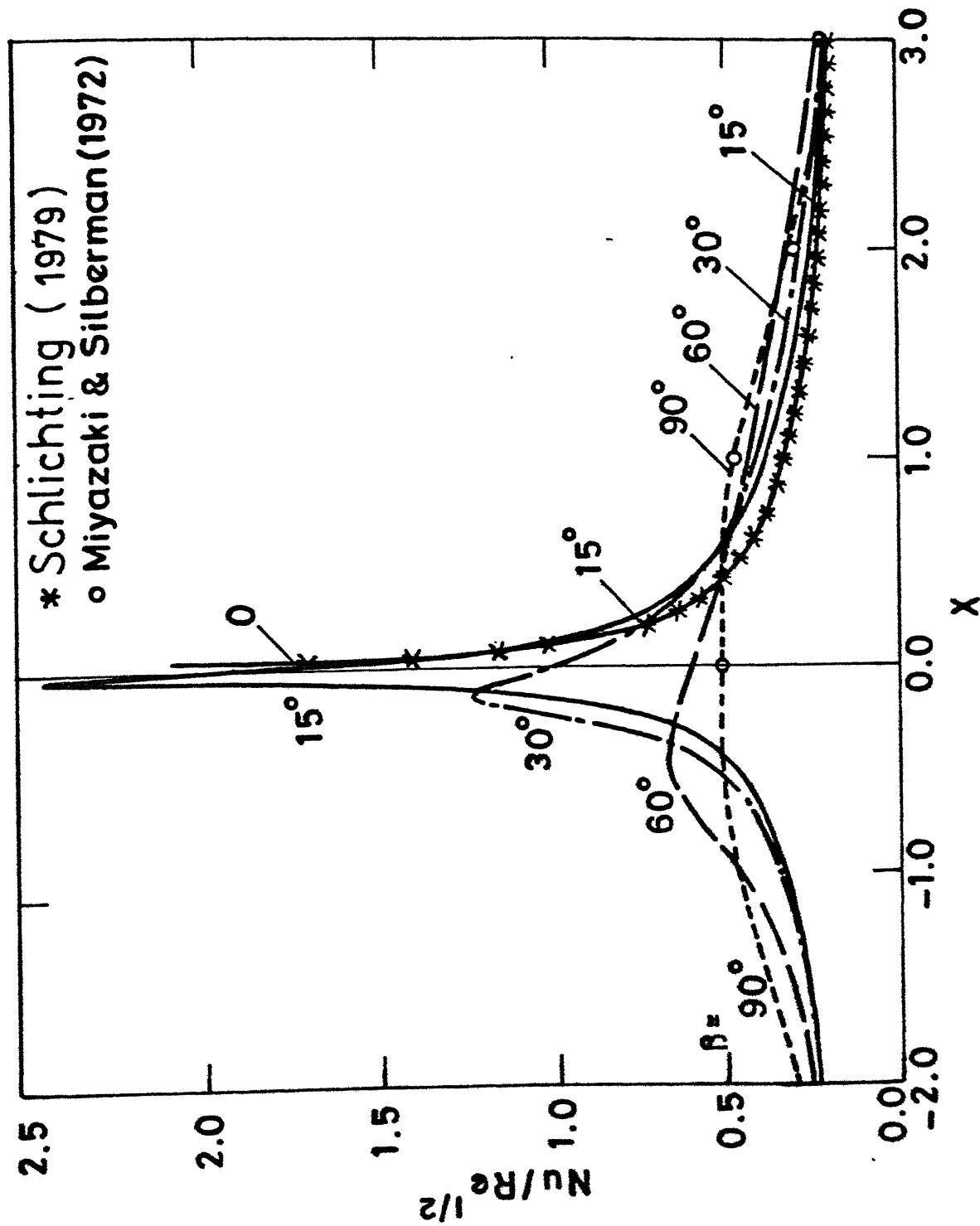
Fig. 4.28 Local Nusselt number over an isothermal plate (Pr = 1 , Ec = 0)
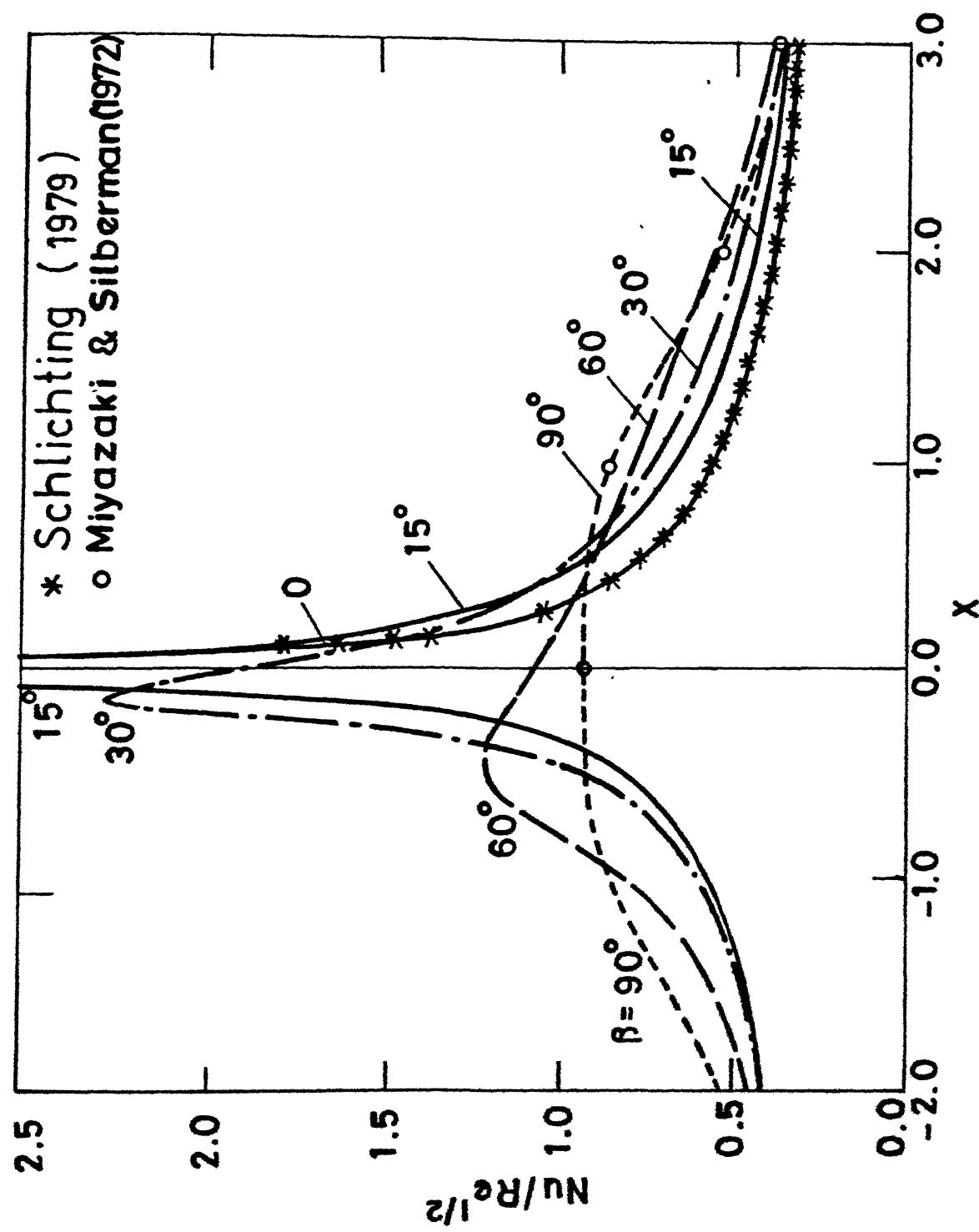
Fig. 4.29 Local Nusselt number over an isothermal plate
($Pr = 5$, $Ec = 0$)
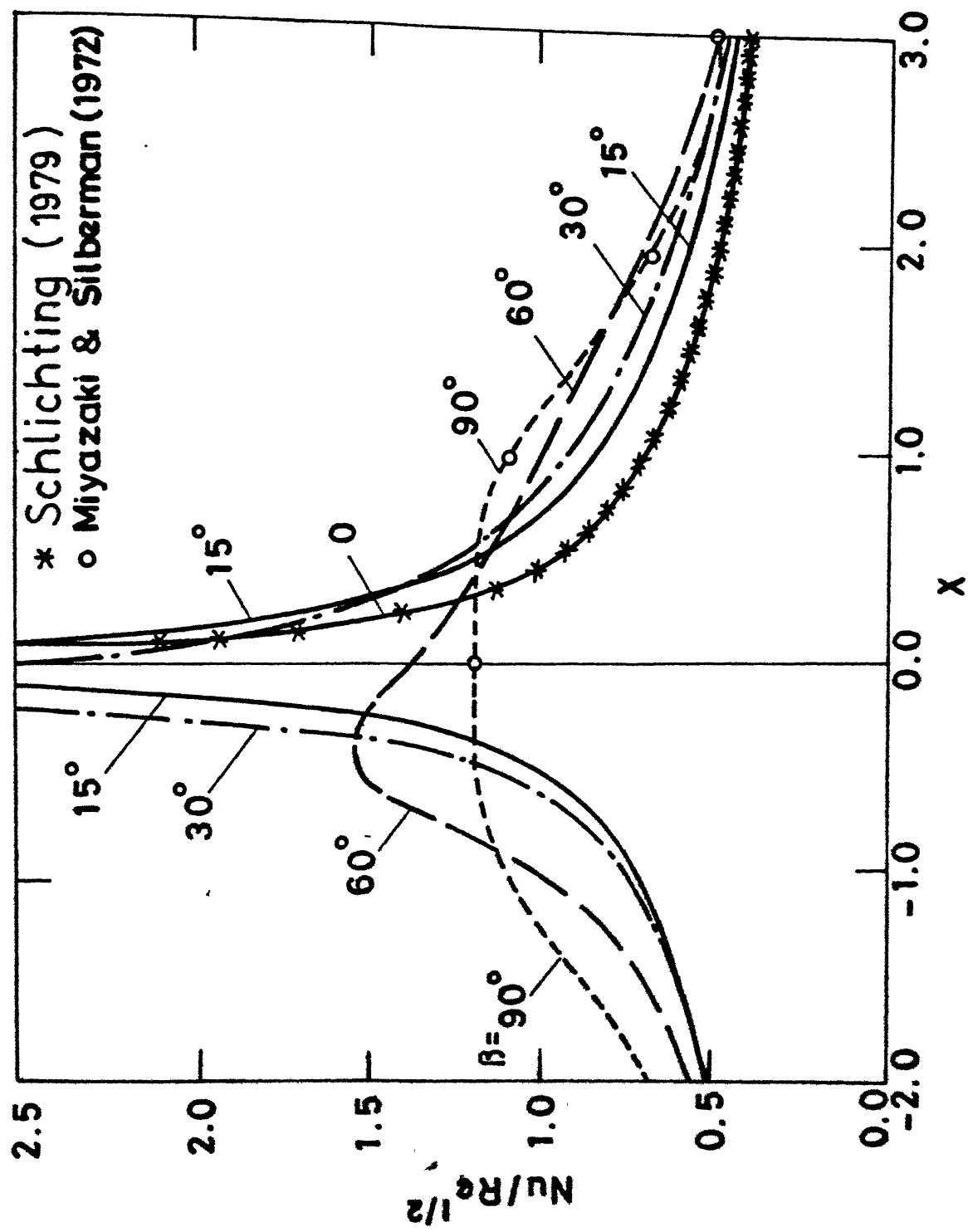
Fig. 4.30 Local Nusselt number over an isothermal plate (Pr=10 , Fc=0)
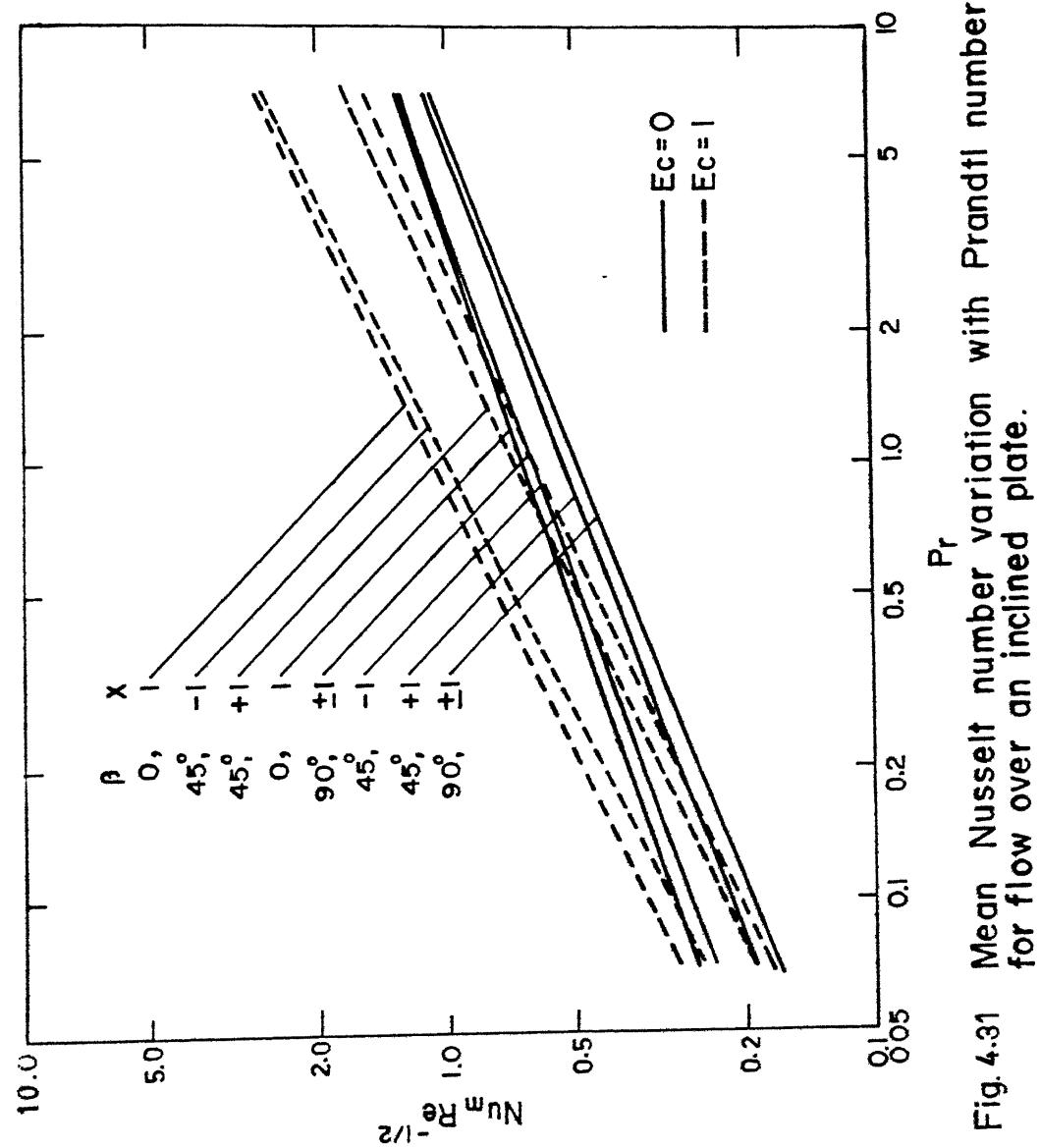
Fig. 4.31   Mean Nusselt number variation with Prandtl number for flow over an inclined plate.

135
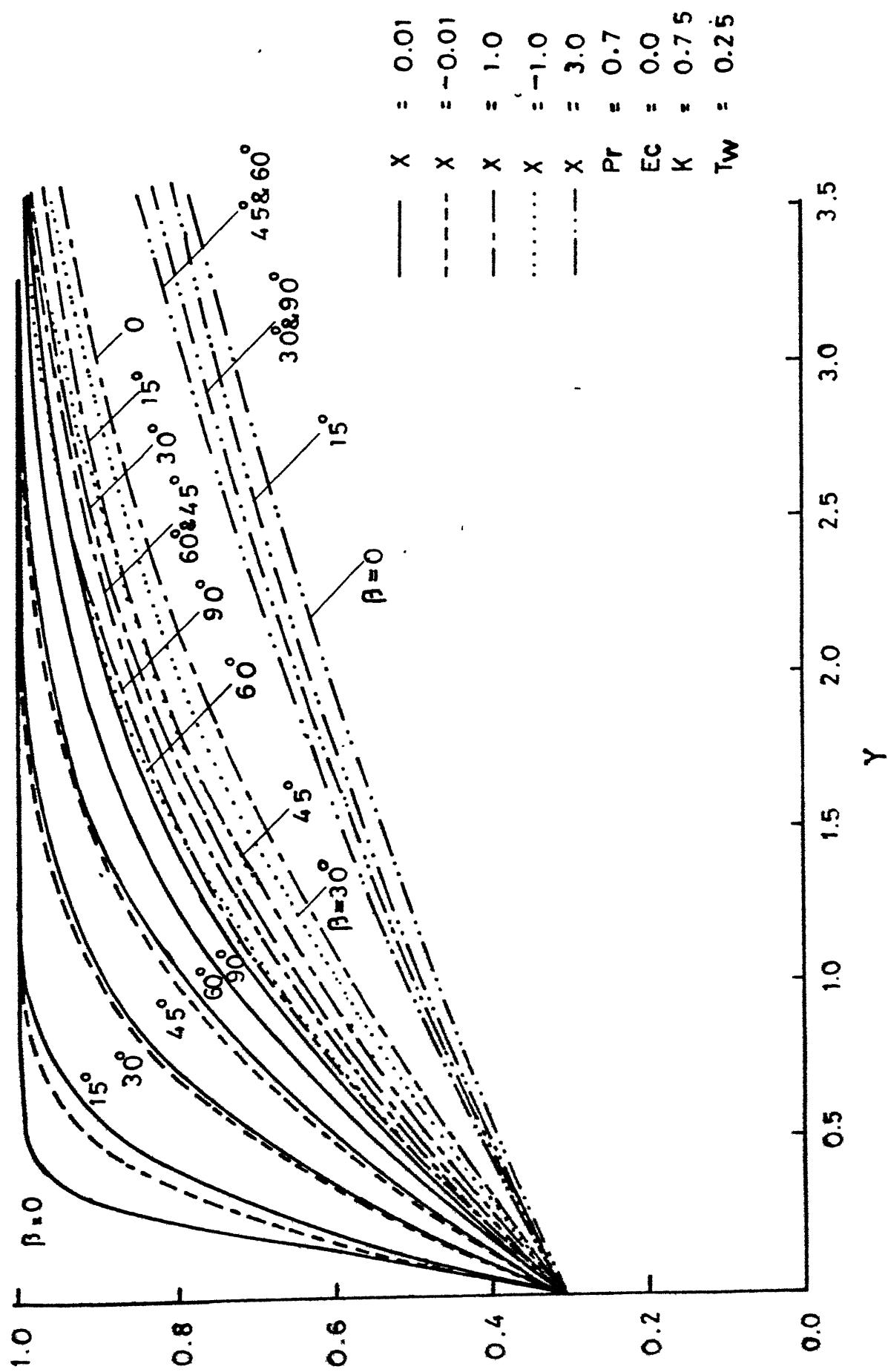
Fig.4.32 Particle concentration profiles for a cold inclined plate
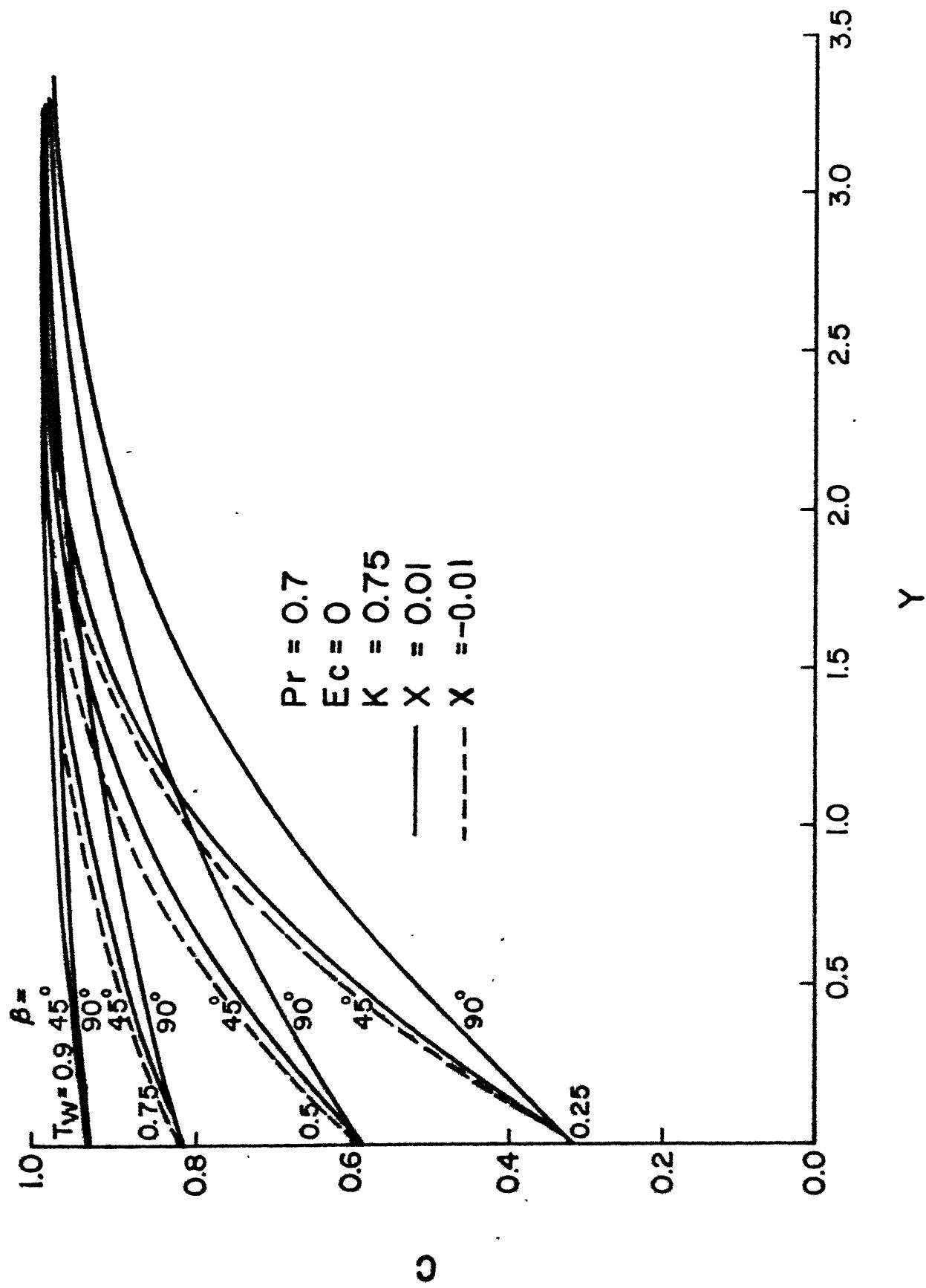
Fig.4.33 Particle concentration profiles as a function of temperature of the cold wall at X= ± 0.01

137
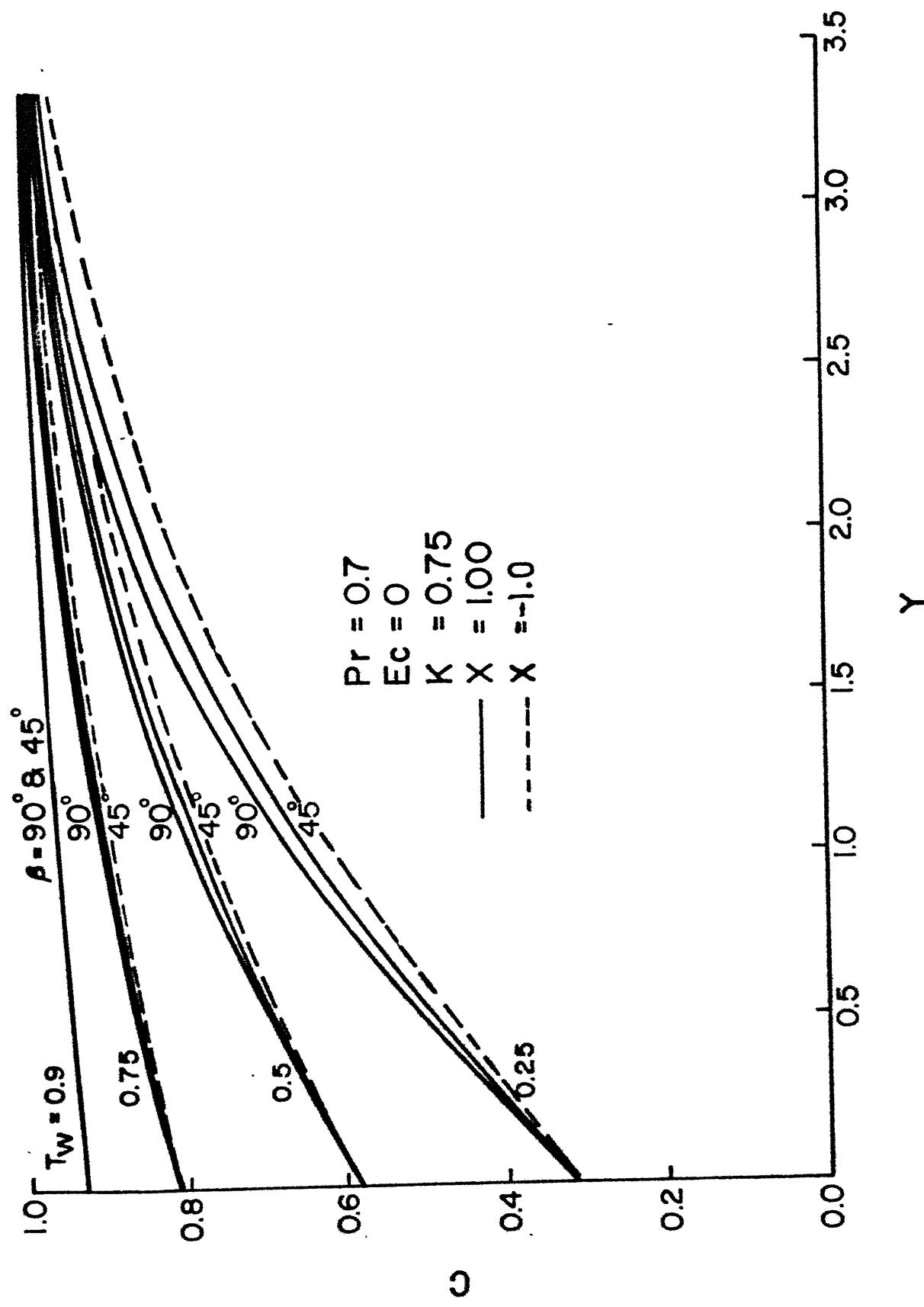
Fig. 4.34 Particle concentration profiles as a function of temperature of the cold wall at X = ±1.0
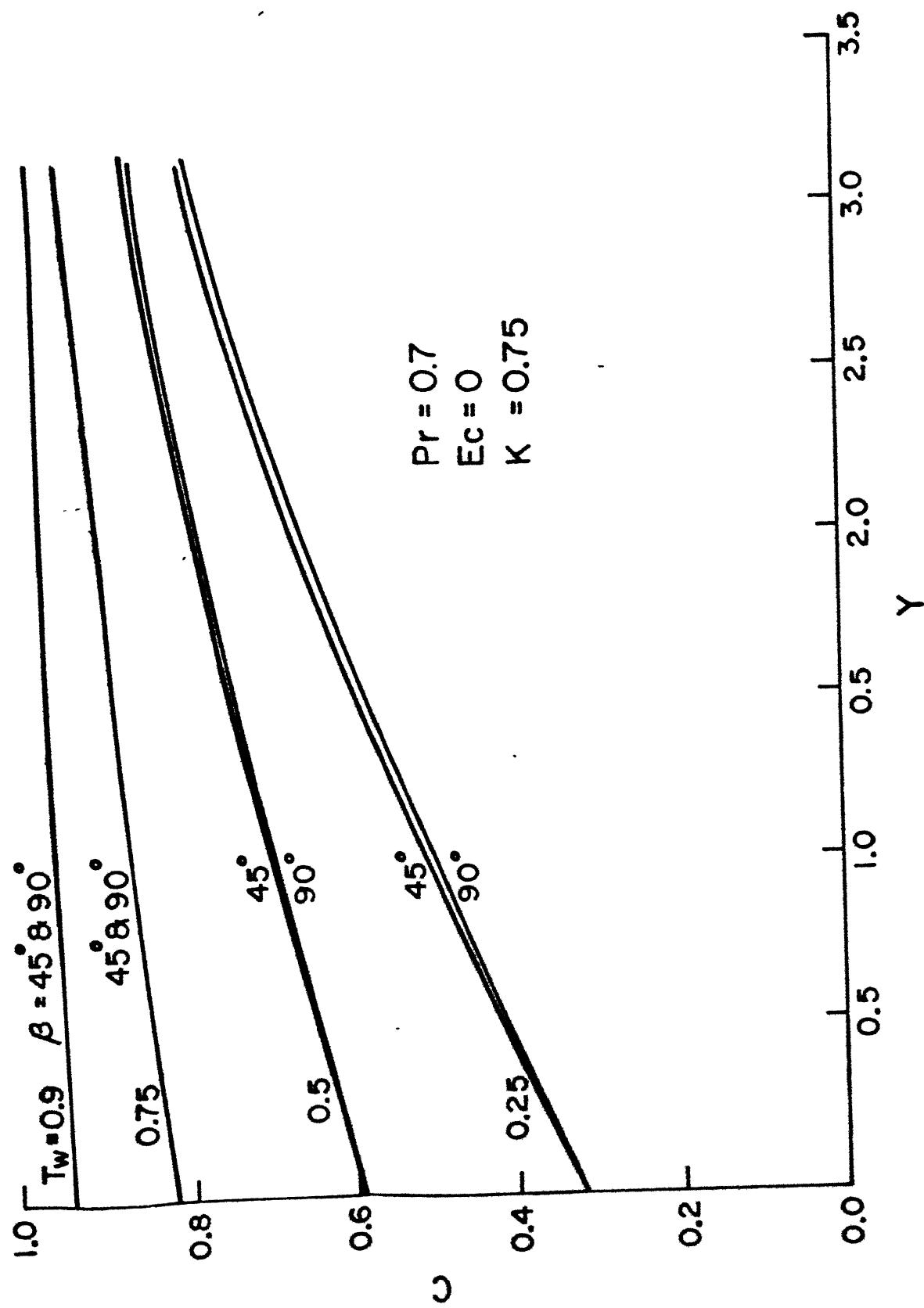
Fig. 4.35 Particle concentration profiles as a function of temperature of the cold wall at X = 3.0
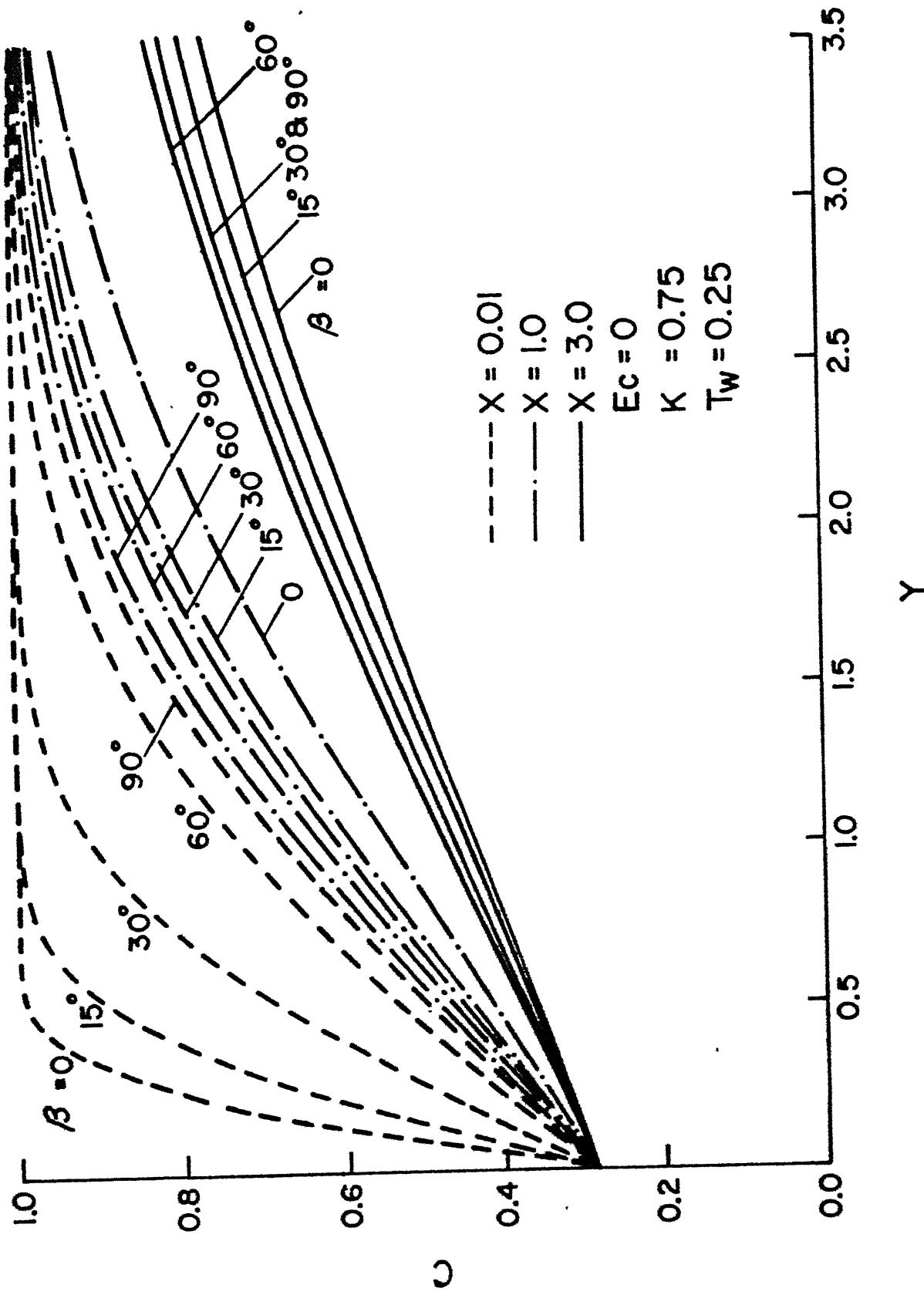
Fig. 4.36 Concentration profiles over a cold plate (Pr = 1)
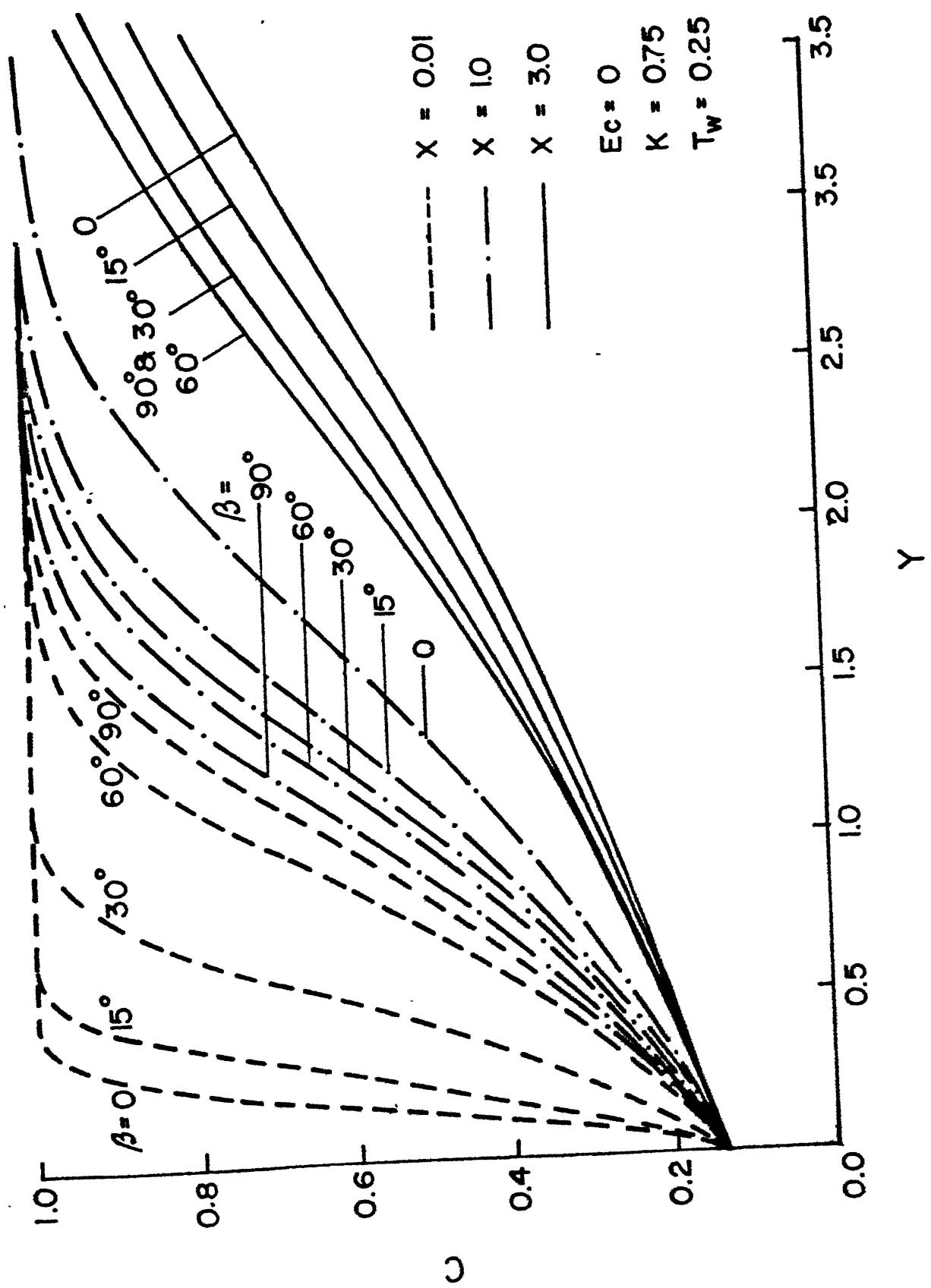
Fig. 4.37 Concentration profiles over a cold plate (Pr = 5)
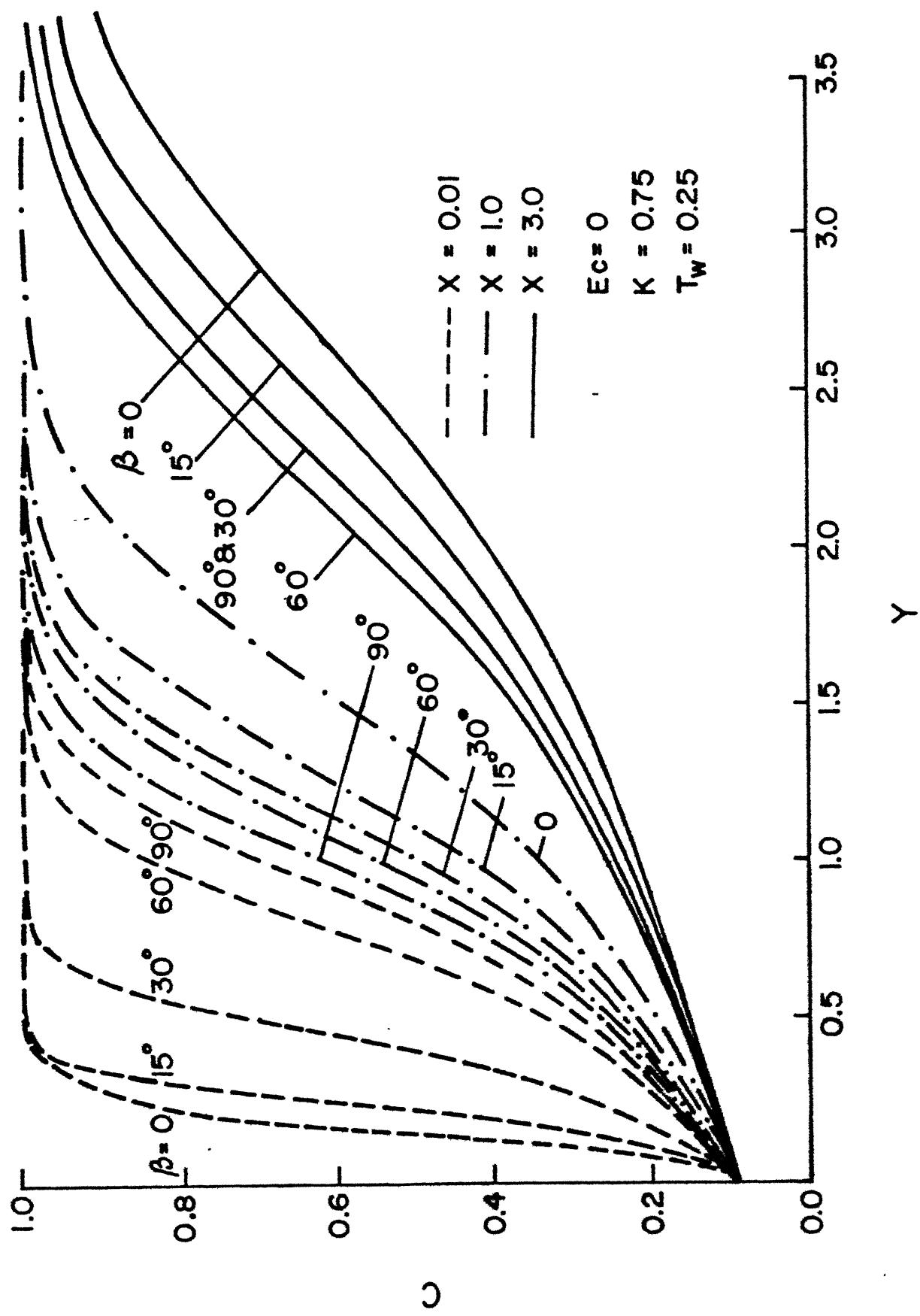
Fig. 4.38 Concentration profiles over a cold plate (Pr = 10)
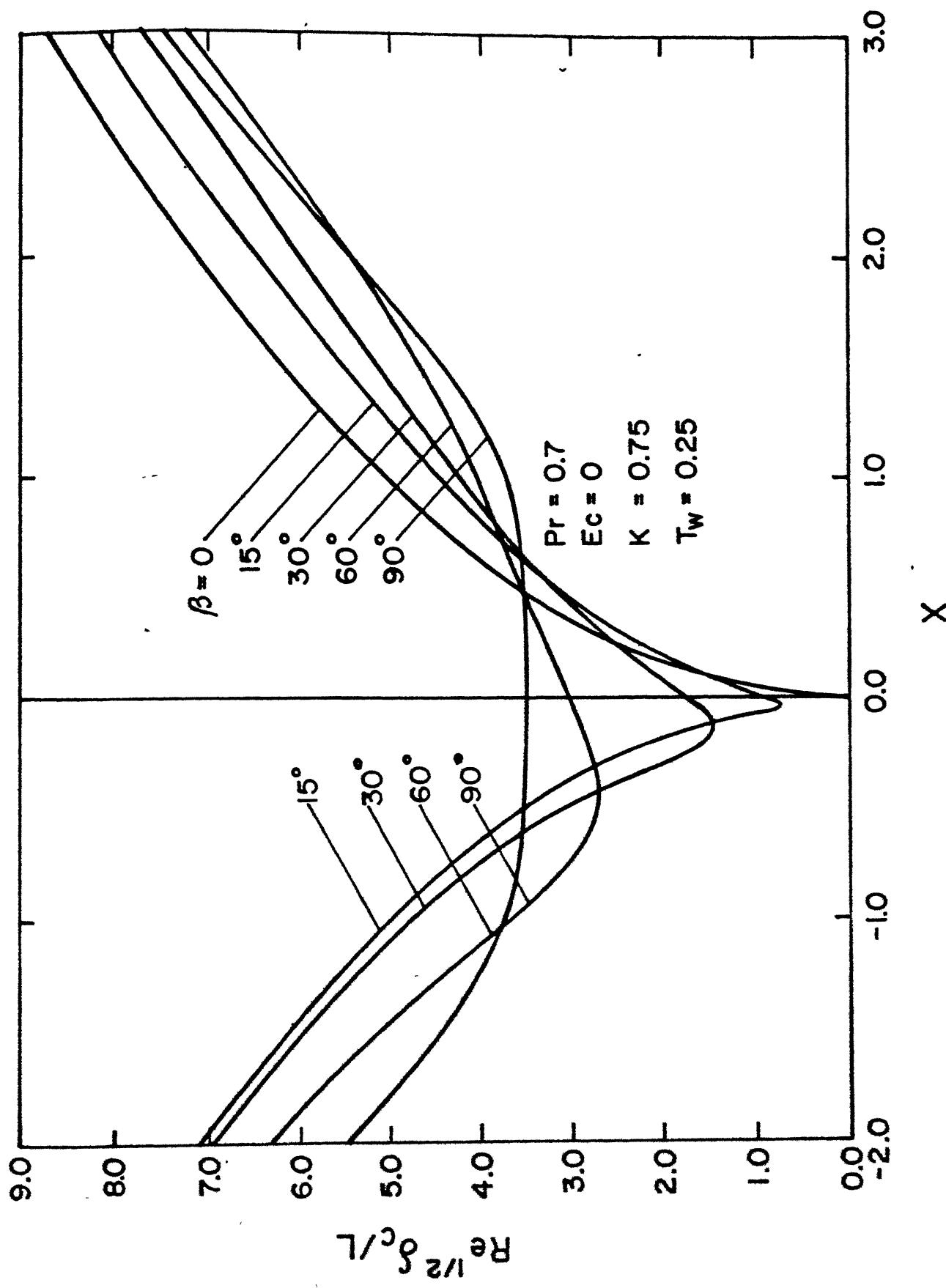
Fig. 4.39 Concentration boundary layer thickness over a cold plate
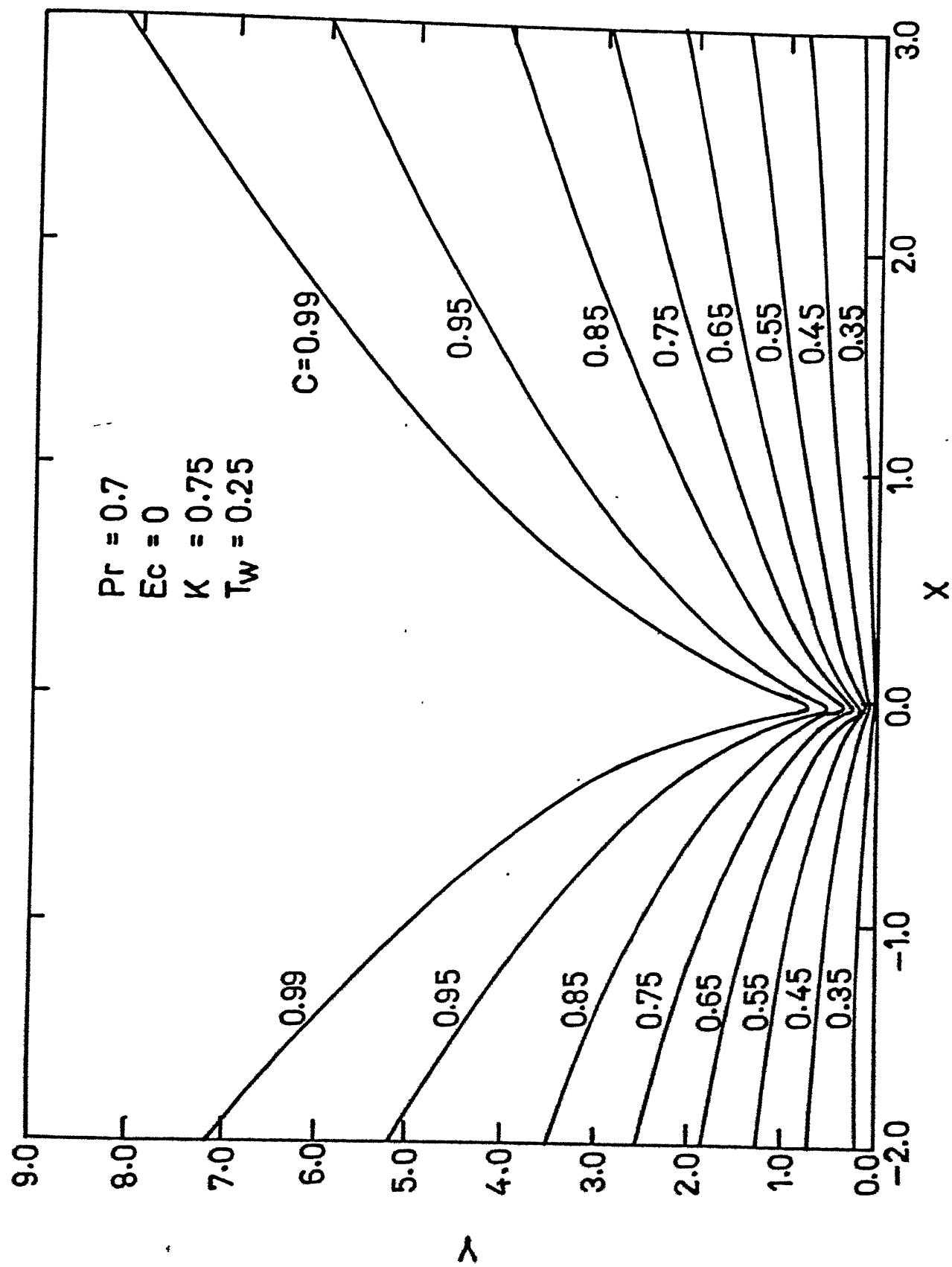
Fig.4.40 Isoconcentration curves for $\beta = 15°$
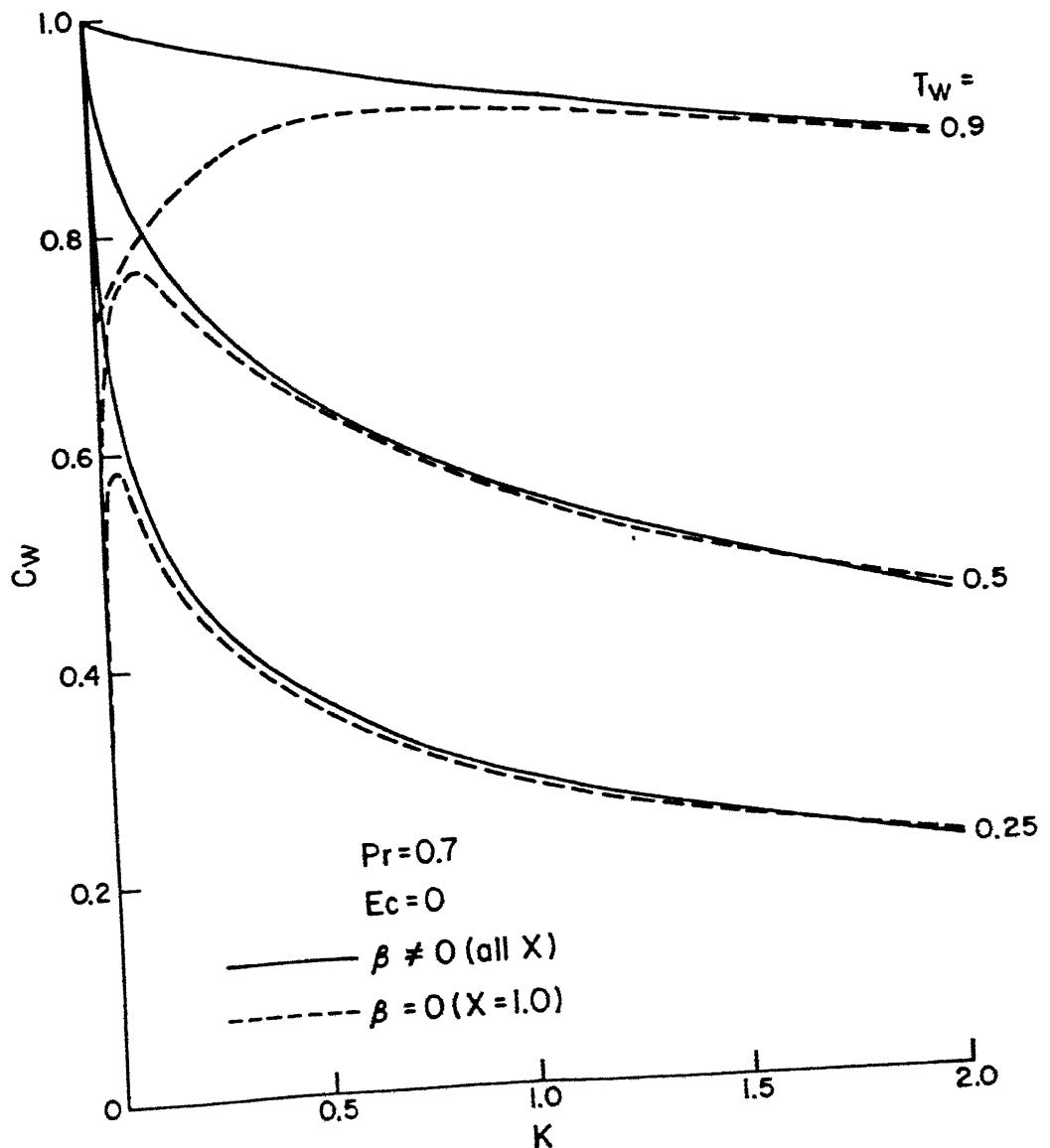
Fig.4.41 Variation of concentration at the cold plate with K
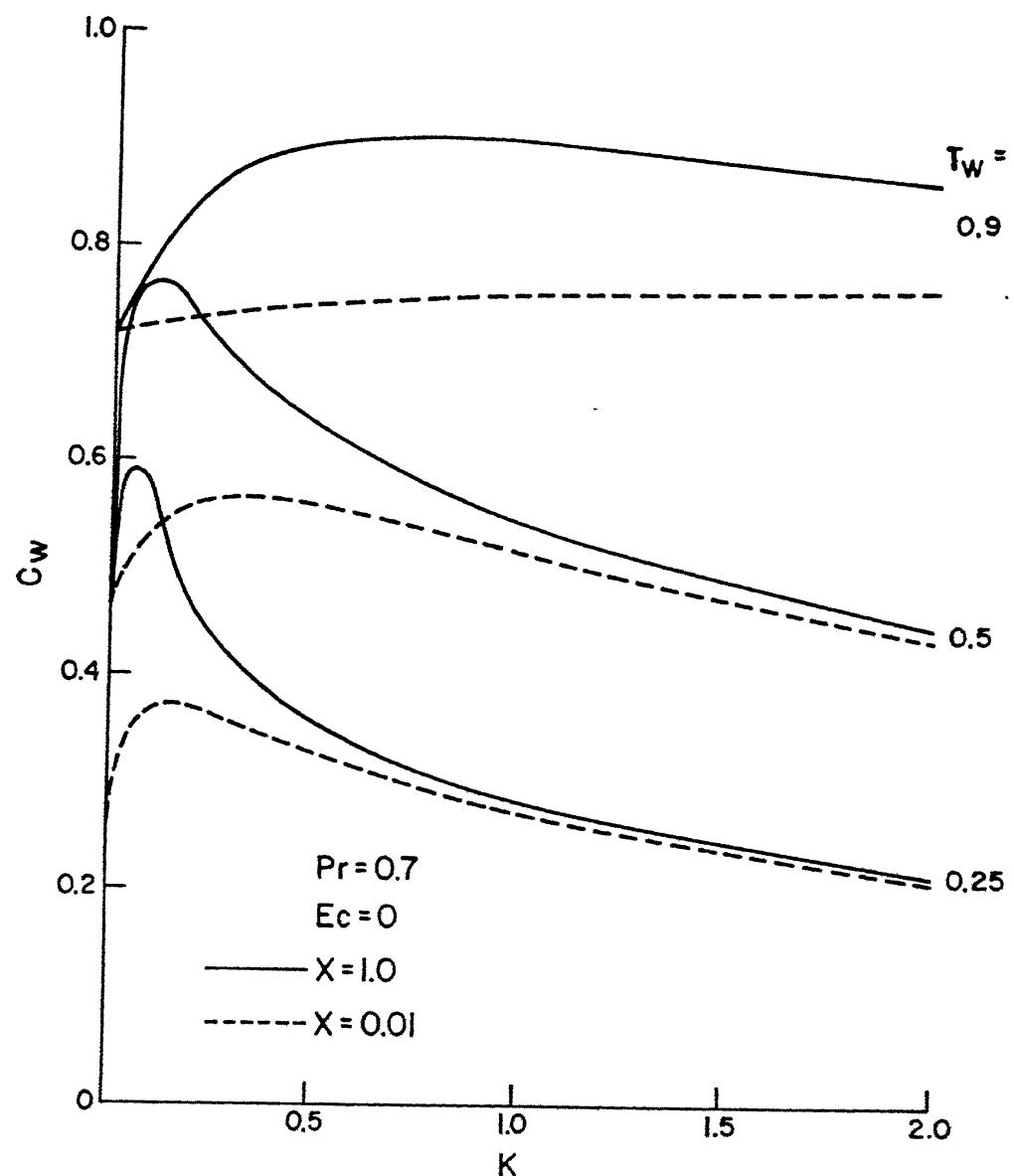
Fig.4.42 Variation of concentration at the cold plate
with K at β = 0
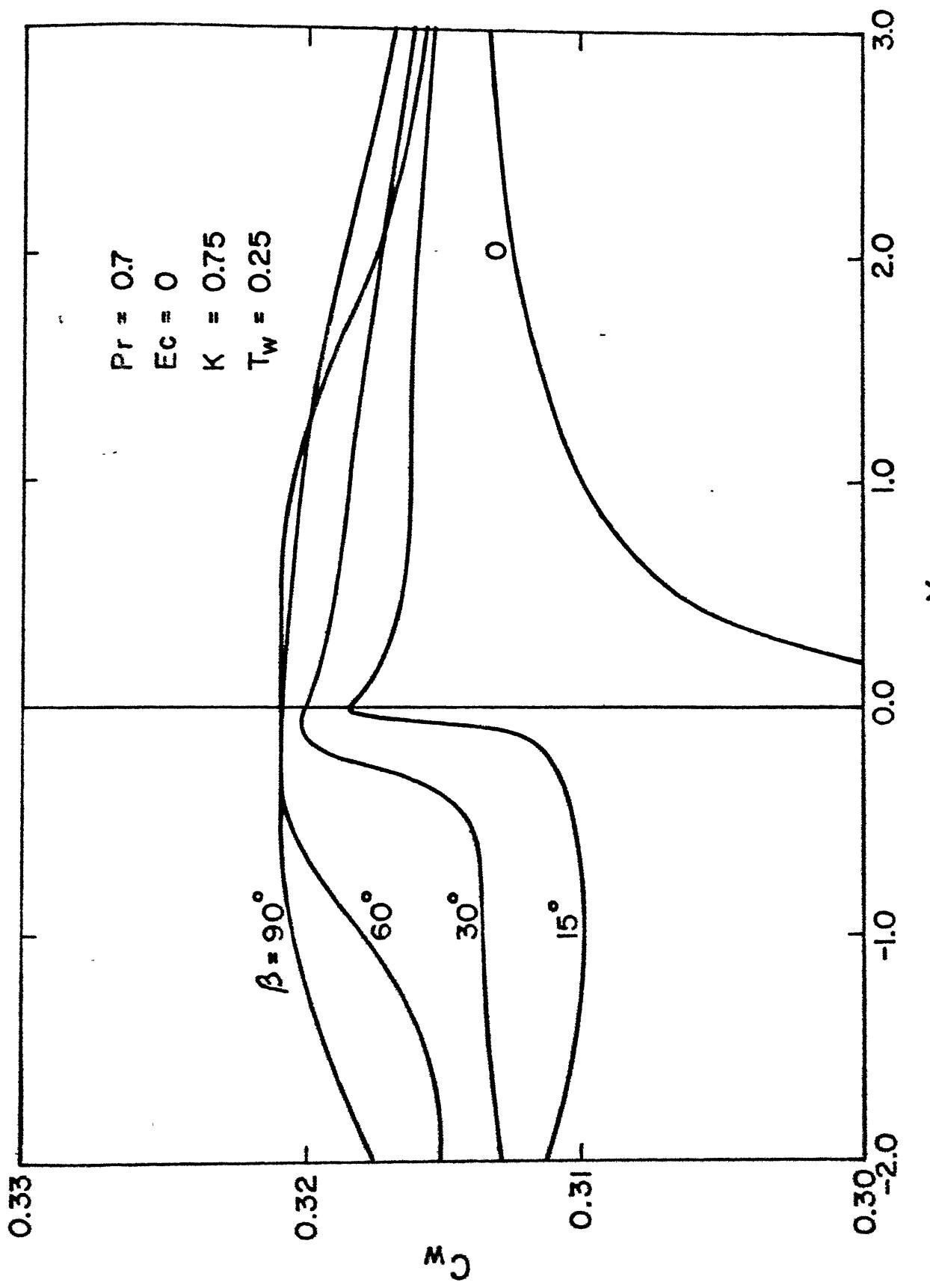
Fig. 4.43 Variation of concentration at the cold plate with X

Pr = 0.7
Ec = 0
K = 0.75
T_W = 0.25
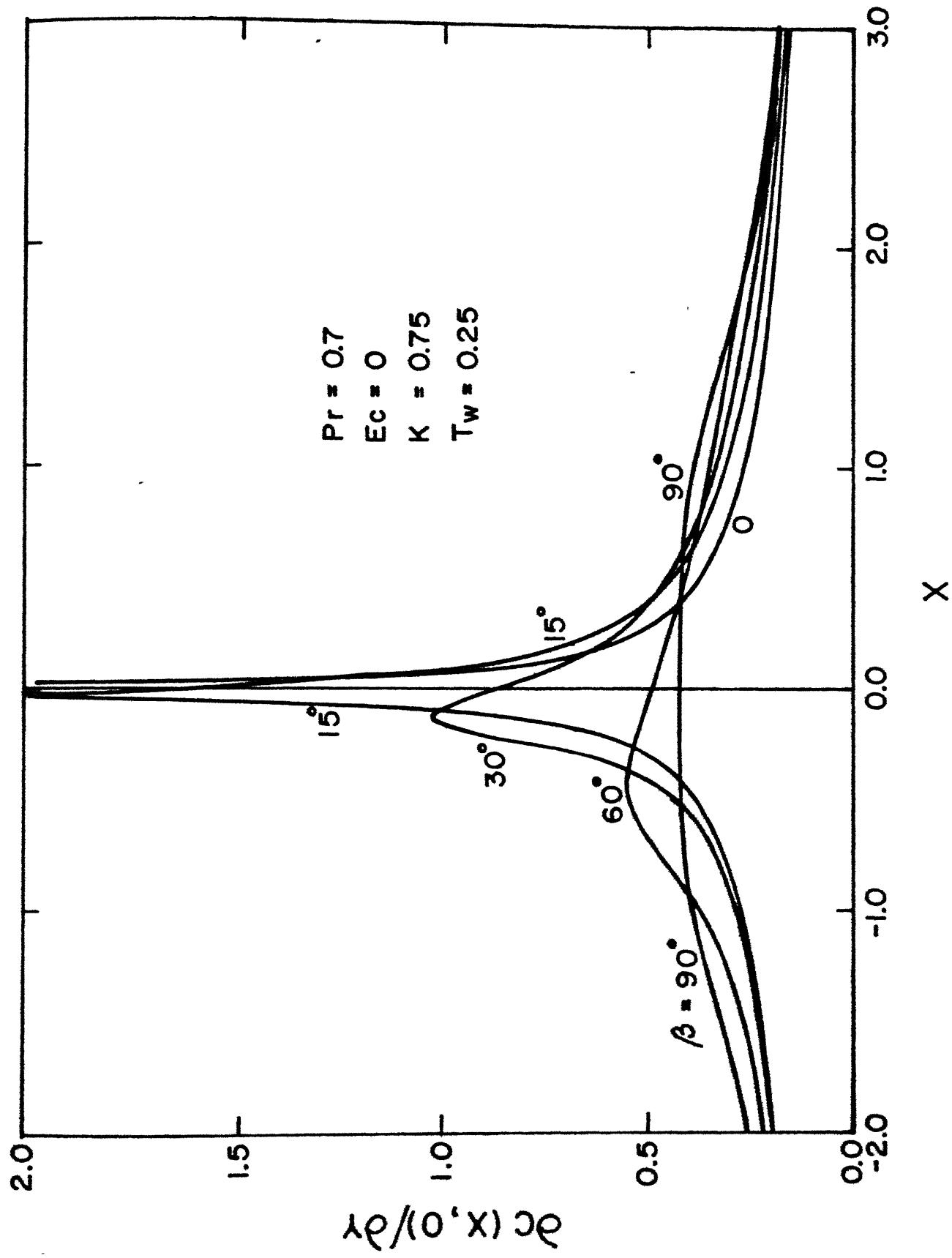
Fig.4.44 Variation of concentration gradient at the cold plate with X
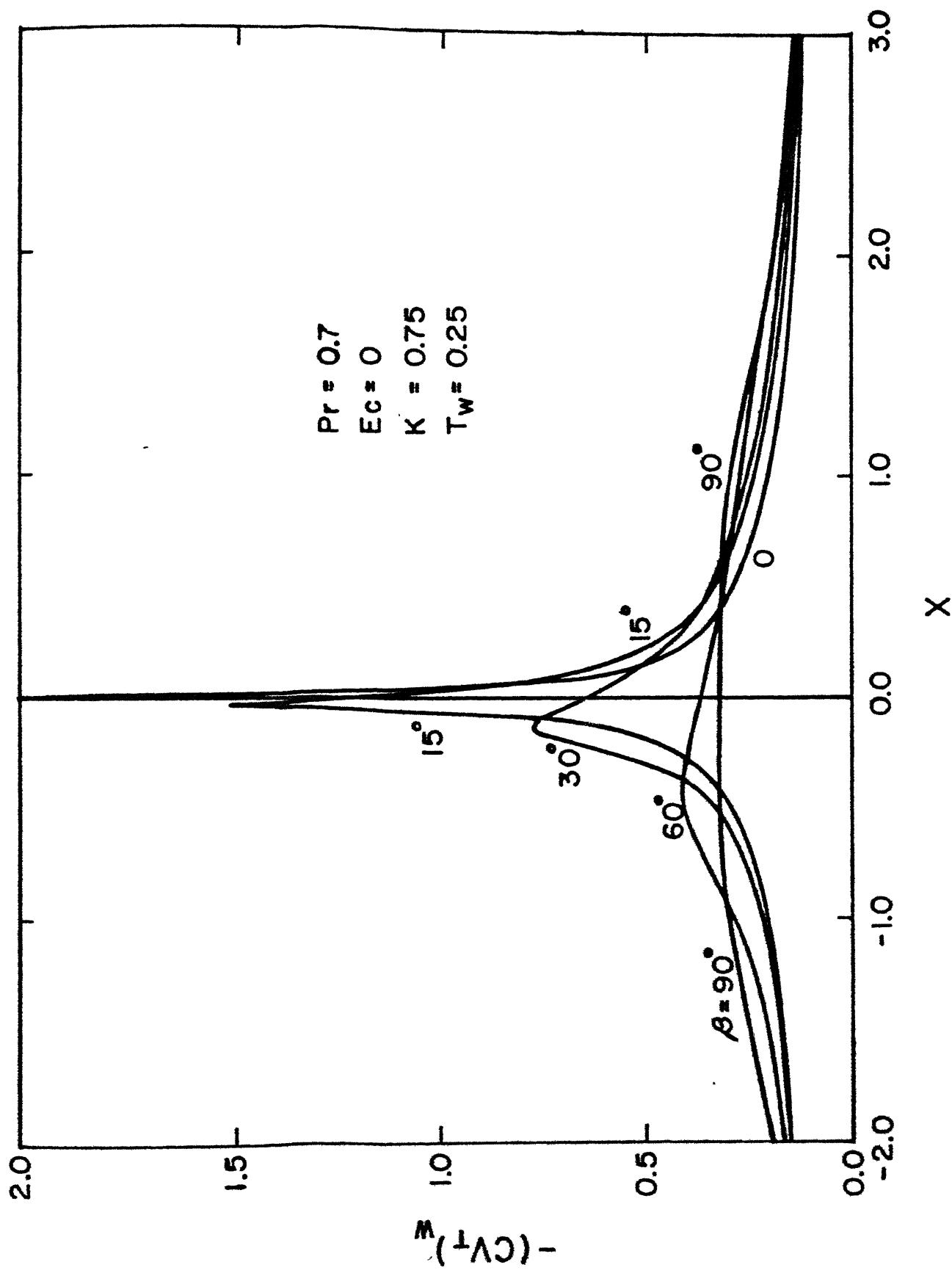
Fig. 4.45 Variation of local dimensionless concentration flux at the cold plate with X
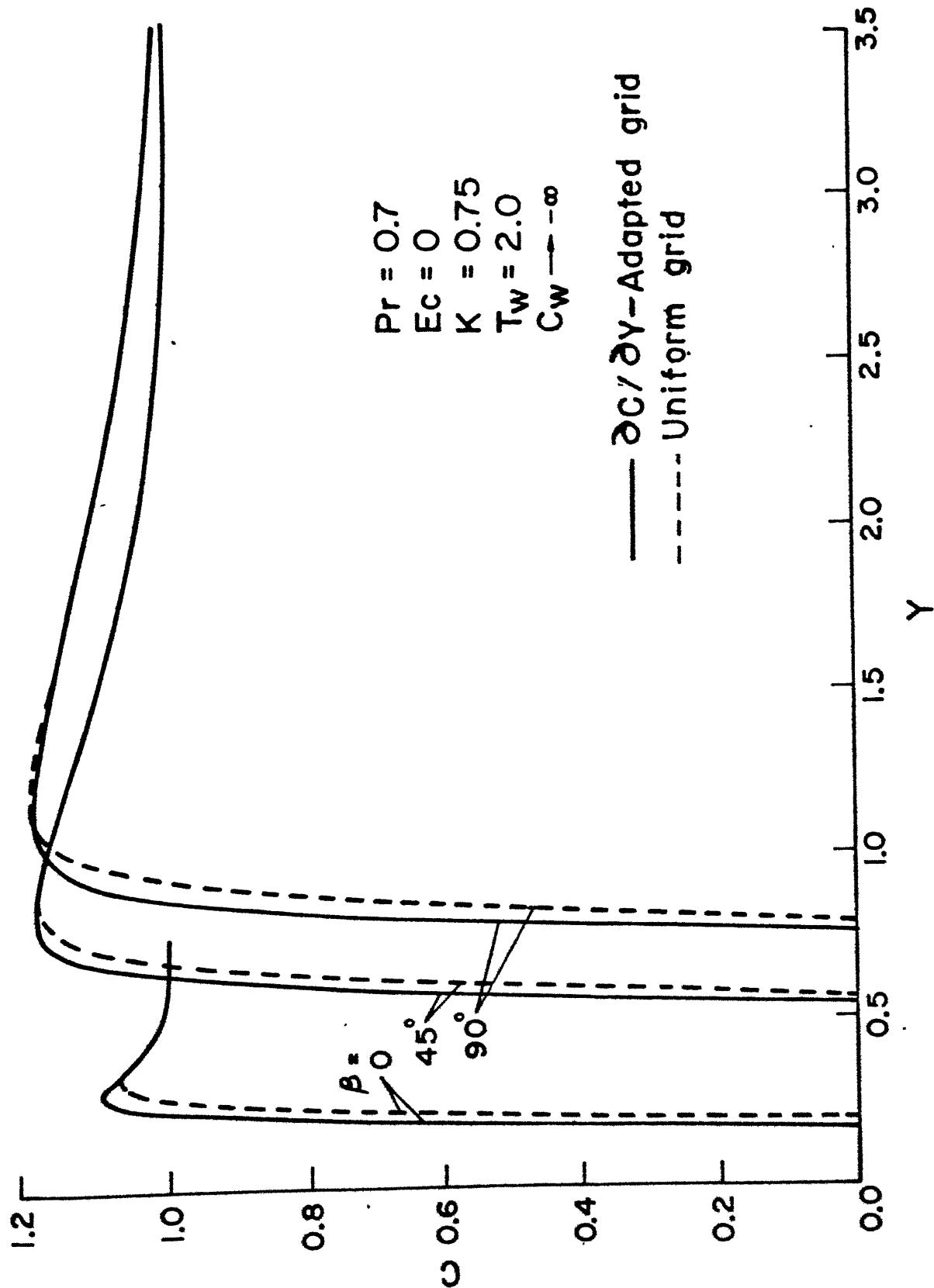
Fig. 4.46 Effect of self-adaptive grid on concentration profile computation for hot wall ($X = 0.01$)
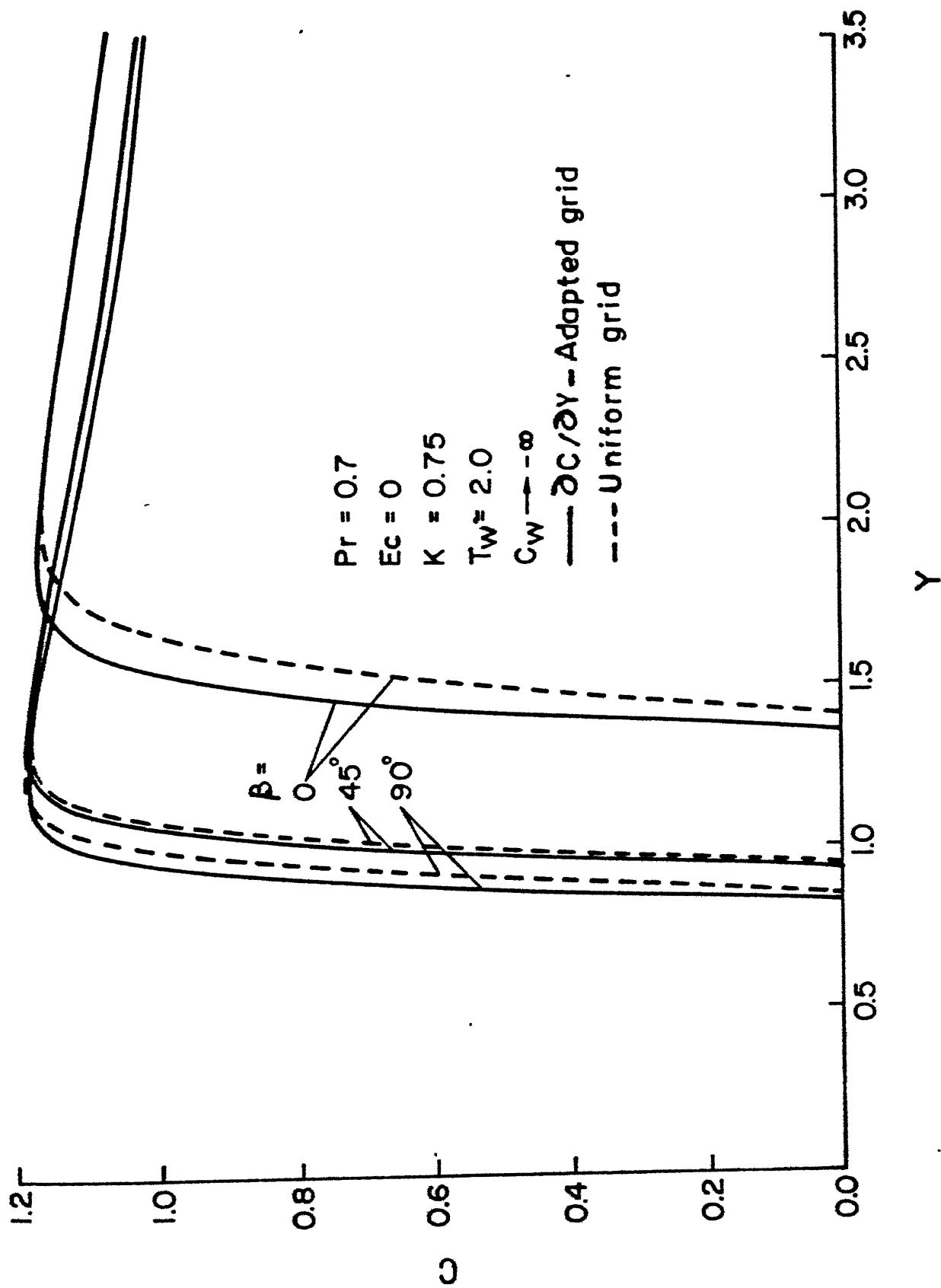
Fig. 4.47 Effect of self-adaptive grid on concentration profile computation for hot wall (X=1.0)
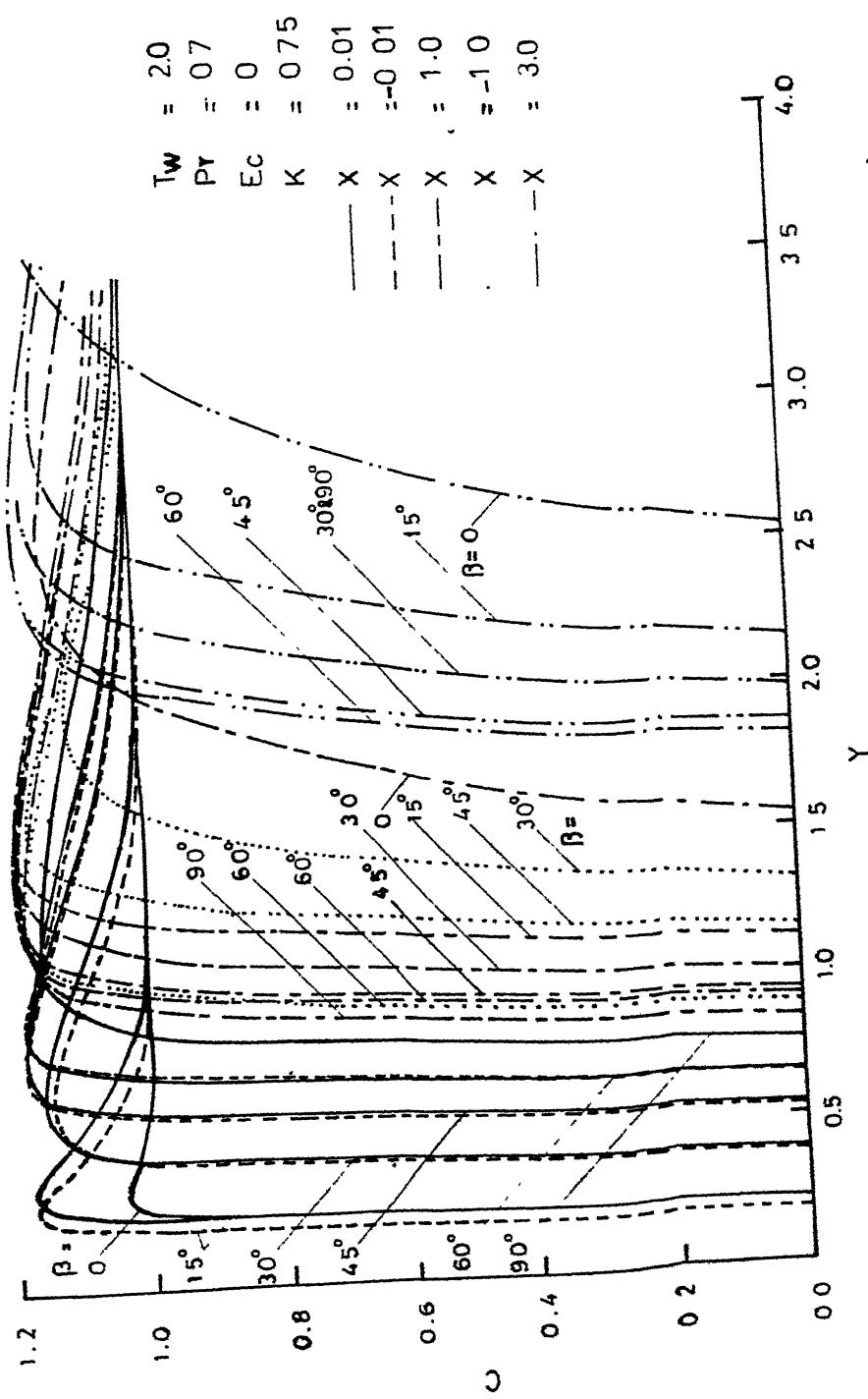
Fig. 4.48 Particle concentration profiles for a hot inclined plate (Pr. K<1)
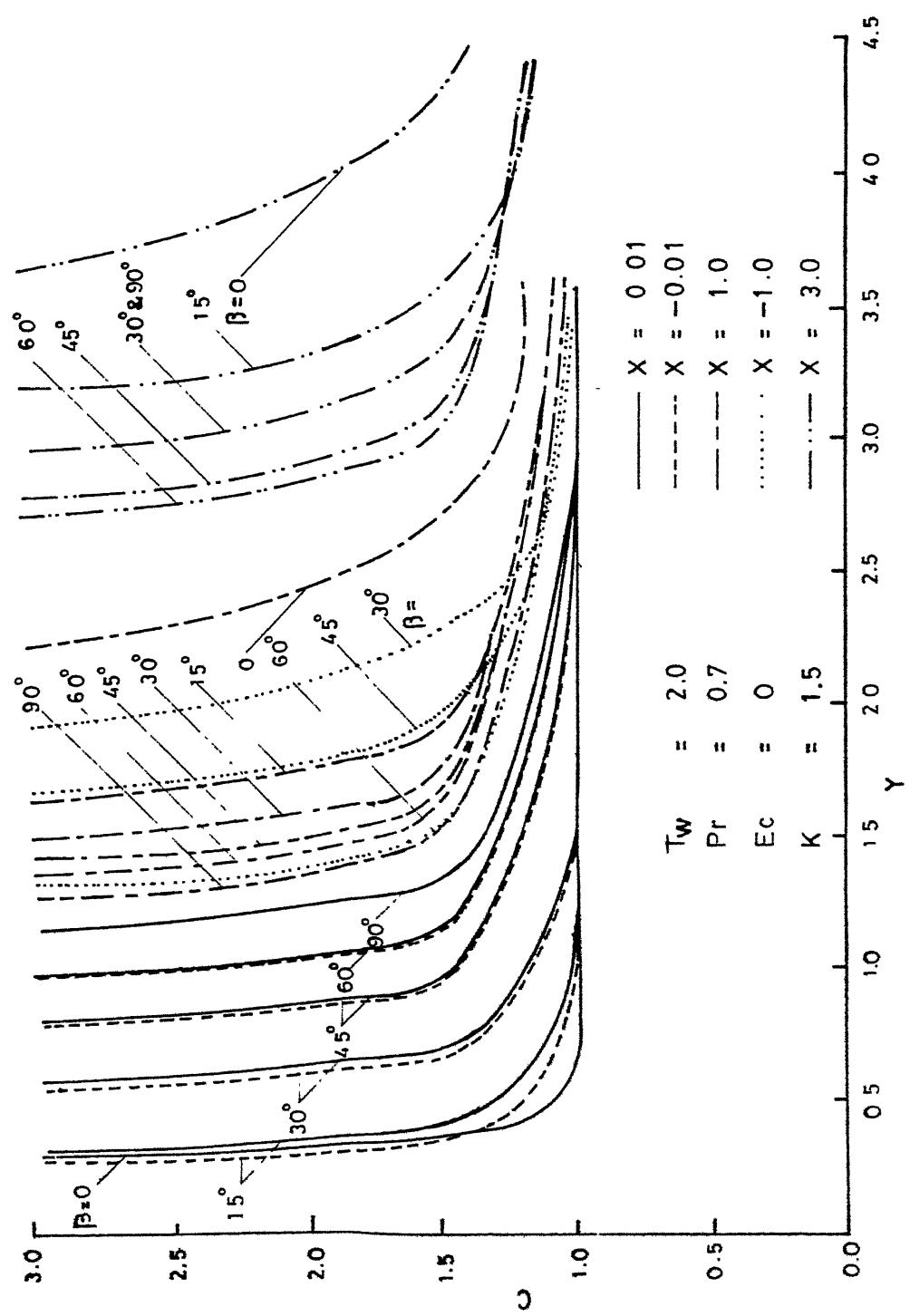
Fig. 4.49 Particle concentration profiles for a hot inclined plate (Pr. K>1)
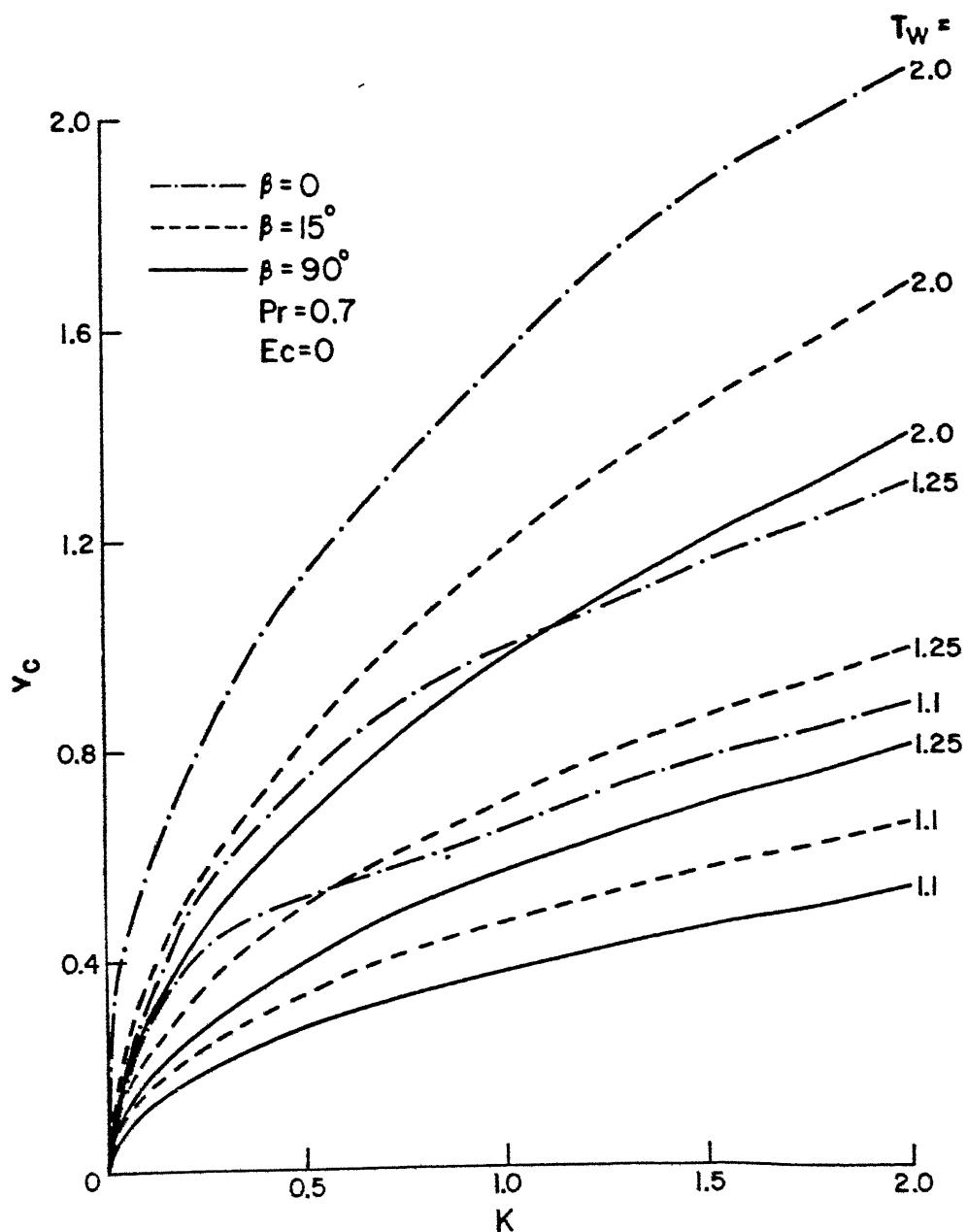
Fig.4.50 Critical layer thickness as a function of K
with T_W and β as parameters at X = 1.0
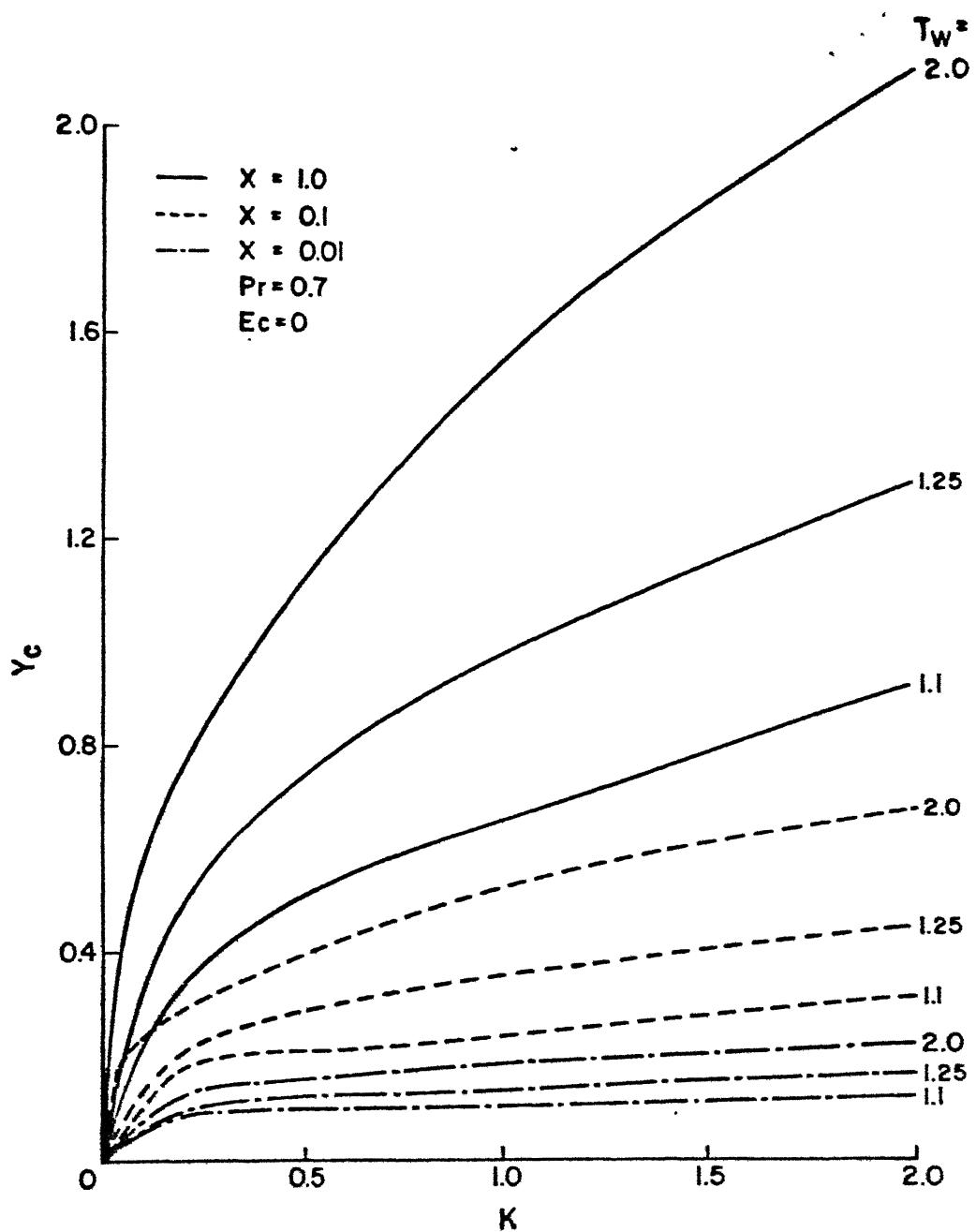
Fig.4.52 Critical layer thickness as a function of K
with T_w and X as parameters for $\beta = 0$
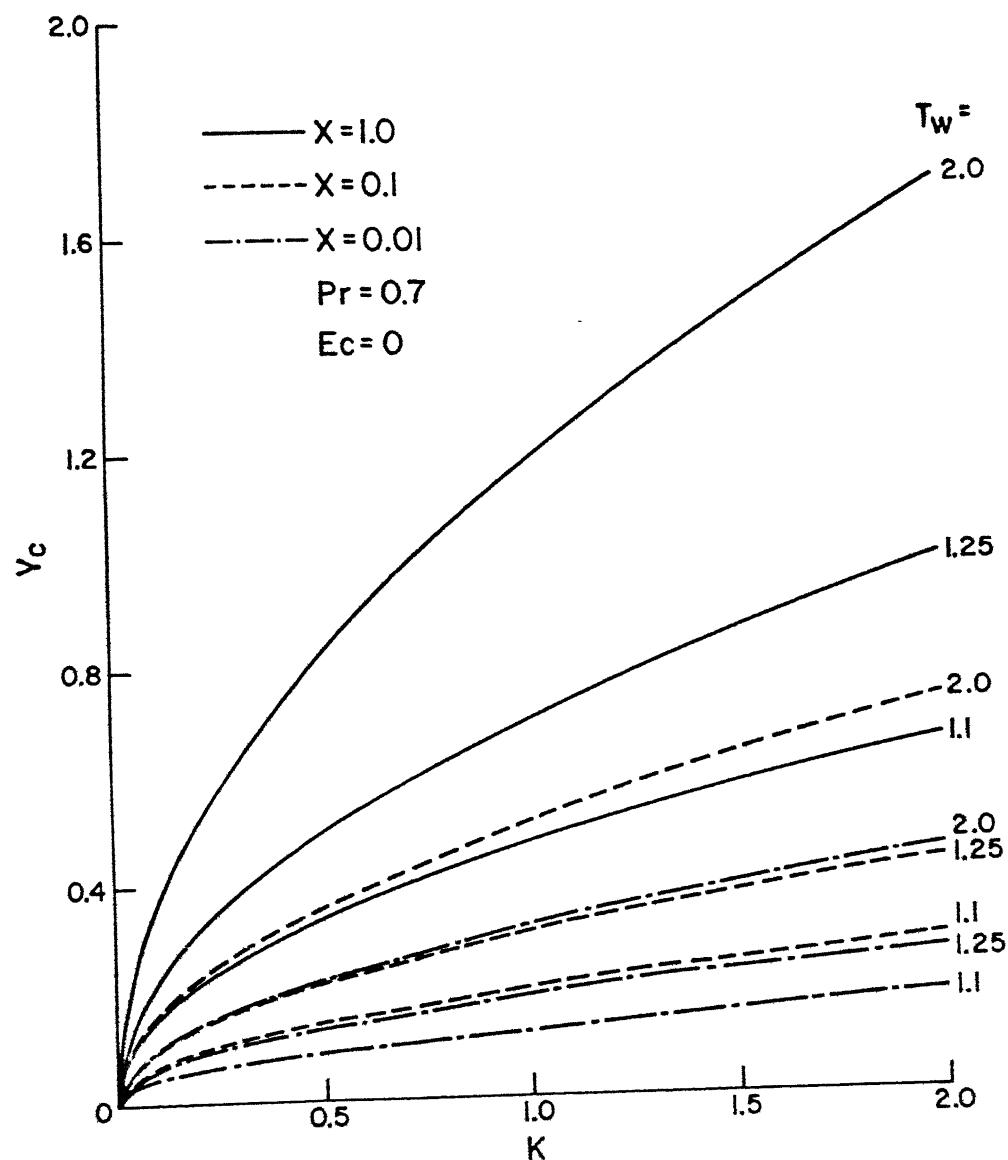
Fig. 4.53 Critical layer thickness as a function of K
with T_w and X as parameters for $\beta = 15°$
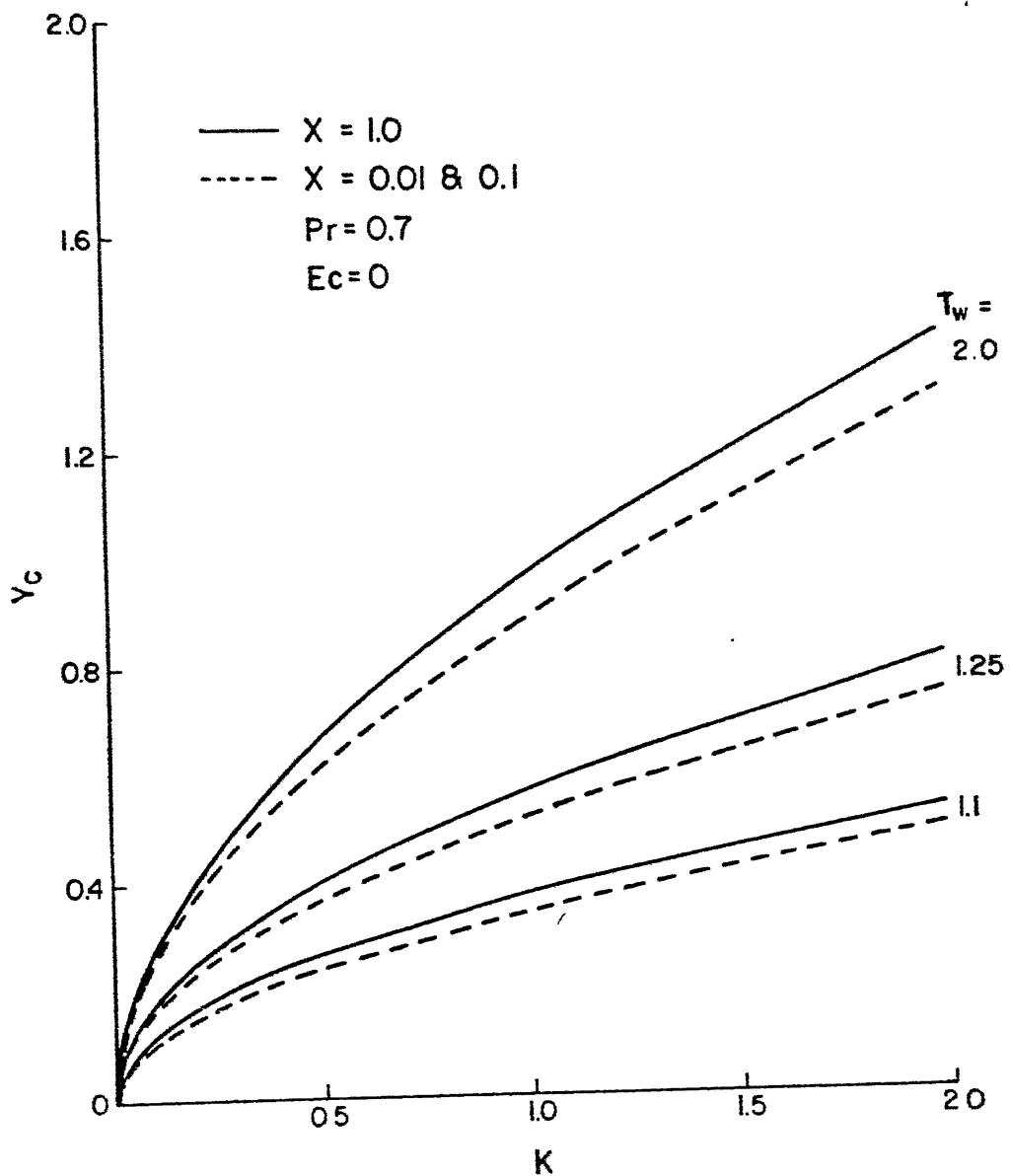
Fig.4.54 Critical layer thickness as a function of K with T_W and X as parameters for $\beta=90°$
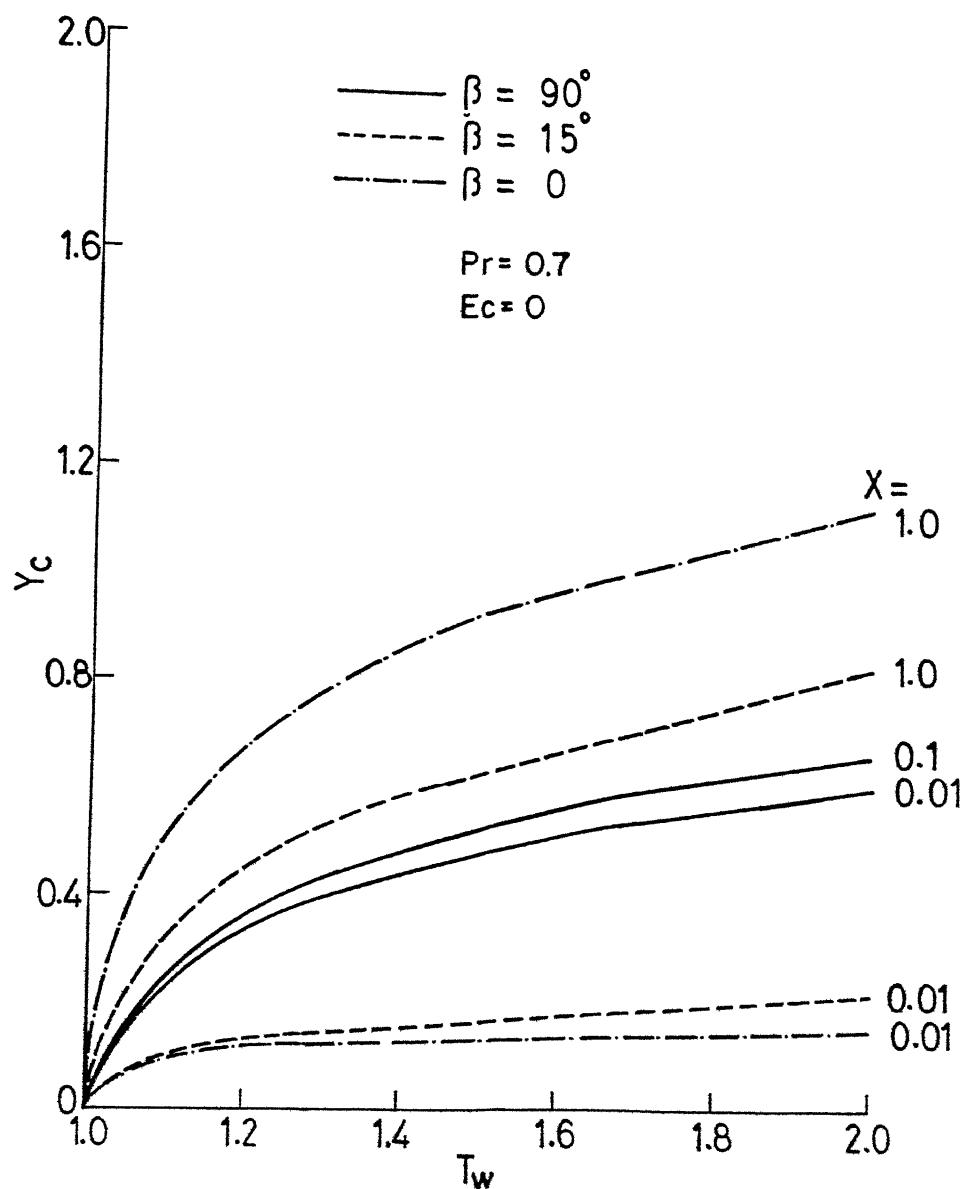
Fig. 4.55 Variation of critical layer thickness
with wall temperature at K=0.5
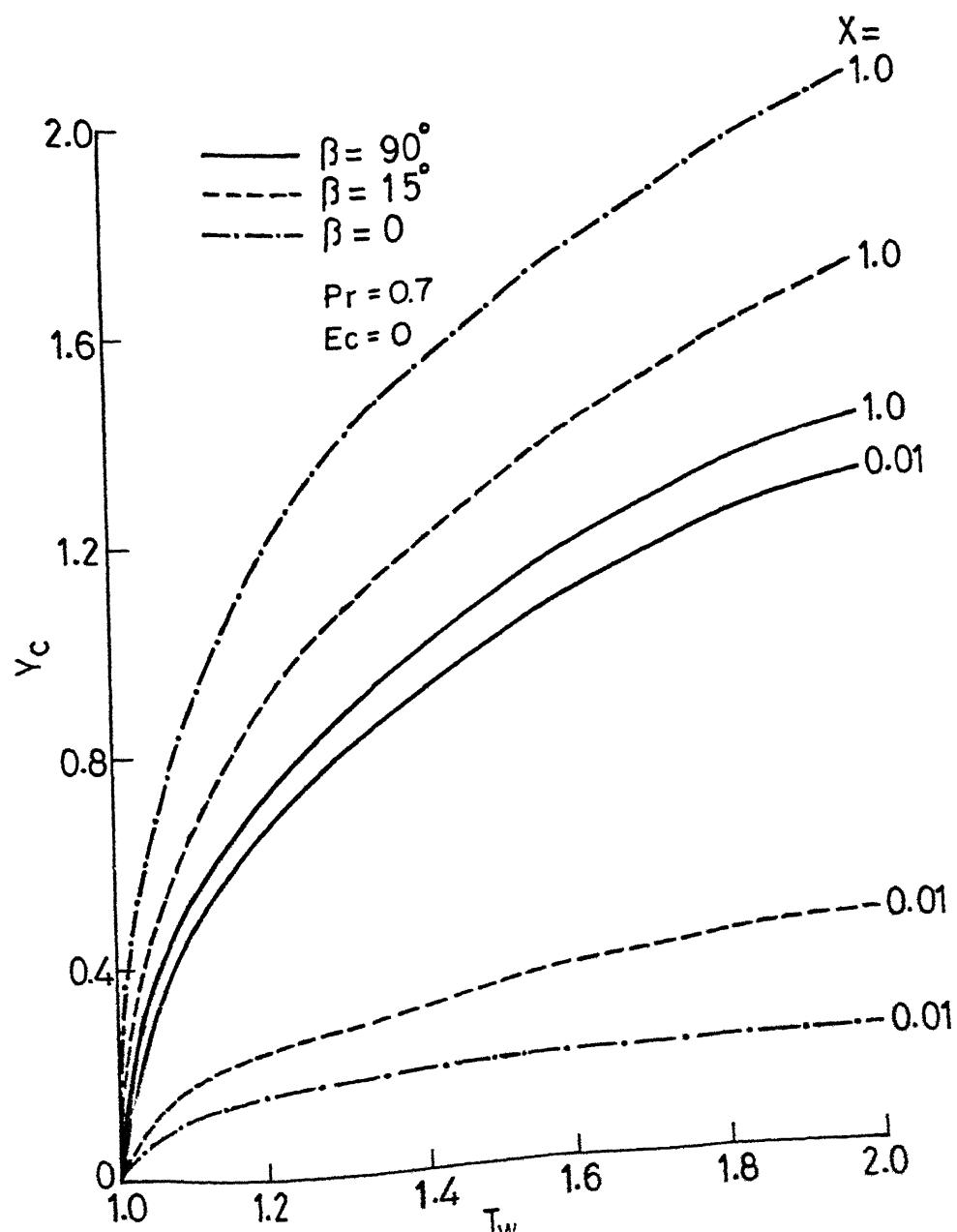
Fig.4.56 Variation of critical layer thickness with wall temperature at K = 2.0
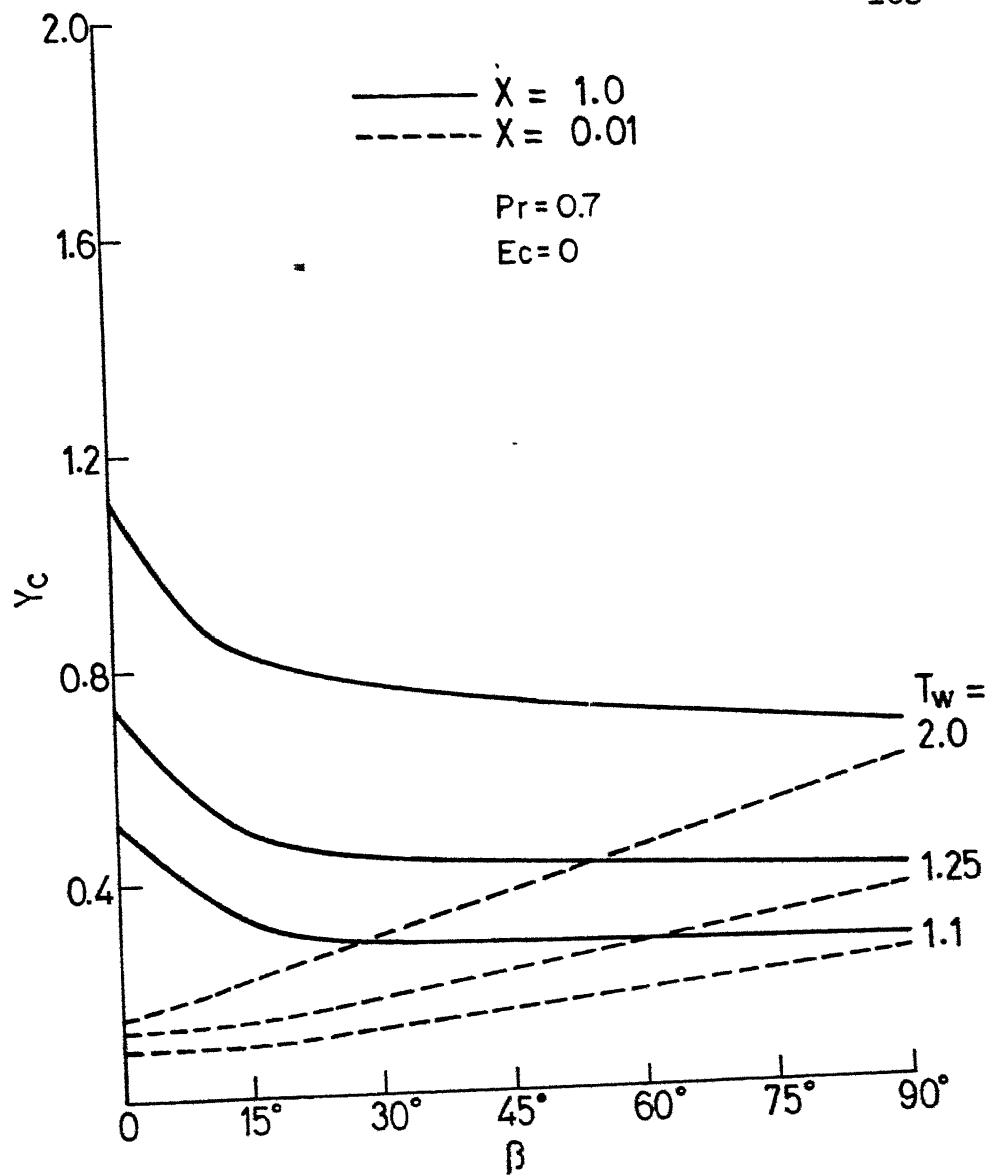
Fig. 4.57 Variation of critical layer thickness
with angle of inclination at K = 0.5
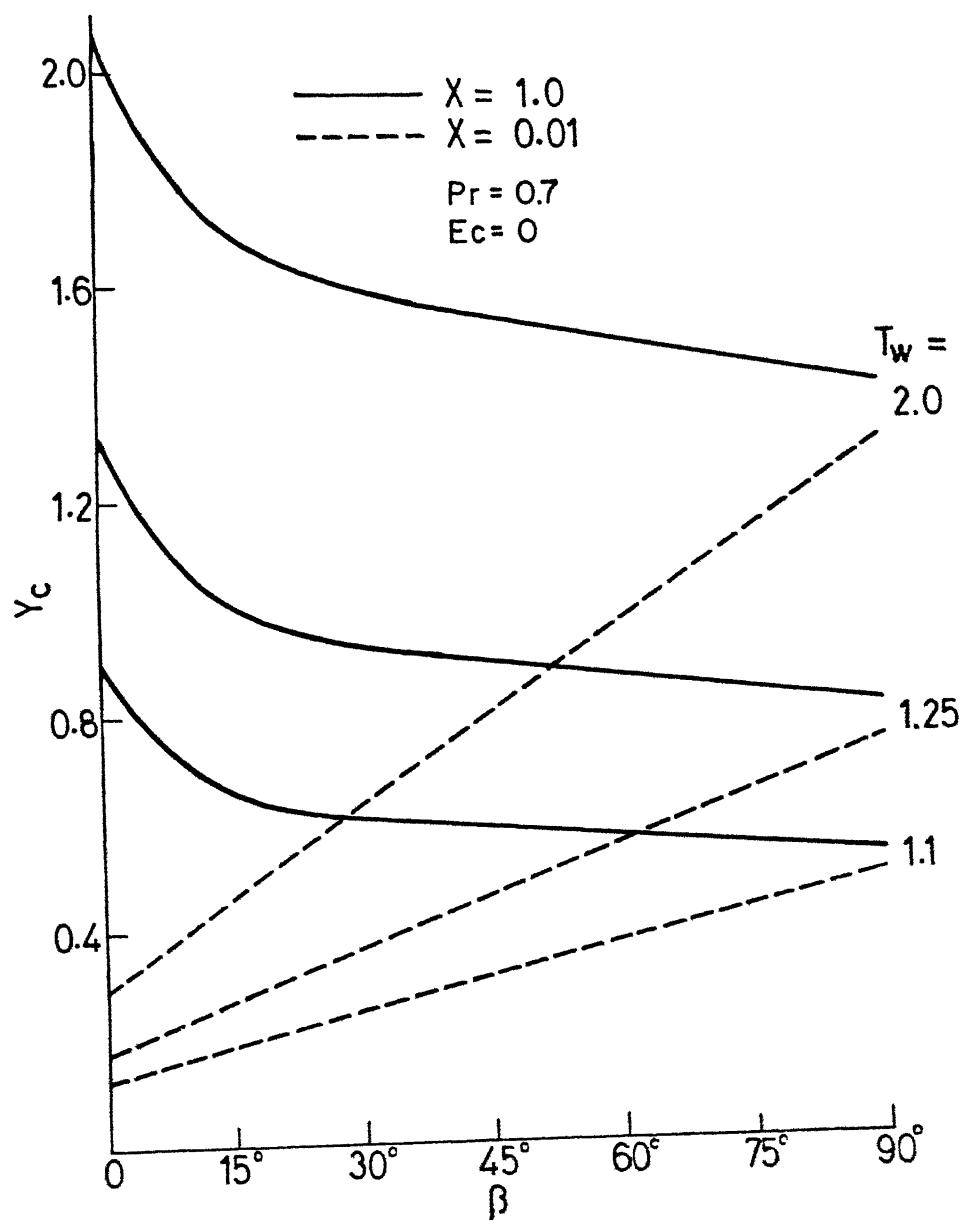
Fig. 4.58 Variation of critical layer thickness with angle of inclination at K = 2.0
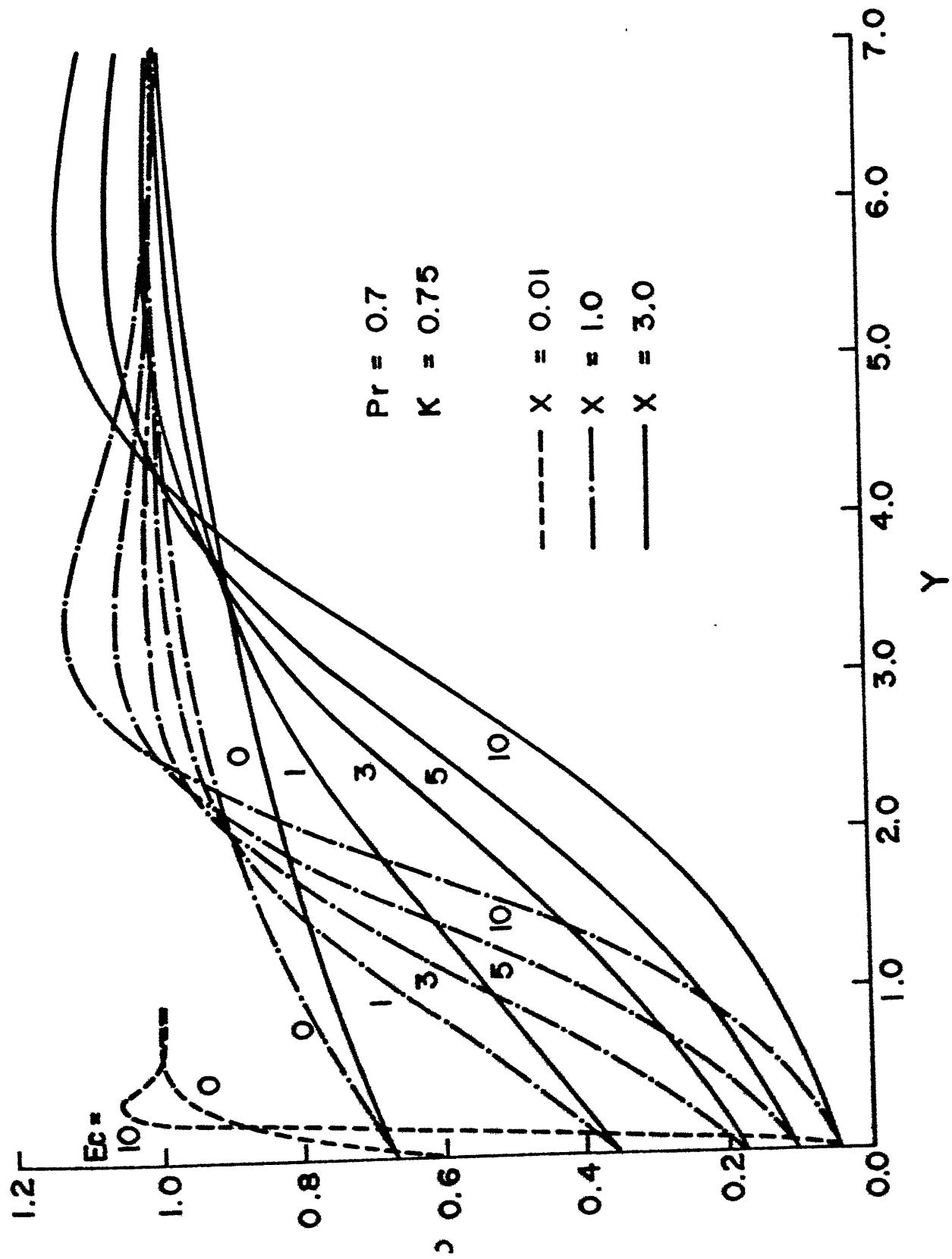
Fig.4.59 Particle concentration profiles for flow past a cold plate at different rates of viscous dissipation ($\beta=0$, $T_w=0.6$)
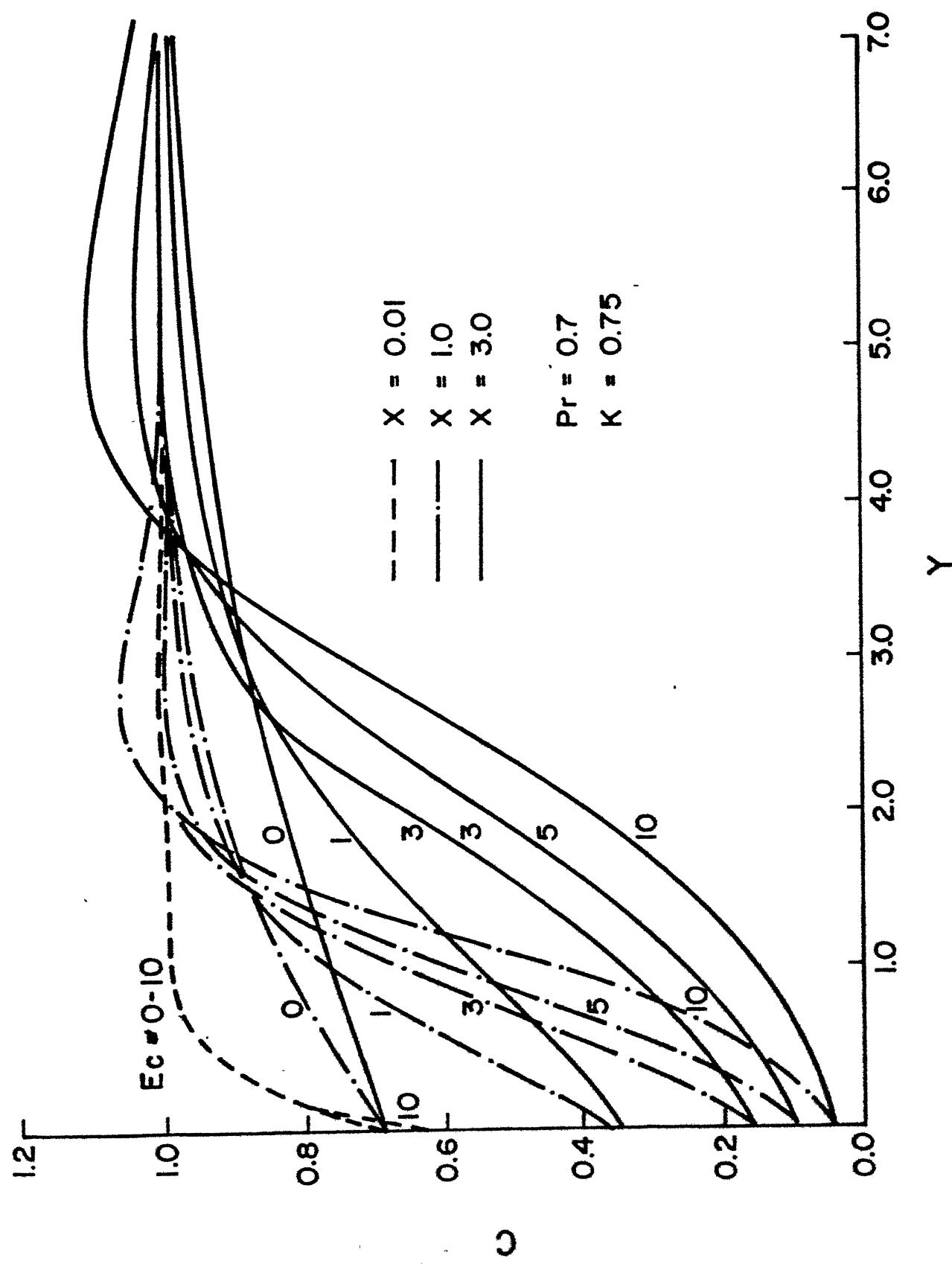
Fig. 4.60 Particle concentration profiles for flow past a cold plate at different rates of viscous dissipation ($\beta = 15°$, $T_w = 0.6$)
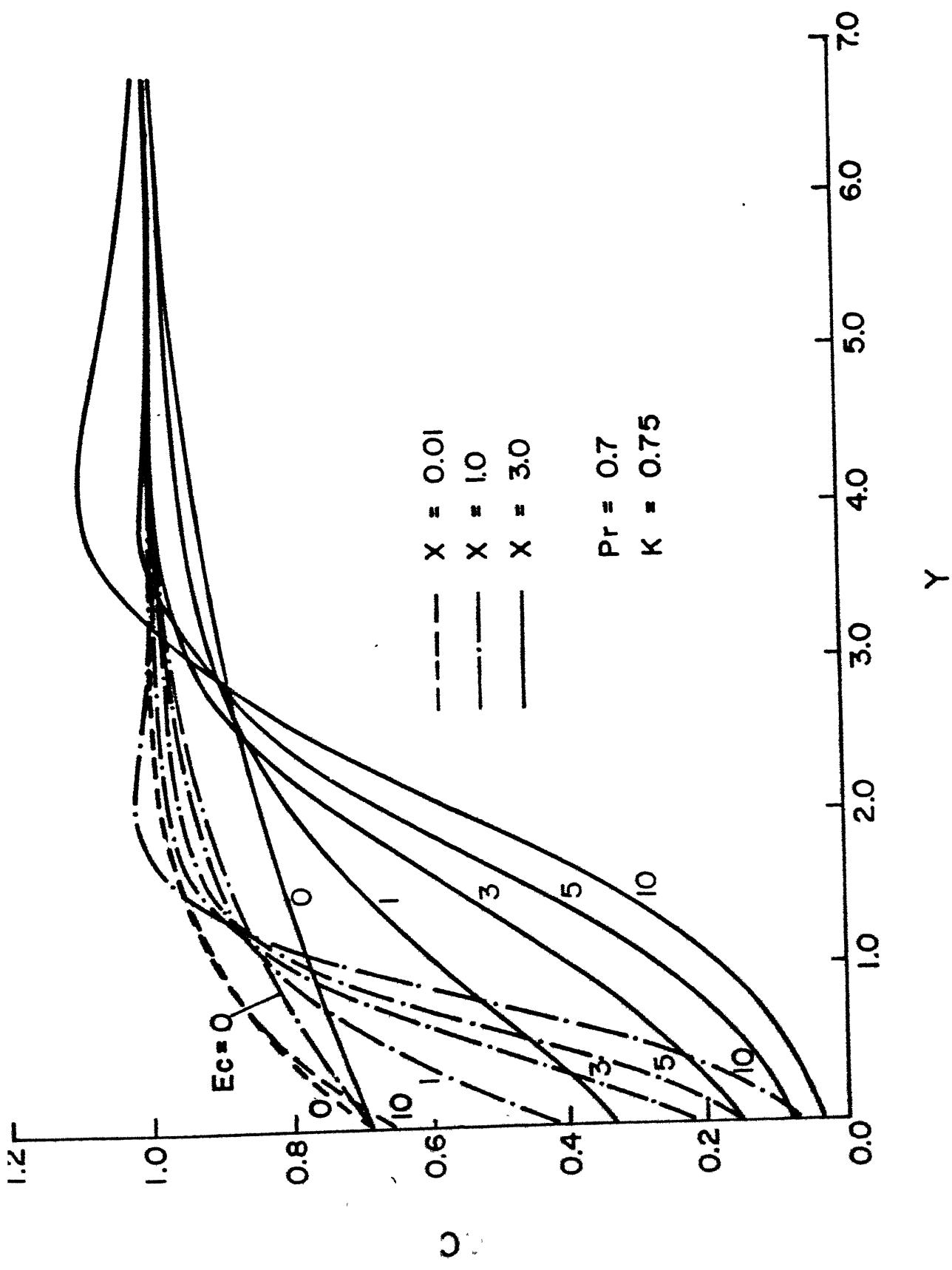
Fig. 4.61 Partical concentration profiles for flow past a cold plate at different rates of viscous dissipation ($\beta = 45°$, $T_w = 0.6$)

165
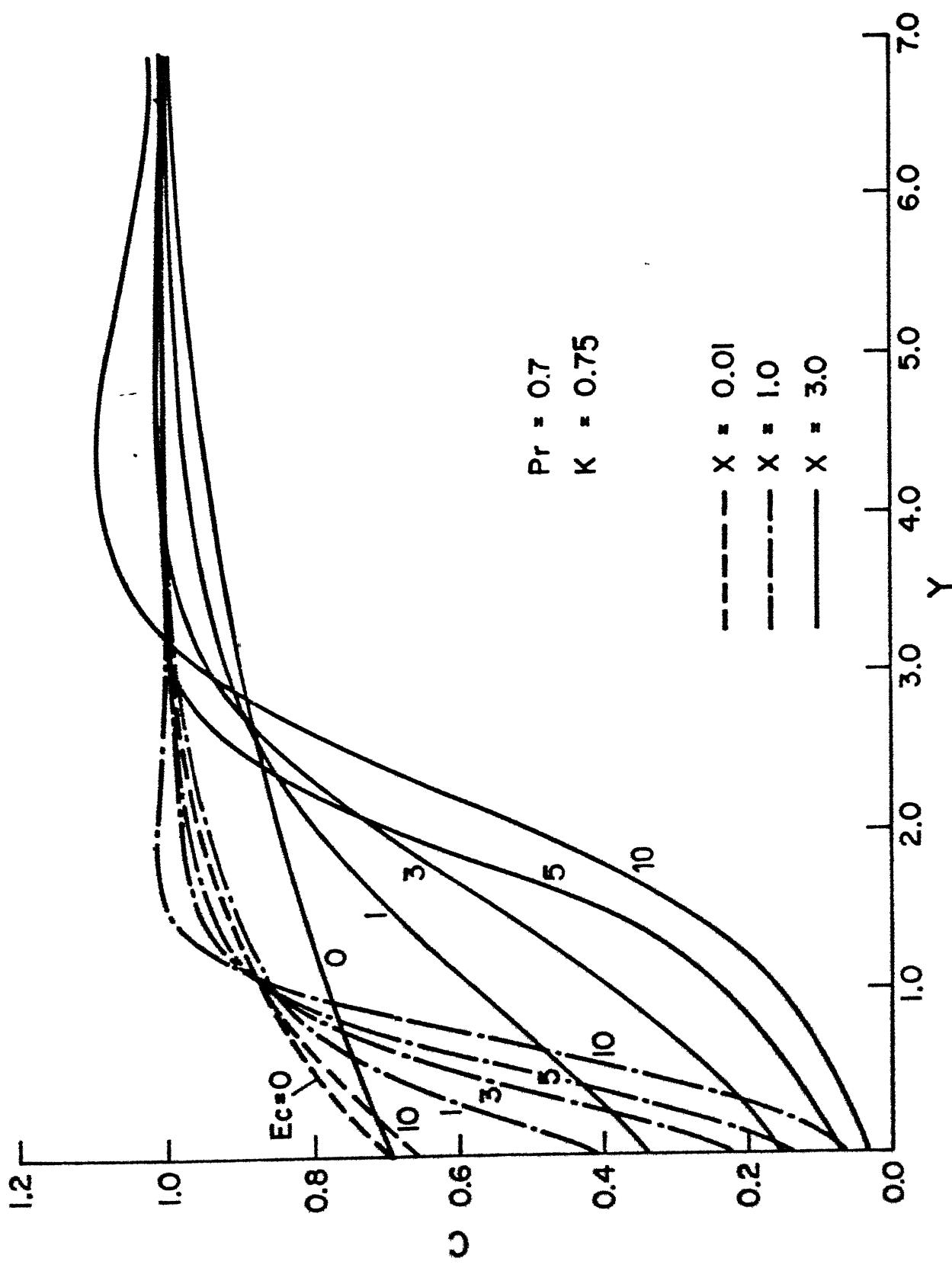
Fig. 4.62 Particle concentration profiles for flow past a cold plate at different rates of viscous dissipation ($\beta = 90°$, $T_w = 0.6$)
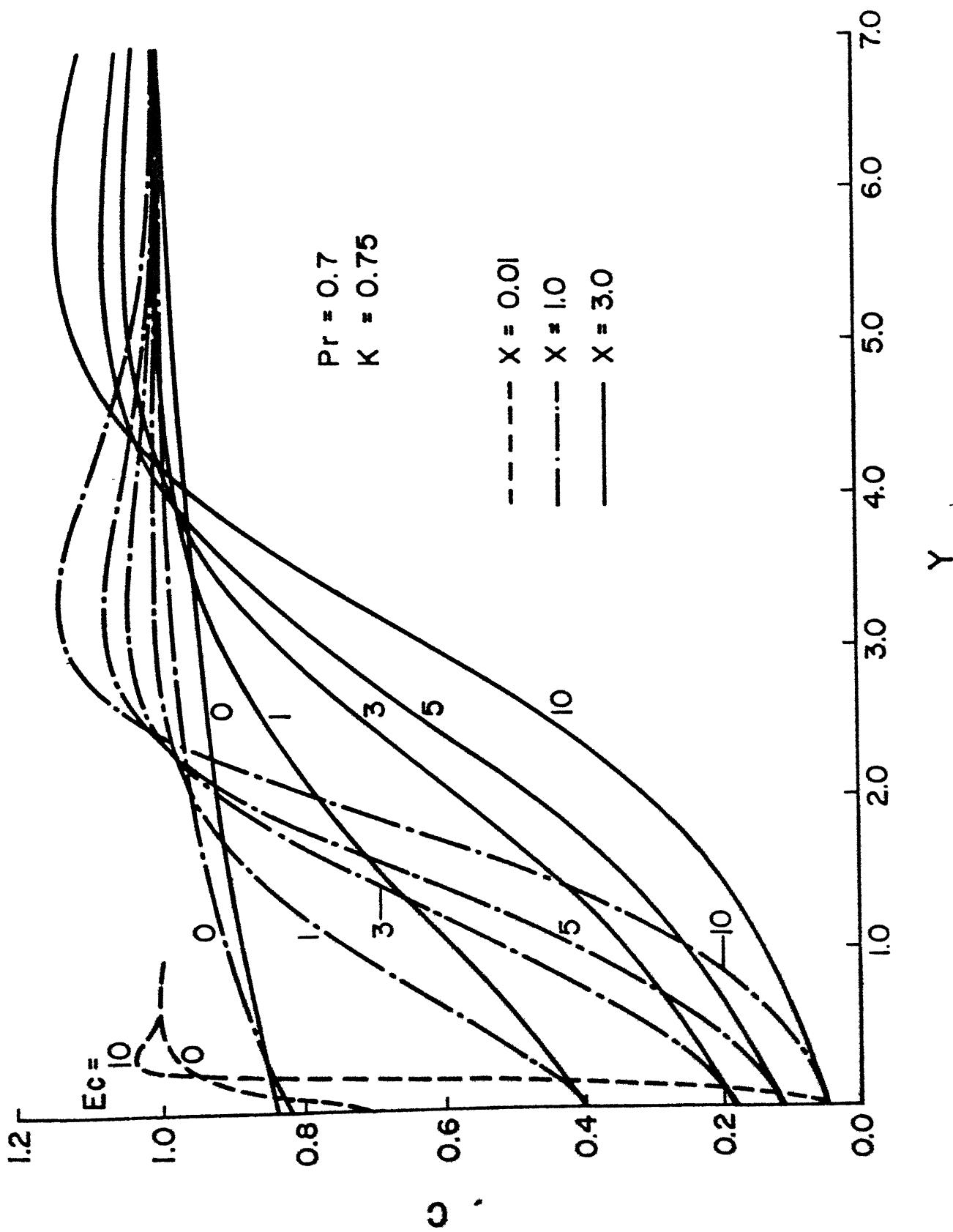
Fig. 4.63 Particle concentration profiles for flow past a cold plate at different rates of viscous dissipation ($\beta = 0$, $T_w = 0.8$)
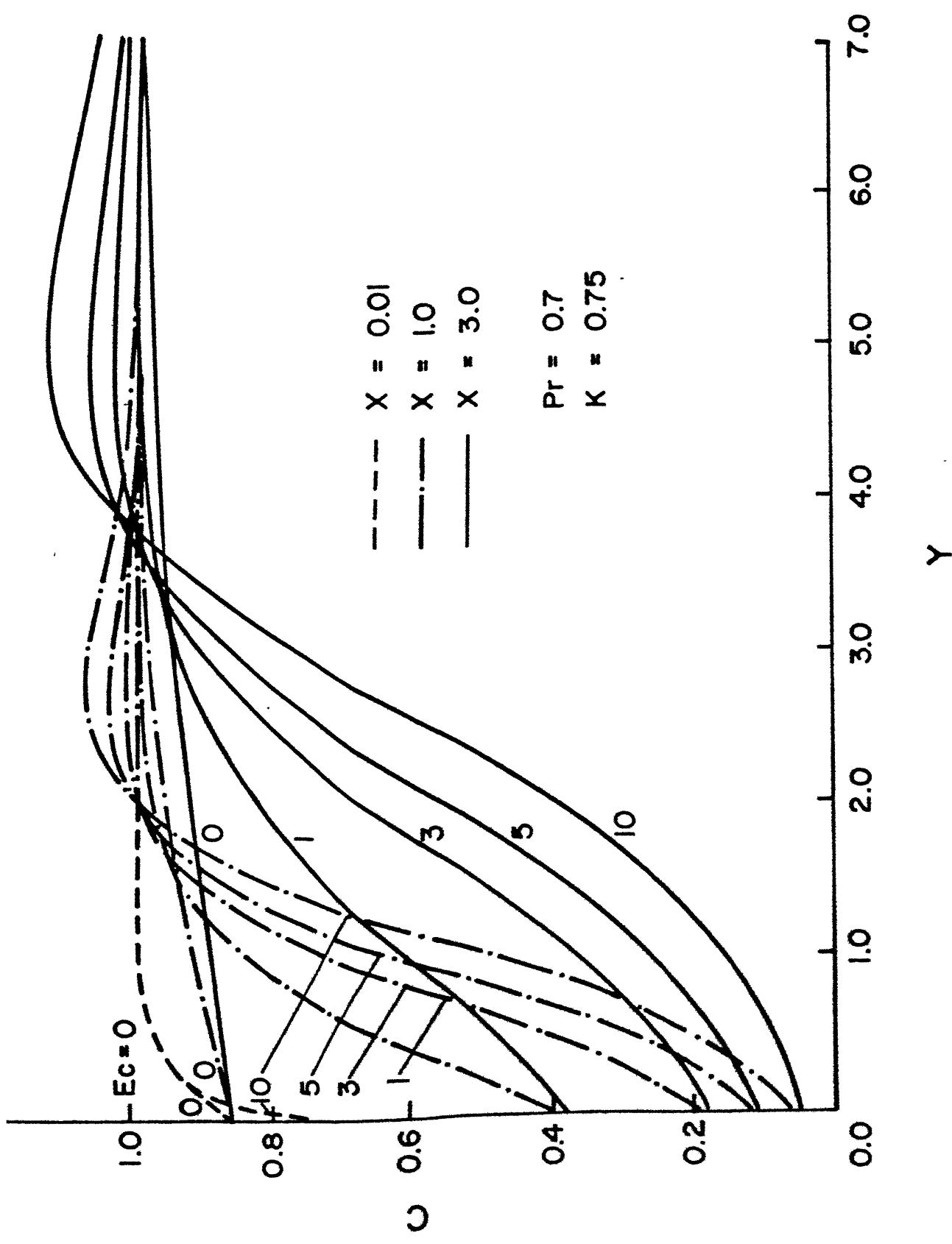
Fig. 4.64 Particle concentration profiles for flow past a cold plate at different rates of viscous dissipation ($\beta = 15°$, $T_w = 0.8$)
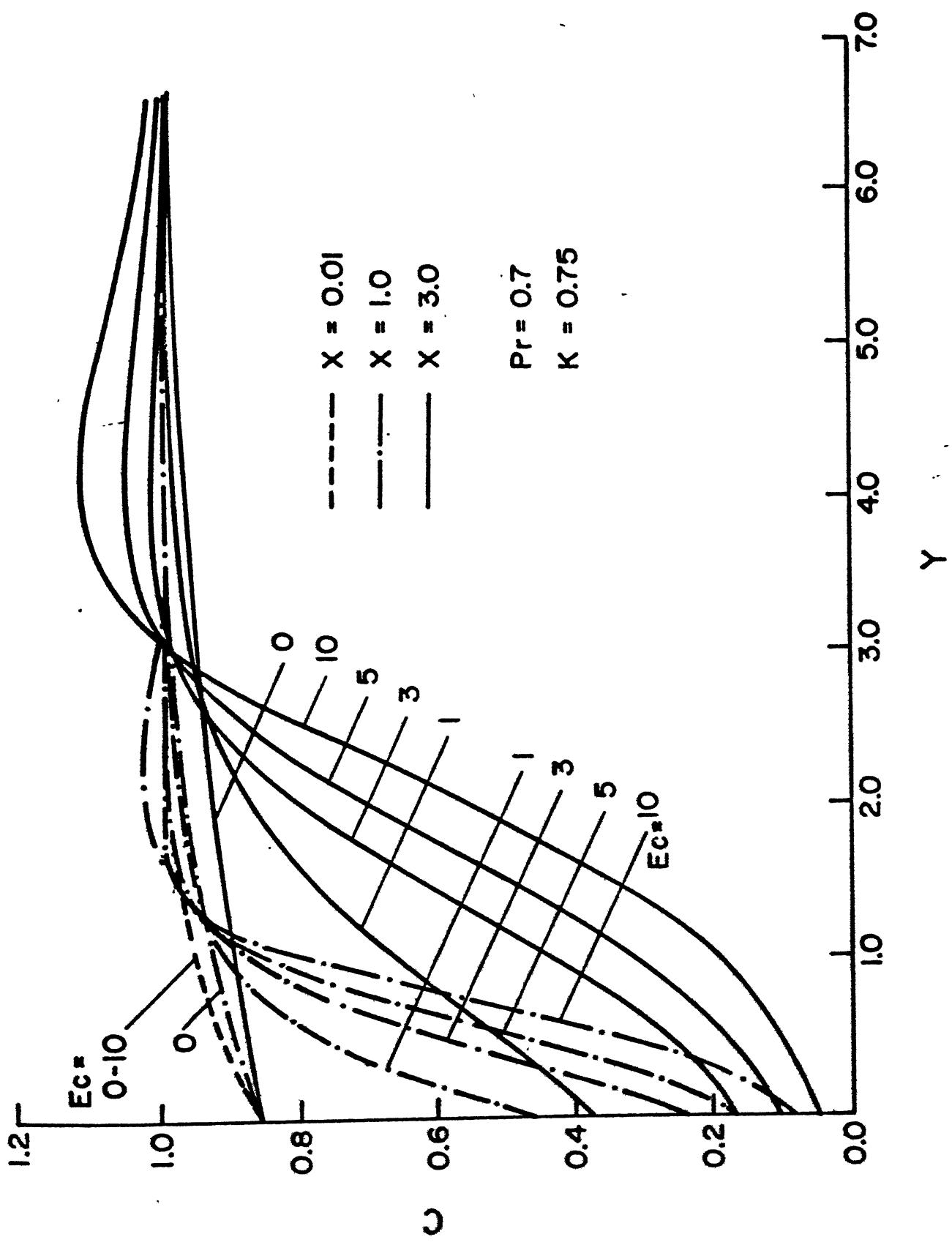
Fig 4.65 Particle concentration profiles for flow past a cold plate at different rates of viscous dissipation ($\beta=45°$, $T_f=0.8$)
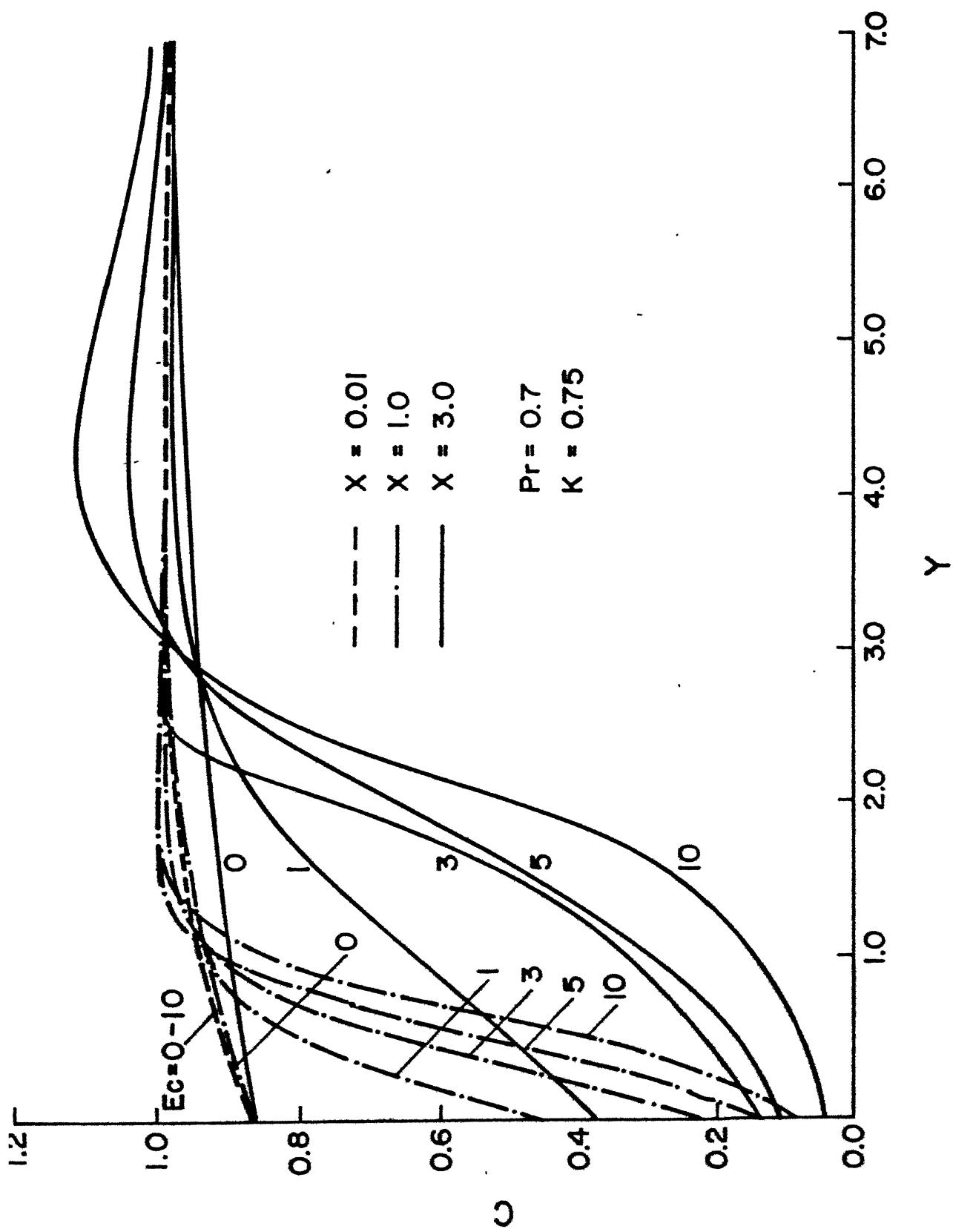
Fig. 4.66 Particle concentration profiles for flow past a cold plate at different rates of viscous dissipation($\beta = 90°, T_w = 0.8$)
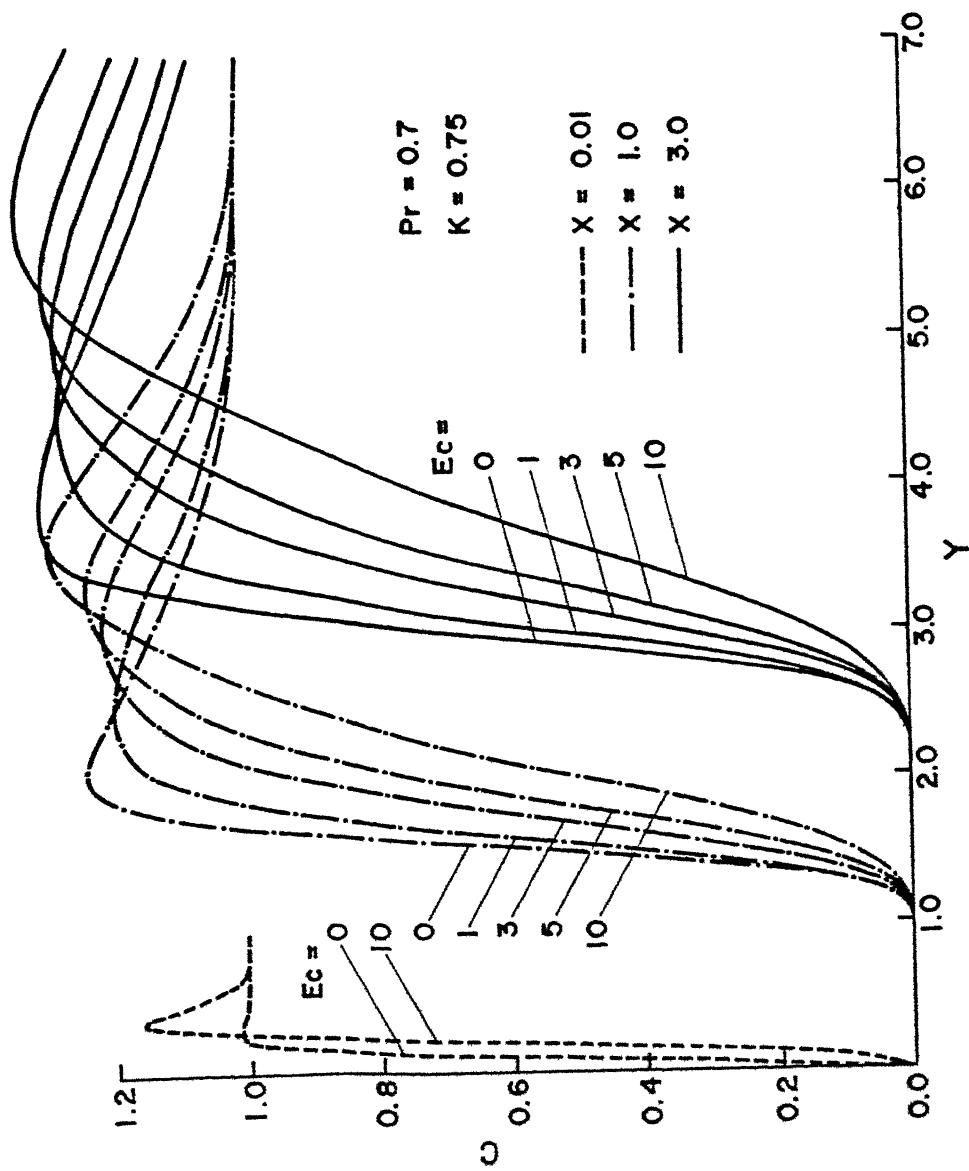
Fig. 4.67 Particle concentration profiles for flow past an adiabatic plate at different viscous dissipation rates ($\beta = 0$)
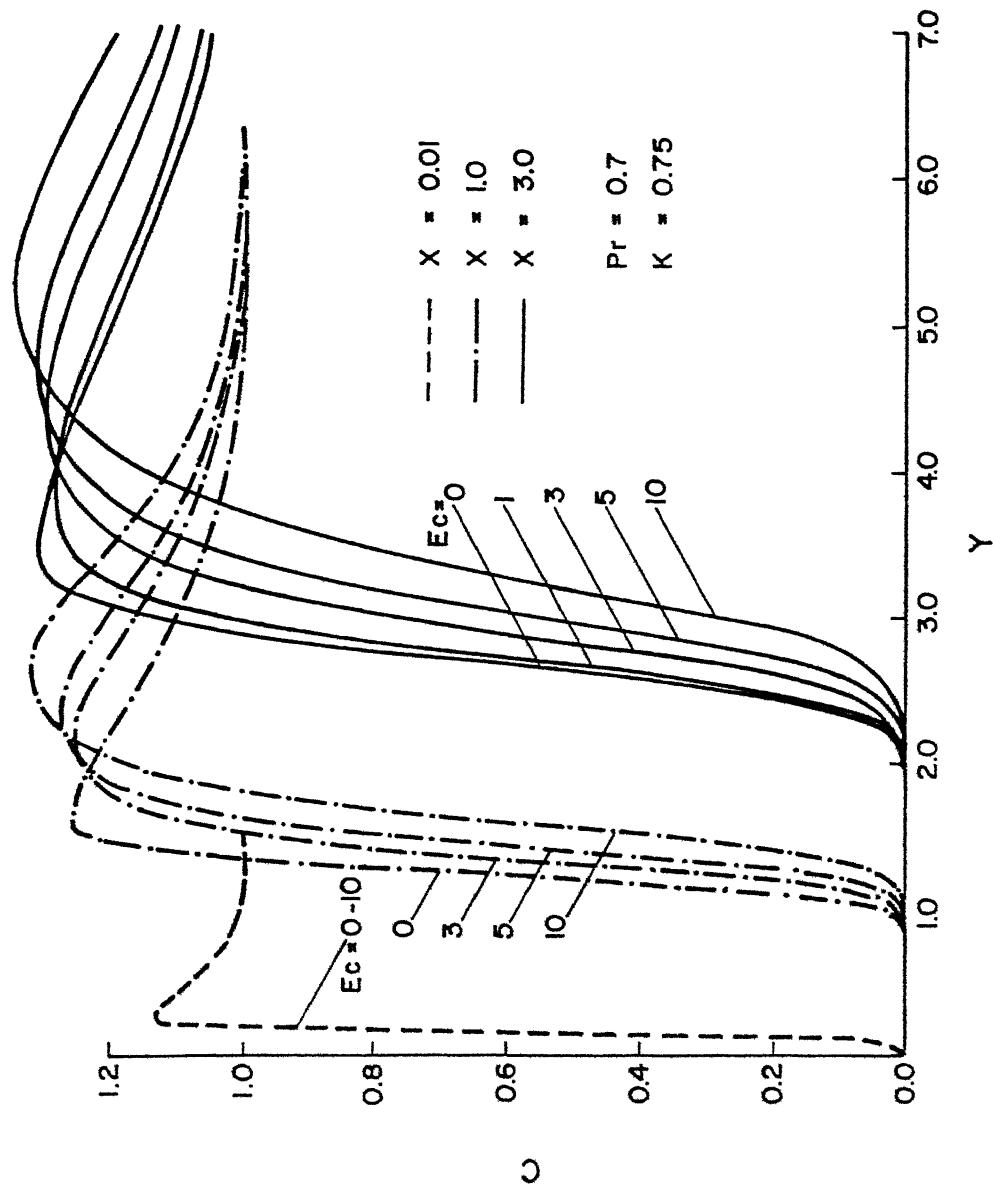
Fig. 4.68 Particle concentration profiles for flow past an adiabatic plate at different viscous dissipation rates (β = 15°)
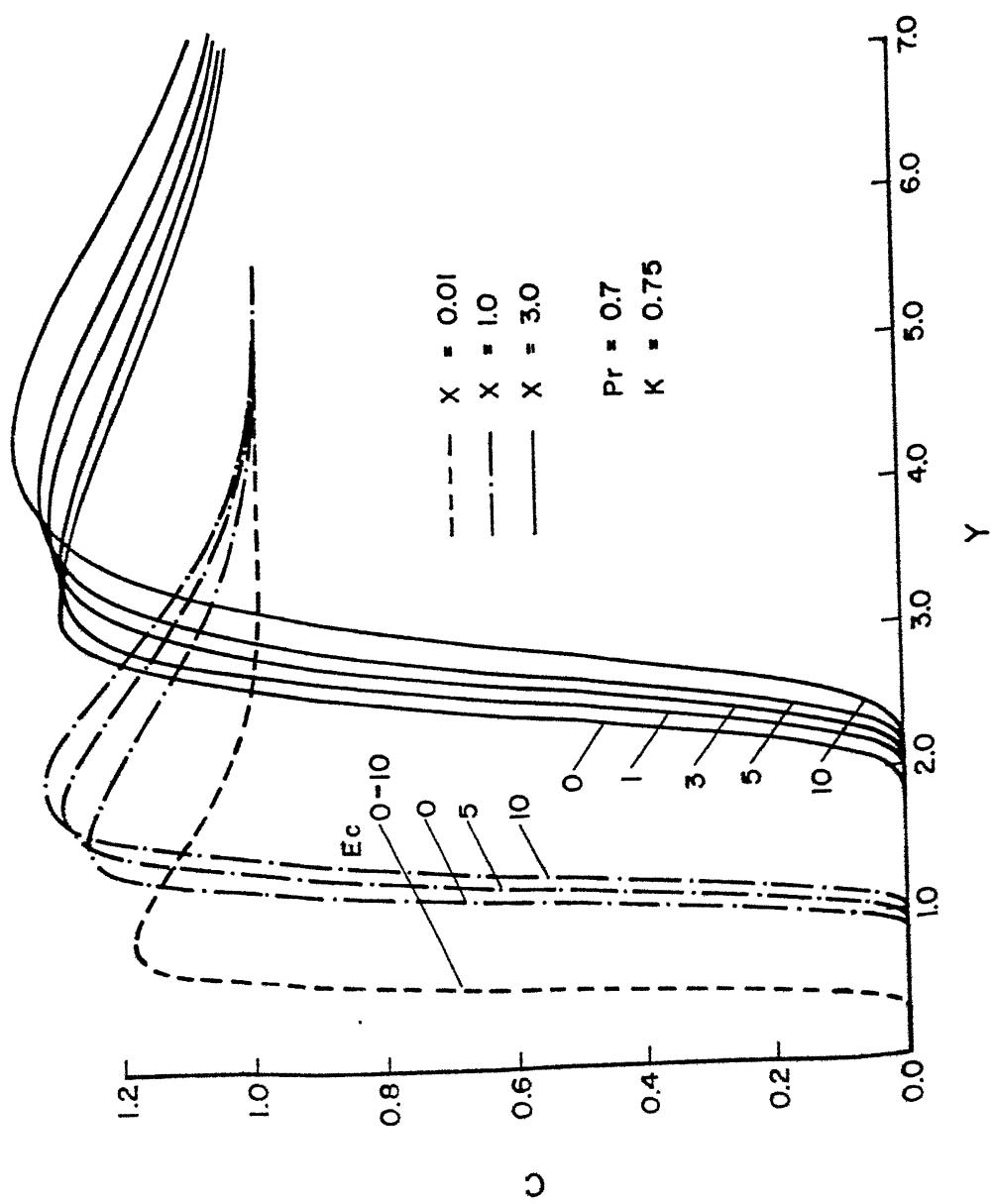
Fig.4.69 Particle concentration profiles for flow past an adiabatic plate at different viscous dissipation rates (β = 45°)
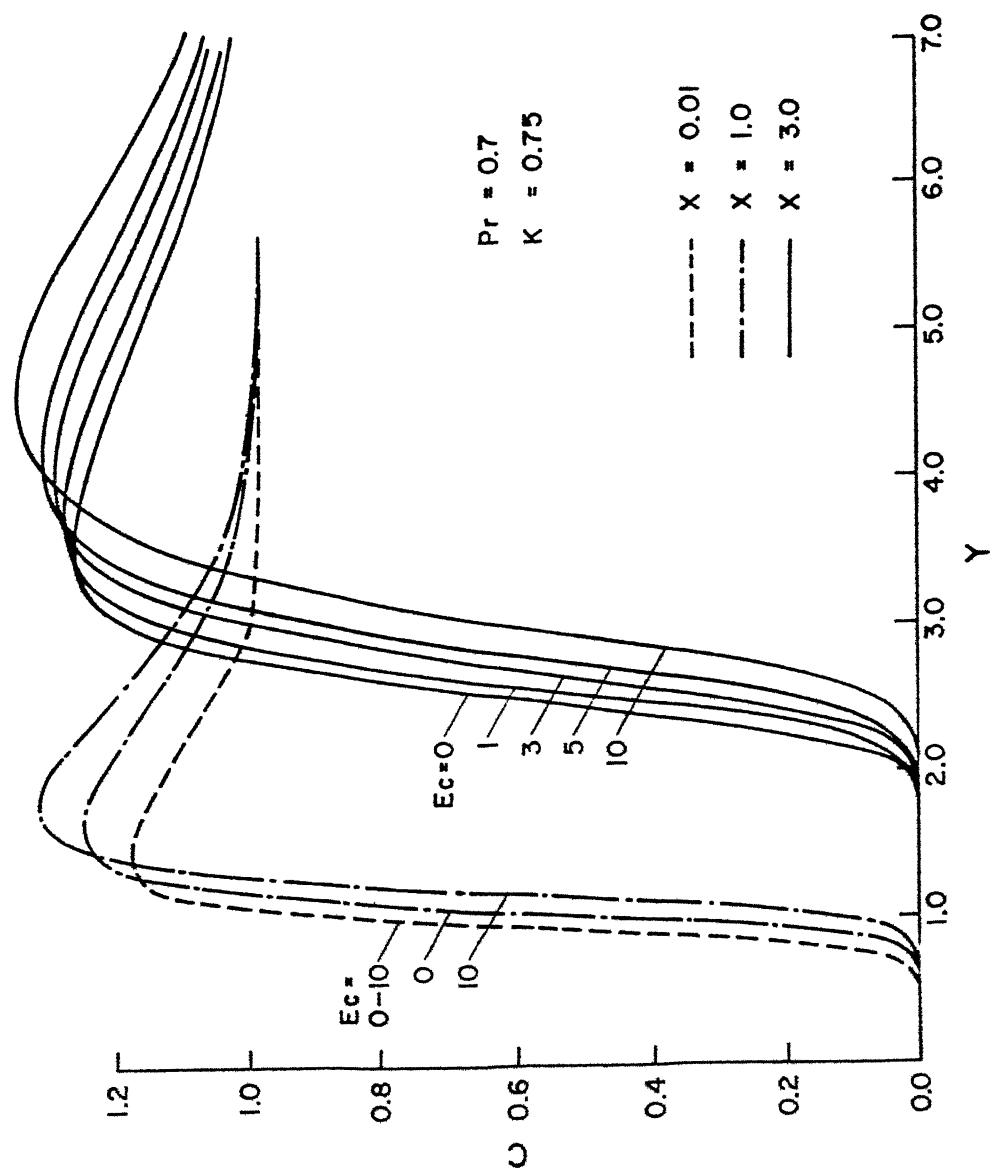
Fig. 4.70 Particle concentration profiles for flow past an adiabatic plate at different viscous dissipation rates (β= 90°)

CHAPTER 5

RESULTS FOR A CIRCULAR CYLINDER

The governing equations for thermophoresis over a
circular cylinder in cross flow and over an inclined
plate are identical. However, the evaluation of pre-
ssure gradient term in the momentum equation (2.28) is
different in the two cases. As described in Sec. 2.4.2
pressure gradient in the boundary layer over a circular
cylinder in cross flow is given by Eqn. (2.42) or Eqn.
(2.44). Thus the computer code developed and tested
for the inclined plate was used for the circular cylin-
der as well after replacing the subroutine for deter-
mining the pressure gradient. Several cases were run
in order to cover a wide range of parameter values for
the theoretical as well as the experimental pressure
distribution given by Eqns. (2.42) and (2.44) respecti-
vely. It was found that the boundary layer separates
over the cylinder at 105.5° and 81° respectively for the
theoretical and experimental pressure distributions.
This is in perfect agreement with the values reported in
literature (cf. White, 1974).

Results are presented here for the velocity, temperature and concentration boundary layers with cold, hot and adiabatic wall boundary conditions. These profiles are shown versus the non-dimensional distance Y in the boundary layers at different locations over the cylinder upto the separation point, starting from a location very close to the stagnation point. A comparison between the distributions obtained by theoretical and experimental pressure gradients is illustrated in each case. The Prandtl number is kept constant at 0.7. Also the effect of viscous dissipation on particle concentration profiles is presented for the cold as well as the adiabatic cylinder. For a hot cylinder, this effect is not shown since it is similar to that for the adiabatic cylinder.

5.1 Hydrodynamic and Thermal Boundary Layers

The hydrodynamic and thermal boundary layers over a circular cylinder have been investigated quite extensively by various authors (cf. Schlichting, 1979 and White, 1974). These boundary layer calculations can be carried out by several methods, such as the Blasius series, momentum and energy integral method, weighted residuals method, finite-difference method, etc. The results for velocity and

temperature boundary layers presented in this section are
therefore not new. They are included here for the sake of
completeness.

5.1.1 Longitudinal Velocity Profiles

The dimensionless longitudinal velocity (U/U_s) pro-
files at various locations (ϕ) on the cylinder are seen
plotted in Fig. 5.1. These are obtained for the theore-
tical pressure distribution. The velocity profiles for
$\phi > 90°$ possess a point of inflection and the point of
separation is reached at $\phi_{sep.} = 105.5°$. Velocity dis-
tributions obtained for the experimental pressure gradient
at three locations on the cylinder are presented in
Fig. 5.2, along with the corresponding profiles for theore-
tical pressure gradient at these locations. In this case
the separation occurs at $\phi_{sep.} = 81°$. Since the two
pressure gradients are widely different for $\phi \gtrsim 60°$, the
velocity profiles are also considerably different from
each other.

5.1.2 Transverse Velocity Profiles

The transverse velocity (V) profiles are shown in
Fig. 5.3 for the theoretical pressure distribution. Just

like the flow over an inclined plate (Sec. 4.1.2) the transverse velocity for flow over a cylinder is also negative over a substantial portion of the cylinder surface (upto $\phi \approx 70^{\circ}$). This is due to the presence of the stagnation point which makes the pressure distribution much different from that for the Blasius flow. A comparison of V-profiles for the theoretical and experimental pressure distributions is shown in Fig. 5.4 at the same three locations (ϕ) as for the U-velocity profile. The transverse velocity profiles for the two pressure distributions are also quite different for $\phi \gtrsim 60^{\circ}$.

5.1.3 Normalised Temperature Profiles

Figure 5.5 shows the normalised temperature distribution [$\theta = (T-1)/(T_w-1)$] obtained for the theoretical pressure gradient in the momentum equation and without viscous dissipation for $Pr = 0.7$. The thermal boundary layer behaviour in this case is quite similar to the hydrodynamic boundary layer behaviour. Just like the longitudinal velocity profiles, the temperature profiles also have a point of inflection for $\phi > 90^{\circ}$. Figure 5.6 shows the temperature distributions at $\phi = 1^{\circ}, 60^{\circ}$ and 81° for both the theoretical and experimental pressure distributions. Conclusions similar to those for U/U_s

profiles can be made for the temperature profiles as well.

The change in temperature profile due to increase in Ec (with constant wall temperature) is demonstrated in Fig. 5.7. A small value of Ec is not sufficient to cause a temperature maxima within the boundary layer but, eventually, as Ec is increased we observe the maxima in the temperature profile. Note that for $T_w < 1$, $\theta < 0$ implies $T > 1$. Thus the maxima in T corresponds to the minima in θ . This affects the thermophoretic deposition of particles as we will see later.

The normalised temperature profiles for flow past an adiabatic cylinder with different viscous dissipation rates are shown in Fig. 5.8. With the adiabatic wall condition the different rates of non-zero viscous dissipation have only a marginal effect on the temperature profiles at any location over the cylinder.

5.2 Concentration Boundary Layer

5.2.1 Particle Concentration Profiles

Since the transverse velocity around the stagnation point is negative for flow past a circular cylinder,

Eqn. (3.5) or Eqn. (3.7) is used for obtaining the concentration profiles depending upon the cold or hot wall condition respectively. The particle concentration profiles are presented in this section for both wall conditions and with theoretical and experimental pressure distributions in the boundary layer.

5.2.1.1 Cold Cylinder

In Figs. 5.9 and 5.10 non-dimensional particle concentration (C) profiles are given at various locations (ϕ) for flow past a circular cylinder with $K = 0.75$, $T_w = 0.25$, $Ec = 0$ and $Pr = 0.7$. Note that like the velocity and temperature profiles, the concentration profiles near the point of separation display a point of inflection. A non-zero wall concentration occurs in this case and its value is almost independent of the ϕ-location and the pressure distribution, just as for the cold inclined plate (cf. sec. 4.3.1). Though Eqns. (1.6) and (1.7) were proposed by Epstein et al. (1985) for natural convection flow from a vertical plate, they are found to hold for flow past a circular cylinder as well. Table 5.1 gives a token comparison of C_w values obtained presently by solving particle concentration equation (2.31) with those obtained using Eqns. (1.6) and (1.7).

Table 5.1 Particle concentration at a cold cylinder surface obtained from
Eqns. (2.31), (1.6) and (1.7) for Pr = 0.7, Ec = 0, K = 0.75

ϕ (degrees)	T_w = 0.5			T_w = 0.75			T_w = 0.883		
	Eqn. (2.31)	Eqn. (1.6)	Eqn. (1.7)	Eqn. (2.31)	Eqn. (1.6)	Eqn. (1.7)	Eqn. (2.31)	Eqn. (1.6)	Eqn. (1.7)
0	0.5819	0.5821		0.8139	0.8146		0.9196	0.9247	
5	0.5827	0.5828		0.8143	0.8143		0.9200	0.9231	
20	0.5827	0.5827		0.8142	0.8145		0.9200	0.9231	
40	0.5825	0.5824	0.5875	0.8142	0.8145	0.8120	0.9199	0.9233	0.9164
60	0.5821	0.5821		0.8140	0.8142		0.9199	0.9226	
80	0.5812	0.5814		0.8137	0.8142		0.9198	0.9230	
90	0.5804	0.5806		0.8133	0.8139		0.9197	0.9225	
100	0.5785	0.5787		0.8126	0.8133		0.9194	0.9223	

Table 5.2 Local particle deposition flux over a cold
cylinder (Pr = 0.7, Ec = 0, K = 0.75)

ϕ (degrees)	$-(C\ V_T)_w$		
	T_w = 0.5	T_w = 0.75	T_w = 0.883
0	0.3304	0.1547	0.0697
5	0.3278	0.1534	0.0689
20	0.3221	0.1508	0.0677
40	0.3038	0.1421	0.0639
60	0.2728	0.1276	0.0574
80	0.2267	0.1061	0.0477
90	0.1960	0.0917	0.0412
100	0.1511	0.0707	0.0318

Notwithstanding the almost uniform particle concentration at the cylinder surface, the concentration gradient at the cylinder surface, and the local deposition flux, $-(CV_T)_w$, vary nearly parabolically as shown in Figs. 5.11 and 5.12, respectively, for the theoretical pressure distribution on the cylinder and for $Pr = 0.71$, $Ec = 0$, $K = 0.8$, and various values of T_w. Figure 5.11 also shows the variation of the local Nusselt number (based on the cylinder radius) with ϕ . Just as in the case of the inclined plate, the Nu curve is similar to the concentration gradient curve. The coupled variation of the temperature and concentration gradients at the cylinder surface causes the wall concentration to remain constant irrespective of the location and the boundary layer pressure distribution.

In accordance with the results of Homsy et al. (1981), and Alam and Mehrotra (1987), which are also shown in Fig. 5.12, the local deposition flux decreases monotonically from a maximum value at the stagnation point as one moves towards the point of separation ($\phi \simeq 104.5^\circ$ for the theoretical pressure distribution). Note that the deposition flux at any point on the cylinder decreases as T_w rises to unity. For $T_w = 1$, of course, the deposition flux is zero everywhere on the cylinder. It may be pointed out that the local deposition flux obtained by Homsy et al. as well as by Alam and Mehrotra has to be multiplied by a factor of $\sqrt{2}$ before comparison with our results is possible. This is due to our Re being only half of theirs. While our

value of the deposition flux matches exactly with that of

Homsy et al. for T_w = 0.5 at the stagnation point, the diff-

erence between the two results increases as one moves away

from the stagnation point. This is expected, however, since

the results of Homsy et al. involve an increasing error at lar-

ger values of ϕ due to the increasing inaccuracy of the tru-

ncated Blasius series used by them for solution. In fact,

Homsy et al. report physically impossible negative values at

large enough values of ϕ due to the use of truncated Blasius

series. The comparison in Fig. 5.12 shows an error of only

1.66 % at ϕ = 20° but an error of 72.6 % at ϕ = 90° for

the results of Homsy et al. Comparison with the results

of Alam and Mehrotra is really meaningless since they do not

provide the values of various parameters used for their

results. The best that could be ascertained (Alam, 1987) is

that most probably their results hold for Pr = 0.7, Ec = 0

and K = 0.8. However, T_w is still unknown for their

results. Their result is shown in Fig. 5.12 only for the

sake of completeness. Table 5.2 gives the presently com-

puted values for the local deposition flux at different

locations for Pr = 0.7, Ec = 0, K = 0.8 and T_w = 0.5,

0.75 and 0.883.

It is interesting to note that for conditions pertaining to Figs. 5.9 and 5.10 (T_w = 0.25, K = 0.75, Pr = 0.7 and Ec = 0) the wall concentration obtained is $\simeq$ 0.32 which is almost the same as that for flow over an inclined plate under identical conditions (see Fig. 4.32). Thus thermophoresis yields an almost uniform concentration of aerosol particles over any two-dimensional surface under laminar flow conditions. It is also found that the concentration at the wall increases almost linearly with the wall temperature (T_w < 1) as shown in Fig. 5.13. The particle concentration profiles near the stagnation point and just before separation (with theoretical dP/dX) at different wall temperature values are presented in Fig. 5.14. The point of inflection in the concentration profile at $\phi_{sep.}$ = 105.5^o is observed only when T_w is small.

5.2.1.2 Heated Cylinder

For a heated cylinder (T_w > 1) results obtained with

Pr = 0.7, Ec = 0, K = 0.75 and T_w = 2.0 are illustrated in Figs. 5.15 and 5.16 (Pr.K < 1). The presence of a critical layer adjacent to the cylinder surface together with concentration just outside this layer exceeding that in the free stream is demonstrated in these figures. The critical layer thickness increases with ϕ as shown in Fig. 5.17 for the theoretical pressure distribution, and for T_w = 2.0, 1.25 and 1.1. However, the maximum particle concentration attained adjacent to the critical layer remains more or less constant irrespective of the location and the pressure distribution (theoretical or experimental). Computations with other wall temperatures also yield similar results except that the critical layer thickness and the maximum concentration attained just outside it are different in each case (both increasing with wall temperature).

5.2.2 Viscous Dissipation Effect

Computations were also made for flow past a circular cylinder with non-zero Eckert numbers in the range 1 to 10, thereby taking into account the different rates of viscous dissipation in the energy equation (2.29). Both cold wall and adiabatic wall boundary conditions are considered along with theoretical as well as experimental pressure distribution

in the boundary layer over the cylinder. The resulting concentration profiles are presented in Figs. 5.18 to 5.21.

5.2.2.1 Cold Cylinder

Figure 5.18 illustrates the influence of viscous dissipation rate on the particle concentration profiles for flow past a cold cylinder with $Pr = 0.7$, $K = 0.75$ and $T_w = 0.5$. The main features of Fig. 5.18 are :

(i)   No effect of Ec on the concentration profile at a location close to the stagnation point, and

(ii) Away from the stagnation point ($\phi = 60^o$) a sudden drop in the wall concentration as Ec is raised from 0 to 1.

This drop becomes gradual as Ec is raised further. Particularly striking is the zero concentration obtained on the cylinder wall at $\phi = 60^o$ for Ec = 10. A maximum non-dimensional concentration of about 1.2 is noted in this profile around Y = 1.3 even though at infinity (Y $\gtrsim$ 3 for practical purposes) the concentration drops to unity. This implies that at larger rates of viscous dissipation the rapid heating makes the profiles to behave similar to those for flow past a heated cylinder (Sec. 5.2.1.2). Temperature within the boundary layer increases enormously

especially at large Ec values (see Fig. 5.7). Thus at large Ec the particles are blown away from the surface because of positive value of V_T. Consequently, a drastic reduction in particle concentration is noted near the wall along with a corresponding increase to values greater than unity at the end of this lean layer. The experimental pressure distribution in the hydrodynamic boundary layer gives a marginal increase in the wall concentration at non-zero Eckert numbers (Fig. 5.19). Consequently, the peak concentration achieved in this case is smaller in comparison to that obtained with theoretical pressure distribution.

5.2.2.2 Adiabatic Cylinder

Results for the flow past an adabatic circular cylinder are presented in Figs. 5.20 and 5.21 for different rates of viscous dissipation, the two pressure distributions, and for Pr = 0.7 and K = 0.75. The peak value of the particle concentration achieved in this case is even more than 1.4 for Ec = 10. The general nature of the profiles is similar to that for flow past a heated cylinder presented in Sec. 5.2.1.2, except near the wall where $V_T = 0$ since $\partial T/\partial Y\big|_{Y=0} = 0$. A marginal increase in the critical

layer thickness and a slight decrease in the peak concentration are the main features of the particle concentration profiles obtained with experimental pressure distribution (Fig. 5.21). The marginal changes in the concentration profiles with respect to Eckert number obviously follow from the marginal differences in the temperature distributions at non-zero Ec values (see Fig. 5.8).
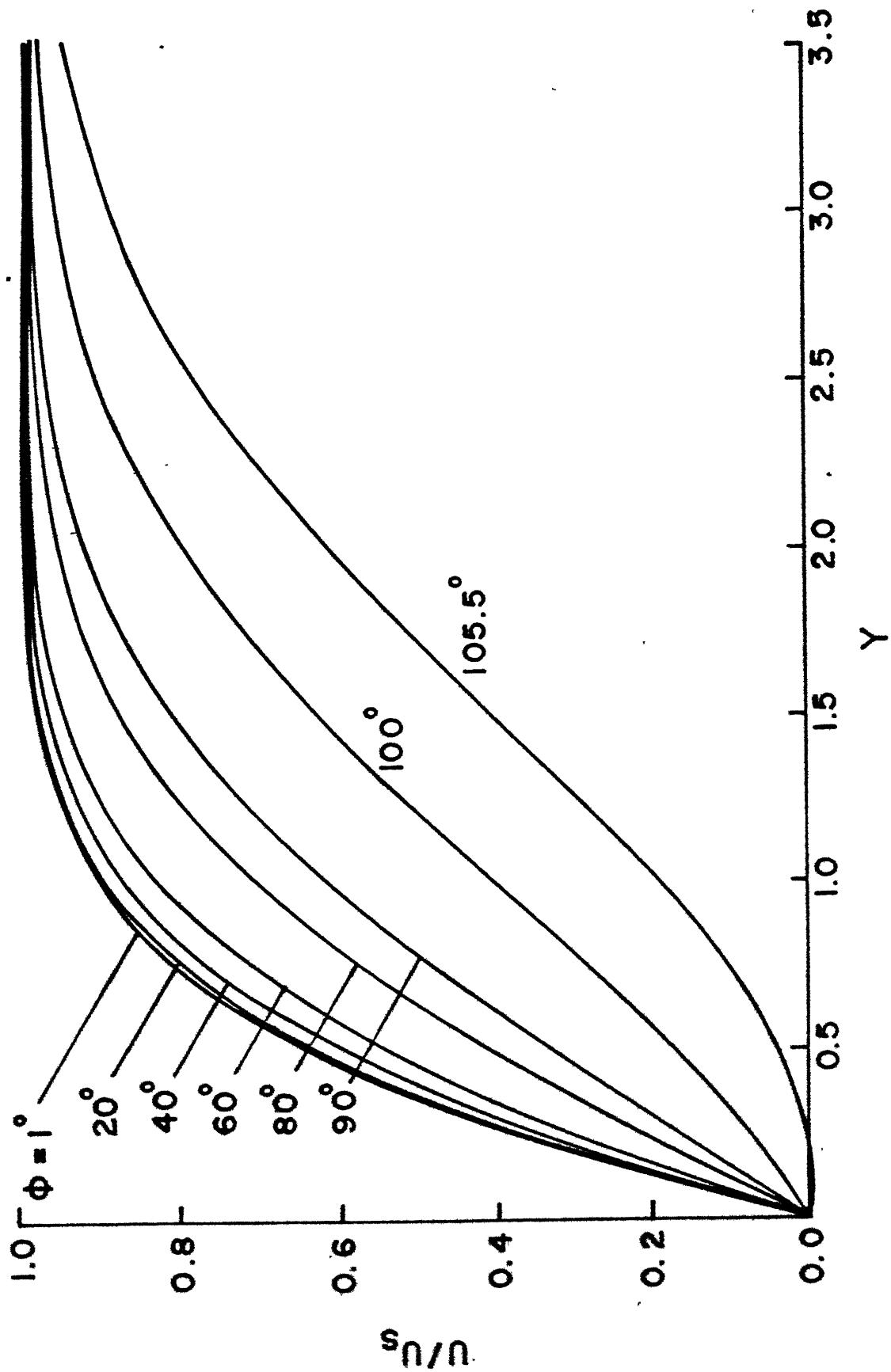
Fig. 5·1 Longitudinal velocity distribution in the boundary layer on a cylinder at different locations (Theoretical pressure distribution)
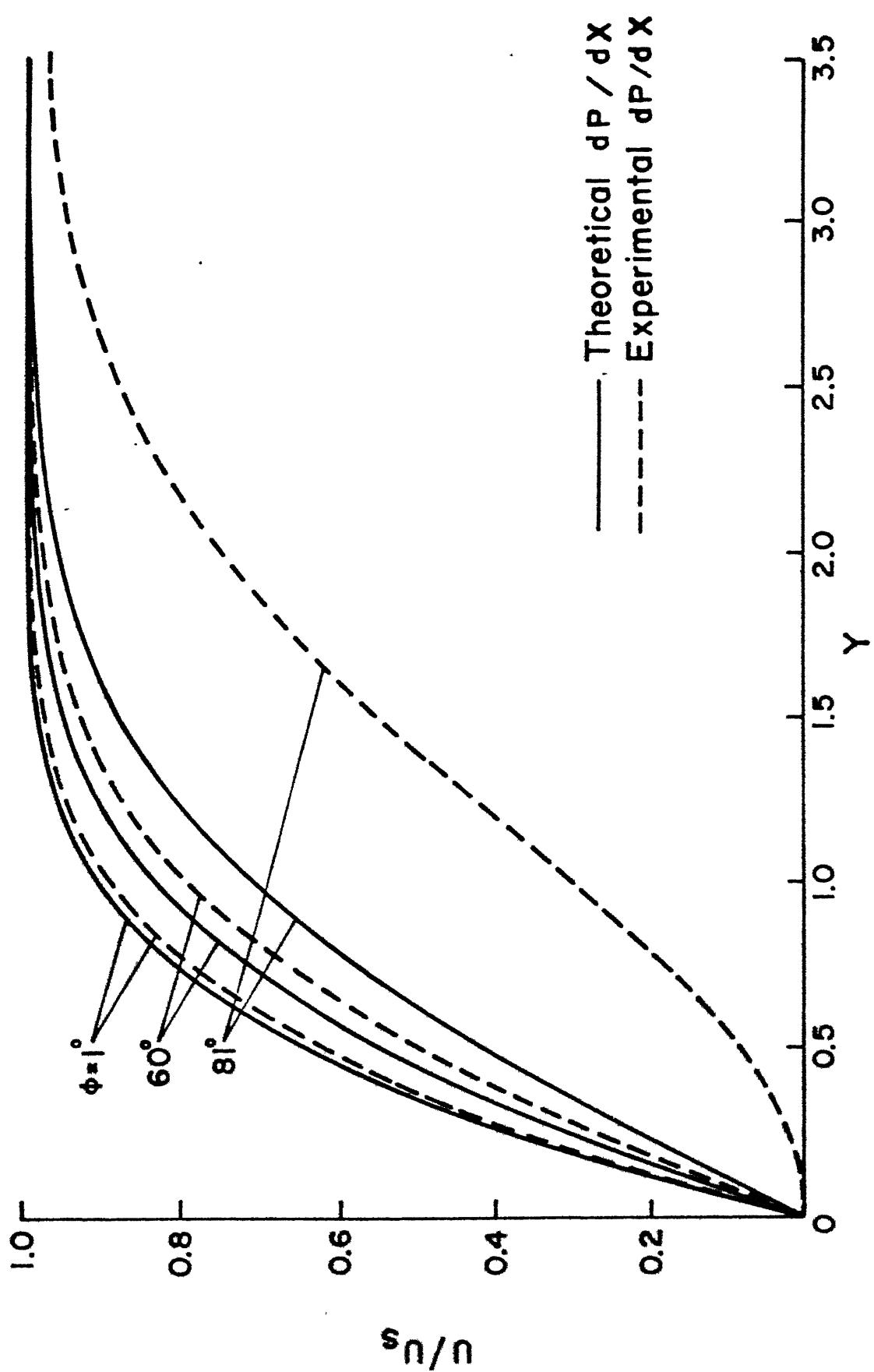
Fig.5.2 Effect of pressure distribution on the longitudinal velocity distribution for flow past a cylinder
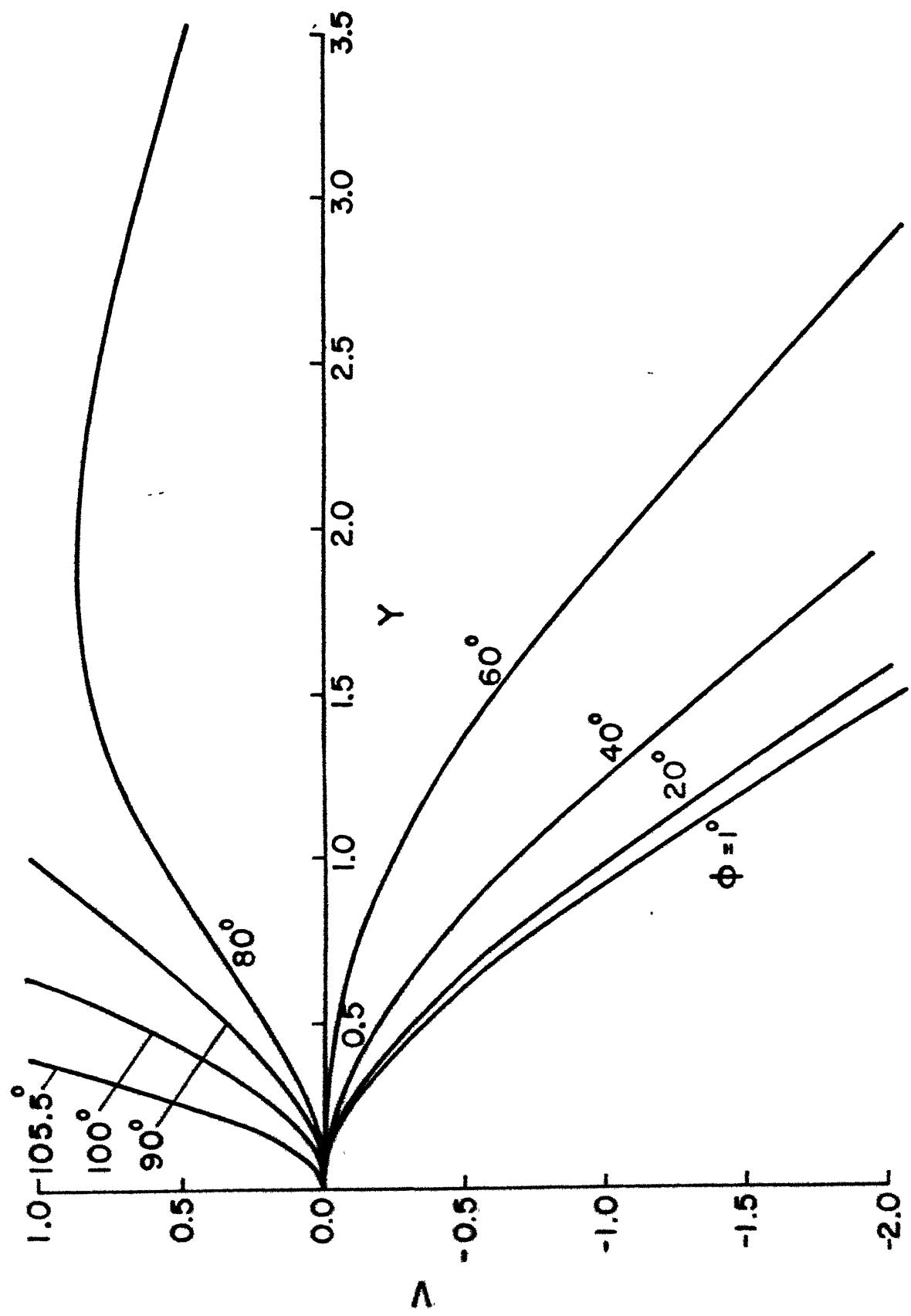
Fig. 5·3 Transverse velocity distribution in the boundary layer on a cylinder at different locations (Theoretical pressure distribution)
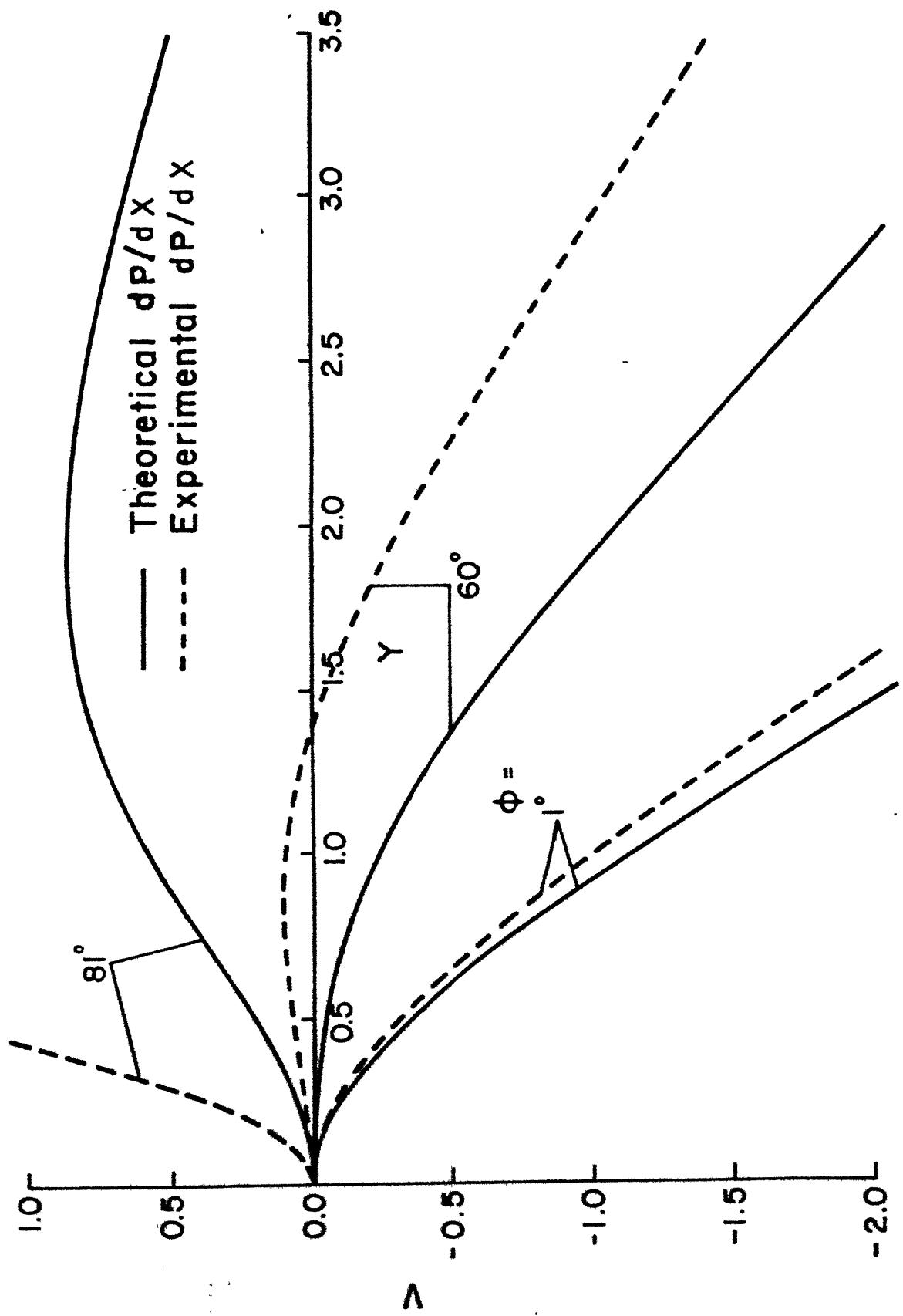
Fig.5.4 Effect of pressure distribution on the transverse velocity distribution for flow past a cylinder
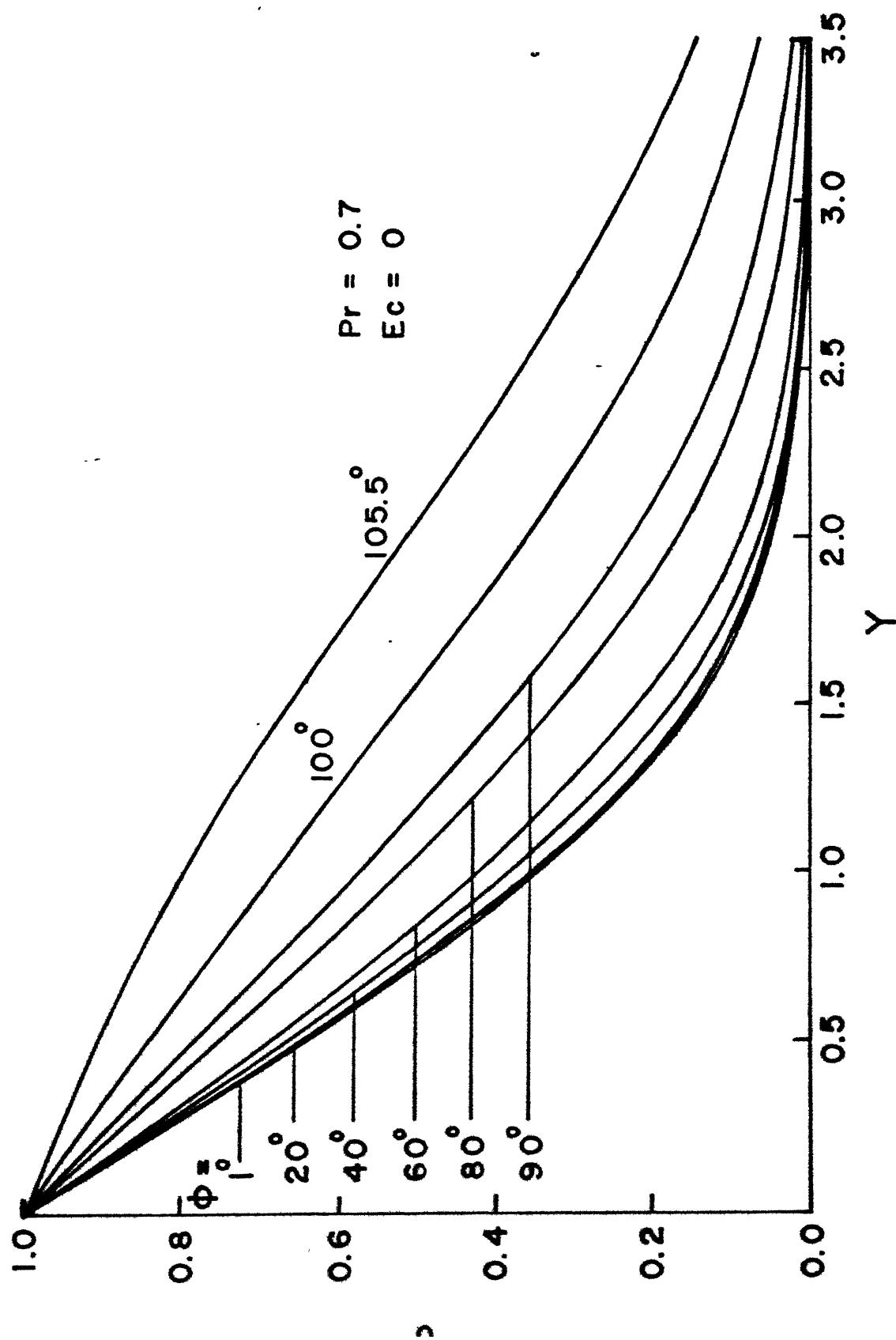
Fig. 5·5 Normalised temperature distribution in the boundary layer on a cylinder at different locations (Theoretical pressure distribution)
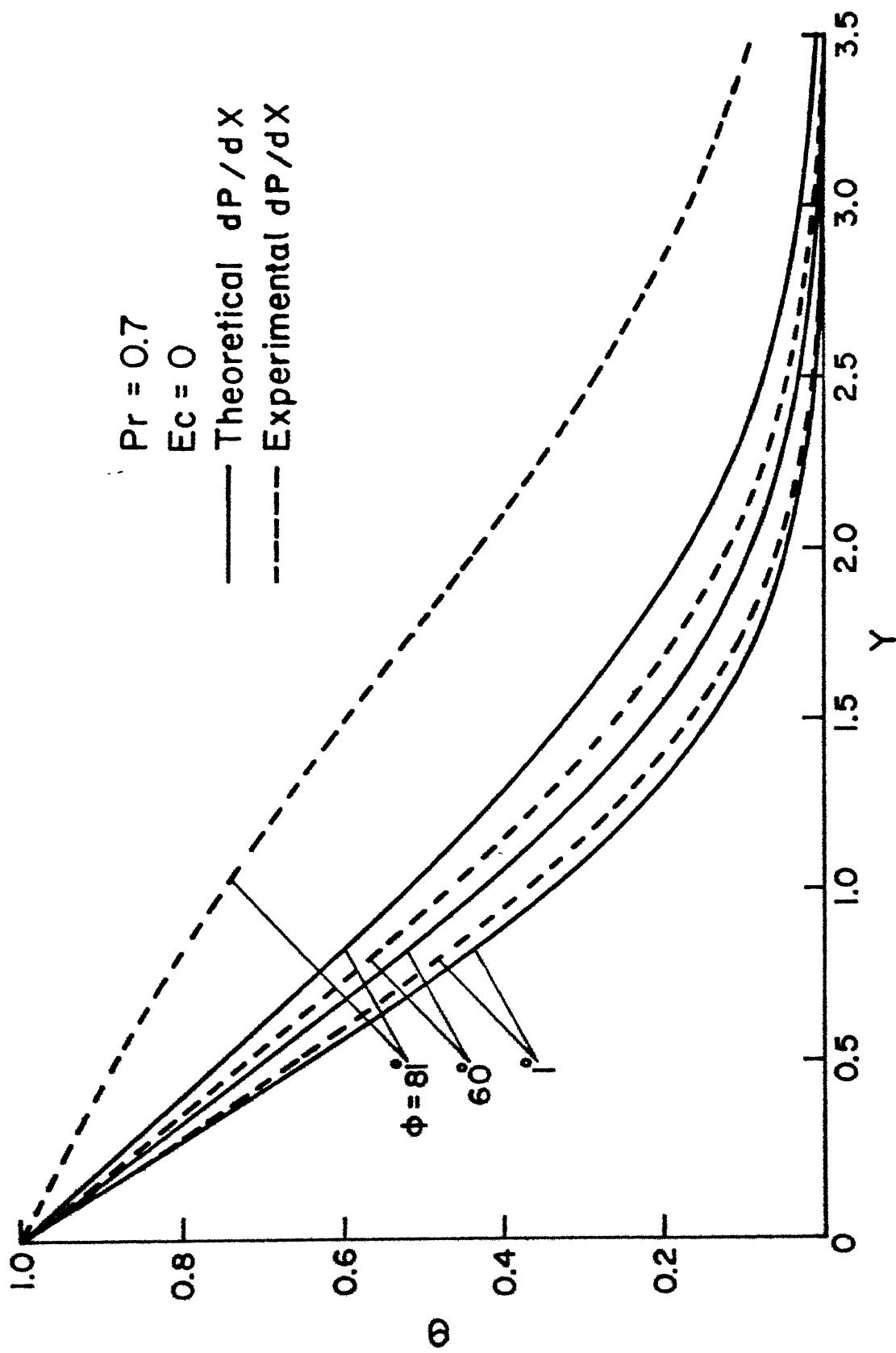
Fig.5.6 Effect of pressure distribution on the normalised temperature distribution for flow past a cylinder
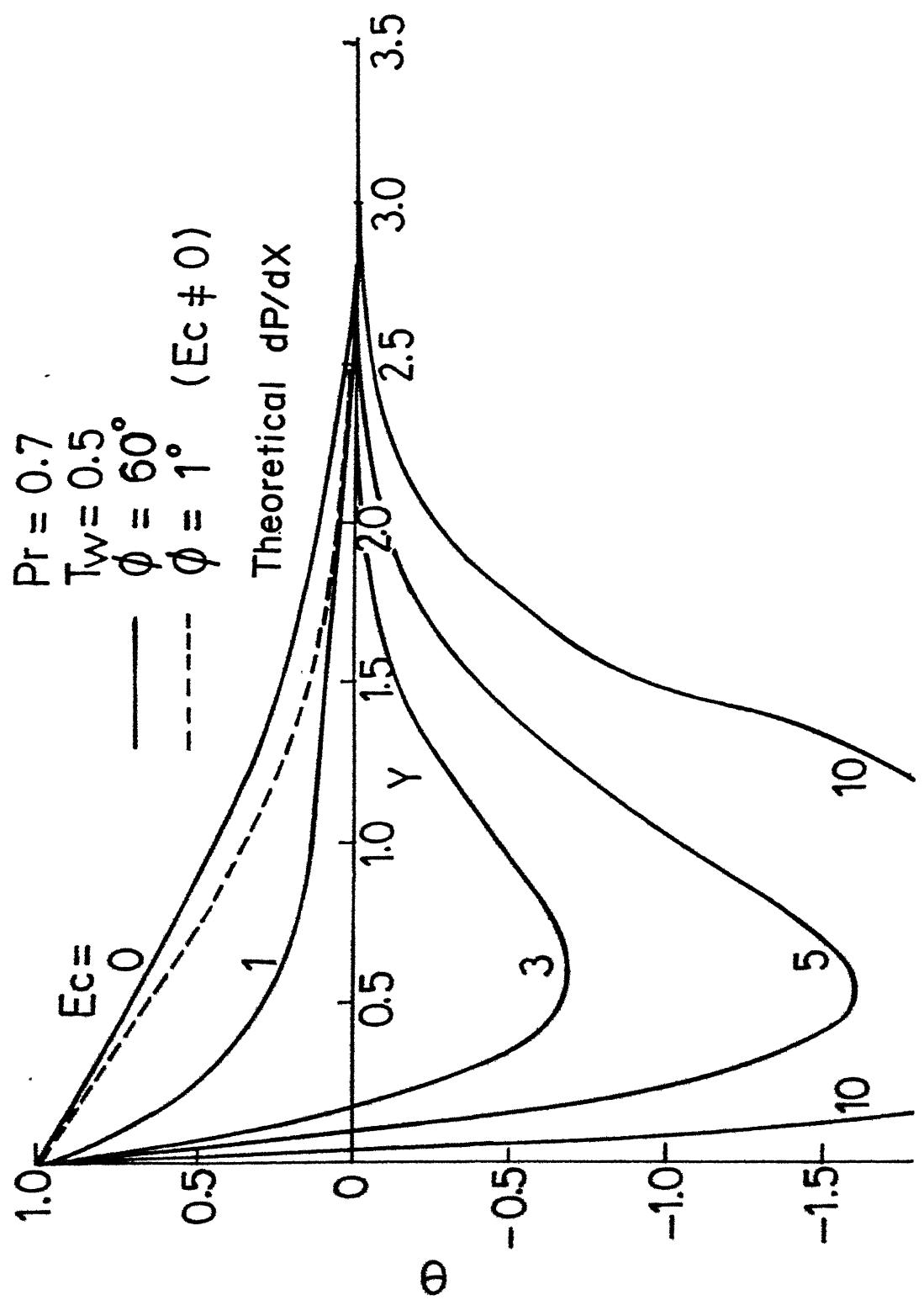
Fig. 5.7 Effect of viscous dissipation on the normalised temperature profiles for flow past a cold cylinder
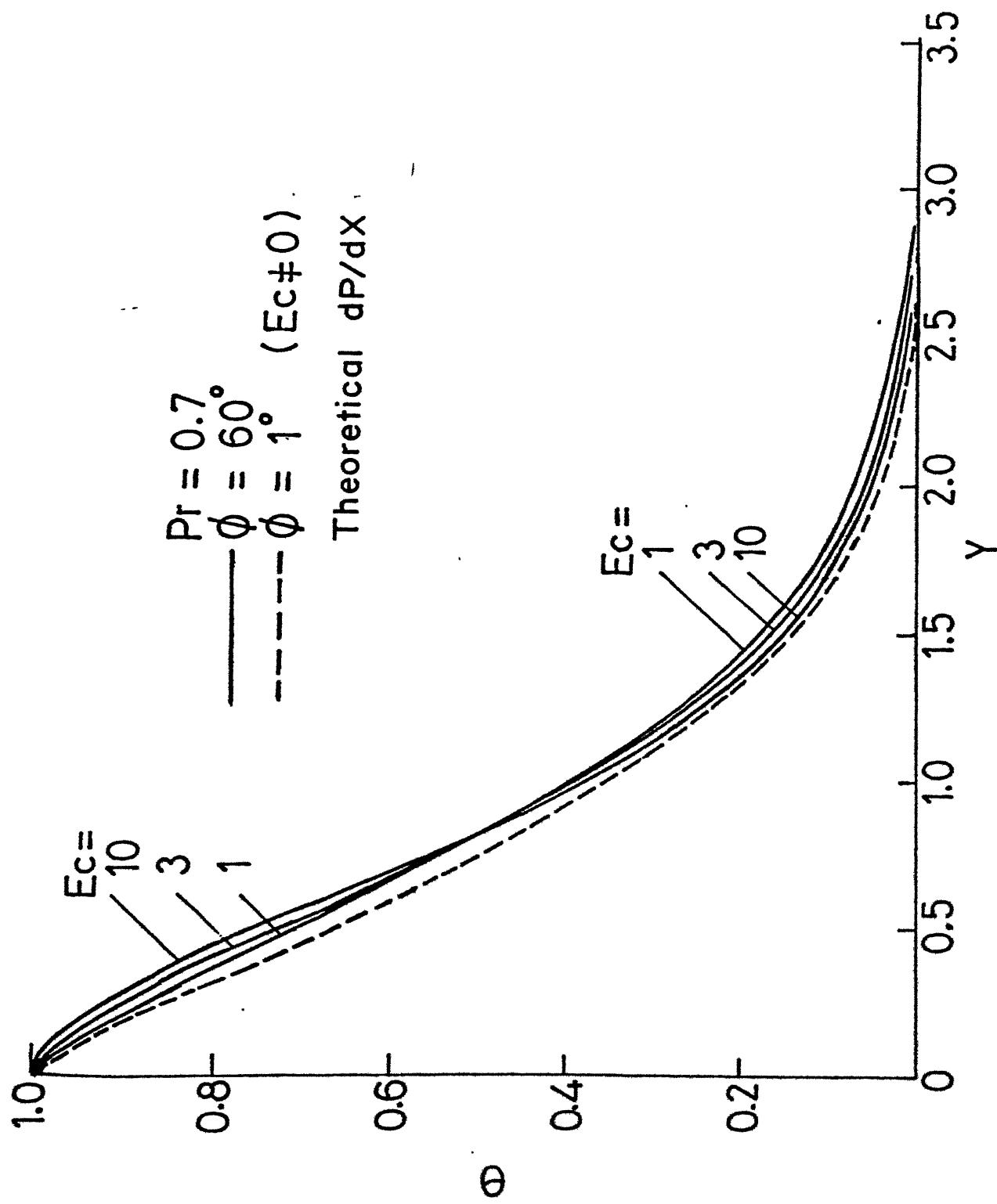
Fig. 5.8 · Normalised temperature profiles for flow past an adiabatic cylinder with different viscous dissipation rates
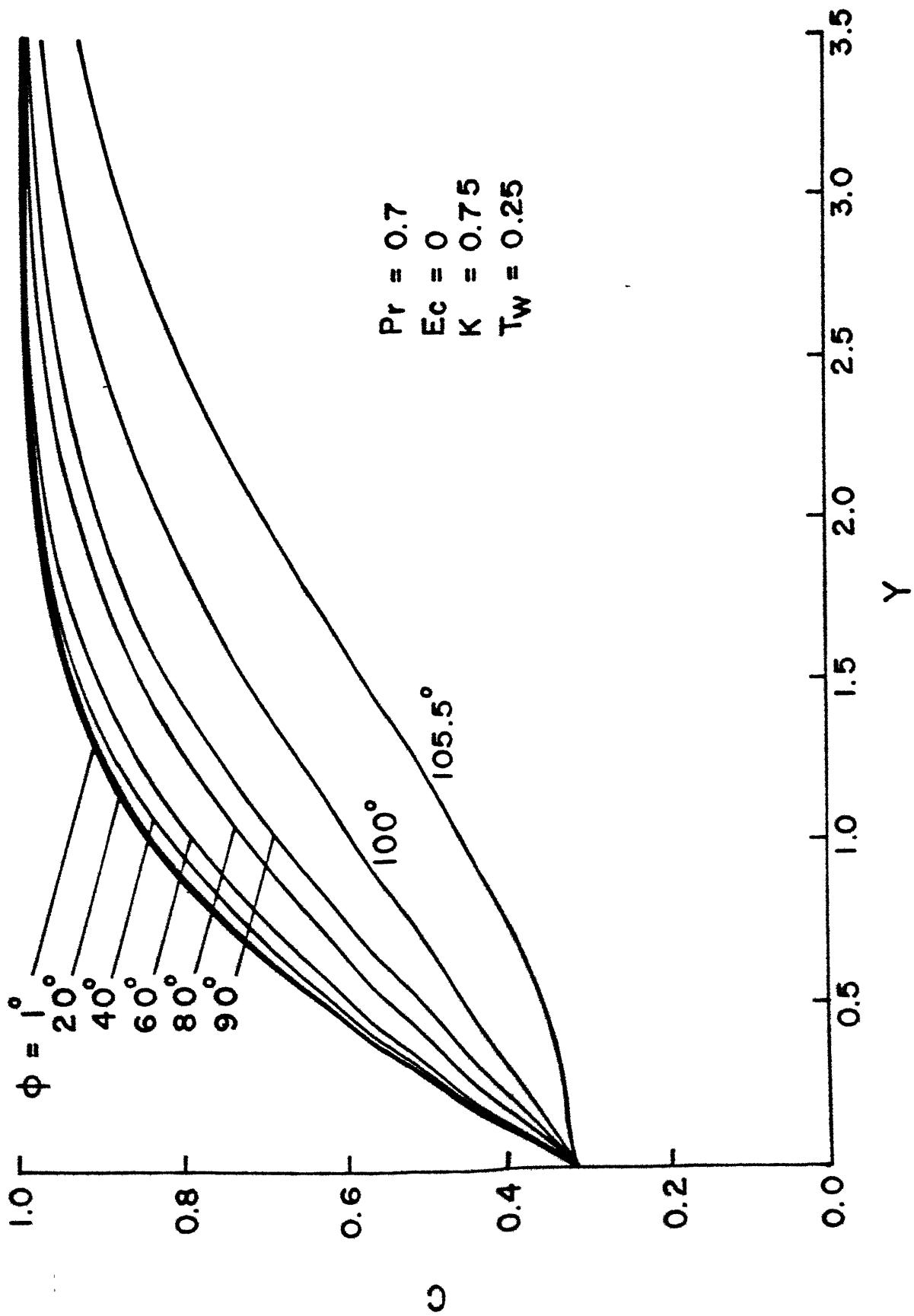
Particle concentration profiles over a cold cylinder at
different locations (Theoretical pressure distribution)

5.9
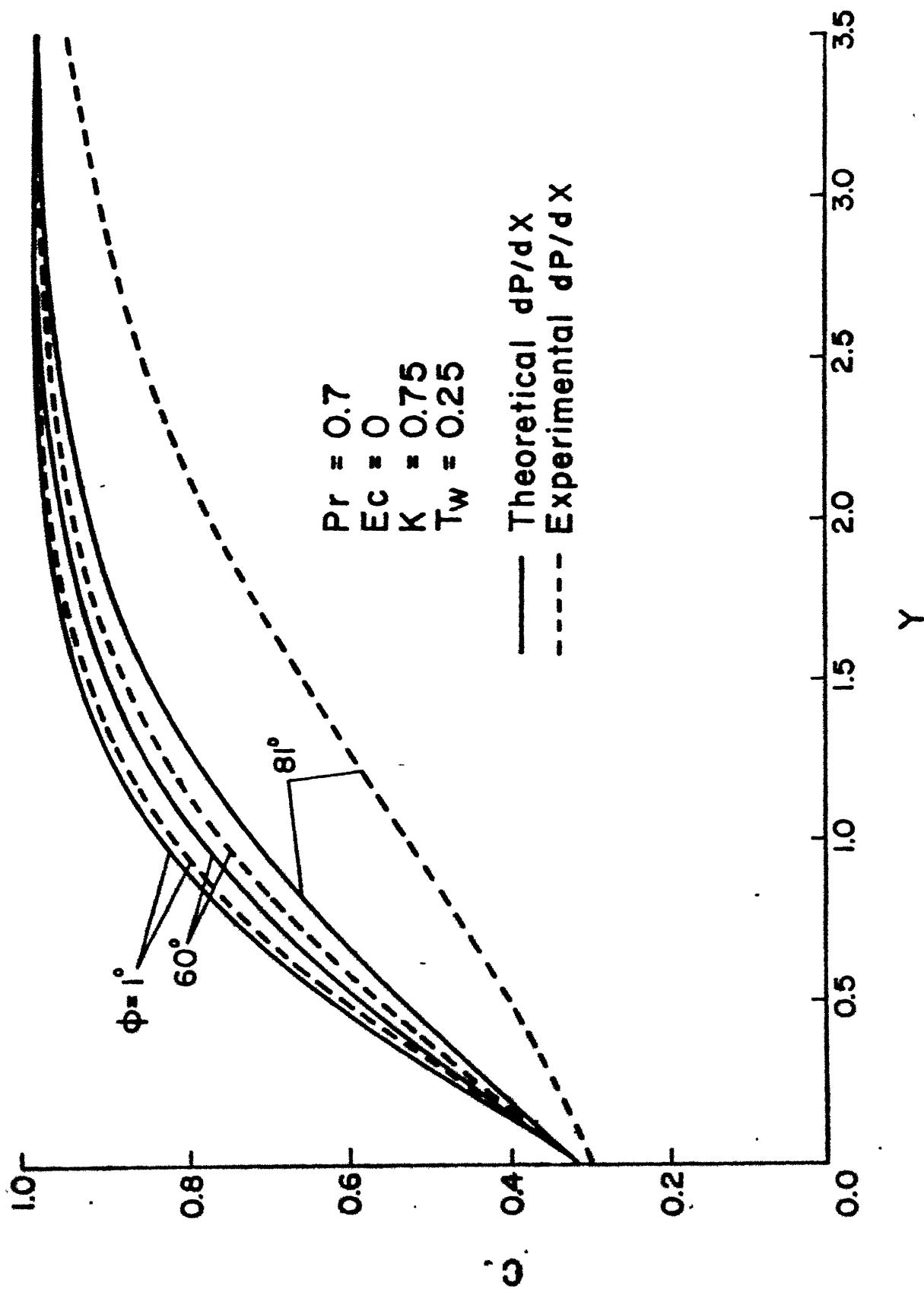
Fig.5.10 Effect of pressure distribution on the particle concentration profiles for flow past a cold cylinder

Pr = 0.7
Ec = 0
K = 0.75
Tw = 0.25

—— Theoretical dP/dX
----- Experimental dP/dX

$\phi = 1°$
$60°$
$81°$
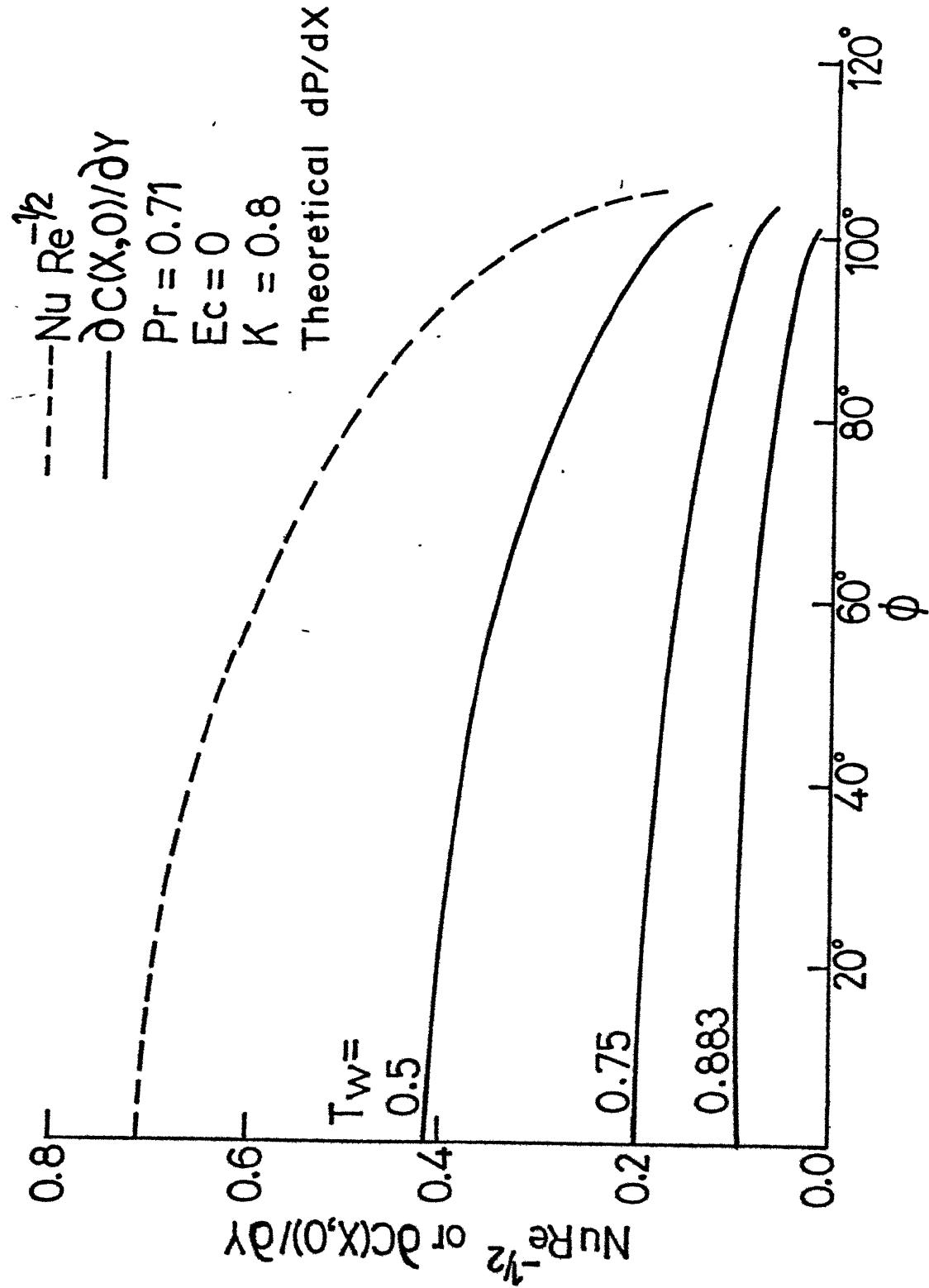
Fig. 5.11 Local Nusselt number and concentration gradient at a cold cylinder surface
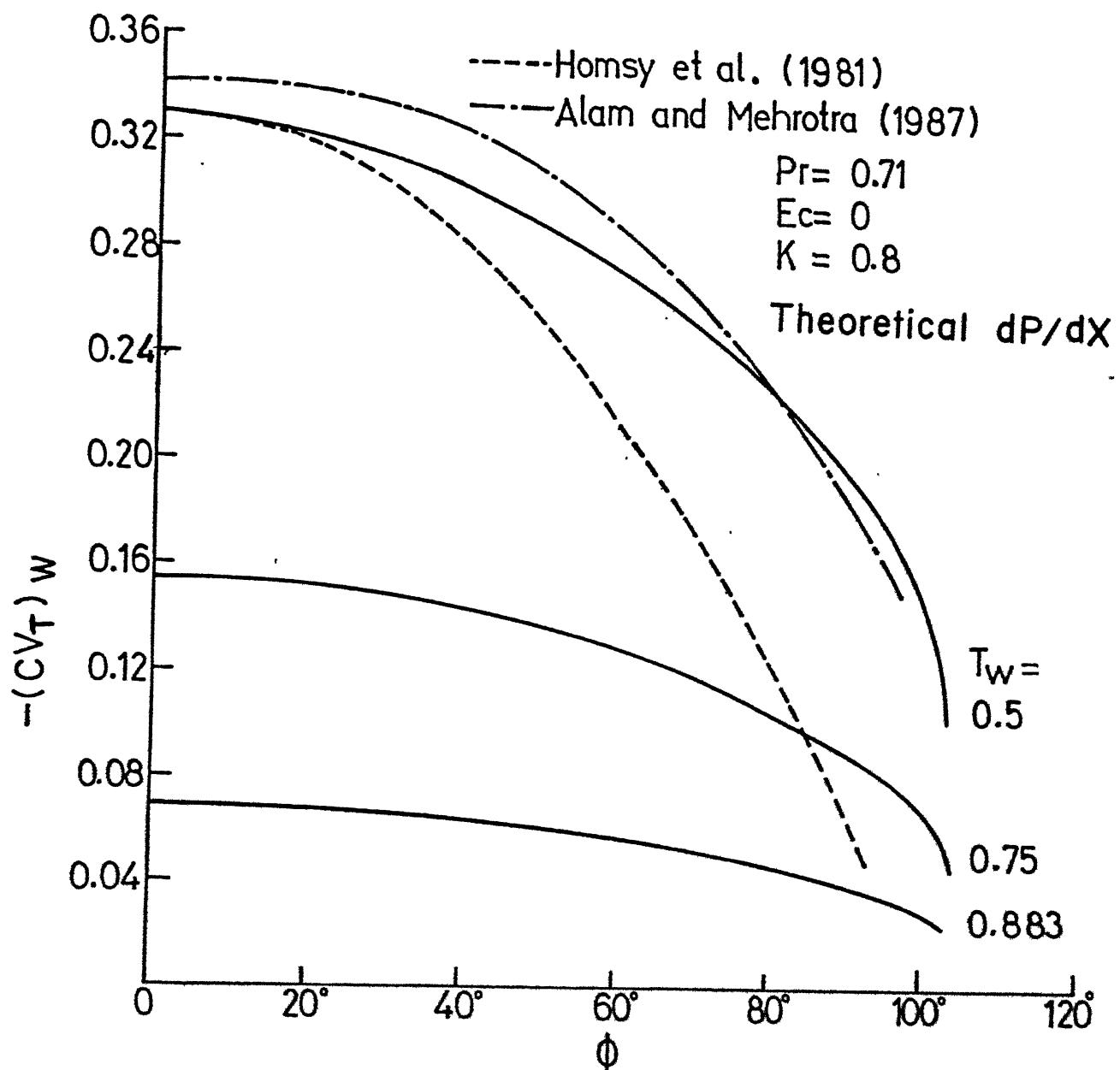
Fig.5.12　Particle flux at a cold cylinder surface
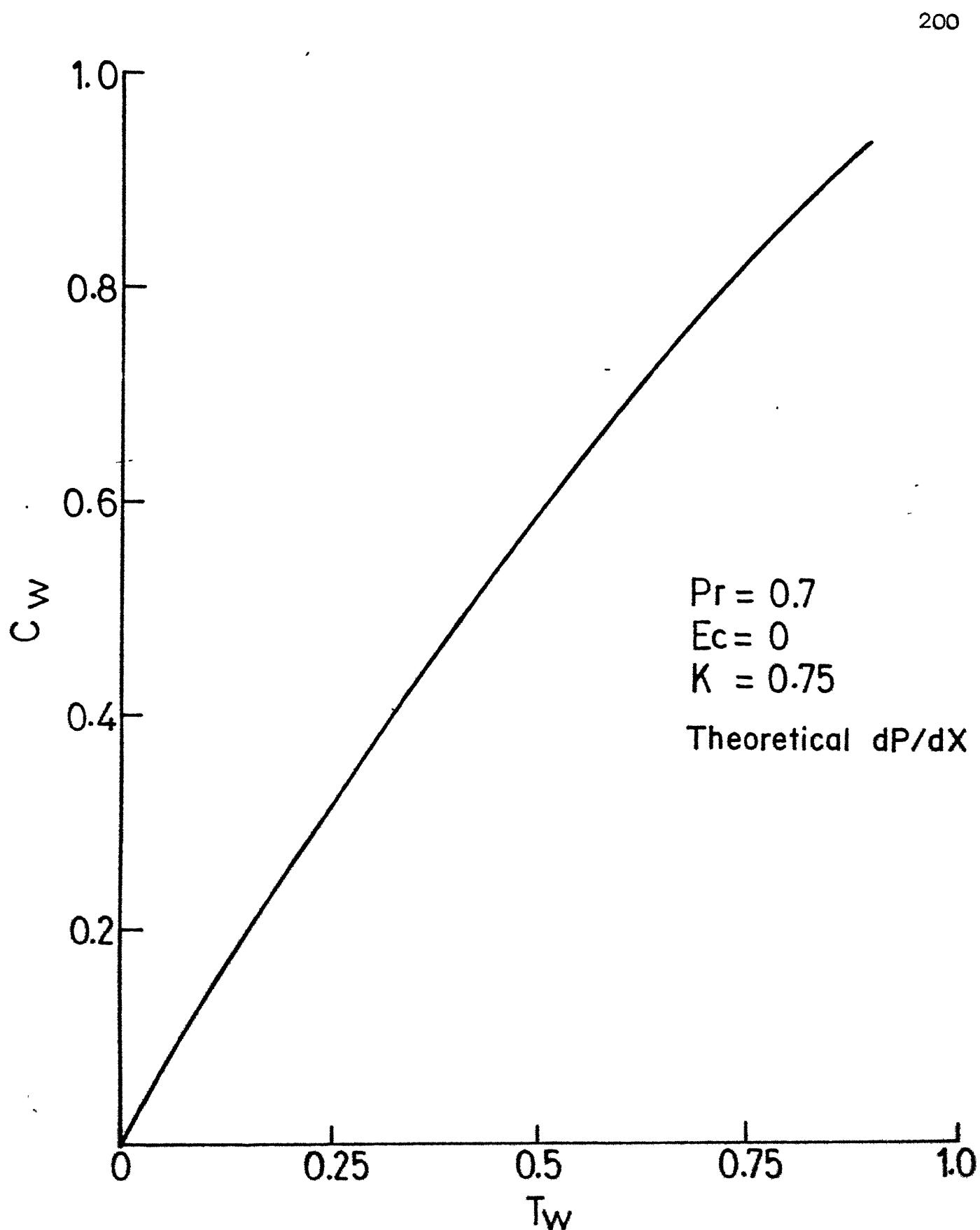
Fig. 5.13 Variation of wall concentration with cylinder wall temperature
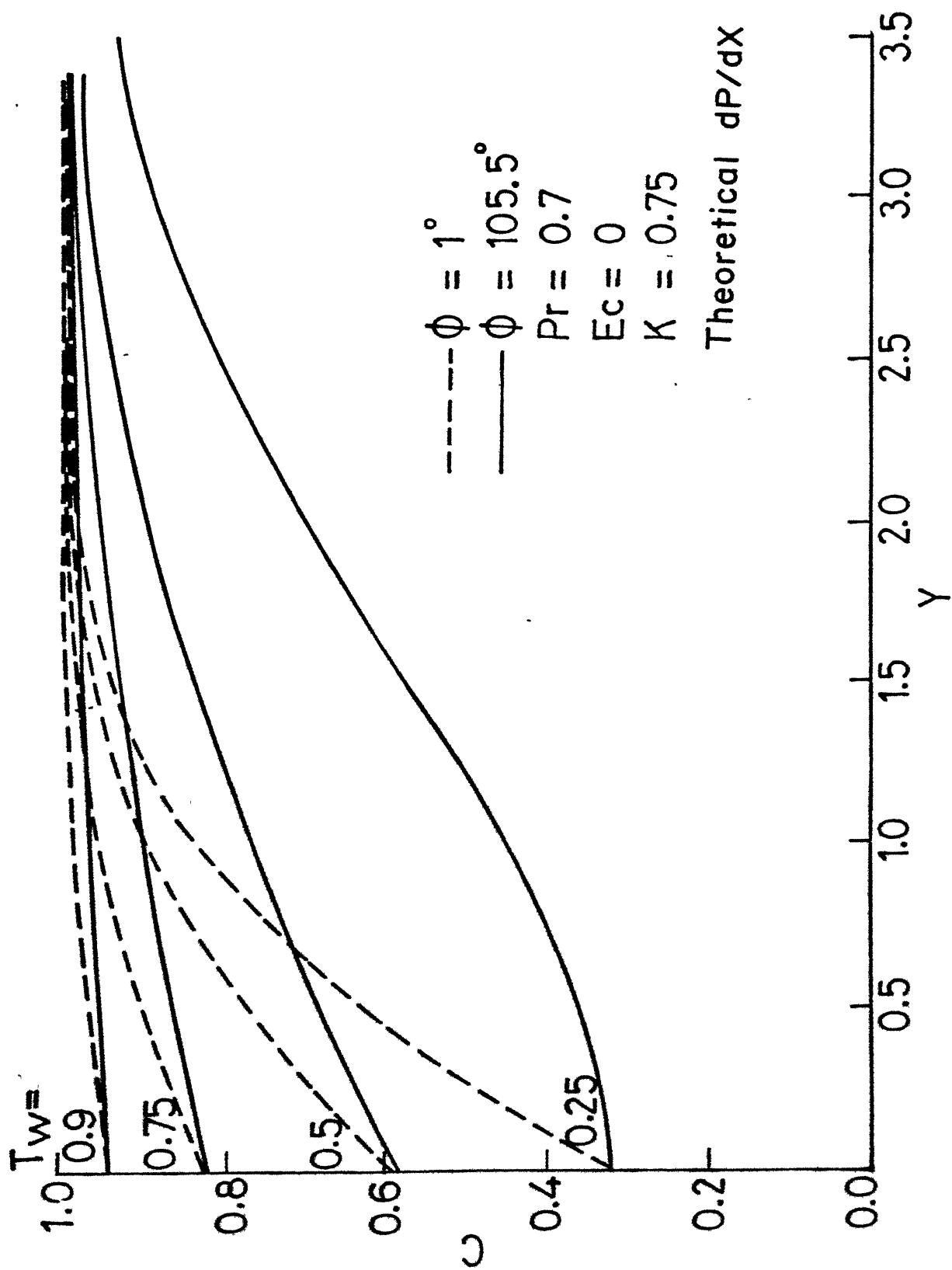
Fig. 5.14 Effect of wall temperature on the concentration profiles over a cold cylinder

Legend within figure:

- - - - $\phi = 1°$
——— $\phi = 105.5°$
$Pr = 0.7$
$Ec = 0$
$K = 0.75$
Theoretical dP/dX

$T_w =$ 0.9, 0.75, 0.5, 0.25

Axes: C (vertical), Y (horizontal)
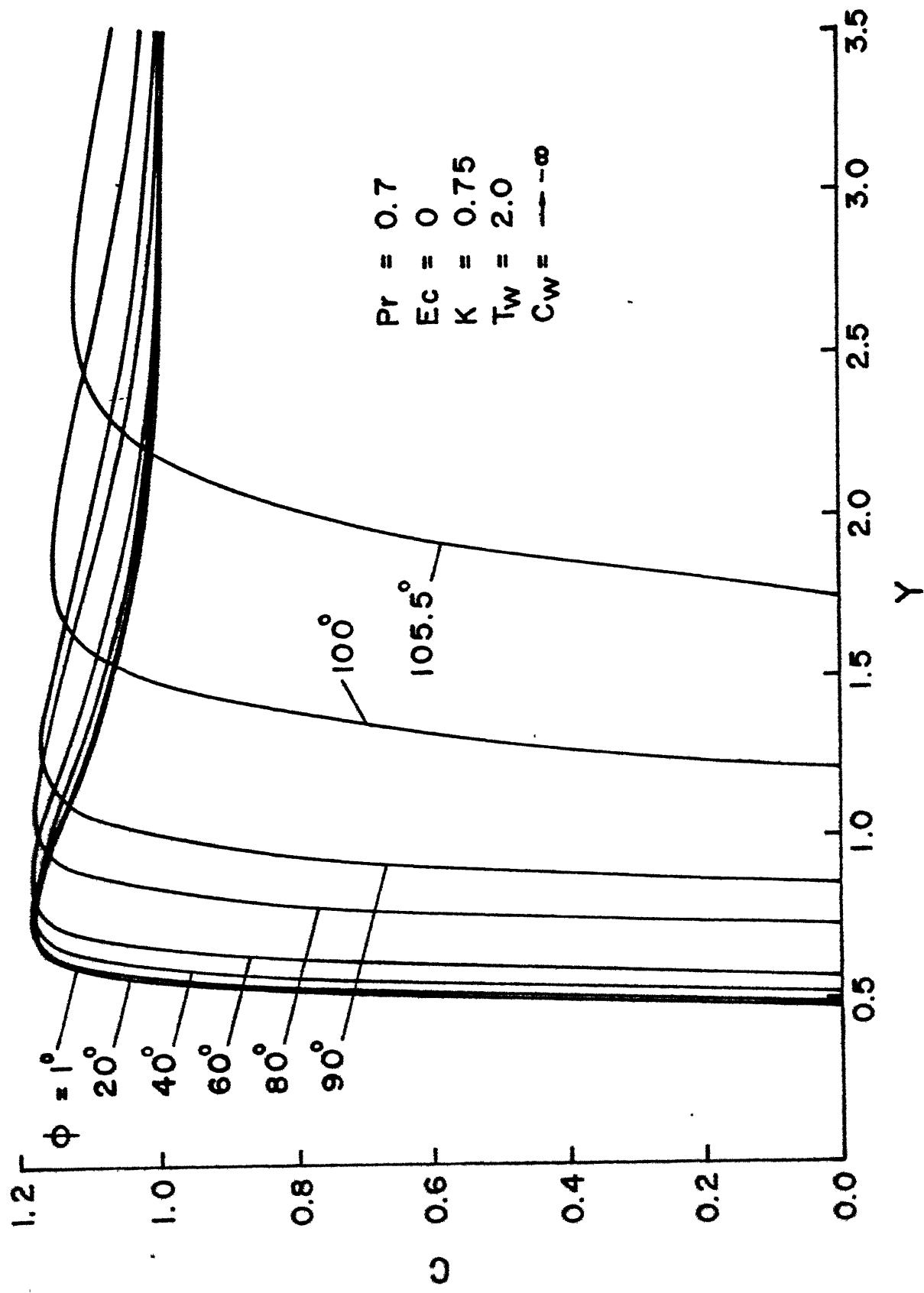
Fig. 5.15 Particle concentration profiles over a hot cylinder at different locations (Theoretical pressure distribution)
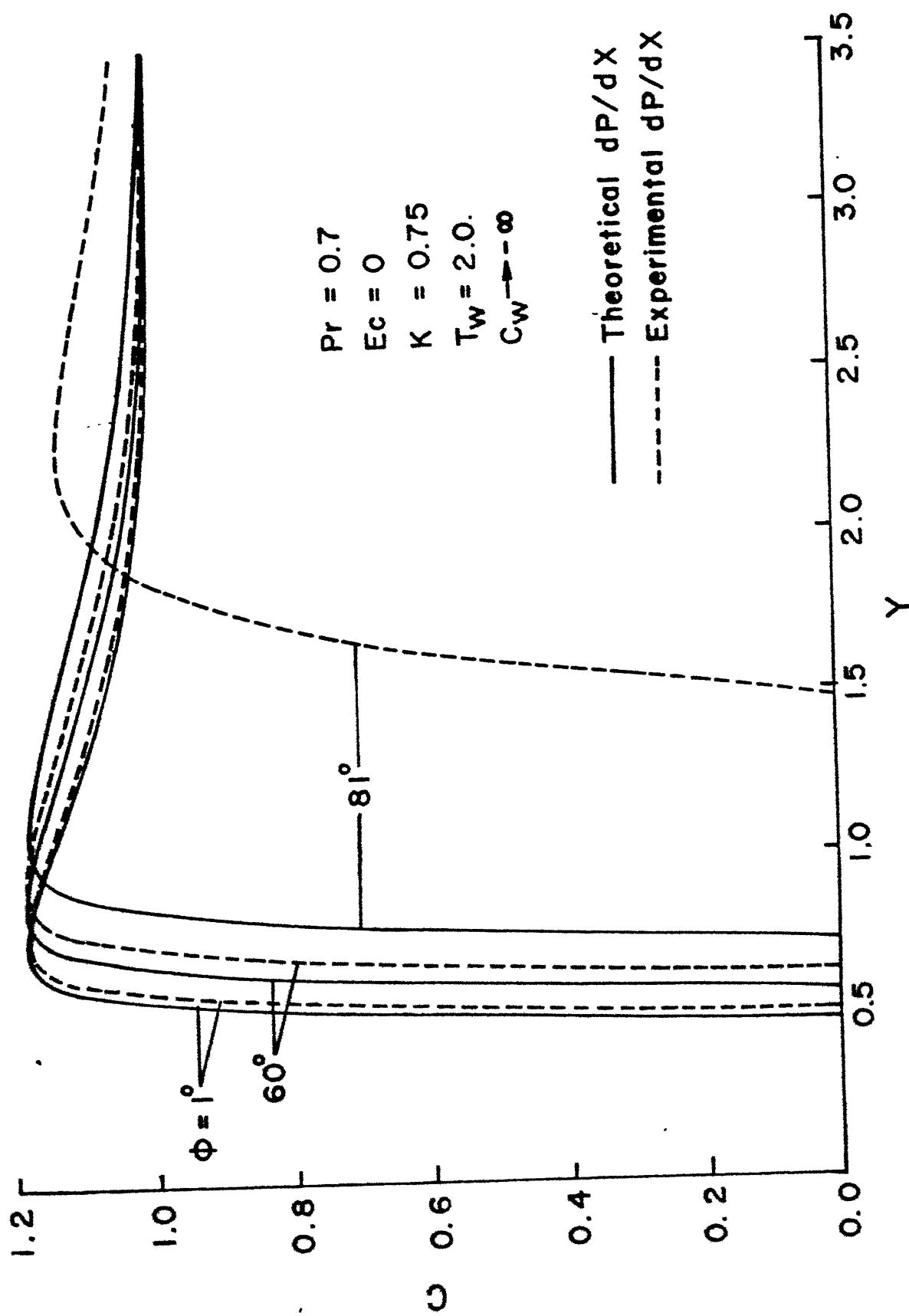
Fig.5.16 Effect of pressure distribution on the particle concentration profiles for flow past a hot cylinder

Pr = 0.7
Ec = 0
K = 0.75
T_w = 2.0.
$C_w \longrightarrow \infty$

——————— Theoretical dP/dX

- - - - - - - Experimental dP/dX

Y

C

$\phi = 1°$

60°

81°
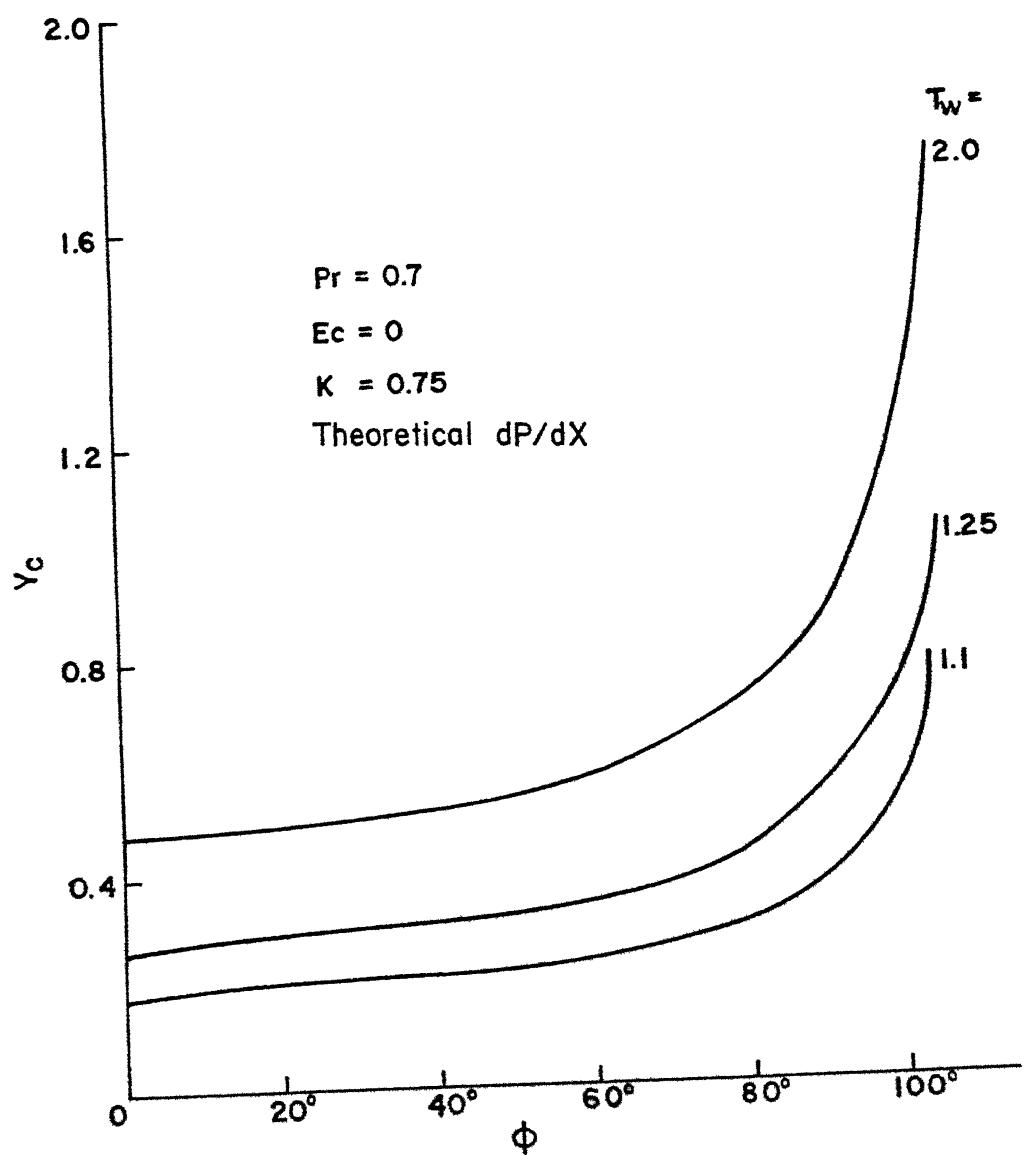
Fig. 5.17 critical layer thickness at different locations over a hot cylinder.
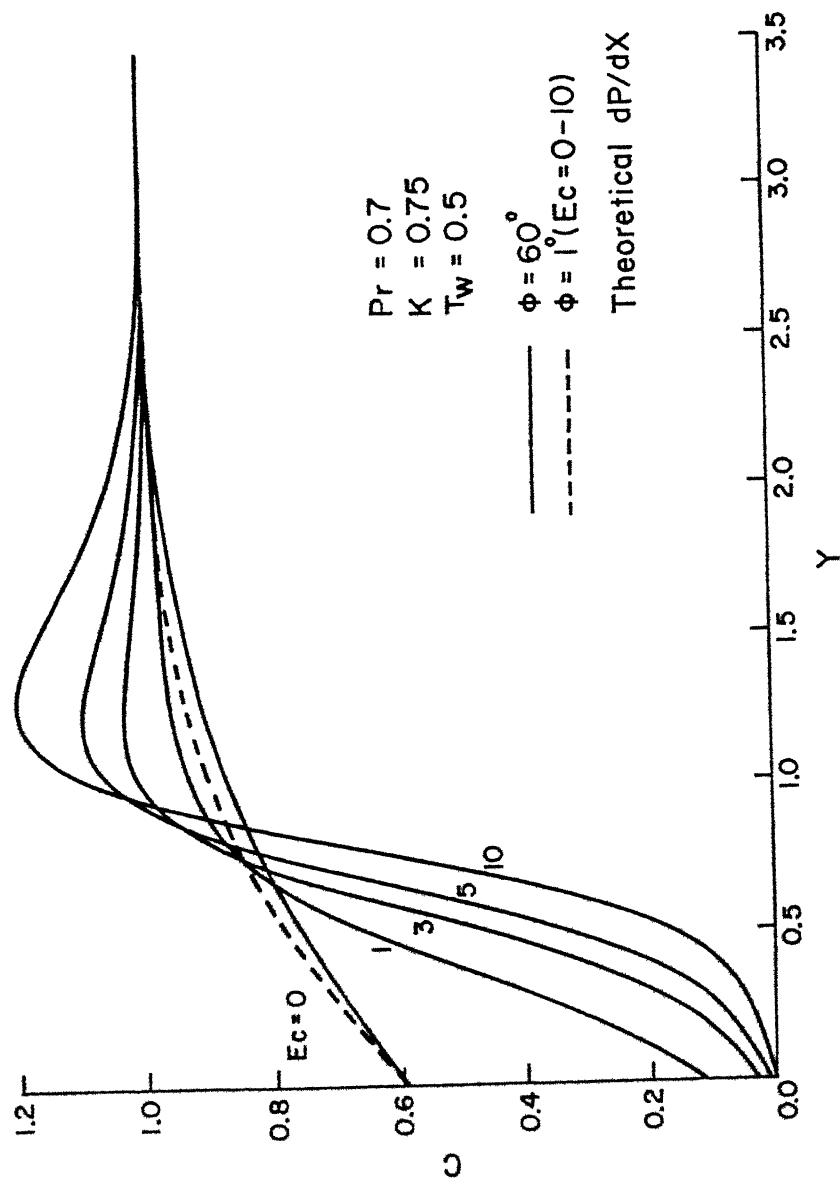
Fig. 5.18 Influence of viscous dissipation on the particle concentration
profiles for flow past a cold cylinder

Pr = 0.7
K = 0.75
Tw = 0.5

$\phi = 60°$
$\phi = 1°(Ec = 0-I0)$

—— Theoretical dP/dX
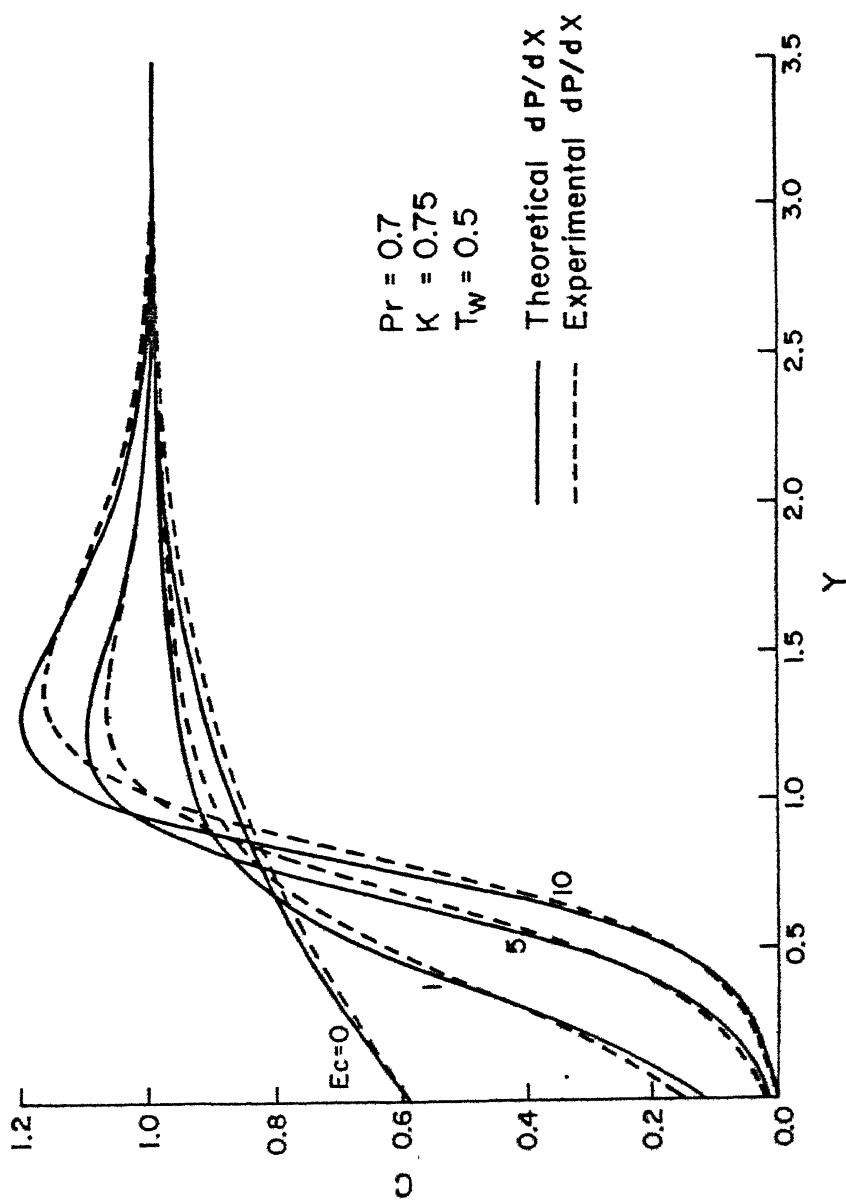
Fig. 5.19 Effect of pressure distribution on particle concentration profiles for flow past a cold cylinder with different viscous dissipation rates ($\phi = 60°$)
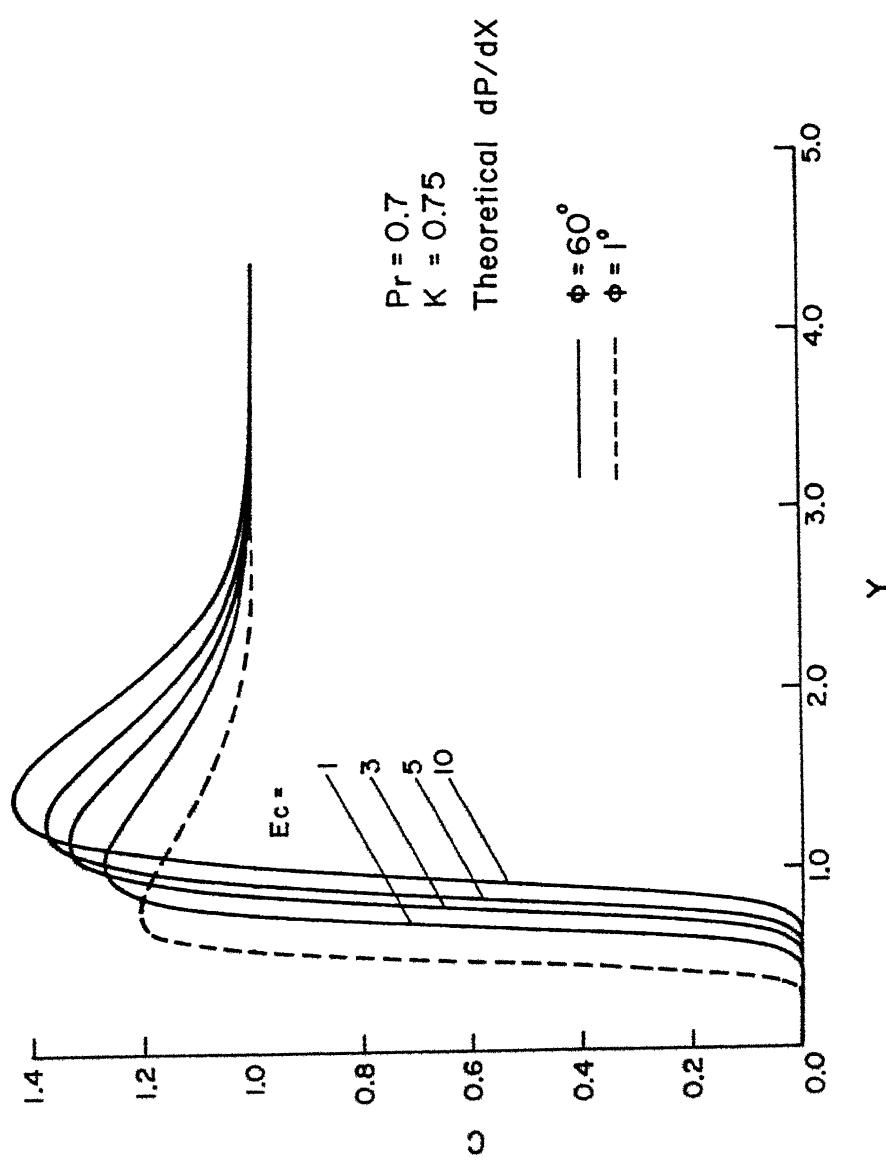
Fig. 5.20 Influence of viscous dissipation on the particle concentration profiles for flow past an insulated cylinder
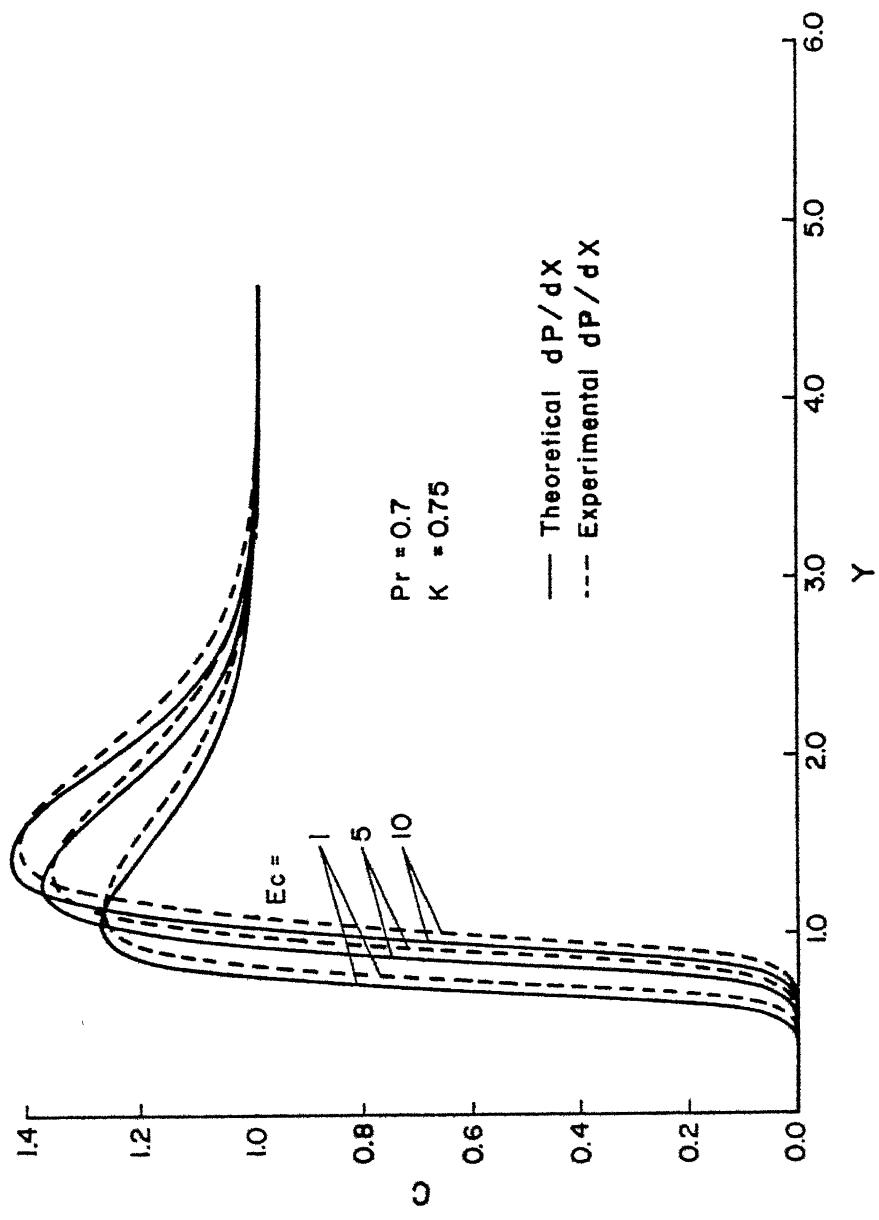
Fig. 5.21 Effect of pressure distribution on particle concentration profiles for flow past an insulated cylinder with different viscous dissipation rates ($\phi = 60°$)

CHAPTER 6

CONCLUSIONS

A finite-difference solution for laminar two-dimensional thermophoretic flow with non-zero pressure gradient in the flow field is obtained. A better understanding is achieved about the mechanisms that account for thermophoretic deposition in such situations. Two specific examples of flow due to the impingement of a slot jet on a flat plate at any angle of inclination (0-90°) and cross flow over a circular cylinder are considered. A marching technique along with self-adaptive grid in the direction normal to the body surface is used.

A drastic change in the behaviour of some of the boundary layer parameters due to the presence of the stagnation point are demonstrated. The presence of a stagnation point for non-zero angles of the plate significantly affects both the pressure distribution over the plate and the potential flow velocity U_s at the plate. Also the non-zero angle causes a drastic change in the

transverse velocity distribution in the boundary layer. Near the stagnation point the hydrodynamic and thermal boundary layers are thinner for lower angles of impingement but away from the stagnation point they are thinner for higher angles of impingement except for $\beta = 90^{\circ}$. The local skin friction coefficient shows a large value close to the stagnation point at small angles of inclination of the plate. Near the stagnation point the local Nusselt number attains a value as high as ten times that far from the stagnation point for $\beta = 15^{\circ}$. However, this ratio reduces to less than two for $\beta = 90^{\circ}$. At zero angle of inclination of the plate the present procedure yields the standard C_f and Nu values for Blasius flow. Also, the present results for $\beta = 90^{\circ}$ match exactly with earlier results. For other values of β, this is the first study.

The particle concentration boundary layer is studied for a wide range of parameters. Its behaviour on a cold wall ($T_w < 1$) is found to be similar to that of the velocity and temperature profiles. The concentration of particles at the cold wall is found to be almost independent of the X-location and the value of the pressure gradient when T_w and K are held constant. This is

interesting since it implies an almost uniform
particle concentration at the wall in
any external laminar flow situation as long as the wall
temperature (less than the free stream temperature) and
thermophoretic coefficient are constant. Moreover, the
value of the particle concentration at the cold wall
increases with the wall temperature. Increase in con-
centration at the cold wall is also noted for lower
thermophoretic coefficients. However, this is not true
for Blasius flow for which the wall concentration first
rises, then drops as the thermophoretic coefficient is
reduced to zero.

For the heated wall condition ($T_w > 1$) presence of
a critical layer adjacent to the wall and particle con-
centration just outside this layer higher than that in
the free stream are notable characteristics of the con-
centration profiles, when the product of Prandtl number
and thermophoretic coefficient is less than unity. When
this product is greater than unity, a critical layer with
very high particle concentration exists adjacent to the
plate. The critical layer thickness is a strong function
of the pressure gradient and the location from the stag-
nation point. However, only a marginal change in peak

concentration value is noted with respect to these parameters.

The dissipation of mechanical energy in the fluid also has a significant effect on the particle concentration behaviour. In the cold wall case, particle concentration at the wall drops suddenly first as Ec is increased from 0 to 1 and slowly thereafter reaching a zero value for Ec = 10 in the case of flow past a cylinder. The cold wall temperature profiles exhibit a maximum within the boundary layer at higher Ec values. Larger Ec with adiabatic wall conditions yields concentration profiles similar to that for a hot wall except that $C_w = 0$ and concentration gradient at the wall also vanishes. Overall, the effect of viscous dissipation is significant at $\beta = 0$ ($dP/dX = 0$) but small at $\beta = 90^\circ$ and for the flow past a cylinder.

The numerical solution procedure employed for the present analysis is quite general and can be used for a number of similar problems of engineering importance on thermophoresis. Variable properties and compressible flow can be easily considered. Analysis can also be carried out on similar lines for internal flow situations, for example, for the thermophoretic study of developing flow

in the entrance region of pipes and channels. Of course,
in such flows, the pressure gradient is unknown apriori.
However, methods to solve for the hydrodynamically and
thermally developing flow in a pipe or channel (without
thermophoresis) are well known (Hornbeck, 1973). The
effect of radiation neglected in the present analysis can
become a serious limitation in some cases. For example,
radiation effects cannot be neglected for the laser modi-
fication of the MCVD or OVD processes currently used for
the fabrication of graded index optical fiber preforms.
More importantly for the flows studied here, the boundary
layer is turbulent in practical applications. The present
method can also be used in such a case along with appro-
priate models of turbulence.

APPENDIX A

TRIDIAGONAL ALGORITHM

The discretized form of momentum, energy and particle concentration equations (3.11) through (3.16) written for all $k = 1$ (1) n transverse Y-locations at any marching X-location (j+1) leads to a set of simultaneous equations. The coefficient matrix of these equations have non-zero elements clustered on the three main diagonals. In some cases, the concentration equation yields non-zero elements on two main diagonals only. All the remaining elements of the coefficient matrix are zero. Generally, this set of equations may be represented in the following form.

$$
\begin{bmatrix}
B_1 & C_1 & & & & & \\
A_2 & B_2 & C_2 & & & & \\
& A_3 & B_3 & C_3 & & & \\
& & & \ddots & & & \\
& & & A_k & B_k & C_k & \\
& & & & \ddots & & \\
& & & & A_{n-1} & B_{n-1} & C_{n-1} \\
& & & & & A_n & B_n
\end{bmatrix}
*
\begin{bmatrix}
X_1 \\
X_2 \\
X_3 \\
\vdots \\
X_k \\
\vdots \\
X_{n-1} \\
X_n
\end{bmatrix}
=
\begin{bmatrix}
R_1 \\
R_2 \\
R_3 \\
\vdots \\
R_k \\
\vdots \\
R_{n-1} \\
R_n
\end{bmatrix}
\qquad (A.1)
$$

The method used for solving this tridiagonal matrix problem is a special adaptation of the Gaussian elimination procedure, which is commonly known as the Thomas algorithm (cf. Roache, 1973). To keep the size of the round-off errors down, Richtmyer and Morton (1967) show that it is sufficient that

$$A_k \leq 0, \quad B_k > 0, \quad C_k \leq 0 \quad \text{and} \quad B_k \geq |A_k + C_k| , \qquad (A.2)$$

for all k from k = 1 to k = n.

In the procedure used for solution, a series of matrix operations are carried out to make all the diagonal elements one and the lower non-zero diagonal elements vanish. The resulting set of equations is of the form

$$
\begin{bmatrix}
1 & C_1' & & & & & & \\
& 1 & C_2' & & & & & \\
& & 1 & C_3' & & & & \\
& & & \ddots & & & & \\
& & & & 1 & C_k' & & \\
& & & & & \ddots & & \\
& & & & & & 1 & C_{n-1}' \\
& & & & & & & 1
\end{bmatrix}
*
\begin{bmatrix}
X_1 \\
X_2 \\
X_3 \\
\vdots \\
X_k \\
\vdots \\
X_{n-1} \\
X_n
\end{bmatrix}
=
\begin{bmatrix}
R_1' \\
R_2' \\
R_3' \\
\vdots \\
R_k' \\
\vdots \\
R_{n-1}' \\
R_n'
\end{bmatrix}
\qquad (A.3)
$$

From (A.3) it directly follows that

$$X_n = R'_n \qquad\qquad (A.4)$$

All the remaining X_k values are calculated in sequence from $k = n-1$ to $k = 1$ by back substitution.

This method has the great advantage that all initially zero elements of the tridiagonal band in (A.1) remain zero throughout all operations. As a result, these elements do not require storage on the digital computer. Thus the only storage required is for the tridiagonal band and the unknown and right side column vectors. The total storage required is therefore (5n-2) locations rather than (n^2+2n) required for a complete matrix representation. In addition, the diagonals A_k, B_k and C_k may be represented as vectors rather than as elements of a matrix. This eliminates the necessity of using matrix notation which requires additional operations in the system and hence additional computer time. The most important time saving with this method, however, is brought about by the fact that the number of necessary operations is of $O(n)$, whereas for the usual Gaussian elimination for a filled matrix, the number of operations is of $O(n^3)$.

A slightly improved version of the FORTRAN code of Hornbeck (1973) is used for solution in the present analysis. Sets of equations with n of the order of several hundred are readily and accurately handled using this routine.

APPENDIX B

VARIABLE MESH TECHNIQUE

For computational efficiency but without sacrificing accuracy of the solution, a variable grid size is required in both X and Y-directions. The mesh size in the marching X-direction can be changed at will without any modification in the discretized equations since only first order forward differences of error $O(\Delta X)$ are involved. However, the real necessity for a variable mesh is evident along the Y-direction in which variation in the gradients of velocity, temperature and concentration is quite large. Accordingly, a self-adaptive grid scheme (Sec. 3.4) was employed to determine the appropriate mesh size along the Y-direction. The mesh size (ΔY) is automatically made fine in regions of large gradients and relatively coarse away from it by the self-adaptive grid scheme. This makes every ΔY uniquely different from the other.

The modification used here in the discretized equations due to a variable ΔY is essentially of the same nature as that described by Hornbeck (1973). A variable

ΔY presents no difficulty in the calculation of particle concentration (using Eqns. (3.13) through (3.16)) since only forward or backward first order differences of error $O(\Delta Y)$ are used in these equations. However, the use of central differences in the Y-direction for discretizing the momentum and the energy equations (Eqns. (3.2) and (3.3) respectively in which the error is $O(\Delta Y^2)$), makes it impossible to vary ΔY without some modification in the previously presented Eqns. (3.11) and (3.12).

Suppose the mesh size is to be changed from a smaller ΔY_2 to a larger ΔY_1 at the transverse position corresponding to $k = p$, as shown in Fig. B.1(a). A velocity $U_{j+1,q}$ (or temperature $T_{j+1,q}$ in the case of energy equation) at a point ΔY_2 above the point $k = p$ is determined by passing a parabola through the values $U_{j+1,p+1}$, $U_{j+1,p}$ and $U_{j+1,p-1}$ and then interpolating for $U_{j+1,q}$ yielding

$$U_{j+1,q} = \frac{\sigma-1}{\sigma+1} U_{j+1,p-1} + 2(1-\sigma) U_{j+1,p}$$

$$+ 2 \frac{\sigma^2}{1+\sigma} U_{j+1,p+1} \, , \qquad (B.1)$$

where σ is the ratio of smaller to larger mesh size, i.e.,

$$\sigma = \Delta Y_2 / \Delta Y_1 \qquad (B.2)$$

Similarly, for the change of mesh size from a larger value (ΔY_1) to a smaller value (ΔY_2) as shown in Fig. B.1(b) the corresponding relation for $U_{j+1,q}$ is

$$U_{j+1,q} = 2\,\frac{\sigma^2}{1+\sigma}\,U_{j+1,p-1} + 2(1-\sigma)\,U_{j+1,p}$$

$$+ \frac{\sigma-1}{\sigma+1}\,U_{j+1,p+1} \;, \tag{B.3}$$

where σ is given again by Eqn. (B.2).

The proper value of $U_{j+1,q}$ found in Eqn. (B.1) or Eqn. (B.3) can be used directly at every k location where the adjacent mesh sizes are not equal. When the mesh size changes from small to large, substitution of Eqn. (B.1) in the discretized momentum equation (3.11) and energy equation (3.12) gives, after rearrangement, respectively :

$$\left[\,\left\{-\frac{V^{*}_{j+1,k}}{2(\Delta Y)} - \frac{1}{(\Delta Y)^2}\right\} + \frac{\sigma-1}{\sigma+1}\left\{\frac{V^{*}_{j+1,k}}{2(\Delta Y)} - \frac{1}{(\Delta Y)^2}\right\}\,\right] U_{j+1,k-1}$$

$$+ \left[\,\left\{\frac{U^{*}_{j+1,k}}{\Delta X} + \frac{2}{(\Delta Y)^2}\right\} + 2(1-\sigma)\left\{\frac{V^{*}_{j+1,k}}{2(\Delta Y)} - \frac{1}{(\Delta Y)^2}\right\}\,\right] U_{j+1,k}$$

$$+ \left[2\,\frac{\sigma^2}{1+\sigma}\left\{\frac{V^{*}_{j+1,k}}{2(\Delta Y)} - \frac{1}{(\Delta Y)^2}\right\}\,\right] U_{j+1,k+1}$$

$$= \frac{U_{j+1,k}}{\Delta X}\,U_{j,k} - \frac{dP}{dX} \;, \tag{B.4}$$

$$[\; \{ - \frac{V_{j+1,k}}{2(\Delta Y)} - \frac{1}{Pr(\Delta Y)^2} \} + \frac{\sigma-1}{\sigma+1} \{ \frac{V_{j+1,k}}{2(\Delta Y)} - \frac{1}{Pr(\Delta Y)^2} \} \;] \; T_{j+1,k-1}$$

$$+ \; [\; \{ \frac{U_{j+1,k}}{\Delta X} + \frac{2}{Pr(\Delta Y)^2} \} + 2(1-\sigma) \{ \frac{V_{j+1,k}}{2(\Delta Y)} - \frac{1}{Pr(\Delta Y)^2} \} \;] \; T_{j+1,k}$$

$$+ \; [\; 2 \frac{\sigma^2}{1+\sigma} \{ \frac{V_{j+1,k}}{2(\Delta Y)} - \frac{1}{Pr(\Delta Y)^2} \} \;] \; T_{j+1,k+1}$$

$$= \frac{U_{j+1,k}}{\Delta X} T_{j,k} + \frac{Ec}{(\Delta Y)^2} [\frac{\sigma^2}{1+\sigma} U_{j+1,k+1}$$

$$+ (1-\sigma) \; U_{j+1,k} - \frac{1}{1+\sigma} U_{j+1,k-1}]^2 \; . \qquad\qquad (B.5)$$

The relations obtained by substituting Eqn. (B.3) into the momentum and energy equations, while the mesh size changes from a large to a small value, are identical to (B.4) and (B.5). These modifications in the coefficients of the tridiagonal matrix are incorporated in the computer code while solving momentum and energy equations for U and T respectively.
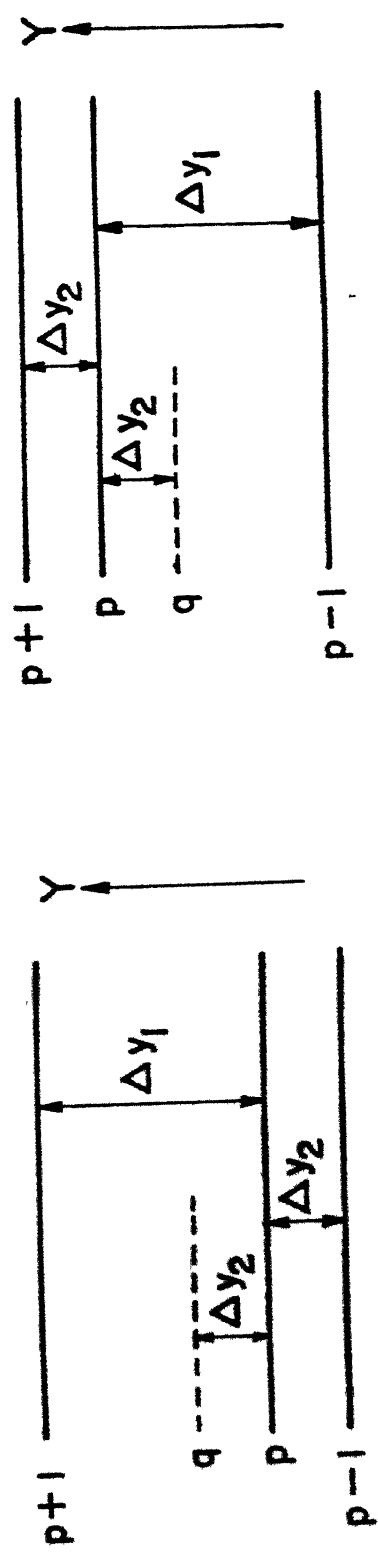
(a) Small mesh to large mesh   (b) Large mesh to small mesh

Fig. B.1 Change of mesh size

REFERENCES

1. Alam, M.K., 1987, Private communication.

2. Alam, M.K. and Mehrotra, S., 1987, 'Thermophoretic Deposition of Particles in Optical Fiber Preform Fabrication,' ASME Paper No. 87-HT-6, 24th Nat. Heat. Transfer Conf., Pittsburgh, Aug. 1987.

3. Brock, J.R., 1962, 'On the Theory of Thermal Forces Acting on Aerosol Particles,' J. Colloid Sci., Vol. 17, pp. 768-770.

4. Derjaguin, B.V., Storozhilova, A.I. and Rabinovich, Ya I., 1966, 'Experimental Verification of the Theory of Thermophoresis of Aerosol Particles,' J. Colloid Interface Sci., Vol. 21, pp. 35-58.

5. Derjaguin, B.V., Rabinovich, Ya I., Storozhilova, A.I. and Shcherbina, G.I., 1976, 'Measurement of the Coefficient of Thermal Slip of Gases and the Thermophoresis Velocity of Large Size Aerosol Particles,' J. Colloid Interface Sci., Vol. 57, pp. 451-461.

6. Derjaguin, B.V. and Yalamov, Yu, 1965, 'Theory of Thermophoresis of Large Aerosol Particles,' J. Colloid Sci., Vol. 20, pp. 555-570.

7. Epstein, M., Hauser, G.M. and Henry, R.E., 1985, 'Thermophoretic Deposition of Particles in Natural Convection Flow from a Vertical Plate,' ASME J. Heat Transfer, Vol. 107, pp. 272-276.

8. Fuchs, N.A., 1964, <u>The Mechanics of Aerosols</u>, p. 59, Pergamon Press, New York.

9. Fulford, G.D., Moo-Young, M. and Babu, M., 1971, 'Thermophoretic Acceleration of Particle Deposition from Laminar Air Streams,' <u>Can. J. Ceram. Eng.</u>, Vol. 49, pp. 553-556.

10. Gardon, R. and Akfirat, J.C., 1966, 'Heat Transfer Characteristics of Impinging Two-Dimensional Air Jets,' <u>ASME J. Heat Transfer</u>, Vol. 88, pp. 101-108.

11. Goldsmith, P. and May, F.G., 1966, 'Diffusiophoresis and Thermophoresis in Water Vapour Systems,' <u>Aerosol Science</u>, C.N. Davies, ed., Academic Press, London, pp. 163-194.

12. Gokoglu, S.A. and Rosner, D.E., 1984a, 'Correlation of Thermophoretically - Modified Small Particle Diffusional Deposition Rates in Forced Convection Systems with Variable Properties, Transpiration Cooling and/or Viscous Dissipation,' <u>Int. J. Heat Mass Transfer</u>, Vol. 27, pp. 639-646.

13.   Gokoglu, S.A. and Rosner, D.E., 1984b, 'Effect of Particulate Thermophoresis in Reducing the Fouling Rate Advantages of Effusion - Cooling,' _Int. J. Heat and Fluid Flow_, Vol. 5, pp. 37-41.

14.   Gokoglu, S.A. and Rosner D.E., 1985a, 'Viscous Dissipation Effects on Thermophoretically Augmented Aerosol Particle Transport Across Laminar Boundary Layers,' _Int. J. Heat and Fluid Flow_, Vol. 6, pp. 293-297.

15.   Gokoglu, S.A. and Rosner, D.E., 1985b, 'Thermophoretically Enhanced Mass Transport Rates to Solid and Transpiration - Cooled Walls Across Turbulent (Law-of-the-Wall) Boundary Layers,' _Ind. Eng. Chem. Fundam._, Vol. 24, pp. 208-214.

16.   Gokoglu, S.A. and Rosner, D.E., 1986, 'Thermophoretically Augmented Mass Transfer Rates to Solid Walls Across Laminar Boundary Layers,' _AIAA J._, Vol. 24, pp. 172-179.

17.   Goren, S.L., 1977, 'Thermophoresis of Aerosol Particles in the Laminar Boundary Layer on a Flat Plate,' _J. Colloid Interface Sci._, Vol. 61, pp. 77-85.

18.   Green, H.L. and Lane, W.R., 1964, _Particulate Clouds: Dusts, Smokes and Mists_, 2nd Ed., Chapter 6, E. and F.N. Spon Ltd., London.

19. Hanks, R.W. and Ruo, H.C., 1966, 'Laminar-Turbulent Transition in Ducts of Rectangular Cross Section', Ind. Eng. Chem. Fund., Vol. 5, pp. 558-561.

20. Homsy, G.M., Geyling, F.T. and Walker, K.L., 1981, 'Blasius Series of Thermophoretic Deposition of Small Particles,' J. Colloid Interface Sci., Vol. 83, pp. 495-501.

21. Hornbeck, R.W., 1973, Numerical Marching Techniques in Fluid Flows with Heat Transfer, Chapters 2,6 and 7 and Appendices A and D, SP-297, NASA, Washington, D.C.

22. Kennard, E.H., 1938, Kinetic Theory of Gases, p. 333, McGraw-Hill, New York.

23. Miyazaki, H. and Silberman, E., 1972, 'Flow and Heat Transfer on a Flat Plate Normal to a Two-Dimensional Laminar Jet Issuing From a Nozzle of Finite Height,' Int. J. Heat Mass Transfer, Vol. 15, pp. 2097-2107.

24. Milne-Thomson, L.M., 1960, Theoretical Hydrodynamics 4th Ed., pp. 287-290, Macmillon Co., London.

25. Morse T.F. and Cipolla Jr., J.W., 1984, 'Laser Modification of Thermophoretic Deposition,' J. Colloid Interface Sci., Vol. 97, pp. 137-148.

26. Morse, T.F., Wang, C.Y. and Cipolla Jr., J.W. 1985, 'Laser-Induced Thermophoresis and Particulate Deposition Efficiency,' ASME J. Heat Transfer, Vol. 107, pp. 155-160.

27. Nakahashi, K. and Deiwert, G.S., 1984, 'A Practical Adaptive-Grid Method for Complex Fluid Flow Problems,' NASA, TM-85989.

28. Nakahashi, K. and Deiwert,G.S., 1986, 'Three-Dimensional Adaptive Grid Method,' AIAA J., Vol. 24, pp. 948-954.

29. Nakahashi, K. and Deiwert, G.S., 1987, 'Self-Adaptive-Grid Method with Application to Airfoil Flow,' AIAA J., Vol. 25, pp. 513-520.

30. Richtmyer, R.D. and Morton, K.W., 1967, Difference Methods for Initial-Value Problems, p. 199, John Wiley and Sons, New York.

31. Roache, P.J., 1982, Computational Fluid Dynamics, 2nd Ed., Appendix A, Hermosa Publishers, Albuquerque.

32. Rosner, D.E. and Fernandez de la Mora, J., 1982, 'Small Particle Transport Across Turbulent Nonisothermal Boundary Layers,' ASME J. Engg. Power, Vol. 104, pp. 885-894.

33. Schlichting, H., 1979, Boundary Layer Theory, 7th Ed., Chapters 7, 9, 10 and 12, McGraw-Hill, New York.

34. Simpkins, P.G., Greenberg-Kosinski, S. and Macchesney, J.B., 1979, 'Thermophoresis: The Mass Transfer Mechanism in Modified Chemical Vapor Deposition,' J. Appl. Phys., Vol. 50, pp. 5676-5681.

35. Smith, A.M.O. and Clutter, D.W., 1963, 'Solution of the Incompressible Laminar Boundary Layer Equations,' AIAA J., Vol. 1, pp. 2062-2071.

36. Springer, G.S., 1970, 'Thermal Force on Particles in the Transition Regime,' J. Colloid Interface Sci., Vol. 34, pp. 215-220.

37. Street, R.E., 1960, 'A Study of Boundary Conditions in Slip-Flow Aerodynamics,' Rarefied Gas Dynamics, F.M. Devienne, ed., Pergamon Press, London, pp.276-292.

38. Talbot, L., Cheng, R.W., Schefer, R.W. and Willis D.R., 1980, 'Thermophoresis of Particles in a Heated Boundary Layer,' J. Fluid Mech., Vol. 101, part 4, pp. 737-758.

39. Waldmann, L., 1959, 'Uberdie Kraft eines inhomogenen Gases anf Kleine suspendierte Kugeln,' Z. Naturforsch, Vol. 14 A, pp. 589-599 .

40. Waldmann, L. and Schmitt, K.H. 1966, 'Thermophoresis and Diffusiophoresis of Aerosols,' Aerosol Science, C.N. Davies, ed., Academic Press, London, pp. 137-162.

41. Walker, K.L., Geyling, F.T. and Nagel S.R., 1980, 'Thermophoretic Deposition of Small Particles in the Modified Chemical Vapour Deposition (MCVD) Process,' J. Amer. Ceram. Soc., Vol. 63, pp. 552-558.